FOREWORD

The work reported herein was sponsored by the United States Army Research Office, Durham, under Contract No. DA-31-124-ARO-D-246. This report was presented by Teng Hsueh Chuang as partial fulfillment of the requirements for the Doctors of Philosphy degree at The Ohio State University.

The authors wish to thank Dr. E. R. Pejack for his suggestions and assistance with the experimental setup used.

ABSTRACT

An experimental and analytical program was undertaken to investigate the behavior of frost formation under an impinging electric wind induced by a positive wire-plane corona in a non-uniform electric field. A vertical test plate precooled to subfreezing temperatures was exposed to the ambient air and the effects of electric fields were studied through the application of a high voltage between the grounded test plate and a corona wire. Considerable increases in heat and mass transfer were found. The changes were attributed to the alteration of flow field from free convection to forced convection.

A simple theoretical model was developed for predicting the effects of electric fields upon the heat and mass transfer processes associated with frost formation. Two regions of the flow field created by the impinging electric wind are of primary importance in heat and mass transfer, namely the stagnation flow and the wall jet regimes. In the stagnation flow, a linear relation for the local heat and mass transfer coefficients was assumed between the stagnation point and the wall jet region. In the wall jet, the analysis was based on laminar flow. The mass transfer predicted by this model agrees quite satisfactorily with experimental results, but discrepancy between theory and experiment was observed in heat transfer.

An analysis was also made of a simplified model of transient heat conduction in a frost layer. Using a method due to Portnov the position and the temperature of the progressing frost-air interface was obtained in a series expansion in powers of $\sqrt{t}$. The coefficients up to the power $n = 6$ were given.

TABLE OF CONTENTS

TABLE OF CONTENTS - continued

LIST OF ILLUSTRATIONS

LIST OF ILLUSTRATIONS - continued

LIST OF ILLUSTRATIONS - continued

LIST OF ILLUSTRATIONS - continued

SYMBOLS

A	constant
a	thermal diffusivity
a	ampere
a_1, a_2, a_3	coefficients of the velocity boundary layer
B	defined as $(w_\infty - w_{1_f})/(1 - w_{1_f})$
B	beta function
B', B"	defined on page
B_s	incomplete beta function
b	defined as $(w_{1_f} - w_{1_w})/(T_f - T_w)$
b_j	width of a uniform impinging jet
b_1, b_2, b_3	profile coefficients of the thermal boundary layer
C_1, C_2	defined by Eqs. (2.7) and (2.8), respectively
C_3, C_4	defined on page
c_1, c_2, c_3	profile coefficients of the material boundary layer
c	specific heat of refrigerant
c_p	specific heat at constant pressure
D	diffusion coefficient
D_1, D_2	constants defined on page
d	distance between emitter and collector
d_1, d_2	constants defined by Eqs. (5.100) and (5.101), respectively
$\vec{E}$	electric field intensity
E	magnitude of $\vec{E}$
E_x, E_y	x and y component of E, respectively
F	function of velocity profile

F	electric force
F, F_1, F_2	functions defined on page
f	dimensionless function
G	function of temperature profile
Gr	average Grashoff number
Gr'	average Grashoff number for mass transfer
g	function defined as $f = g^2$
H	function of material profile
h	local convective heat transfer coefficient
$\bar{h}$	average convective heat transfer coefficient
h_m	local mass transfer coefficient
$\overline{h_m}$	average mass transfer coefficient
I	current
$\vec{J}$	current density
J	magnitude of $\vec{J}$
J_x, J_y	x and y component of current density, respectively
K	ion mobility
K_0, K_1, K_2	constants defined by Eqs. (5.25) and (5.27), respectively
k	thermal conductivity
L	length of vertical plate
Le	Lewis number
L_f	latent heat of sublimation of the frost
ℓ	length constant
M_1, M_2	molecular weight of species 1 and 2, respectively
m	mass flux

m, n	exponential constants
m_{tot}	total mass transfer rate
Pr	Prandtl number
p	independent variable introduced in Laplace transform
p	pressure
Q	total heat transfer rate
q	heat flux
q_{tot}	total convective heat transfer rate
R	defined by Eq. (5.7)
r_a	radius of corona wire
$\mathcal{S}$	area
Sc	Schmidt number
Sh	Sherwood number
s	defined as $s = (1 - g^3)$
T	temperature
t	time
U	unit function
U	defined by Eq. (5.8)
U	free stream velocity in x direction
u	velocity in x direction
u_{max}	maximum value of u
V	voltage
V_o	impinging velocity
$\vec{v}$	velocity vector
v	velocity in y direction

v_c	electric wind velocity at the collector
v_j	impinging velocity of a uniform jet
v_{max}	maximum value of v
W	mass flow rate
w_1	mass fraction of water vapor
w_a	specific humidity
x	direction along surface and direction of flow
$x_{½}$	value of x at which $u = u_{max}$
Y	frost layer thickness
y	direction normal to surface
$y_{½}$	value of y at which $v = v_{max}$
$\bar{y}$	defined as $y = y\sqrt{a}\,z$
z	dummy variable
z	distance from nozzle exit

Greek Letters

α	defined on page
α_1, α_2, α_3	constants defined by Eq. (5.56)
β	defined on page
β_m	concentration coefficient of expansion
β_T	coefficient of thermal expansion
γ	defined on page
Δ_m	defined as $\Delta_m = \delta_m/\delta$
Δ_T	defined as $\Delta_T = \delta_T/\delta$
ΔT	temperature difference
δ	thickness of velocity boundary layer

δ_m	thickness of material boundary layer
δ_T	thickness of thermal boundary layer
δ^*	displacement thickness
δ^{**}	momentum thickness
δ_m^{**}	defined by Eq. (4.33)
δ_τ^{**}	defined by Eq. (4.32)
ϵ	permittivity
ζ	defined as $y = \sqrt{a\zeta}Y(\tau)$
η	defined by Eq. (5.8)
θ, θ_0, θ_1	dimensionless temperatures
λ	characteristic of pressure gradient
λ	defined as $\lambda = Y/\sigma$
μ	viscosity
μa	microampere
ν	kinematic viscosity
ρ	density of air
ρ_e	charge density
ρ_f	density of frost
ρ_r	density of refrigerant
σ	defined as $\sigma = 2\sqrt{a\tau}$
τ	independent variable replacing t
φ	dimensionless mass fraction of water vapor
φ_1, φ_2	functions of ω
ψ	stream function
$\vec{\omega}$	vorticity

ω	defined as $\omega = Y\zeta$

Subscripts

f	frost surface
w	test plate surface
∞	ambient conditions

CHAPTER I

INTRODUCTION

1.1 INTRODUCTORY REMARKS

In recent years, there has been a significant increase of interest in electrohydrodynamics. Problems in this area are confronted in developing controlled thermal nuclear devices, ion drag pumping arrangements, ion propulsion systems as well as exotic heat transfer schemes, to mention four areas.

In the area of heat transfer, investigations have thus far mostly been confined to the case of two-phase (liquid-gas) heat transfer. This type of heat transfer is highly dependent on the force field experienced by the fluid. It has been shown by Choi[1] that electric field can enhance significantly the boiling heat transfer properties of a device. In their recent work, Velkoff and Miller[2], and Choi[3] demonstrated independently a similar improvement in condensation heat transfer. The instability of the liquid-gas interface caused by polarization and free charge interaction under the action of an external electric field has direct bearing on these phenomena.

The effects of electric wind on heat transfer from a heated plate to ambient air has been investigated by Velkoff[4]. He showed that considerable increase in heat transfer rate could be obtained through the use of the corona discharge. Similar observations have been reported by Godfrey[5] for forced convection at low free stream velocity.

The influence of electric fields on heat and mass transfer processes between humid air and solid surface under frosting conditions has received little attention. The problem is complicated because of the following facts. First, frost formation is essentially a transient process. As the frost grows not only the heat transfer rate and the frost-air interface temperature vary continuously with time, but also the frost properties change unpredictably from one instant to another. Second, the frost layer is a heterogeneous porous medium whose structure strongly depends on the conditions under which it is formed. It is impossible at the present time to delineate with any degree of assurance the quantitative effect of the system independent variables upon the density of deposited frost. Correlation of the experimental frost thermal conductivity data with the analytical results evaluated on the basis of the available methods for predicting the conductivities of heterogeneous materials is, as yet, not satisfactory. Finally, it does not appear that the microscopic study of the physical process of frosting has received attention previously. In the absence of such fundamental knowledge, difficulties are encountered in predicting the possible effects of electric fields on the formation of frost. Furthermore, unlike the cases of condensation and boiling heat transfer where

the electric field effect manifests itself in the form of the instability of the deformable liquid-gas interface, the frost-air interface can hardly be expected to play a similar role, for such interface is non-deformable.

In spite of the absence in the literature of studies on frost formation in an electric field, some work on the effects of electric fields upon the growth of ice crystals from the vapor has been reported by meteorologists in the past few years. In a study of the effects of electric fields on ice crystals growing from the vapor, Bartlett et al[6] observed that ice crystals grew rapidly in the form of long thin needles when an electric field in excess of a certain minimum value was applied. Their experiments were carried out in a diffusion chamber under supersaturation conditions. Whether similar phenomenon will be observed when frost layer grows from the ambient air is still a question mark.

In his study of the electric deposition of ice in a non-uniform field, Arabadzhi[7] mounted two point electrodes right above a container with warm water which released the vapor into the surrounding air. A positive potential of 9 kv was applied to one electrode and the other was grounded. When the air temperature was between -10°C to -12°C, he observed that on the zero electrode first clear ice was deposited and then hoar frost began to form. When the temperature was below -15°C, an abundance of fluffy frost deposited right away at the zero electrode. He beleived that the electro-deposition effects were due to corona discharges between the electrodes. However, no detailed description of this mechanism was given.

It is the purpose of this study to undertake an exploratory investigation of the influence of electric fields on heat and mass transfer processes in association with the formation of frost. In the next section, some preliminary experimental observations are reported. And in the section following, the problem to be treated is described.

1.2 PRELIMINARY EXPERIMENTAL OBSERVATIONS

To determine the possible effects of electric fields on the frost formation, preliminary exploratory tests were conducted using a variety of electrode configurations to provide the fields. In all the tests, the test plate which served as the forsting surface was grounded, unless otherwise stated. The temperature of the plate was maintained at about 10°F. The average temperature and specific humidity of the ambient air were about 73°F and 0.01 lb of vapor per lb of dry air respectively. The experimental setup is to be described in Chapter VI. Here only the following observations are reported:

1. Uniform field. A 4-mesh screen was used as positive electrode to provide uniform electric field. The screen was parallel to and at a distance $\frac{1}{2}$ inch from the test plate.

When the potential applied to the screen was increased to 12 kv, no observable changes in the frosting phenomenon were observed. In this case, no current was measured across the field since there was no corona discharge and the electric wind was absent.

2. Positive wire-plane corona. A non-uniform electric field was produced by applying a high potential to a 0.006 inch corona wire also located at $\frac{1}{2}$ inch from the plate. When the potential was below the critical potential for the corona discharge, approximately 7.6 kv for this case, there was no current and no changes in frost formation could be observed. However, when the potential was increased above the critical potential, the frost first appeared directly under the wire in the form of a fine strip, then grew laterally to the sides of the wore, forming a wider frost strip. Thus at the initial stages of frost formation the frost layer thickness decreased with increasing distance from the centerline of the strip. As the process of frosting continued, the thickness of the layer was more or less evened out for the whole plate. But a definite non-uniformity in the density of the frost layer was evidenced by the reduction in color of the frost layer as the distance from the frost strip centerline was increased. Upon close examination of the frost strip, it was further noticed that the frost thickness was not uniform along the strip. In certain portions of the strip, the deposited frost had the appearance of periodic ridges transverse to the strip. These could best be observed when the current was around 150 μa. The scale of periodicity of the ridges is about 1/8 inch. Photographs of the growth of frost and distribution of frost thickness along the test plate are shown in Appendix A.

3. Positive wire-screen corona. In this test, grounded 4-mesh screen was inserted between the wire and the frosting surface, the latter being electrically neutral. When the corona discharge took place between the wire and the screen the induced electric wind passed through the screen impinging normally on the frosting surface. A frost strip appeared as in the case of positive wire-plane corona, but transverse ridges could no longer be observed. Instead, transverse grooves appeared under each screen wire. Apparently, the grooves were due to the obstruction to the passage of the wind by the screen wires.

4. Negative and a-c wire-plane coronas. When the wire was subjected to a negative or a-c potential obove the critical potential, the frost formed along under the wire comprised of irregular patches. This may be accounted for by the fact that corona on negative or a-c wire is concentrated at points along the wire. Observations indicated that for a

given current, more frost was depoisted for positive than for negative or a-c corona.

5. Positive point-plane corona. When positive potential higher than the critical potential was applied to a needle point, the frost layer was approximately symmetrical about the point, as might be expected. Because of the low current obtainable for a given applied potential, its influence on frost deposition is not as significant as positive wire corona.

On the basis of the above experimental findings, the following comments can be made:

1. A uniform electric field does not seem to have any observable effects on the frosting phenomenon, at least at the early stages of frost formation. Because of the limitations of the experimental setup, no tests which last longer than one hour have been attempted. It remains to be determined if a uniform field will affect the growth of frost at a later stage when loose frost begins to form.

2. A non-uniform field has significant effects on frost formation only when corona discharges take place in the space between the electrodes. Of the various corona discharges and in so far as the enhancement in the amount of deposited frost is concerned, the positive wire-plane corona is the most effective.

3. Under the conditions of the experiments, it is not likely that the positive ions, which are presented in the space between the electrodes as a result of corona discharge, will act as nuclei for the frost crystals. The reason is nucleation requires the air to be supersaturated. The increase in frost deposition under the action of a corona discharge thus cannot be attributed to nucleations effected by ions.

4. The formation of water vapor clusters centered at the ions can neither account for the increase in frost deposition. Calculations (see Appendix B) indicated that a cluster of the order of 10^5 water molecules for each ion is required for the postulate to be valid. Such clusters hardly exist under the test conditions.

5. The test on positive wire-screen corona strongly suggests that impinging electric wind produced by the corona discharges is the crucial mechanism which effects the changes in frost formation.

6. A possible mechanism to explain the ridges observed in the frost strip is the secondary flow resulting from electrohydrodynamic instability. The secondary flow consists of Goertler vortices having the shape shown in Fig. 1, their axes being parallel to the basic flow direction. The inflowing parts of Goertler vortices would enhance the frost deposition and outward flowing parts would retard it, so that the frost thickness on the wall would vary periodically in the direction normal to the plane of the flow.

1.3 DESCRIPTION OF THE PROBLEM

In the light of the observations and comments made in the preceding section, the problem of interest can now be described: the determination of heat and mass transfer characteristics of impinging electric wind under frosting conditions. Figure 2 shows the overall schematic of the physical model of the present study. The frosting surface is assumed to extend to infinity and maintained at a constant subfreezing temperature T_w. The wire, located at a distance d from and parallel to the frosting surface, is subject to a positive potential V. The temperature and the vapor mass fraction of the surrounding air are T_∞ and w_∞, respectively. The frost layer thickness is designated by Y and the frost-air interface temperature by T_f.

When the applied potential of the wire exceeds the critical potential at which corona starts, ionization takes place in the immediate vicinity of the wire where an intense field exists. The positive ions thus formed move away from the wire under the influence of the electric fields. As they are driven towards the cathode plate, the ions make many collisions with the neutral molecules so that a streaming of the air results through momentum transport. As a consequence of the impingement of the induced air stream, which is at the same temperature and specific humidity as the surrounding air, heat and mass are transported between the ambient air and the frost layer.

The problem of frost formation has, in practice, two phases. The convective region determines the convective heat and mass transfer between the surface of the deposited layer and the external stream. On the other hand, the frost properties, the frost layer thickness as well as the surface conditions of the frost layer such as temperature and specific humidity are determined by the transport mechanisms in the frost layer itself. Of course, the two phases are interrelated, for the temperature and material distributions in the convective region depend on the surface conditions of the frost layer, whereas the determination of the transport processes in the frost layer requires a specification of the boundary conditions imposed by the convective flow on the frost-air interface. Although the main object of this study, as has already been pointed out, is the convective transport processes in connection with the impinging electric wind, a chaper (Chapter II)

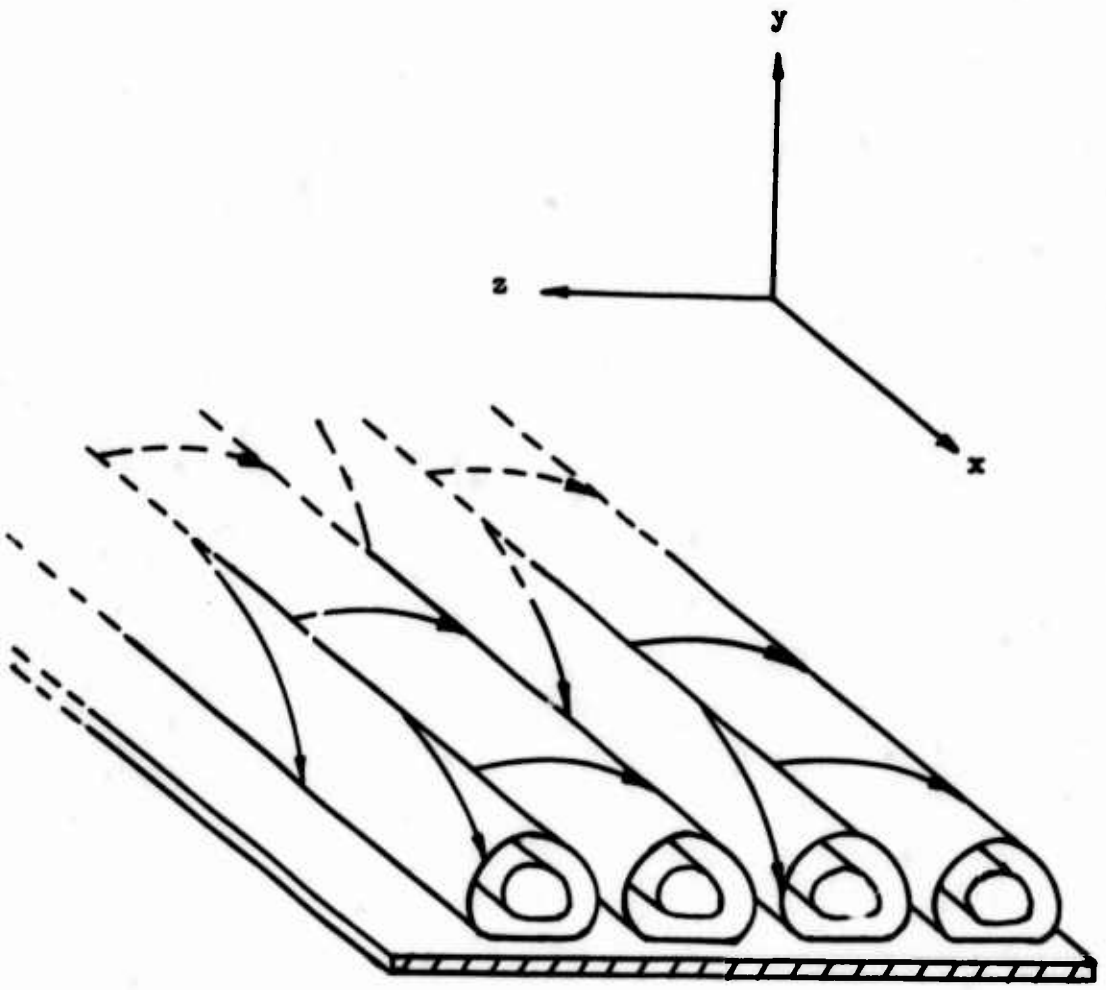

Fig. 1 Expected Goertler vortices in two-dimensional stagnation flow under the impinging electric wind

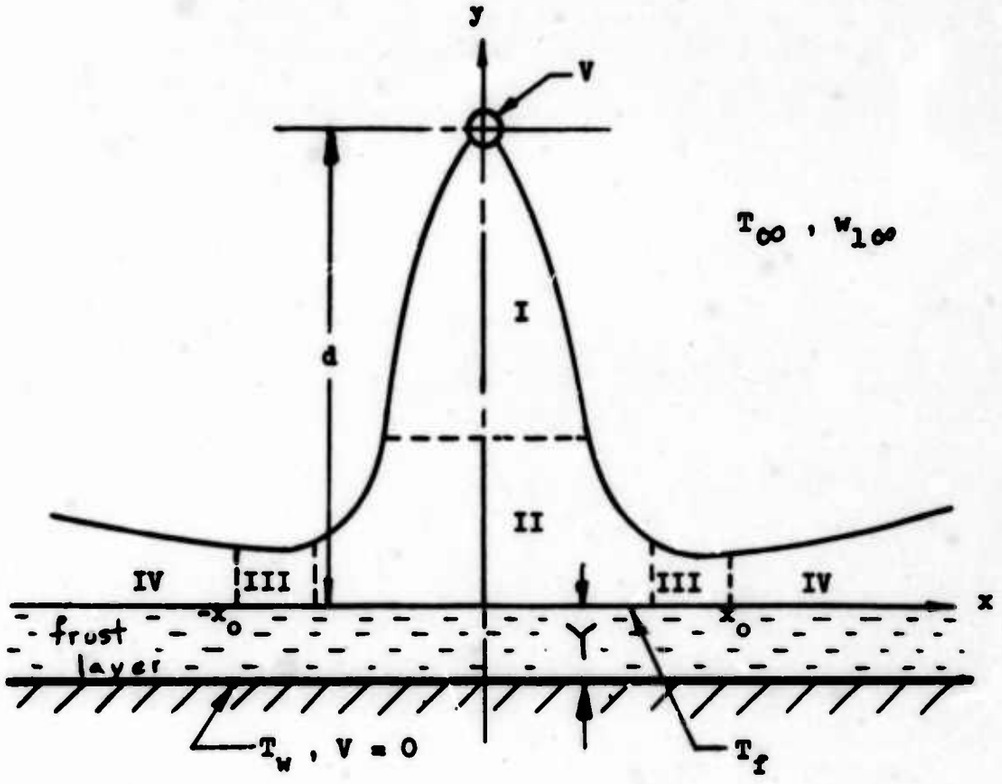

Fig. 2 Over-all schematic of the physical model

I : Electric wind region

II : Stagnation region

III : Transition region

IV : Wall jet region

is devoted to the study of transient heat conduction in an idealized frost layer. It is intended to bring out the relative importance of the parameters which affect the frost layer thickness and the temperature of the frost-air interface. No estimate of the variations of the frost properties with time is attempted.

In analogy with the corresponding problem for impinging free jet[8,9,10], the flow field of the impinging electric wind can be divided into four regions, if one follows the flow development along the centerline of the wind to the stagnation point and then from the stagnation point along the solid boundary. The air stream starts out from a very narrow region close to the wire and is accelerated by the electric field before finally being retarded by the plate. This zone may be called the electric wind proper. At certain distance from the plate, the jet of electric wind begins to be affected by the plate. The velocity decelerates rapidly along the centerline of the jet as the plate is approached and the pressure grows to a maximum value at the stagnation point. The jet is then deflected and spread over the plate. This is the zone of the two-dimensional stagnation flow. In the immediate neighborhood of this stagnation zone lies a transition zone which ends at a distance x_o from the stagnation point along the plate. Beyond x_o follows the zone of two-dimensional wall jet which flows parallel to the plate.

In the case of impinging free jet, the entire flow field will be turbulent in most practical examples owing to the low critical Reynolds number for a free mixing layer. No attempt is made in this study to consider the turbulent flows created by the impinging electric wind, since the velocities obtainable from the corona wind in air are very small, of the order of a few feet per second. Moreover, it is felt that the understanding of the ideal laminar flow field appropriate to the actual flow is a necessary preliminary to the understanding of the actual aerodynamic processes associated with the impinging electric wind.

The heat and mass transfer processes between the impinging air stream and the frost layer is in reality non-stationary, for the temperature of the frost-air interface is a function of time. The extent of the deviation of the instantaneous heat and mass transfer rates at the surface from the quasi-steady values corresponding to the instantaneous surface temperature at a given instant, depends on the rapidity of the variation of the surface temperature and the response characteristics of the boundary layer to a sudden change of the boundary conditions. The process of frost formation in ambient air is in general very slow, the variation of the frost layer surface temperature being at most of the order of a few °F per minute, and the response of the boundary layer in air to a sudden variation of the boundary conditions is generally very fast. Consequently, it will be assumed that quasi-steady conditions prevail in the impinging flow of an electric wind.

Despite the fact that the experimental study was carried out on a vertical plate, the effect of free convection is disregarded in the analysis. In virtue of the smallness of the v[illegible]cities obtainable from the corona wind, this assumption may not be ju[illegible]ied. The aim of this investigation, however, is to throw light on the actions of electric wind upon heat and mass transfer mechanisms, it appears logical to consider electric wind effects alone.

The problem of electrohydrodynamic instability and its influence on heat and mass transfer processes is beyond the scope of the present investigation. Nevertheless, it is worthwhile to make a few remarks in this regard. Two types of electrohydrodynamic instability phenomena may be distinguished: those caused by surface forces, and those induced by body forces. The former take place at the interface of two media having different dielectric properties (usually liquid-gas or liquid-liquid interface), while the later occur in the bulk of the medium itself. Another difference between these two classes of instability is that in the first case the media are electrically neutral except possibly at the interface, whereas in the second case the presence of space charges in the medium is a must for the instability to occur. Theories for the first category of EHD instability have been developed by Malkus and Veronis[11], by Melcher[12], by Taylor and McEwan[13], and more recently be Lee and Choi[14]. The theory for the second category of instability is still in its infancy. Stach[15], in consideration of flows in two-dimensional flat channel, assumed the instability to be in the form of propagating waves (i.e. the Tollmien-Schliching waves) and jumped to the conclusion that the problem on hand was analogous to that of stratified flows. He failed, however, to realize that for stratified flows the density distribution of the fluid was such that the arrangement was stable, while for the flows he was considering the arrangement had to be unstable in order for the instability to set in. A different approach, proposed by Chuang and Welkoff[16] in consideration of quiescent fluid between two concentric cylinders, is to assume that the instability takes the form of stationary waves (i.e. Taylor-Goertler vortices). Although it has been observed experimentally that stationary periodic waves exist in annular flows[17], further experimental evidence is required to verify the validity of the postulate.

CHAPTER II

TRANSIENT HEAT CONDUCTION IN THE FROST LAYER

2.1 FORMULATION OF THE FROBLEM

Consider a flat plate precooled to a constant subfreezing temperature T_w and located at y=0 (Fig. 3). When the plate is exposed to the moist ambient air at constant temperature T_∞ and vapor mass fraction $w_{1\infty}$, the frost starts to grow on the surface of the plate. The frost formation occurs progressively at the frost-air interface as a result of heat and mass transfer from the surroundings. Heat flows by convection from the ambient air to the frost-air interface and by conduction through the frost layer to the flat plate.

The transient process of heat transfer effected by the growth of the frost layer is extremely complicated. Since the temperature of the frost-air interface varies with the time as the frost grows, the heat and mass transfer coefficients are not constant, but functions of time. In addition, the density and the thermal conductivity of the frost layer vary unpredictably through a wide range. It appears that an exact mathematical solution to the problem is extremely difficult if all the numerous variables are considered.

In the present study, the problem is idealized as follows: It is assumed that the frost forms uniformly along the surface so that the problem is one-dimensional. It is also assumed that the frost properties and the heat and mass transfer coefficients do not vary with time. Furthermore, all water vapor transferred by convection from the ambient air to the frost-air interface is assumed to deposit as frost and is responsible for the increment in frost thickness. Special attention is directed towards the time-dependence of the frost layer thickness and of the frost-air interface temperature, particularly the latter.

Thus the problem of frost formation can be formulated as a boundary value problem in which the governing equation is the one-dimensional heat conduction equation for the solid phase without heat generation

$$\frac{\partial T}{\partial t} = a\frac{\partial^2 T}{\partial y^2} \tag{2.1}$$

subject to the boundary conditions that

$$\text{at } y = 0: \qquad T = T_w \tag{2.2}$$

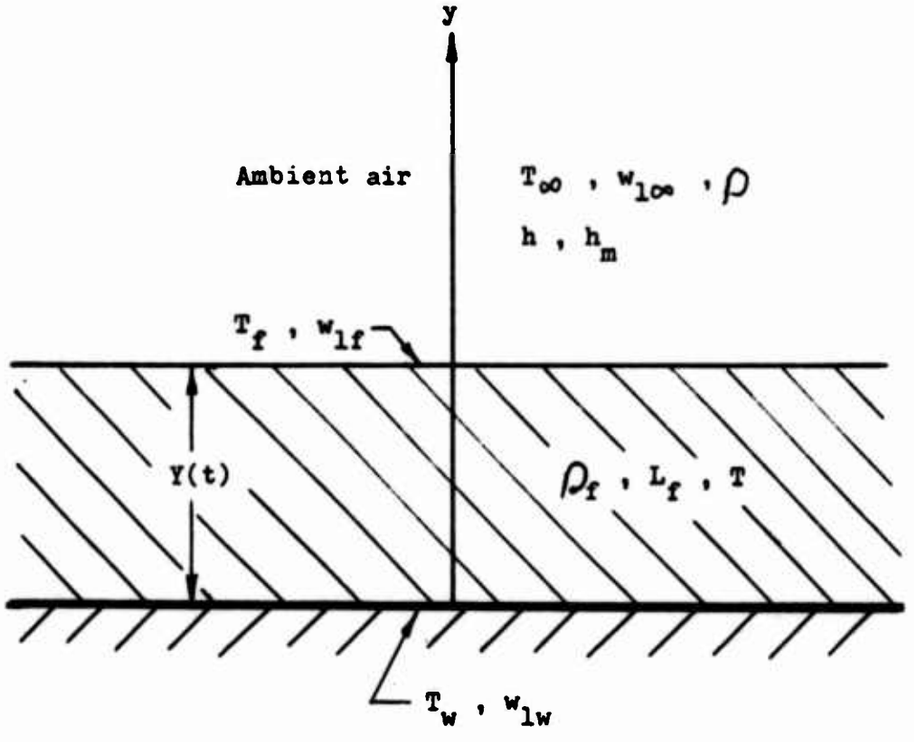

Fig. 3 Schematic of idealized frost layer

$$\text{at } y = Y(t): \qquad k\frac{\partial T}{\partial y} = \rho_f L_f \frac{dY}{dt} + h(T_\infty - T_f) \tag{2.3}$$

$$\rho_f \frac{dY}{dt} = \rho h_m (w_{1\infty} - w_{1f}) \tag{2.4}$$

and the initial condition that

$$Y(0) = 0 \tag{2.5}$$

where a = thermal diffusivity of the frost,

h = convective heat transfer coefficient,

h_m = convective mass transfer coefficient,

L_f = latent heat of sublimation of the frost,

t = time,

T = temperature,

T_f = temperature at the frost-air interface,

w_{1f} = vapor mass fraction at the frost-air interface,

Y = thickness of the frost layer,

ρ = density of the moist ambient air

ρ_f = density of the frost

and k = thermal conductivity of the frost.

In the boundary condition (2.3), the superheat of the vapor is neglected.

To complete the formulation of the problem it is necessary to specify the relation between w_{1f} and T_f. Since $(T-T_w)$ is usually small, it can be assumed that (18)

$$(w_1 - w_{1w}) = b(T - T_w)$$

where b is a constant of proportionality and w_{1w} is the vapor mass fraction of the saturated air at T_w. In the present case

$$b = (w_{1f} - w_{1w})/(T_f - T_w)$$

Writing

$$w_{1\infty} - w_{1f} = (w_{1\infty}-w_{1w}) - (w_{1f}-w_{1w})$$

$$= (w_{\infty}-w_{1w}) - b(T_f-T_w)$$

Eq. (2.4) becomes

$$\rho_f \frac{dY}{dt} = \rho h_m [(w_{1\infty}-w_{1w}) - b(T_f-T_w)]$$

or

$$\frac{dY}{dt} = C_1 - C_2 T_f \tag{2.6}$$

Here the constants C_1 and C_2 are defined as

$$C_1 = \frac{\rho}{\rho_f} h_m [(w_{1_\infty}-w_{1w}) + bT_w] \tag{2.7}$$

and

$$C_2 = \rho h_m b/\rho_f \tag{2.8}$$

Substituting Eq. (2.6) in (2.3), there is obtained an alternative form for condition (2.3).

$$k \frac{\partial T}{\partial y} = \rho_f C_1 L_f - \rho_f C_2 L_f T_f + h(T_\infty - T_f)$$

Or, after rearrangement

$$k \frac{\partial T}{\partial y} = C_3 - C_4 T_f \tag{2.9}$$

where

$$C_3 = \rho_f C_1 L_f + hT_\infty$$

and

$$C_4 = \rho_f C_2 L_f + h$$

The boundary value problem as formulated above is written down once more for reference.

Governing equation:

$$\frac{\partial T}{\partial t} = a\frac{\partial^2 T}{\partial y^2} \tag{2.10}$$

Boundary conditions:

$$\text{at } y=0: \qquad T = T_w \tag{2.11}$$

$$\text{at } y=Y: \qquad k\frac{\partial T}{\partial y} = C_3 - C_4 T_f \tag{2.12}$$

$$\frac{dY}{dt} = C_1 - C_2 T_f \tag{2.13}$$

Initial condition:

$$Y(0) = 0 \tag{2.14}$$

The essential features of the problem are the existence of a moving surface of separation between the solid and gaseous phases and the dependence on time of the temperature of this moving surface. The simplicity of Eq. (2.10) is misleading. The time-dependent boundary conditions (2.12) and (2.13) render the problem one of considerable difficulty. It is only recently that an exact solution of Eq. (2.10) which satisfies any arbitrary initial and boundary conditions has been developed. By application of the two-sided Laplace transform Portnov[15] was able to obtain an exact solution in the form of Poisson integral.

2.2 PORTNOV'S METHOD OF SOLUTION

In this section, Portnov's method of exact solution to Eq. (2.10) in the form of Poisson integral is briefly described. For details and rigorous proofs of the procedure, reference should be made to Portnov's original paper.

Letting $t = \tau$ and $y = \sqrt{a}\zeta Y(\tau)$, it follows that

$$\frac{\partial T}{\partial t} = \frac{\partial T}{\partial \tau} + \frac{\partial T}{\partial \zeta}\frac{\partial \zeta}{\partial \tau} = \frac{\partial T}{\partial \tau} - \frac{Y'(\tau)}{Y^2(\tau)}\frac{y}{\sqrt{a}}\frac{\partial T}{\partial \zeta} = \frac{\partial T}{\partial \tau} - \frac{Y'(\tau)}{y(\tau)}\zeta\frac{\partial T}{\partial \zeta}$$

and

$$\frac{\partial^2 T}{\partial y^2} = \frac{1}{Y^2(\tau)} \frac{\partial^2 T}{\partial \zeta^2}$$

Thus Eq. (2.10), in terms of the new set of variables τ and ζ, reduces to the form

$$Y^2(\tau) \frac{\partial T}{\partial \tau} - Y(\tau)Y'(\tau)\, \zeta \frac{\partial T}{\partial \zeta} = \frac{\partial^2 T}{\partial \zeta^2} \qquad (2.15)$$

where prime denotes differentiation of a function with respect to its argument.

Now, applying to Eq. (2.15) the two-sided Laplace transform[20] with respect to ζ(τ being treated a parameter) it is obtained

$$Y^2(\tau) \frac{\partial T}{\partial \tau} + Y(\tau)Y'(\tau)\, p \frac{\partial T}{\partial p} = p^2 T \qquad (2.16)$$

where p is a new independent variable introduced in the Laplace transform.

The general solution to Eq. (2.16) is

$$T(p,\tau) = \exp[p^2\tau/Y^2(\tau)]F(p/Y) \qquad (2.17)$$

where $F(p/Y)$ is an arbitrary function of its argument. If the function F is represented as

$$F(p/Y) = F_1(p/Y) + F_2(p/Y) \qquad (2.18)$$

and it is assumed that the functions F_1 and F_2 are both Laplace transform images of the arbitrary one-sided functions φ_1 and φ_2, i.e.

$$F_1(p/Y) \doteqdot \varphi_1(Y\zeta)U(Y\zeta)$$

$$F_2(p/Y) \doteqdot \varphi_2(Y\zeta)U(-Y\zeta)$$

where $\doteqdot$ denotes the Laplace transform and U denotes the unit function, inverse transform of Eq. (2.17) yields

$$T(\zeta,\tau) = \frac{1}{\sqrt{\pi}} \int_{-\infty}^{\infty} \exp\left[-\frac{Y^2(\zeta-z)^2}{4\tau}\right] \left\{ \varphi_1(\sqrt{a}\, Yz)U(\sqrt{a}\, Yz) + \varphi_2(\sqrt{a}\, Yz)U(-\sqrt{a}\, Yz) \right\} \frac{Y\, dz}{2\sqrt{\tau}} \tag{2.19}$$

or

$$T(\zeta,\tau) = \frac{1}{\sqrt{\pi}} \left\{ \int_0^{\infty} \exp\left[-\frac{Y^2(\zeta-z)^2}{4\tau}\right] \varphi_1(\sqrt{a}\, Yz) \frac{Y\, dz}{2\sqrt{\tau}} + \int_{-\infty}^{0} \exp\left[-\frac{Y^2(\zeta-z)^2}{4\tau}\right] \varphi_2(\sqrt{a}\, Yz) \frac{Y\, dz}{2\sqrt{\tau}} \right\} \tag{2.20}$$

In terms of the original variables, Eq. (2.19) reads

$$T(y,t) = \frac{1}{\sqrt{\pi}\sigma} \int_{-\infty}^{\infty} \exp\left[-\frac{(y-\bar{y})^2}{\sigma^2}\right] f(\bar{y})d\bar{y} \tag{2.21}$$

and Eq. (2.20) becomes

$$T(y,t) = \frac{1}{\sqrt{\pi}\sigma} \left\{ \int_0^{\infty} \exp\left[-\frac{(y-\bar{y})^2}{\sigma^2}\right] \varphi_1(\bar{y})d\bar{y} + \int_{-\infty}^{0} \exp\left[-\frac{(y-y)^2}{\sigma^2}\right] \varphi_2(\bar{y})d\bar{y} \right\} \tag{2.22}$$

where $\sigma = 2\sqrt{a\tau}$, $\bar{y} = Y\sqrt{a}z$ and $f(y) = \varphi_1(y)U(y) + \varphi_2(y)U(-y)$. Thus Eq. (2.22) represents the temperature distribution in an infinite slab with an initial temperature of $f(y)$. More specifically, the functions $\varphi_1(y)U(+y)$ and $\varphi_2(y)U(-y)$ represent the initial temperature for $y > 0$ and $y < 0$ respectively. For the case of frost formation, both φ_1 and φ_2 represent fictitious initial temperatures since the frost layer does not exist at $t = 0$.

The unknown functions Y, φ_1 and φ_2 in Eq. (2.22) are to be determined by using the initial and boundary conditions for the specific problem under consideration. The general method is to assume that these functions can be expanded in power series

$$\varphi_1(\omega) = \sum_{n=0}^{\infty} \varphi_{1n}\omega^n \tag{2.23a}$$

$$\varphi_2(\omega) = \sum_{n=0}^{\infty} \varphi_{2n}\omega^n \tag{2.23b}$$

$$Y(\sigma) = \sum_{n=1}^{\infty} Y_n\sigma^n \tag{2.23c}$$

where Eq. (2.23c) satisfies the initial condition (2.14). Then Eq. (2.22) with Y, φ_1 and φ_2 substituted from Eqs. (2.23) is used in each of the boundary conditions, the resulting equations being repeatedly differentiated with respect to σ and the equations thus obtained being evaluated at $\sigma = 0$. Each set of the resulting stimultaneous algebraic equations may be solved for the successive coefficients of the unknown series (2.23). Once these have been found, Eq. (2.22) becomes

$$T(y,t) = \frac{1}{\sqrt{\pi}}\left\{\int_{y/\sigma}^{\infty} e^{-\alpha^2} \sum_{n=0}^{\infty} \varphi_{1n}(\alpha\sigma + y)d\alpha \right.$$

$$\left. \int_{-\infty}^{-y/\sigma} e^{-\alpha^2} \sum_{n=0}^{\infty} \varphi_{2n}(\alpha\sigma + y)d\alpha \right\} \tag{2.24}$$

where

$$\alpha^2 = \frac{(y-\bar{y})^2}{\sigma^2}$$

Eq. (2.24) can also be written as

$$T(y,t) = \tfrac{1}{2} \sum_{n=0}^{\infty} n!\sigma^n \left[\varphi_{1n}\, i^n \operatorname{erfc}\left(-\frac{y}{\sigma}\right) + (-1)^n \varphi_{2n}\, i^n \operatorname{erfc}\left(\frac{y}{\sigma}\right)\right] \tag{2.25}$$

where

$$i^n \operatorname{erfc}(y) = \frac{2}{\sqrt{\pi}} \int_y^{\infty} e^{-\bar{y}^2} \frac{(\bar{y}-y)^n}{n!}\, d\bar{y}$$

denotes the nth order repeated integral of the complementary error function.

2.3 SERIES SOLUTION OF THE FROSTING PROBLEM

Portnov derived Eq. (2.22) without using any boundary conditions. Since the integral can be shown to be a solution of Eq. (2.10) tending to f(y) as t approaches zero, this integral form of solution has been assumed to apply in problems involving melting and freezing of finite slabs by Jackson[21] and by Westphal[22]. In the present study the same method is applied to frosting problem.

To determine the unknown functions Y, φ_1 and φ_2, use is made of the boundary condition (2.11) through (2.13). When Eq. (2.22) is substituted into Eq. (2.11), it is found

$$T_w = \frac{1}{\sqrt{\pi}}\left[\int_0^\infty e^{-\beta^2}\,\varphi_1(\beta\sigma)d\beta + \int_{-\infty}^0 e^{-\beta^2}\,\varphi_2(\beta\sigma)d\beta\right] \tag{2.26}$$

where

$$\beta^2 = \frac{(-y)^2}{\sigma^2}$$

Substituting Eq. (2.23) into Eq. (2.26) and letting $\sigma \to 0$, the following relation is obtained

$$T_w = \tfrac{1}{2}\,(\varphi_{1o} + \varphi_{2o}) \tag{2.27}$$

Differentiation of Eq. (2.22) with respect to y gives the temperature gradient

$$\frac{\partial T}{\partial y} = \frac{1}{\sqrt{\pi}\,\sigma}\left\{\int_0^\infty \left[-\frac{2(y-\bar{y})}{\sigma^2}\right] \exp\left[-\frac{(y-\bar{y})^2}{\sigma^2}\right] \varphi_1(\bar{y})d\bar{y} + \int_{-\infty}^0 \left[-\frac{2(y-\bar{y})}{\sigma^2}\right] \exp\left[-\frac{(y-\bar{y})^2}{\sigma^2}\right] \varphi_2(\bar{y})d\bar{y}\right\} \tag{2.28}$$

Substitution of Eqs. (2.22) and (2.28) into Eq. (2.12) yields

$$2k\left[\int_{y/\sigma}^\infty \gamma e^{-\gamma^2}\,\varphi_1(\gamma\sigma+Y)d\gamma + \int_{-\infty}^{-y/\sigma} \gamma e^{-\gamma^2}\,\varphi_2(\gamma\sigma+Y)d\gamma\right]$$

$$= \sqrt{\pi}\,\sigma\;C_3 - \sigma C_4\left[\int_{-y/\sigma}^\infty e^{-\gamma^2}\,\varphi_1(\gamma\sigma+Y)d\gamma + \int_{-\infty}^{-y/\sigma} e^{-\gamma^2}\,\varphi_2(\gamma\sigma+Y)d\gamma\right] \tag{2.29}$$

where

$$\gamma^2 = \frac{(y-\bar{y})^2}{\sigma^2}$$

Substituting Eqs. (2.23) into Eq. (2.29) and letting $\sigma \to 0$, it is found

$$\varphi_{10}\int_{-Y_1}^{\infty} \gamma e^{-\gamma^2}\, d\gamma + \varphi_{20}\int_{-\infty}^{-Y_1} \gamma e^{-\gamma^2}\, d\gamma = 0 \tag{2.30}$$

To determine Y_1, substitute Eq. (2.22) into Eq. (2.13) to yield

$$2\,\frac{a}{\sigma}\,\frac{dY}{d\sigma} = C_1 - \frac{C_2}{\sqrt{\pi}}\left[\int_{-y/\sigma}^{\infty} e^{-\gamma^2}\,\varphi_1(\gamma\sigma+Y)d\gamma + \int_{-\infty}^{-y/\sigma} e^{-\gamma^2}\,\varphi_2(\gamma\sigma+Y)d\gamma\right] \tag{2.31}$$

Substituting Eqs. (2.23) into Eq. (2.31) and letting $\sigma \to 0$, it is obtained

$$Y_1 = 0 \tag{2.32}$$

Using Eq. (2.32) in Eq. (2.30), it is found

$$\varphi_{10} - \varphi_{20} = 0 \tag{2.33}$$

Thus, from Eqs. (2.27), (2.32) and (2.33), the first coefficients of the unknown functions Y, φ_1 and φ_2 are found to be

$$\varphi_{10} = \varphi_{20} = T_w \quad , \qquad Y_1 = 0$$

The next set of coefficients Y_2, φ_{11} and φ_{21} are obtained by taking first derivatives of Eqs. (2.26), (2.29) and (2.31), substituting Eqs. (2.23) into the equations thus obtained, letting $\sigma \to 0$ and evaluating the resulting definite integrals.

The first derivative of Eq. (2.26) with respect to σ is

$$0 = \frac{1}{\sqrt{\pi}}\left[\int_0^{\infty} \beta e^{-\beta^2}\,\varphi_1^{(1)}(\beta\sigma)d\beta + \int_{-\infty}^{0} \beta e^{-\beta^2}\,\varphi_2^{(1)}(\beta\sigma)d\beta\right] \tag{2.34}$$

where superscripts indicate the order of differentiation with respect to σ. Substituting for φ_1 and φ_2 from Eqs. (2.23) and letting $\sigma \to 0$, Eqs. (2.34) becomes

$$0 = \frac{1}{\sqrt{\pi}}\left[\varphi_{11} \int_0^{\infty} \beta e^{-\beta^2}\, d\beta + \varphi_{21} \int_{-\infty}^{0} \beta e^{-\beta^2}\, d\beta \right] \tag{2.35}$$

Or, after evaluation of the definite integral,

$$\varphi_{11} - \varphi_{21} = 0 \tag{2.36}$$

The first derivative of Eq. (2.29) with respect to σ is

$$\begin{aligned} 2k\Big[\int_{\lambda}^{\infty} \gamma(\gamma+Y^{(1)}) e^{-\gamma^2}\, \varphi_1{}^{(1)}(\gamma\sigma+Y)d\gamma + \lambda^{(1)}\lambda e^{-\lambda^2}\, \varphi_1(0) \\ + \int_{-\infty}^{-\lambda} \gamma(\gamma+Y^{(1)}) e^{-\gamma^2}\, \varphi_2{}^{(1)}(\gamma\sigma+Y)d\gamma - \lambda^{(1)}\lambda e^{-\lambda^2}\, \varphi_2(0)\Big] \\ = \sqrt{\pi}\, C_3 - C_4\Big[\int_{-\lambda}^{\infty} e^{-\gamma^2}\, \varphi_1(\gamma\sigma+Y)d\gamma + \int_{-\infty}^{-\lambda} e^{-\gamma^2}\, \varphi_2(\gamma\sigma+Y)d\gamma \Big] \\ - \sigma\, C_4\Big[\int_{-\lambda}^{\infty} (\gamma+Y^{(1)}) e^{-\gamma^2}\, \varphi_1{}^{(1)}(\gamma\sigma+Y)d\gamma + \lambda^{(1)} e^{-\lambda^2}\, \varphi_1(0) \\ + \int_{-\infty}^{-\lambda} (\gamma+Y^{(1)}) e^{-\gamma^2}\, \varphi_2{}^{(1)}(\gamma\sigma+Y)d\gamma - \lambda^{(1)} e^{-\lambda^2}\, \varphi_2(0)\Big] \end{aligned} \tag{2.37}$$

where

$$\lambda = Y/\sigma \quad .$$

Substitution of Eqs. (2.23) into Eq. (2.37) and letting $\sigma \to 0$ yields

$$\tfrac{1}{2}(\varphi_{11}+\varphi_{21}) = \frac{1}{k}(C_3 - C_4 T_w) \tag{2.38}$$

In obtaining Eqs. (2.38), φ_{10}, φ_{20} and Y_1 have been substituted from the previous results.

To obtain Y_2, differentiate Eq. (2.31) with respect to σ

$$2aY^{(2)} = C_1 - \frac{C_2}{\sqrt{\pi}}\Big[\int_{-\lambda}^{\infty} e^{-\gamma^2}\,\varphi_1(\gamma\sigma+Y)d\gamma + \int_{-\infty}^{-\lambda} e^{-\gamma^2}\,\varphi_2(\gamma\sigma+Y)d\gamma$$

$$- \sigma\frac{C_2}{\sqrt{\pi}}\Big[\int_{-\lambda}^{\infty} (\gamma+Y^{(1)})e^{-\gamma^2}\,\varphi_1{}^{(1)}(\gamma\sigma+Y)d\gamma\Big]$$

$$+ \lambda^{(1)}e^{-\lambda^2}\,\varphi_1(0) + \int_{-\infty}^{-\lambda}(\gamma+Y^{(1)})e^{-\gamma^2}\,\varphi_2{}^{(1)}(\gamma\sigma+Y)d\gamma$$

$$- \lambda^{(1)}e^{-\lambda^2}\,\varphi_2(0)\Big] \qquad (2.39)$$

Substituting Eqs. (2.23) into Eq. (2.39) and letting $\sigma \to 0$, it is obtained

$$4aY_2 = C_1 - \frac{C_2}{2}(\varphi_{10} + \varphi_{20})$$

which, on substituting for φ_{10} and φ_{20}, yields

$$Y_2 = \frac{C_1 - C_2T_w}{4a} \qquad (2.40)$$

Thus the second set of coefficients Y_2, φ_{11} and φ_{21} are

$$\varphi_{11} = \varphi_{21} = \frac{1}{k}(C_3 - C_4T_w)$$

$$Y_2 = (C_1 - C_2T_w)/4a$$

To obtain higher order coefficients of the unknown functions Y, φ_1 and φ_2, it is necessary to continue in the manner described above, i.e. obtain higher order derivatives of Eqs. (2.26), (2.29) and (2.31), let $\sigma \to 0$ and evaluate the definite integrals appearing in the resulting equations. The first six sets of coefficients are listed in Appendix C.

2.4 FROST LAYER THICKNESS

Substituting in Eq. (2.24) the coefficient Y_n's from Appendix C, there results an expression for the frost layer thickness.

$$Y(t) = \frac{\rho}{\rho_f} h_m(w_{1\infty}-w_{1w})t - \frac{kb}{2}\left(\frac{\rho}{\rho_f}\frac{h_m}{k}\right)^2 \left[\rho_f L_f h_m(w_{1\infty}-w_{1w}) + h(T_\infty-T_w)\right](w_{1\infty}-w_{1w})t^2 + \frac{kb}{288}\left(\frac{\rho h_m}{\rho_f k}\right)^3 (w_{1\infty}-w_{1w}) \cdot \left\{(\rho b L_f h_m + h)\left[\rho L_f h_m(w_{1\infty}-w_{1w}) + h(T_\infty-T_w)\right] \cdot (w_{1\infty}-w_{1w}) + \frac{3b}{4}\left[\rho L_f h_m(w_{1\infty}-w_{1w}) + h(T_\infty-T_w)\right]^2\right\} t^3 + \cdots \quad (2.41)$$

It is noted that the higher order terms are due to the unsteadiness of w_{1f}. A few remarks can be made concerning this equation. For small times, higher order terms in the equation are negligible as compared with the first term. Hence the frost layer grows linearly with time. The rate of change of the frost thickness is given by the coefficient of the first term, which represents the ratio between the mass flux of the water vapor to the frost surface by convection and the frost density. This is in accordance with the boundary condition (2.4), for at t=0, w_{1f} is equal to w_{1w}. As t increases, the higher order terms become more and more significant and the rate of increase of the frost thickness tapers off gradually. The frost thickness asymptotically approaches its maximum value as t tends to infinity, a direct consequence of the fact that Eq. (2.24) can be shown to converge uniformly for all σ[19].

Physically, the mass transfer process can not go on indefinitely, since, in principle, as soon as the concentration of water vapor at the surface of the deposited layer reaches a value equal to that of the ambient air, an equilibrium state is then established and no further mass transfer is possible. As for the phenomenon of frost formation two cases may be distinguished[23]. Where the air dew point is below 32°F, deposition of frost will stop when the frost surface reaches the dew point. When the dew point of the air is above 32°F, the frost surface temperature can not exceed 32°F. In the latter case, it is generally observed that after a temperature of 32°F is attained at frost surface a steady-state condition is reached in which water vapor will condense as liquid. This liquid will, if the frost is porous, soak into the frost layer and eventually freeze resulting in a continuous increase in the density as well as the thermal conductivity of the frost layer approching the value of solid ice.

From the second term of Eq. (2.41), it is noted that the heat transfer rate $h(T_\infty-T_w)$ between the wall and the surroundings has the effect of reducing the amount of frost deposited. If the temperature

difference between the wall and the free stream or the surrounding air becomes extremely large, considerable deviation of the actual frost deposited from the calculated mass transfer by convection $\rho h_m(w_{1\infty}-w_{1w})$ is expectable. It has been reported by Barron[24] that the magnitude of the mass transfer rate measured experimentally at cryogenic temperature was approximately one order of magnitude less than the theoretically predicted correlation. Barron tried to interpret the discrepancy between theory and experiment in terms of the resistance to diffusion of water molecules by the presence of frost particles which, supposedly formed by nucleation, were observed to exist in the boundary layer in his investigation. Equation (2.41) seems to suggest that, in addition to the appearance of the visibile frost particles, large values of $(T_\infty-T_w)$ may also be responsible for the discrepancy.

2.5 FROST-AIR INTERFACE TEMPERATURE

The expression for the frost-air interface temperature as a function of time up to the fourth term may be obtained by substituting in Eq. (5.25) the coefficients of φ_1 and φ_2 listed in Appendix C and evaluating the resulting expression at y=Y, namely,

$$
\begin{aligned}
T_f(t) = T_w &+ \frac{Y}{k}\left[\rho L_f h_m(w_{1\infty}-w_{1w}) + h(T_\infty-T_w)\right] \\
&- \tfrac{1}{4}\left(Y\sigma^2+\frac{2}{3}Y^3\right)\frac{\rho h_m}{\rho_f k^2 a}(\rho b L_f h_m+h)(w_{1\infty}-w_{1w}) \\
&\cdot\left[\rho L_f h_m(w_{1\infty}-w_{1w}) + h(T_\infty-T_w)\right] \\
&+ \frac{\sigma^5}{3}\left(\frac{1}{12}\frac{Y}{\sigma}+\frac{5}{12}\frac{Y^3}{\sigma^3}+\frac{5}{16}\frac{Y^5}{\sigma^5}\right)\frac{(\sigma b L_f h_m+h)}{90k}(w_{1\infty}-w_{1w}) \\
&\cdot\left\{\left[\left(\frac{\rho h_m}{\rho_f a k}\right)^2(w_{1\infty}-w_{1w})(\rho b L_f h_m+h)\right]\right. \\
&\cdot\left[\rho L_f h_m(w_{1\infty}-w_{1w}) + h(T_\infty-T_w)\right] \\
&\cdot\left[\frac{9}{2}+\frac{1}{20}\left(\frac{\rho h_m}{\rho_f a k}\right)(w_{1\infty}-w_{1w})\right] + \frac{3b}{4}\left(\frac{\rho h_m}{\rho_f a k}\right)^2 \\
&\cdot\left.\left[\rho L_f h_m(w_{1\infty}-w_{1w}) + h(T_\infty-T_w)\right]^2\right\} + \cdots
\end{aligned}
\tag{2.42}
$$

Without recourse to numerical computations, it is seen directly from the equation that at $t = 0$, $T_f = T_w$. Obviously this is true, for then the frost thickness is zero. To a first approximation, the frost-air interface temperature is proportional to the frost layer thickness as well as the total heat flux to the frost surface. When Y and the latent heat of sublimation of the frost are small as compared with convective heat flux, the latter is an important parameter in determining the instantaneous frost surface temperature. It is also noted from Eq. (2.42) that the variation in time of T_f is essentially effected by the growth of the frost thickness as expected.

It is of interest to mention here the temperature distribution in the frost layer. An expression for such temperature distribution is readily reduced from Eq. (2.42), namely,

$$T(y,t) = T_w + \frac{Y}{k}\left[\rho L_f h_m(w_{1\infty}-w_{1w}) + h(T_\infty-T_w)\right]$$

$$- \tfrac{1}{4}\left(y\sigma^2+\frac{2}{3}y^3\right)\frac{\rho h_m}{\rho_f a k^2}(\rho b L_f h_m+h)(w_{1\infty}-w_{1w})$$

$$\cdot\left[\rho L_f h_m(w_{1\infty}-w_{1w}) + h(T_\infty-T_w)\right] + \cdots \qquad (2.43)$$

where $y < Y$. Clearly this equation indicates that at any instant, the frost temperature increases from T_w at the plate to T_f at the frost-air interface. But the increase is non-linear because of the presence of higher order terms in powers of y. The rate of increase in T decreases with increasing y. On the other hand the temperature at a fixed point in the frost layer varies with time. The third term in Eq. (2.43) is the most important term in the determination of the temperature history throughout the frost layer. Consider the point $y = y_1$ and suppose the frost starts to form at t=0. When the frost-air interface reaches the point $y = Y(t_1) = y_1$, the temperature at y_1 takes the value $T_f(t_1)$. As the frost continues to grow, i.e. for $t > t_1$, $T(y_1)$ decreases with time until a steady state is reached where T_f assumes a value corresponding to the maximum physically possible frost surface temperature.

2.6 THE HEAT TRANSFER RATE

To determine the heat transfer rate across a surface parallel to the plate per unit area of the surface, Eq. (2.43) must be differentiated with respect to y. The heat flux at a point y and time t is as follows:

$$q = -k\left(\frac{\partial T}{\partial y}\right) = -\left[\rho L_f h_m(w_{1\infty}-w_{1w}) + h(T_\infty-T_w)\right]$$

$$+ \frac{1}{4}(\sigma^2+2y^2)\frac{\rho h_m}{\rho_f k^2 a}(\rho b L_f h_m+h)(w_{1\infty}-w_{1w})$$

$$\cdot\left[\rho L_f h_m(w_{1\infty}-w_{1w}) + h(T_\infty-T_w)\right]$$

$$-\frac{1}{3}\left(\frac{1}{12}\sigma^4+\frac{5}{4}\sigma^2y^2+\frac{25}{16}y^4\right)\frac{(\rho b L_f h_m+h)}{90}$$

$$\cdot\left[\left(\frac{\rho h_m}{\rho_f a k}\right)^2(w_{1\infty}-w_{1w})^2(\rho b L_f h_m+h)\right]$$

$$\cdot\left\{\left[\rho L_f h_m(w_{1\infty}-w_{1w}) + h(T_\infty-T_w)\right]\right.$$

$$\cdot\left[\frac{9}{2}+\frac{1}{20}\left(\frac{\rho h_m}{\rho_f a k}\right)(w_{1\infty}-w_{1w})\right]$$

$$\left.+\frac{3}{4}b\left(\frac{\rho h_m}{\rho_f a k}\right)^2\left[\rho L_f h_m(w_{1\infty}-w_{1w}) + h(T_\infty-T_w)\right]\right\}^2$$

(2.44)

From this equation it may be concluded qualitatively, that the instantaneous heat flux in the frost layer decreases with y. This is because the local heat storage in the frost layer decreases with decreasing y as does the local frost temperature, and a certain amount of heat is expected to be released and transferred in the negative y direction, resulting in a heat flux increase in that direction. The minimum flux occurs at the frost-air interface and is equal to $\rho l_f h_m(w_{1\infty}-w_{1f})$ + h(+ $h(T_\infty-T_f)$ as given by the boundary condition (2.3). The maximum heat flux is at the plate. The second term in Eq. (2.44) accounts for the fact that the frost layer has insulating effect upon heat transfer. Another point worth noting is the unsteadiness of the local heat flux. It is apparent from Eq. (2.44) that the local heat flux decreases with time.

2.7 CLOSURE

The analysis developed in this chapter has, essentially, no direct bearing with the remainder of this dissertation and is included here as an independent topic. As has been emphasized in Section 1.3, the transient heat conduction in the frost layer is an important phase of the problem of frost formation. It is thus felt that this subject deserves a discussion even in an investigation which concerns primarily with the convective transport processes associated with frost formation.

Because of the complex nature of the problem no satisfactory theory has been developed. The present study represents a new but preliminary attempt to bring out the important parameters which affect the heat transfer rate across the frost layer and the temperature at the frost surface. To facilitate the analysis, a simplified model of the frost layer has been considered. Deviation of the theory from the actual frost formation is, therefore, expected and the results remain to be validated.

In reality the frost properties such as density and thermal conductivity are strongly dependent on time. A recent investigation in this connection has been reported by Yonko and Sepsy[25]. A re-examination of the analysis discussed in this chapter indicates that the method also applies to the case of variable frost properties provided the thermal conductivity and density of the frost are functions of σ (σ being two times the square root of the product of frost thermal diffusivity and time). For this case proper care has to be exercised in carrying out the differentiations with respect to σ, for k, C_1, C_2, C_3 and C_4 are also functions of σ.

CHAPTER III

THE ELECTRIC WIND

3.1 GENERAL NATURE OF THE ELECTRIC WIND

The phenomenon of electric wind (also called corona wind) is a characteristic feature of asymmetric field corona discharge such as point-plane or wire-plane corona. Although the first theory of electric wind was given by Chattock[26] as early as 1899, very little work has been reported in the literature ever since. As a result the actual flow processes of the induced air stream is still not well understood. Of the scant work available, all authors discussed essentially only one-dimensional cases. Typical examples are plane-parallel, coaxial-cylindrical and concentric-spherical electrode configurations. An exhaustive historical review and bibliography has recently been presented by Robinson[27] and no further literature survey will be attempted here. In this chapter the analysis will only be developed to the extent as is required for proper interpretation of the experimental data to be presented in Chapter VI.

Before proceeding to the discussion of the electric wind generated by specific electrode configurations, the general nature of the problem in question will be examined first. It appears that one of the main reasons why the phenomenon of corona wind has received rather inactive attention is that the phenomenon is too involved to permit analytical solutions for physically realistic models. To help illustrate the complexity of the problem the governing equations are listed as follows:

Electrodynamic equations:

$$\nabla \cdot \vec{E} = \rho_e/\epsilon \tag{3.1}$$

$$\nabla \times \vec{E} = 0 \tag{3.2}$$

$$\nabla \cdot \vec{J} = 0 \tag{3.3}$$

$$\vec{J} = \rho_e(\vec{v}+K\vec{E}) \tag{3.4}$$

Hydrodynamic equations:

$$\nabla \cdot \vec{v} = 0 \tag{3.5}$$

$$\rho \frac{\partial \vec{v}}{\partial t} + \rho(\vec{v}\cdot\nabla)\vec{v} = \rho_e\vec{E} - \nabla p + \mu\nabla^2\vec{v} \tag{3.6}$$

It is assumed here that the flow is incompressible and that the Coulomb's force is the only extraneous force. In Eq. (3.4) the charge flux due to diffusion is neglected.

An understanding of the actual aerodynamic processes of the electric wind necessarily demands a solution of the equations of motion (3.6), which in turn requires and expression for the electrostatic body force (that is the Coulomb's force). The task of solving the non-linear Navier-Stokes equations even in the absence of extraneous forces is already a difficult one; not to mention that the determination of the Coulomb's force is not easy as well. In fact it is evident from Eqs. Eqs. (3.1) to (3.6) that the electrodynamic and hydrodynamic equations are coupled when the velocity of the fluid is comparable to the drift velocity of the space charges. In gases it is generally considered that $\vec{v}$ is negligible as compared to $K\vec{E}$, resulting in decoupling of the two sets of equations. This, however, does not resolve the difficulties involved in the problem, for even then the Poisson equation (3.1) can only be solved for a few special cases. The common feature of these special cases is that the geometrical configuration of the electrodes should be such that the charge density ρ_e could be expressed, with the aid of Eqs. (3.3) and (3.4), in terms of the electric field intensity, the appropriate spatial coordinate, and an experimentally determinable quantity (usually the total current at the cathode). The electrode configurations possessing this property include parallel planes, coaxial cylinders and concentric spheres.

For the actual physical situation of wire-plane or point-plane corona, the electric field intensity, the charge density, and hence the current density are strong functions of the relevant spatial coordinates. Lack of an explicit relation between ρ_e and E, and hence the Coulomb's force can not be determined analytically. Experimentally only the current density distribution along the plane electrode has been measured. The data obtained by Chattock[26] for point-plane corona and those to be presented in Chapter VI for wire-plane corona exhibit a bell-shaped distribution of current density, when the latter is plotted against the distance from the center or centerline of the plane which is taken to be the point or line of normal projection of the point or wire electrode. This implies that the electric wind is confined to a very narrow region around the point or wire, and its velocity distribution is strongly non-uniform.

The non-uniformity of the jet of electric wind suggests that the flow generated by the non-uniform electric field is rotational. It can be shown that the rotationality might be a direct consequence of the non-conservative electrostatic force and needs not necessarily be a result of viscous effects. If one takes the curl of Eq. (3.6) and goes through some mathematical manipulations, there results an expression for the rate of change of vorticity

$$\frac{D\vec{\omega}}{Dt} = \frac{1}{\rho}\vec{E} \times \nabla\rho_e + (\vec{\omega}\cdot\nabla)v + \mu\nabla^2\vec{\omega} \qquad (3.7)$$

where

$$\frac{D}{Dt} \equiv \frac{\partial}{\partial t} + (\vec{v}\cdot\nabla$$

is the substantial derivative. From this equation it is seen that in the absence of viscous effects an electric wind will remain irrotational (if it is initially so) only either when the charge density is constant or when the electric field is colinear with the gradient of the charge density. Neither condition is satisfied in a wire-plane or point-plane corona and the electric wind thereby induced is rotational.

To gain a further insight into the nature of an electric wind, it is helpful to compare it with a free jet. Despite the fact that the two flows are governed by different equations of motion (the difference being in the extraneous force term), a parallel between them may be drawn in certain aspects. An electric wind is analogous to a free jet in the sense that both discharge into a still fluid of the same kind. While the total momentum of a free jet in the direction of jet axis remains constant and independent of distance from the orifice, the quantity which possesses similar characteristics for an electric wind is the total force (considering the case $\vec{v} \ll K\vec{E}$). Theoretically a free jet can be regarded as emerging from a line source (the discussion having been restricted to two-dimensional case, similar statements apply to axisymmetric situation) which issues, in one direction only, a finite volume of flow with a finite momentum (28, 29). In the case of electric wind, the air stream is generated by a finite force

$$F = \frac{1}{k}\int_{-\infty}^{\infty} J dx = \frac{I}{k} \text{ (x being transverse to the direction of the wind)}$$

at a very thin region near the emitting corona wire facing the collecting electrode. It appears that an electric wind could, therefore, be considered as emerging from a line source in a direction normal to the collector through the action of a finite force F. However, a discrepancy exists between the two types of line sources; whereas in a free jet the discharging fluid is introduced externally, the streaming air in an electric wind must come from the surroundings (presumably from the region behind the wire). Emerging from a slit with uniform velocity, the free jet carries with it some of the surrounding fluid originally at rest because of free mixing developed on its periphery as a result of friction, an action usually referred to as entrainment. The electric wind induced by a wire-plane corona is inherently non-uniform; the velocity vanishes at its periphery mainly because the space charge density there is zero. It is thus speculated that entrainment at the boundaries of an electric wind is probably not as significant as in a free jet.

3.2 ONE-DIMENSIONAL MODEL

The case considered first is a one-dimensional electric wind generated by parallel plane electrodes shown in Fig. 4. The emitting electrode (the anode) is considered to consist of closely spaced parallel corona wires located at x=0; while the collecting electrode (the cathode) is in the form of a plane wire screen (at $x=x_2$) which allows the induced wind to pass through. A voltage of V (kv) impressed across the electrodes causes a current I (amp) to flow, producing a current density $J = I/S$ (amp/m^2). Since the electrodes can not sustain any pressure gradient, the atmospheric pressure prevails throughout the entire space between the electrodes, and the action of the electrostatic body force on the air molecules results in the streaming of the electric wind.

For one-dimensional approximation, $\vec{J}$ $\vec{E}$ and $\vec{v}$ have only a component in the x direction and are functions of x alone. In the absence of solid boundaries and disregarding the free mixing region along the edges of the electrodes, viscous effects on the flow can be neglected. The governing equations thus reduce to, for steady flow,

$$\epsilon \frac{dE}{dx} = \rho_e \tag{3.8}$$

$$\frac{dJ}{dx} = 0 \tag{3.9}$$

$$J = \rho_e(u+KE) \tag{3.10}$$

$$\rho u \frac{du}{dx} = \rho_e E \tag{3.11}$$

Combination of Eqs. (3.8) and (3.11) gives

$$\rho u \frac{du}{dx} = \epsilon E \frac{dE}{dx}$$

which can be solved to yield

$$\rho u^2 - \epsilon E^2 = \text{constant} = K_1 \tag{3.12}$$

From Eq. (3.9), it is apparent that the current density is constant. Using Eqs. (3.10) and (3.12) in Eq. (3.8), there is obtained an equation determining the electric field intensity E.

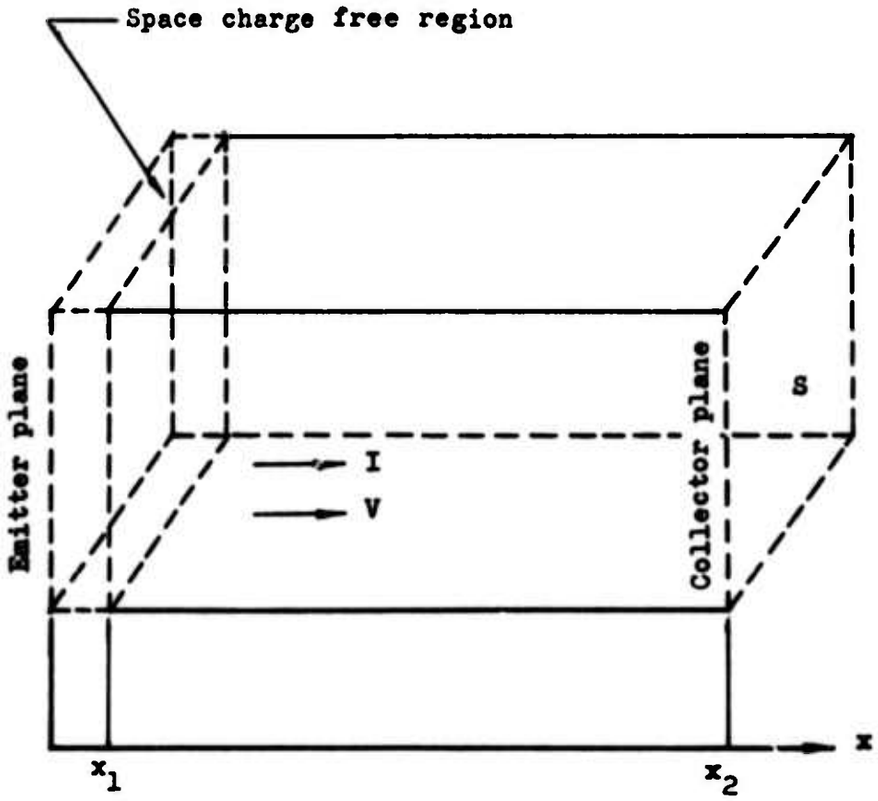

Fig. 4 One-dimensional model of electric wind

$$\epsilon \left[\sqrt{\frac{\epsilon}{\rho}} \sqrt{E^2 + E_1/\epsilon} + KE \right] \frac{dE}{dx} = J$$

Upon integration, it is found

$$\frac{\sqrt{\epsilon/\rho}}{2} \left\{ E \sqrt{E^2 + (K_1/\epsilon)} + (K_1/\epsilon) \ln \left[E + \sqrt{E^2 + (K_1/\epsilon)} \right] \right\} + \frac{KE^2}{2} = Jx + K_2 \tag{3.13}$$

where K_2 is a constant of integration.

It remains to determine the two constants K_1 and K_2. The fact that the highly ionized region constituting the corona envelope occupies only a very small volume (say between $x = 0$ and $x = x_1$) near the emitter provides the appropriate boundary conditions at the emitter. In this region the positive and negative ions are approximately equal in number. Therefore, it may be assumed that $\rho_e = 0$ there and hence the absence of electric force. At $x = x_1$ the field strength is equal to the spark-breakdown field strength E_1. Disregarding the entrainment of air molecules from the surroundings ($x < 0$) the velocity of the air at $x = x_1$ may be assumed zero. There conditions permit the determination of K_1 and K_2. They are

$$K_1 = - \epsilon E_1^2$$

and

$$K_2 = \frac{\epsilon}{2} E_1^2 (K - \sqrt{\frac{\epsilon}{\rho}} \ln E_1) - Jx_1$$

Thus Eqs. (3.12) and (3.13) becomes

$$\rho u^2 = \epsilon (E^2 - E_1^2) \tag{3.14}$$

and

$$\epsilon \frac{\sqrt{\epsilon/\rho}}{2} \left[E \sqrt{E^2 - E_1^2} - E_1^2 \ln \left(E + \sqrt{E^2 - E_1} \right) \right] + \frac{K}{2} E^2 \Bigg\}$$

$$= J(X - x_1) + \frac{\epsilon E_1^2}{2} \left(K - \sqrt{\epsilon/\rho} \ln E_1 \right) \tag{3.15}$$

For the sake of simplicity, it will be assumed that E_1 is zero and x_1 is negligible against x_2. With these assumptions the velocity of the induced electric wind at the screen electrode is found to be

$$u_2 = \sqrt{2Jx_2/\rho(\sqrt{\epsilon/\rho}+K)} \tag{3.16}$$

and the velocity at x is

$$u = \sqrt{2J(x-x_1)/\rho(\sqrt{\epsilon/\rho}+K)} \tag{3.17}$$

That the assumption of zero field at emitter is far from true has been emphasized by Stuetzer[30]. Fortunately a similar expression can be derived in an alternative manner. When u is negligible as compared to KE, Eq. (3.11) can be written

$$\rho u \frac{du}{dx} = \frac{J}{K} \tag{3.18}$$

which, upon integration, yields

$$u = \sqrt{2J(x-x_1)/\rho K} = \sqrt{2I(x-x_1)/\rho KS} \tag{3.19}$$

At $x=x_2$, the velocity is approximately

$$u_2 = \sqrt{2Jx_2/\rho K} = \sqrt{2Ix_2/\rho KS} \tag{3.20}$$

A great disadvantage of the one-dimensional model of electric wind is that the continuity equation is not satisfied. It is therefore concluded that continuous streaming of the electric wind requires replenishment from the surroundings by entrainment.

3.3 TWO-DIMENSIONAL MODEL

The electric field associated with wire-plane electrode configuration is two dimensional and the electric wind thereby induced is two-dimensional as well. Referring to Fig. 4, instead of a plane of parallel wires, it is now considered that the emitting electrode is a single wire. The physical model and the coordinate system are depicted in Fig. 5. The asymmetry of the electric field and the absence of a theory of breakdown in non-uniform fields make it not possible to determine analytically the distribution of the electric wind, certain assumptions have to be made:

1. The transverse velocity component u of the jet of electric wind is small compared to the longitudinal velocity component v.

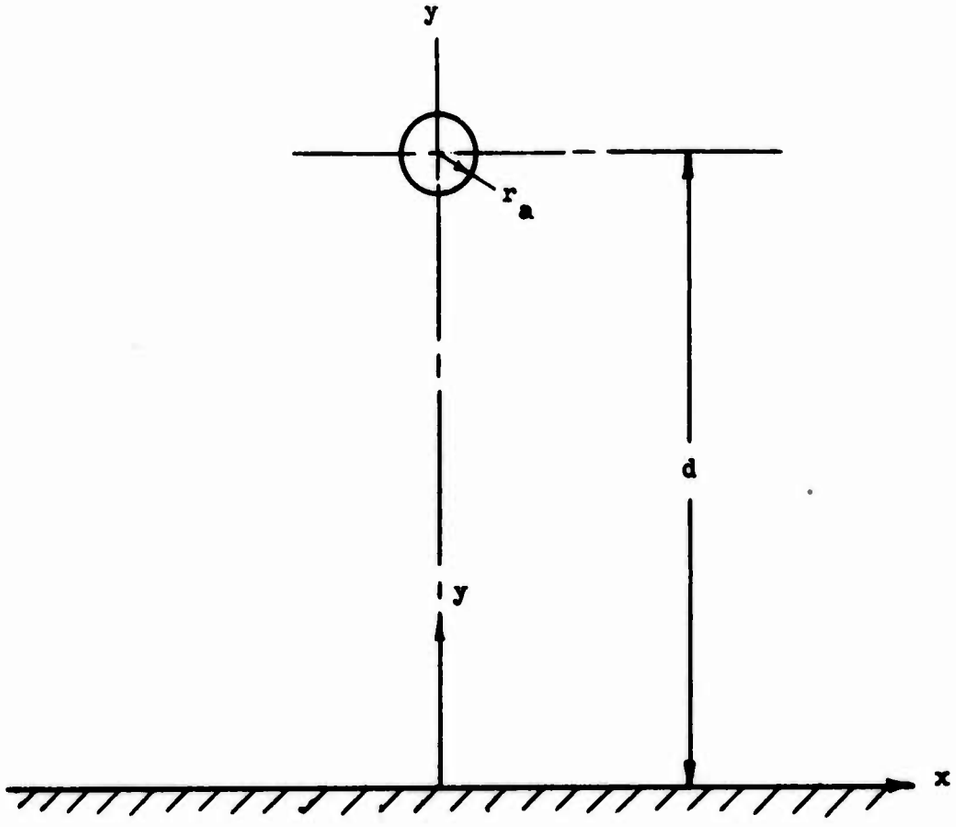

Fig. 5 Two-dimensional model of electric wind

2. $\partial E_x/\partial x$ is small compared to $\partial E_Y/\partial y$, so that the Poisson's equation (3.1) may be approximated by

$$\frac{\partial E_y}{\partial y} = \frac{\rho_e}{\epsilon}$$

3. For a first approximation, the value of E_y in the absence of space charges will be used to replace the actual E_y.

On the basis of the first two assumptions, the equations of motion reduce to a single equation

$$\rho v \frac{\partial v}{\partial y} = \epsilon E_y \frac{\partial E_y}{\partial y} \tag{3.21}$$

which upon integration becomes

$$\rho v^2 - \epsilon E_y^2 = f_o(x) \tag{3.22}$$

where $f_o(x)$, a function of x only, is introduced through integration.

Once again the wind will be considered to start blowing from at rest near the wire so that the boundary condition which must be satisfied by Eq. (3.22) is, assuming the radius of the wire is small against d,

$$u = 0 \qquad \text{when} \qquad [E_y = E_y]_{y=d} = E_y(x,d)$$

Using this the function $f_o(x)$ is found to be

$$f_o(x) = - \epsilon [E_y(x,d)]^2$$

and Eq. (3.22) can be rewritten

$$\rho v^2 = \epsilon \left\{ E_y^2 - [E_y(x,d)]^2 \right\} \tag{3.23}$$

Assuming again the field vanished at the edge of ionization zone near the emitting electrode, Eq. (3.23) takes a simple form

$$v = \sqrt{\epsilon/\rho}\, E_y \tag{3.24}$$

An analogous expression relating the pressure to the field strength ha been deduced by Velkoff[4] by means of a different argument. Neglecting

space charge distortion the electric field, as noted by Velkoff, can be expressed as

$$E_y = - \frac{V}{\ln \frac{2d}{r_a}} \left[\frac{y - d}{x^2 + (y-d)^2} - \frac{y + d}{x^2 + (y+d)^2} \right]$$

when the radius r_a of the wire electrode is small as compared to the distance d of the wire from the plane electrode. Following assumption 3, Eq. (3.24) becomes

$$v = \sqrt{\frac{\epsilon}{\rho}} \frac{V}{\ln \frac{2d}{r_a}} \left[\frac{y - d}{x^2 + (y-d)^2} - \frac{y + d}{x^2 + (y+d)^2} \right] \qquad (3.25)$$

As in one-dimensional case, the assumption of negligible field near the emitting electrode is unrealistic. It has been pointed out by Kapzow[31] that at the emitter the field is the highest in the system. The validity of Eq. (3.25) thus needs further justification.

A different approach makes use of the relation $\rho_e E_y = J_y/K$ and assumption 1, the other two assumptions being discarded. Thus in place of Eq. (3.21), an expression similar to Eq. (3.18) is obtained

$$\rho v \frac{\partial v}{\partial y} = J_y/K \qquad (3.26)$$

Integration from the emitter $y = y_e$, where $v = 0$, to the collector $y = y_c$ gives the following relation for the velocity distribution at the collecting electrode

$$v_c = \left[\frac{I}{\rho K} \int_{y_e}^{y_c} J_y dy \right]^{1/2} \qquad (3.27)$$

This equation is similar to the one obtained by Robinson[27], who further considered that J_y is proportional to the total current I and arrived at a relation between v_c and I, for coaxial cylindrical and concentric spherical electrode configuration, namely,

$$v_c = K' \left(\frac{I}{\rho K} \right)^{1/2} \qquad (3.28)$$

where K' is a constant of proportionality to be determined experimentally. Since two-dimensional situation is being considered here, v_c is a function of x, it follows that K' must also depends on x for Eq. (3.28) to be valid.

3.4 INVISCID ELECTRIC WIND WITH STAGNATION

The generation of the electric wind is usually associated with a solid plane which acts as the collecting electrode. The presence of this solid plane tends to make the situation more intractable. When the wind discharges onto the plane, a static pressure gradient is expected to build up near the stagnation point. For the electrode configuration of a wire-plane corona, the electric field component E_x parallel to the plane is in practice negligible as compared to the component E_y normal to the plane near the plane surface. Therefore, the equations of motion for a two-dimensional inviscid flow in the neighborhood of a stagnation point can be written as

$$\rho u \frac{\partial u}{\partial x} + \rho v \frac{\partial u}{\partial y} = - \frac{\partial p}{\partial x} \tag{3.29}$$

$$\rho u \frac{\partial v}{\partial x} + \rho v \frac{\partial v}{\partial y} = - \frac{\partial p}{\partial y} + \rho_e E_y \tag{3.30}$$

Instead of solving these two equations, which is no easy task, a simple relation between the velocity, pressure and electric quantity will be derived. When multiplied by dx and dy respectively and use is made of the relation along a stream line

$$\frac{dx}{u} = \frac{dy}{v}$$

Eqs. (3.29) and (3.30) combine to give an equation of the form

$$d\left[\frac{\rho}{2}(u^2+v^2)\right] + dp - \rho_e E_y dy = 0 \tag{3.31}$$

Upon integration, there results a Bernoulli equation for the problem of interest

$$\frac{\rho}{2}(u^2+v^2) + p - \int_{s.l.} \rho_e E_y dy = \text{constant} \tag{3.32}$$

where s.l. indicates the integration is along a streamline. In general the constant, the so-called Bernoulli constant, takes different values for different streamlines when the flow is rotational. When

$$\frac{\partial E_x}{\partial x} \ll \frac{\partial E_y}{\partial y} \quad ,$$

Eq/ (3.32) can be written

$$\frac{\rho}{2}(u^2+v) + p - \frac{1}{2}\epsilon E_y^2 = \text{constant.} \tag{3.33}$$

If on the other hand the relation $\rho_e E_y = J_y/K$ is used, it follows

$$\frac{\rho}{2}(u^2+v^2) + p - \int_{s.l.} \frac{J_y}{K}\,dy = \text{constant.} \tag{3.34}$$

The x component of the pressure gradient is of utmost importance in considering viscous stagnation flow. Differentiation of Eq. (3.34) with respect to x gives

$$\frac{\partial p}{\partial x} = -\rho u \frac{\partial u}{\partial x} - \rho v \frac{\partial v}{\partial x} + \int_{s.l.} \frac{1}{K}\frac{\partial J_y}{\partial x}\,dy + \frac{\partial}{\partial x}\quad\text{(Bernoulli constant)} \tag{3.35}$$

It is noted from this equation that $\partial p/\partial x$ is determined by the velocity field as well as the electric field.

For one-dimensional electric wind J_y = constant and the Bernoulli constant takes an identical value throughout the flow field. It follows that for this particular case

$$\frac{\partial p}{\partial x} = -\rho u \frac{\partial u}{\partial x} - \rho v \frac{\partial v}{\partial x} \tag{3.36}$$

The relation (3.36) also holds true for two-dimensional potential flows in the absence of extraneous forces. Hence the flow produced by a one-dimensional electric wind impinging on a plane electrode can be treated as a classical two-dimensional stagnation flow. For the latter case the velocity distribution in frictionless potential flow in the neighborhood of the stagnation point is given by[28]

$$u = u_1 x; \qquad v = -u_1 y \tag{3.37}$$

where u_1 is a constant determined by the oncoming stream. Thus

$$\frac{\partial p}{\partial x} = -\rho u \frac{\partial u}{\partial x} = -\rho u_1^2 x \tag{3.38}$$

CHAPTER IV

HEAT AND MASS TRANSFER IN TWO-DIMENSIONAL STAGNATION FLOW

4.1 GENERAL CONSIDERATIONS

In view of the non-uniformity of the impinging two-dimensional jet of electric wind, the flow field in the neighborhood of the stagnation point is rather complex. At the present state of our knowledge, it is impossible to obtain an exact solution for the actual stagnation flow resulted from the impingement of a non-uniform stream with arbitrary velocity distribution. Information on the heat and mass transfer processes at the stagnation point, however, may be secured by consideration of the stagnation flow under an impinging uniform stream.

Consider a uniform electric wind induced by positive corona discharges taking place between a plane of closely-spaced parallel wires and a solid plane wall electrode. Moving in the direction of the electric field, the wind arrives from the y-axis, strikes normally on the plane electrode placed at y=0, divides into two streams on the wall and leaves in both directions, Fig. 6. The temperature and the mass fraction of water vapor of the impinging air are considered to be the same as the surrounding air. The facts that the streaming air, though induced electrically, is actually replenished from the surroundings through entrainment, and that the corona discharge does not have significant effects on the temperature and moisture content of the air, seem to lend strong support to this assumption.

The viscous flow theory for two-dimensional stagnation flow has already been well developed. It has long been recognized that for this type of flow the solution based on Prandtl's boundary layer approximation is also an exact solution to the complete Navier-Stokes equations for two-dimensional flows. For rapid calculations of the heat and mass transfer values near the stagnation point, it is proposed to make use of the integral method based on the boundary layer equations.

The complete set of the differential equations which describe the combined momentum, energy and mass transport in a two-dimensional incompressible steady laminar boundary layer of a binary mixture, which is humid air for this case, are, as given by Eckert and Drake[32],

Continuity:

$$\frac{\partial u}{\partial x} + \frac{\partial v}{\partial y} = 0 \tag{4.1}$$

Momentum:

$$u \frac{\partial u}{\partial x} + v \frac{\partial u}{\partial y} = U \frac{dU}{dx} + \nu \frac{\partial^2 u}{\partial y^2} \tag{4.2}$$

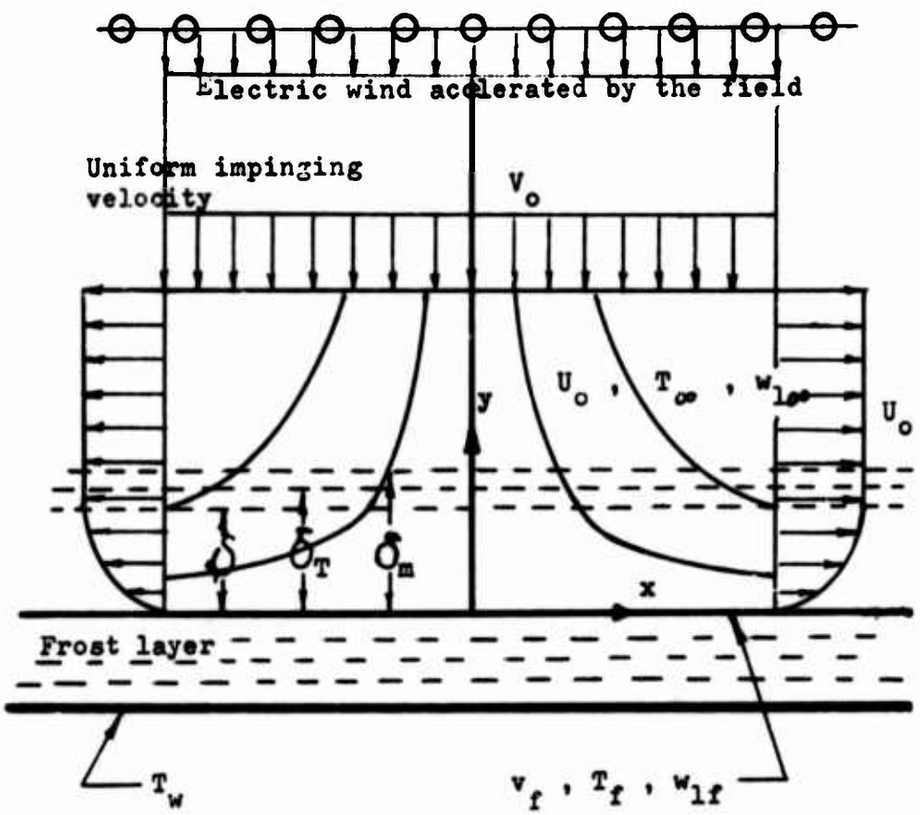

Fig. 6 Two-dimensional stagnation flow under impingement of uniform electric wind

Energy:

$$u \frac{\partial T}{\partial x} + v \frac{\partial T}{\partial y} = a \frac{\partial^2 T}{\partial y^2} \tag{4.3}$$

Diffusion:

$$u \frac{\partial w_1}{\partial x} + v \frac{\partial w_1}{\partial y} = D \frac{\partial^2 w_1}{\partial y^2} \tag{4.4}$$

The pressure gradient term in the momentum equation has been substituted in favor of the free stream velocity. In the energy equation, the viscous dissipation, the thermal diffusion and the diffusion thermo-effect are neglected. The diffusion equation is written in terms of the mass fraction w_1 of the water vapor.

The boundary conditions appropriate to the flow over a frosting surface are

$$\text{At } y = 0 : \quad u = 0 \ , \ v = v_f \ , \ T = T_f \ , \ w_1 = w_{1f} \tag{4.5}$$

$$\text{At } y = \infty : \quad u = U \ , \ T = T_\infty \ , \ w_1 = w_{1_\infty} \tag{4.6}$$

The mass fraction w_{1f} and temperature T_f at the frost surface will be assumed constant. The condition $v = v_f$ accounts for the fact that a convective flow is generally connected with mass transfer from or to a surface. Such a convective flow is always present when the surface is impermeable for one component of the mixture. In order to complete the statement of the problem under consideration, the normal velocity at the frost surface v_f is to be supplied by application of the condition that the mass transfer of air to the frost surface is considered to be zero[24]. The mass flux of air consists of two parts: a diffusive mass flux and a convective flux. In the absence of diffusion thermo-effect and thermal diffusion, the total mass flux of air at the frost surface is

$$-\rho D \frac{dw_2}{dy} + \rho_2 v_f = 0$$

where the subscript 2 denotes the second species of the mixture, which is dry air in this case. The mass fraction of the air can be expressed in terms of the mass fraction of the water vapor by

$$\frac{\rho_2}{\rho} = w_2 \ , \ w_2 = 1 - w_1 \ , \ \frac{dw_2}{dy} = - \frac{dw_1}{dy}$$

This gives

$$v_f = - \frac{D}{1 - w_1} \frac{dw_1}{dy} \tag{4.7}$$

where w_1 and its derivative are to be evaluated at the frost surface.

The integral relations which form the basis of the integral method are most simply obtained by integration from the boundary layer equations (4.1) through (4.4). Equations (4.1) and (4.2) may be written as

$$-\nu \frac{\partial^2 u}{\partial y^2} = U \frac{dU}{dx} - u \frac{\partial u}{\partial x} - v \frac{\partial u}{\partial y}$$

$$0 = (U-u) \frac{\partial u}{\partial x} + (U-u) \frac{\partial v}{\partial y}$$

where Eq. (4.1) has been multiplied by (U-u). By addition of these,

$$-\nu \frac{\partial^2 u}{\partial y^2} = \frac{\partial}{\partial x} (Uu-u^2) + (U-u) \frac{dU}{dx} + \frac{\partial}{\partial y} (vU-vu)$$

Upon integration with respect to y from 0 to ∞ this yields, since $\partial u/\partial y$ and $v(U-u)$ tend to zero as $y \to \infty$, the equation expressing the balance of momentum

$$\nu \frac{\partial u}{\partial y}_{y=0} = \frac{\partial}{\partial x} \int_0^\infty (U-u)u\,dy + \frac{dU}{dx} \int_0^\infty (U-u)\,dy - v_f U \tag{4.8}$$

The same process of integration applies to Eqs. (4.3) and (4.4) leads to similar equations expressing the balance of heat and material. In terms of the new variables θ and φ defined by

$$\theta = \frac{T - T_f}{T_\infty - T_f} , \qquad \varphi = \frac{w_1 - w_{1f}}{w_{1\infty} - w_{1f}}$$

the resulting integral equations have the following forms

$$\frac{\nu}{Pr} \left(\frac{\partial \theta}{\partial y}\right)_{y=0} = \frac{\partial}{\partial x} \int_0^\infty (1-\theta)u\,dy - v_f \tag{4.9}$$

$$\frac{\nu}{Sc} \left(\frac{\partial \varphi}{\partial y}\right)_{y=0} = \frac{\partial}{\partial x} \int_0^\infty (1-\varphi)u\,dy - v_f \tag{4.10}$$

where $Pr = \nu/a$ is the Prandtl number and $Sc = \nu/D$ is the Schmidt number.

Equations (4.8) through (4.10) can equally well be formulated from purely physical reasoning, without recourse to the differential equations.

The normal velocity at the frost surface v_f, when expressed in terms of φ, becomes

$$v_f = - \frac{\nu}{Sc} B \left(\frac{\partial \varphi}{\partial y}\right)_{y=0} \tag{4.11}$$

where

$$B = \frac{w_{1\infty} - w_{1f}}{1 - w_{1f}}$$

4.2 SOLUTION FOR v_f NEGLIGIBLY SMALL

The simpler case where v_f is negligible will be considered first. The problem is simplified considerably as a result of the decoupling of the momentum equation from the diffusion equation when the boundary condition $v = v_f = 0$ is used. Thus the momentum integral equation may be solved independently in exactly the same manner as Pohlhausen's approximate method. An excellent polynomial representation of the velocity profile takes the following form

$$\frac{u}{U} = 2\left(\frac{Y}{\delta}\right) - 2\left(\frac{Y}{\delta}\right)^3 + \left(\frac{Y}{\delta}\right)^4 + \frac{\lambda}{6} \frac{Y}{\delta} \left(1 - \frac{Y}{\delta}\right)^3 \tag{4.12}$$

where $U = u_1 x$, $\lambda = \delta^2 u_1 / \nu$, δ is the boundary layer thickness and u_1 is a proportionality constant having the dimension sec^{-1}. It has been shown in Schlichting[28] that the profile for stagnation point flow corresponds to $\lambda = 7.052$, so that

$$\delta = \left(7.052 \frac{\nu}{u_1}\right)^{1/2} \tag{4.13}$$

In order to solve the energy and the diffusion integral equations, suitable functions have to be chosen for θ and φ. On account of the similarity in form of Eqs. (4.9) and (4.10) in the absence of v_f and the identity of the boundary conditions (4.5) and (4.6) for θ and φ, it is only necessary to carry through the calculation for one of the two equations. The solution thus obtained is also a solution of the other equation provided $Pr = Sc$. If $Pr \neq Sc$, it is necessary to replace Pr by Sc or vice versa, as case may be, in the process of calculation.

As the temperature profile, the function

$$\theta = \frac{3}{2} \frac{Y}{\delta_T} - \frac{1}{2} \left(\frac{Y}{\delta_T}\right)^3 \tag{4.14}$$

which satisfies the following boundary conditions

$$y = 0 \ , \quad \theta = 0 \ , \quad \frac{\partial^2 \theta}{\partial y^2} = 0$$

$$y = \delta_T \ , \quad \theta = 1 \ , \quad \frac{\partial \theta}{\partial y} = 0 \tag{4.15}$$

will be used. Although strictly the conditions at infinity are only approached asymptotically, it is assumed that these conditions can be transferred from infinity to $y = \delta_T$ without appreciable error (similar assumption applies to the velocity and material boundary layers). As seen from Eq. (4.3), the conditions (4.15) are all satisfied by the exact solution. Here the thermal boundary layer thickness δ_T is independent of x, since T_f is assumed to be spatially uniform[33].

Introducing Eqs. (4.12) and (4.14) in Eq. (4.9) and carrying out the indicated integrations and differentiations, v_f being treated zero, there results

$$\frac{\delta_T^2}{\delta}\left(\frac{1}{5} + \frac{\lambda}{60}\right) + \frac{\delta_T^3}{\delta^2}\left(-\frac{\lambda}{48}\right) + \frac{\delta_T^4}{\delta^3}\left(-\frac{\dot{\beta}}{70} + \frac{3\lambda}{280}\right) + \frac{\delta_T^5}{\delta^4}\left(\frac{1}{80} - \frac{\lambda}{480}\right) = \left(\frac{3\nu}{2Pru_1}\right)\left(\frac{1}{\delta_T}\right) \tag{4.16}$$

This expression is only strictly valid of $\delta_T \leq \delta$, which is not usually the case, since Eq. (4.12) is only valid for $y \leq \delta$. However, the algebra would become more cumbersome with little gain in accuracy if the strict expression were used.

Writing $\Delta_T = \frac{\delta_T}{\delta}$, Eq. (4.16) becomes

$$\Delta_T^3(\Delta_T^3 - 14.9315\ \Delta_T^2 + 67.0867\ \Delta_T - 144.991) = -97.1503\left(\frac{1}{Pr}\right) \tag{4.17}$$

An approximation to the solution of this equation when Pr does not differ too much from unity, i.e. $\Delta_T \approx 1$, can be obtained by setting $\Delta_T = 1$ in the parenthesis. Hence, approximately,

$$\Delta_T = (Pr)^{-1/3} \tag{4.18}$$

An accurate solution of Eq. (4.17) for Pr has been calculated by Sparrow[33]. He gave the value $\Delta_T = 1.177$. Calculation based on Eq. (4.18) gives $\Delta_T = 1.14$. Thus the expression (4.18) is in error by less than 5% as compared with the accurate solution.

Similarly, the material profile may be assumed to have the form

$$\varphi = \frac{3}{2}\frac{y}{\delta_m} - \frac{1}{2}\left(\frac{y}{\delta_m}\right)^3 \tag{4.19}$$

which satisfies the boundary conditions

$$y = 0 \ , \quad \varphi = \frac{\partial^2 \varphi}{\partial y^2} = 0$$

$$y = \delta_m \ , \ \varphi = 1 \ , \quad \frac{\partial \varphi}{\partial y} = 0 \tag{4.20}$$

where δ_m is the material boundary layer thickness.

Writing $\Delta_m = \delta_m/\delta$, Eq. (4.17) may now be modified to read

$$\Delta_m^3(\Delta_m^3 - 14.9315\ \Delta_m^2 + 67.0867\ \Delta_m - 144.991) = -\ 97.1503/Sc \tag{4.21}$$

The approximate solution corresponding to Eq. (4.18) now becomes

$$\Delta_m = (Sc)^{-1/3} \tag{4.22}$$

The heat flow to the plate near the stagnation point per unit area is given by, in the absence of mass transfer,

$$q = -\ k\left(\frac{\partial T}{\partial y}\right)_{y=0}$$

Upon substitution from Eq. (4.14), (4.18) and (4.13), it is obtained

$$q = -\frac{3}{2}k\left(\frac{u_1}{7.052\nu}\right)^{1/2}(Pr)^{1/3}(T_w - T_f) \tag{4.23}$$

On the other hand a heat transfer coefficient h can be introduced through "Newton's law of cooling"

$$q = -\ h(T_w - T_f)$$

Equating this last two expressions gives

$$h = \frac{3}{2} k \left(\frac{u_1}{7.052\nu}\right)^{1/2} (Pr)^{1/3} \qquad (4.24)$$

The mass flux to the plate near the stagnation point can be obtained in a similar fashion, namely.

$$m = - \rho D \left(\frac{\partial w_1}{\partial y}\right)_{y=0} = - \frac{3}{2} \rho D \left(\frac{u_1}{7.052\nu}\right)^{1/2} (Sc)^{1/3} (w_{1\infty} - w_{1f}) \qquad (4.25)$$

And the mass transfer coefficient defined as

$$m = - \rho h_m (w_{1\infty} - w_{1f})$$

can be readily deduced from Eq. (4.24)

$$h_m = \frac{3}{2} D \left(\frac{u_1}{7.052\nu}\right)^{1/2} (Sc)^{1/3} \qquad (4.26)$$

4.3 SOLUTION FOR v_f NOT ZERO

To account for the connection of the convective flow at the surface with the over-all transport process, it is required to deal with the coupled system of integral equations (4.8) through (4.10) simultaneously. The method which will be used is essentially similar to that of the preceding section. The only differences are that in selecting the suitable forms of the velocity, temperature and material profiles the boundary condition that $v = v_f$ has to be taken into account and that terms involving v_f are retained in the integral equations. Eckert and Lieblein[34] first applied the method to solve Eqs. (4.8) and (4.10) for the particular case of the vaporization of water from a flat plate in forced convection. An improved version of the method was used by Spalding[35] to find solutions of the same two equations for three types of flows: forced convection from a flat plate, free convection from a vertical plate and the forward stagnation point of a sphere suspended in a fluid stream. All three equations were solved in connection with the frosting plate in forced convection by Sugawara et al[36].

The integral equations (4.8) through (4.10) may be reduced to simplified forms by introduction of new quantities defined in terms of the integrals appearing in the equations. Considering Eq. (4.8) first, it is a well-known fact that, when expressed in terms of the displacement and momentum thicknesses, which are defined, respectively,

$$\delta^* = \int_0^\delta \left(1 - \frac{u}{U}\, dy\right) \tag{4.27}$$

and

$$\delta^{**} = \int_0^\delta \frac{u}{U}\left(1 - \frac{u}{U}\, dy\right) \tag{4.28}$$

the momentum integral equation reduces to

$$\left(\frac{\partial u}{\partial y}\right)_{y=0} + v_f U = \frac{\partial}{\partial x}\left(U^2 \delta^{**}\right) + \delta^* U \frac{dU}{dx} \tag{4.29}$$

Similarly, Eqs. (4.9) and (4.10) can be rewritten as

$$\frac{\nu}{Pr}\left(\frac{\partial \rho}{\partial y}\right)_{y=0} + v_f = \frac{d}{dx}\left(U \delta_T^{**}\right) \tag{4.30}$$

and

$$\frac{\nu}{Sc}\left(\frac{\partial \rho}{\partial y}\right)_{y=0} + v_f = \frac{d}{dx}\left(U \delta_m^{**}\right) \tag{4.31}$$

where δ_T^{**} and δ_m^{**} are defined by

$$\delta_T^{**} = \int_0^{\delta_T} (1-\theta)\frac{u}{U}\, dy \tag{4.32}$$

and

$$\delta_m^{**} = \int_0^{\delta_m} (1-\varphi)\frac{u}{U}\, dy \tag{4.33}$$

Following Spalding, it will be assumed that the velocity, temperature and material profiles can be expressed in cubic polynomial form, namely,

$$\frac{u}{U} = F(y) \quad a_1\frac{y}{\delta} + a_2\left(\frac{y}{\delta}\right)^2 + a_3\left(\frac{y}{\delta}\right)^3 \tag{4.34}$$

$$\theta = G(y) = b_1\frac{y}{\delta_T} + b_2\left(\frac{y}{\delta_T}\right)^2 + b_3\left(\frac{y}{\delta_T}\right)^3 \tag{4.35}$$

and

$$\varphi = H(y) = c_1\frac{y}{\delta_m} + c_2\left(\frac{y}{\delta_m}\right)^2 + c_3\left(\frac{y}{\delta_m}\right)^3 \tag{4.36}$$

The coefficients of these functions may be determined by consideration of the boundary conditions, which are

$$y = 0 : \quad u = 0 , \quad v_f \frac{\partial u}{\partial y} = \nu \frac{\partial^2 u}{\partial y^2} + U \frac{dU}{dx} \tag{4.37}$$

$$\theta = 0 , \quad v_f \frac{\partial \theta}{\partial y} = \frac{\nu}{Pr} \frac{\partial^2 \theta}{\partial y^2} \tag{4.38}$$

$$\varphi = 0 , \quad v_f \frac{\partial \varphi}{\partial y} = \frac{\nu}{Sc} \frac{\partial^2 \varphi}{\partial y^2} \tag{4.39}$$

$$y = \delta : \quad u = U , \quad \frac{\partial u}{\partial y} = 0 \tag{4.40}$$

$$y = \delta_T : \quad \theta = 1 , \quad \frac{\partial \theta}{\partial y} = 0 \tag{4.41}$$

$$y = \delta_m : \quad \varphi = 1 , \quad \frac{\partial \varphi}{\partial y} = 0 \tag{4.42}$$

The second conditions of (4.37) through (4.39), which are direct consequences of the differential equations (4.2) through (4.1), are of particular importance. They determine the curvatures of the velocity, temperature and material profiles near the surface. It is through them that the shapes of the profiles are affected by the convective flow at the surface, thus resulting in changes in the over-all transport process.

Inserting the value of v_f from Eq. (4.11), there is obtained the following relations determining the coefficients of the functions (4.34) through (4.36)

$$\begin{aligned}
&\lambda = 4a_1 - 6 - B''a_1^2 , \\
&a_2 = 3 - 2a_1 , \quad a_3 = a_1 - 2 , \\
&b_1 = \frac{2}{B'} \left[1 - \sqrt{1 - (3/2)B'}\right] , \\
&b_2 = 3 - 2b_1 , \quad b_3 = b_1 - 2 , \\
&c_1 = \frac{2}{B} \left[1 - \sqrt{1 - (3.2)B}\right] , \\
&c_2 = 3 - 2c_1 , \quad c_3 = c_1 - 2
\end{aligned} \tag{4.43}$$

where

$$B' = \frac{PrB}{Sc}\,\frac{\delta_T}{\delta_m}\,\frac{c_1}{b_1}$$

and

$$B'' = \frac{B}{Sc}\,\frac{\delta}{\delta_m}\,\frac{c_1}{a_1}$$

It should be noted that the functions (4.34) through (4.36) represent physically meaningful profiles only when the coefficients are all real. Upon examination of the above expressions, it is evident that when $B > 2/3$ no real coefficients are obtainable. More specifically, the method used here is strictly applicable when and only when $B \leq 2/3$. Fortunately, in frosting problem $(w_{1_w}-w_{1_f})$ is usually very small, of the order of 10^{-2}, and the condition $B \leq 2/3$ is fulfilled.

With the aid of Eqs. (4.34), (4.35), (4.36) and (4.43), the integral equations (4.29), (4.30) and (4.31) can now be rewritten as

$$(1-B'')a_1 = \frac{\delta}{\nu u}\,\frac{d}{dx}\,(U^2\delta^{**}) + \delta^{*}U\,\frac{dU}{dx} \tag{4.44}$$

$$(1-B')b_1 = \frac{Pr\,\delta_T}{\nu}\,\frac{d}{dx}\,(U\delta_T^{**}) \tag{4.45}$$

$$(1-B)c_1 = \frac{Sc\,\delta_m}{\nu}\,\frac{d}{dx}\,(U\delta_m^{**}) \tag{4.46}$$

where, after carrying out the indicated integrations in Eqs. (4.27), (4.28), (4.32) and (4.33),

$$\frac{\delta^{*}}{\delta} = \int_0^1 (1-F)d\left(\frac{Y}{\delta}\right) = \frac{1}{2} - \frac{a_1}{12} \tag{4.47}$$

$$\frac{\delta^{**}}{\delta} = \int_0^1 (1-F)Fd\left(\frac{Y}{\delta}\right) = \frac{9}{70} + \frac{3a_1}{140} - \frac{a_1^2}{105} \tag{4.48}$$

$$\frac{\delta_T^{**}}{\delta} = \frac{\delta_T}{\delta}\int_0^1 (1-F)Fd\left(\frac{Y}{\delta_T}\right) = \Delta_T^2\left[a_1\left(\frac{3}{20} - \frac{b_1}{30}\right) + \Delta_T(3-2a_1)\left(\frac{1}{15} - \frac{b_1}{60}\right)\right.$$

$$\left. + \Delta_T^2(a_1-2)\left(\frac{1}{28} - \frac{b_1}{105}\right)\right] \tag{4.49}$$

and

$$\frac{\delta_m^{**}}{\delta} = \frac{\delta_m}{\delta}\int_0^1 (1-H)Fd\left(\frac{y}{\delta_m}\right) = \Delta_m^2\left[a_1\left(\frac{3}{20} - \frac{c_1}{30}\right) + \Delta_m(3-2a_1)\left(\frac{1}{15} - \frac{c_1}{60}\right)\right.$$

$$\left. + \Delta_m^2(a_1-2)\left(\frac{1}{28} - \frac{c_1}{105}\right)\right] \qquad (4.50)$$

The last two expressions are strictly valid for $\delta_T \leq \delta$ and $\delta_m \leq \delta$.

Solution of the simultaneous ordinary differential equations (4.44), (4.45) and (4.46) for the general boundary layer flow with pressure gradient presents considerable difficulty and will not be attempted. For the particular case of stagnation flow under consideration, advantage may be taken of the information available in the literature. In the absence of mass transfer, i.e. when $v_f = 0$, the boundary layer thickness δ in a stagnation flow is constant, a well-established fact which can be readily seen from Eq. (4.13). An inspection of the existing solutions for mass transfer in laminar flows over flat plate and in free convection from a vertical plate indicates that the presence of v_f does not effect the functional relation between δ and x. On the basis of these above observations, it can be considered that δ remains constant in the stagnation flow when $v_f = 0$. Since $\Delta_T = \delta_T/\delta$ and $\Delta_m = \delta_m/\delta$ are independent of x, it follows that δ^*, δ^{**}, δ_T^{**} and δ_m^{**} are all constant. Hence Eqs. (4.4) through (4.46) reduce to

$$(1-B'')a_1 = \lambda\left(\frac{2\,\delta^{**}}{\delta} + \frac{\delta^*}{\delta}\right) \qquad (4.51)$$

$$(1-B')b_1 = \lambda Pr\Delta_T\,\frac{\delta_T^{**}}{\delta} \qquad (4.52)$$

$$(1-B)c_1 = \lambda Sc\Delta_m\,\frac{\delta_m^{**}}{\delta} \qquad (4.53)$$

Wherein δ^*/δ and δ^{**}/δ are known in terms of a_1 from Eqs. (4.47) and (4.48), while δ_T^{**}/δ and δ_m^{**}/δ come from Eqs. (4.49) and (4.50).

A relation between B'' and a_1 may be found from (4.51) by elimination of λ with the aid of the first relation of Eq. (4.43), namely,

$$B'' = \frac{1 - \left(4 - \frac{6}{a_1}\right)\left(\frac{2\,\delta^{**}}{\delta} + \frac{\delta^*}{\delta}\right)}{1 - a_1\left(\frac{2\,\delta^{**}}{\delta} + \frac{\delta^*}{\delta}\right)} \qquad (4.54)$$

The relation between B" and B may be determined as follows. Equation (4.50) can be rewritten as, with the aid of Eq. (4.48),

$$\frac{\delta_m^{**}}{\delta} = \Delta_m^2 \left\{ \frac{\delta^{**}}{\delta} + a_1 \left[\frac{(c_1-4)(\Delta_m-1)}{30} + \frac{\Delta_m^2-1}{28} + \frac{a_1-\Delta_m^2 c_1}{105} \right.\right.$$

$$\left.\left. + \frac{\Delta_m-1}{5} - \frac{(\Delta_m^2-1)}{14} - \frac{(\Delta_m c_1 - a_1)}{20} + \frac{2(\Delta_m^2 c_1 - a_1)}{105} \right] \right. \qquad (4.55)$$

It has been demonstrated by Spalding that the approximation $\Delta_m \approx 1$ may be substituted in the brackets in the above equation without causing appreciable error. Thus

$$\frac{\delta_m^{**}}{\delta} = \Delta_m^2 \frac{\delta^{**}}{\delta} \left[1 + \frac{(a_1-c_1)\left(\frac{a_1}{105} + \frac{13}{420}\right)}{\frac{\delta^{**}}{\delta}} \right] \qquad (4.56)$$

Dividing Eq. (4.51) by (4.53) and using Eq. (4.56), there results an expression for Δ_m, namely,

$$\Delta_m^3 = \frac{(1-B)c_1}{(1-B")a_1} \frac{\left(\frac{2\,\delta^{**}}{\delta} + \frac{\delta^*}{\delta}\right)}{Sc\ \frac{\delta^{**}}{\delta}\ (1+I)} \qquad (4.57)$$

where

$$I(a_1,c_1) = \frac{(a_1-c_1)\left(\frac{a_1}{105} + \frac{3}{420}\right)}{\frac{\delta^{**}}{\delta}}$$

Since B" has been defined as

$$B" = \frac{Bc_1}{Sc\ \Delta_m a_1}$$

it follows from Eq. (4.57)

$$\frac{(1-B")a_1}{(B"a_1)^3} = Sc^2 \frac{(1-B)c_1}{(Bc_1)^3} \frac{2 + \frac{\delta^*}{\delta^{**}}}{(1+I)} \qquad (4.58)$$

In a similar manner, the relation between B' and B may be obtained by first dividing Eq. (4.52) by (4.53) and using the approximation $\Delta_T \approx \Delta_m \approx 1$ in the brackets of Eqs. (4.49) and (4.50) to give an expression for Δ_T/Δ_m, namely,

$$\left(\frac{\Delta_T}{\Delta_m}\right)^3 = \frac{(1-B')b_1}{(1-B)c_1}\frac{Sc}{Pr} = \frac{(1-B')b_1}{(1-B)c_1} \cdot Le$$

(Le is the Lewis number)

and then substituting this in the equation defining B', that is $B' = \frac{PrB}{Sc}\frac{\delta_T}{\delta_m}\frac{c_1}{b_1}$. The resulting expression is

$$\frac{(1-B')b_1}{Le^2(B'b_1)^3} = \frac{(1-B)c_1}{(Bc_1)^3} \tag{4.59}$$

4.4 DETERMINATION OF THE HEAT AND MASS TRANSFER COEFFICIENTS

The determination of the heat and mass transfer coefficients in the presence of mass transfer is rendered more difficult than in the case where mass transfer is absent. As will be seen below, the heat and mass transfer rates per unit surface area depend on the first coefficients of the temperature and material profiles as well as the thicknesses of the temperature and material boundary layers. The latter in turn are related to the velocity boundary layer thickness. Since it is the quantity B which is normally specified, it is desirable to express the heat and mass transfer coefficients in terms of B. However, this can only be accomplished when it is possible to express explicitly the coefficients of the assumed profiles (4.34) through (4.36) in terms of B. It is evident from the preceding section that such explicit relations are difficult to find. Consequently, the heat and mass transfer coefficients can only be obtained either numerically or graphically for given values of B.

The rate of heat transfer (sensible heat transfer) per unit surface area is, as before, given by

$$q = -k\left(\frac{\partial T}{\partial y}\right)_{y=0}$$

Substituting the expression for the temperature gradient from Eq. (4.35), this leads to

$$q = -kb_1(T_\infty - T_f)/\delta_T$$

Using the equations defining λ, B', and B", the above equation may be put in the following form

$$q = -\frac{kPr}{\delta}\frac{B''}{B'}a_1(T_\infty - T_f) = -kPr\sqrt{\frac{u_1}{\lambda\nu}}\frac{B''}{B'}a_1(T_\infty - T_f) \tag{4.60}$$

In terms of the heat transfer coefficient defined previously,

$$h = kPr \sqrt{\frac{u_1}{\lambda \nu}} \frac{B''}{B'} a_1 \tag{4.61}$$

The procedure for calculating heat transfer rates or coefficients at the two-dimensional stagnation point is as follows:

1. The quantity B is ascertained from the data of the problem.

2. The coefficient c_1 is determined by the seventh relation of Eq. (4.43).

3. B' is obtained from Eq. (4.59) with the help of the fourth relation of Eq. (4.43).

4. B" and a_1 are found by solving simultaneously Eqs. (4.45) and (4.58).

5. The dimensionless quantity λ follows from the first relation of Eq. (4.43).

6. Finally, the heat transfer rates of coefficients are calculated from Eq. (4.60) or (4.61).

For given values of Pr and Sc, approximate values of the heat and mass transfer coefficients or rates may be found rapidly by the use of a graphical method. The expression on the right-hand side of Eq. (4.59) is plotted in Fig. 7. Because of the relation (4.59), interpolating in Fig. 7 enables b_1 and hence B' to be determined. To determine B" and a_1, it is convenient to plot both sides of Eq. (4.58). The left-hand side is plotted, with the aid of Eq. (4.54), in Fig. 8 for various values of a_1; while the right-hand side, excluding the quantity Sc^2, is plotted in Fig. 9 for various values of c_1 with a_1 as parameter. Since I is dependent on both a_1 and c_1, Eq. (4.58) has to be solved by a method of successive approximation. Let the quantity on the left-hand side of Eq. (4.58) be designated by M. For any given value of B and hence C_1, a value of M may be obtained by means of Fig. 9 for an arbitrarily selected value of a_1. Corresponding to this value of M, an a_1 is read from Fig. 8. If this value of a_1 differs from the selected one, go back to Fig. 9 and obtain another value of M, corresponding to the new value of a_1. Repeat the procedure until identical value of a_1 is obtained for successive iterations. This value of a_1 is then the solution of Eq. (4.58) for the given value of B. With a_1 thus found, B" follows from Fig. 10, in which B" is plotted versus a_1 using the relation (4.54). Inserting the values of a_1, B' and B" in Eq. (4.61), the heat transfer coefficient is readily calculated.

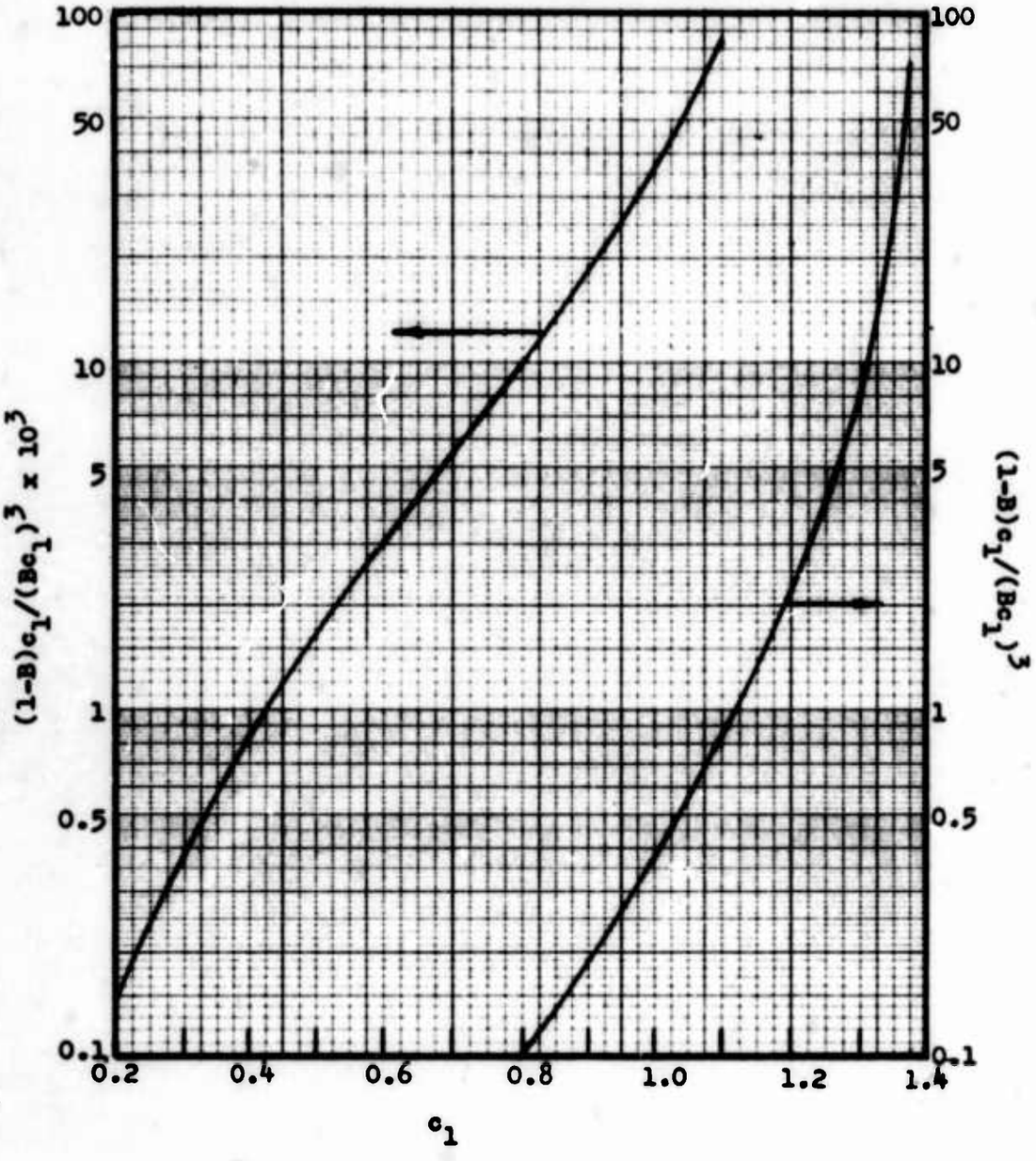

Fig. 7 Diagram for use with equation (4.59)

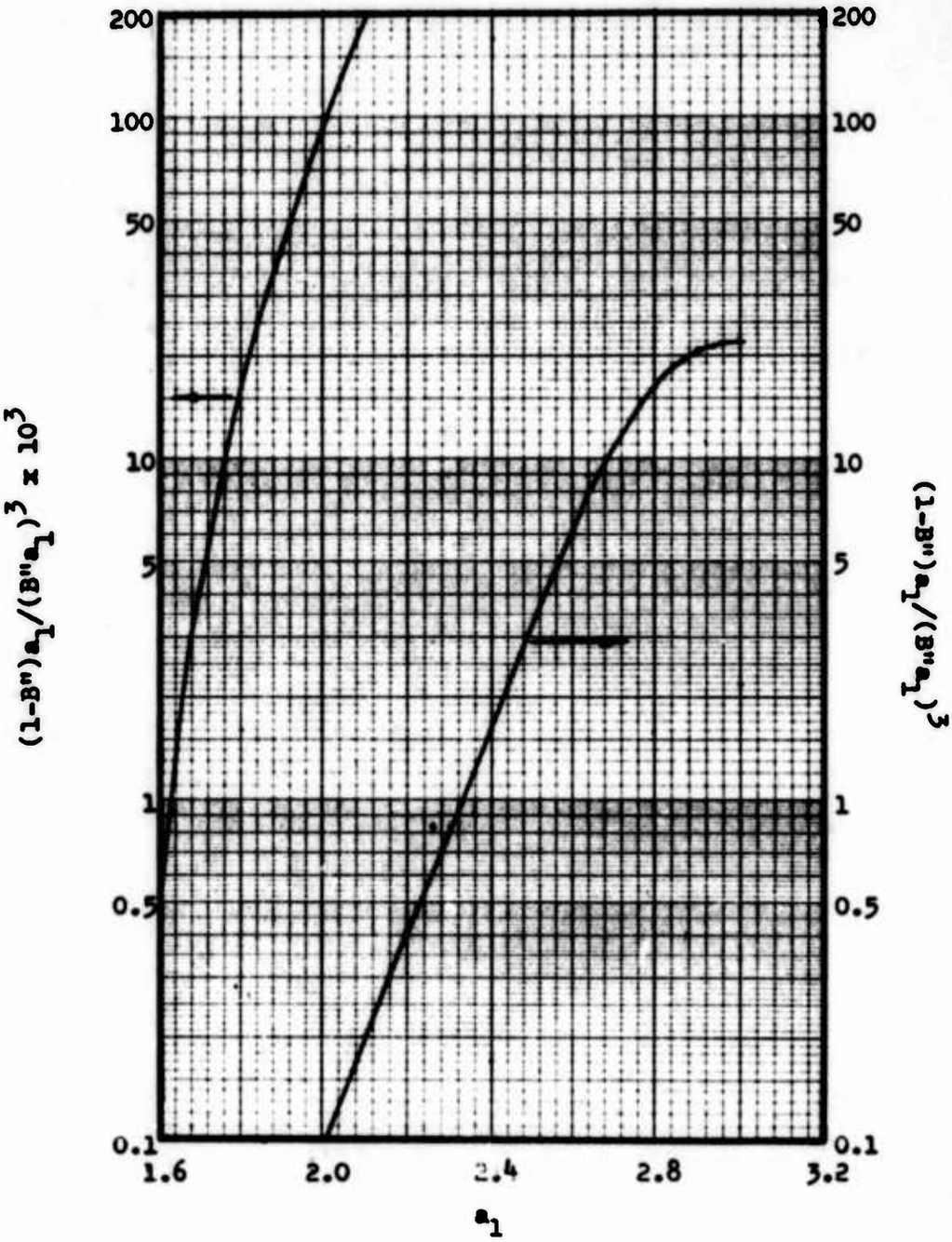

Fig. 8 Diagram for use with equation (4.58)

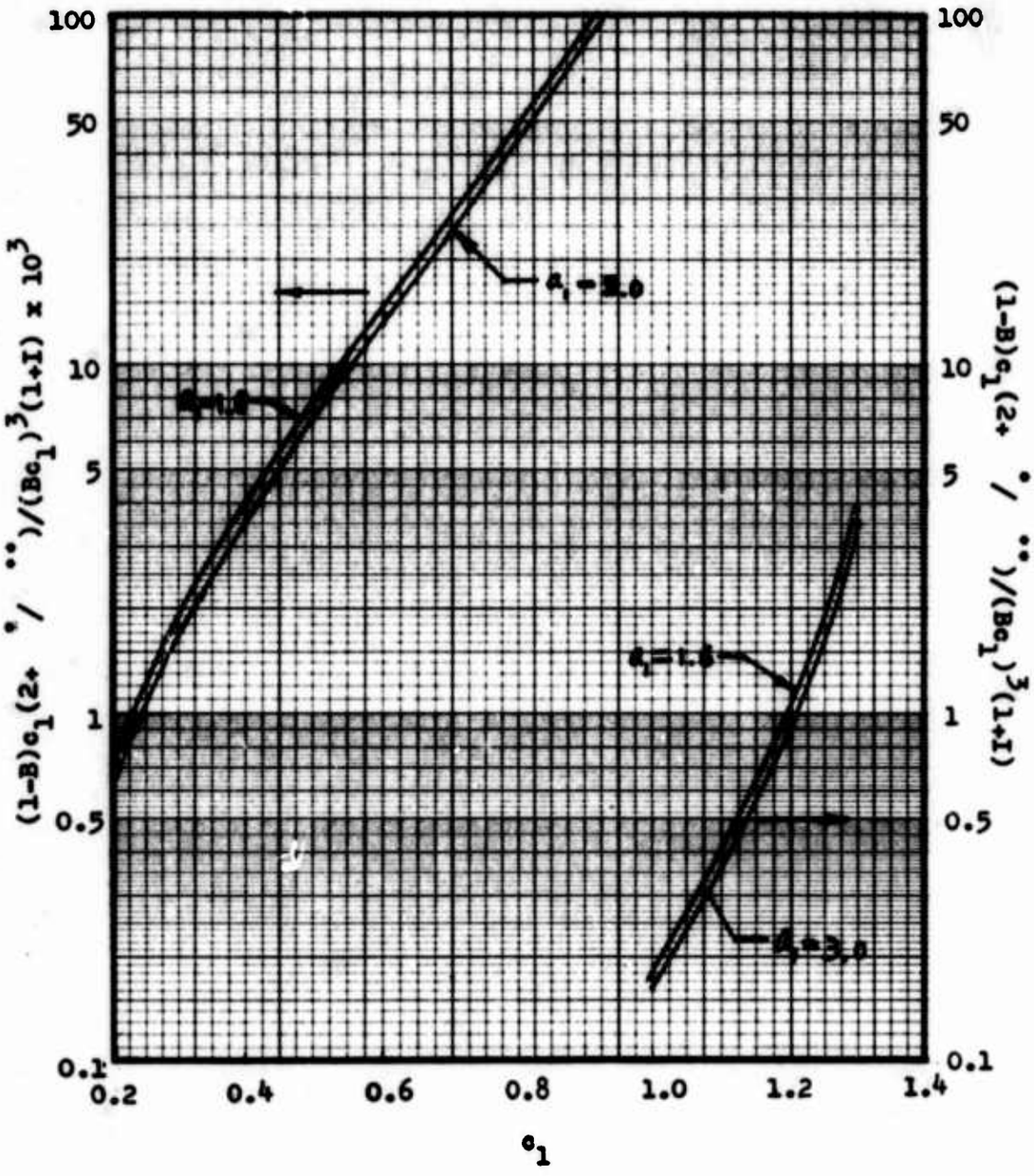

Fig. 9 Diagram for use with equation (4.58)

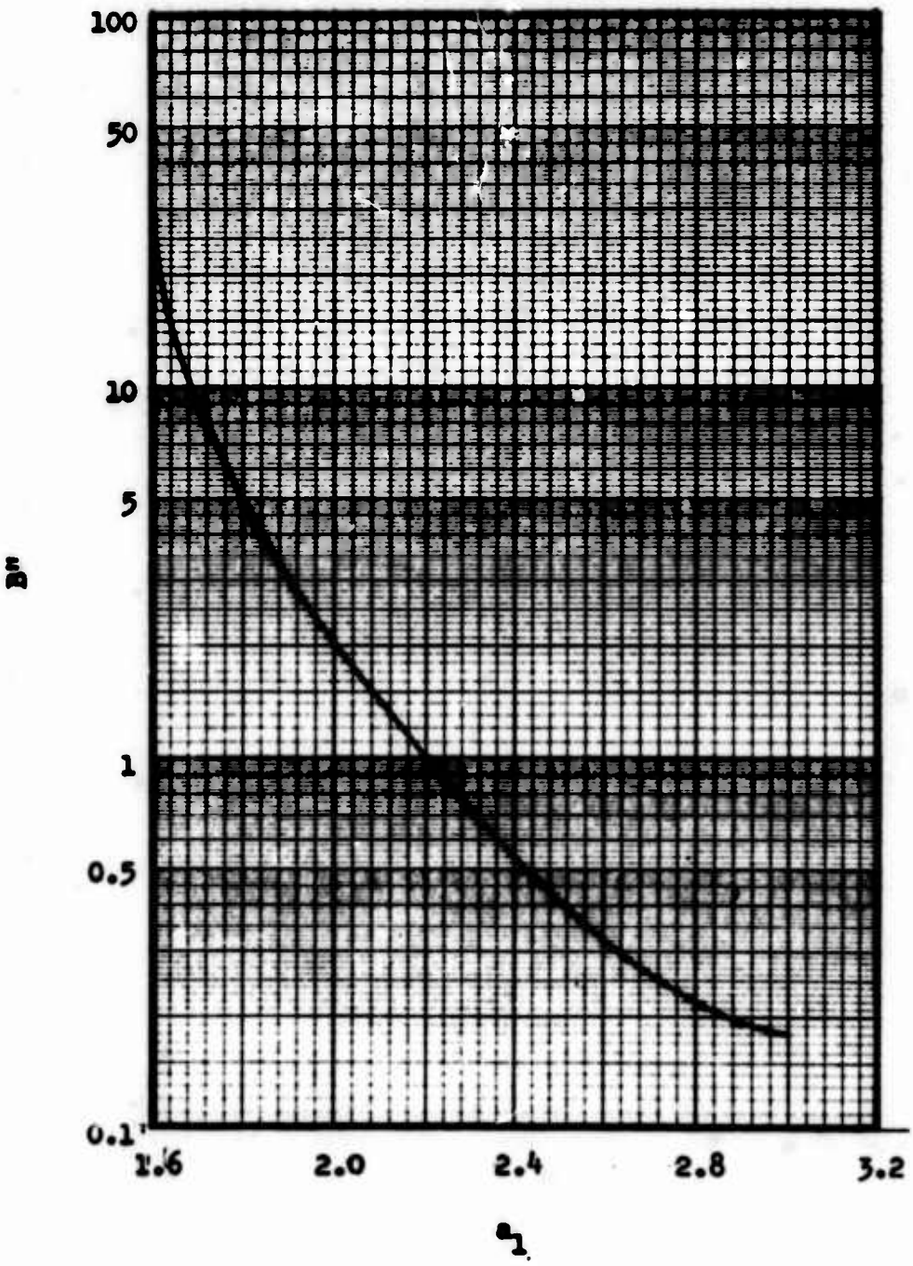

Fig. 10 Relation between B'' and a_1

Similarly, the mass transfer rate is given by

$$m = - \rho D \left(\frac{\partial w_1}{\partial y}\right)_{y=0} = - \rho D c_1 (w_{1\infty} - w_{1_f})$$

Using the definition of B", this becomes

$$m = -\rho \frac{DSc}{\delta} \frac{B''}{B} a_1 (w_{1\infty} - w_{1f}) = - \rho DSc \sqrt{\frac{u_1}{\lambda \nu}} \frac{B''}{B} a_1 (w_{1\infty} - w_{1f}) \tag{4.62}$$

The mass transfer coefficient defined in Section 4.2 assumes the form

$$h_m = \frac{DSc}{\delta} \frac{B''}{B} a_1 = DSc \sqrt{\frac{u_1}{\lambda \nu}} \frac{B''}{B} a_1 \tag{4.63}$$

The technique described above for finding the heat transfer coefficient, omitting the step of determining B', applies here.

CHAPTER V

HEAT AND MASS TRANSFER IN A TWO-DIMENSIONAL WALL JET

5.1 INTRODUCTORY

The term "wall jet" was first introduced by Glauert[37] to describe the flow in a viscous jet bounded on one side by a wall and on the other by the same fluid at rest. Such a jet arises, for example, when a free jet is allowed to impinge normally aganist a plate and spread out over it. The situation envisaged is the final state of the jet when distances from the stagnation point (i.e. the point of intersection between the axis of the impinging jet and the plate) are sufficiently large.

The impingement of a jet of electric wind onto a plane surface provides another example of a wall jet. The measured current density distributions over the plane surface in a positive wire-plane corona reveal a sharp concentration near the stagnation point. At large distances from this point, the current density is essentially zero and the pressure gradient caused by the electro-static force is negligible. Thus the conditions of a wall jet prevail in this region.

The main feature of a wall jet is its hybrid structure common to both the free jet and the ordinary boundary layer. Thus the motion of the fluid is retarded by frictional forces near the wall and the inner layer of the flow may be expected to show a certain structural similarity to a boundary layer. Near the outer edge of the flow, entrainment of quiet fluid occurs and accordingly the outer layer of the flow is likely to resemble a free jet in character.

An important contribution to the theory of laminar wall jet has been made by Glauert[37,38]. He found a similarity solution of the boundary layer equations governing such flow in an incompressible fluid. Riley[39] extended the theory to the case of compressible flow. He also obtained similarity solutions for the energy equation. In this chapter, the similarity solution of the momentum equation first found by Glauert is briefly discussed. A technique used by Riley in obtaining similarity solution of the energy equation for compressible laminar wall jet is employed to seek solutions of the energy and diffusion equations for two-dimensional incompressible laminar wall jets over a frosting surface, under the simplified assumption that the normal velocity at the frost surface is negligibly small. The effects of non-vanishing normal velocity at the frost surface on the flow and the heat and mass transfer are investigated using an approximate method based on the integral equations. The coordinate system shown in Fig. 6 will be used in this chapter.

5.2 BASIC EQUATIONS

The equations governing a two-dimensional laminar jet flowing over a plane surface will now be considered. In view of the fact that a wall jet is in essence of combination of a free jet and a boundary layer flow over a flat plate, the boundary layer approximations may be used. In the absence of a pressure gradient, the momentum equation for incompressible flow may be written

$$u \frac{\partial u}{\partial x} + v \frac{\partial u}{\partial y} = \nu \frac{\partial^2 u}{\partial y^2} \tag{5.1}$$

The energy equation including viscous heating is

$$u \frac{\partial T}{\partial x} + v \frac{\partial T}{\partial y} \quad \frac{\nu}{Pr} \frac{\partial^2 T}{\partial y^2} + \frac{\nu}{c_p} \left(\frac{\partial u}{\partial y}\right)^2 \tag{5.2}$$

Using the mass fraction w_1 of water vapor as dependent variable, the diffusion equation is

$$u \frac{\partial w_1}{\partial x} + v \frac{\partial w_1}{\partial y} = \frac{\nu}{Sc} \frac{\partial^2 w_1}{\partial y^2} \tag{5.3}$$

Here the thermal diffusion and diffusion-thermo effect are not considered. They are important only when the temperature and mass fraction gradients are extremely large. The equation of continuity for two-dimensional incompressible flow is

$$\frac{\partial u}{\partial x} + \frac{\partial v}{\partial y} = 0 \tag{5.4}$$

Turning next to the boundary conditions, it should be noted that in connection with the problem of frost formation, v does not vanish at the surface of the porous frost layer. However, the magnitude of v_f is in practice very small and can be disregarded in forced convection flow without causing appreciable error. (The case where v_f differs from zero will be examined later.) With this in view, the boundary conditions appropriate to the flow of a wall jet over a frosting surface are exactly the same as those for the same flow over an impermeable surface. These conditions are

$$\text{at } y = 0 : \quad u = v = 0 , \quad T = T_f , \quad w_1 = w_{1f} \tag{5.5}$$

$$\text{at } y \quad \infty : \quad u = 0 , \quad T = T_\infty , \quad w_1 = w_{1\infty} \tag{5.6}$$

In order to seek similarity solution of the momentum equation, with $u \propto x^m$, and the jet width $\delta \propto x^n$, two relations are required to determine the exponential constants, m and n. One of the relations is obtained from the momentum equation itself. The second relation is to be provided by the general nature of the flow. For a free jet constancy of the total momentum in the x-direction gives the second relation, and for a boundary layer flow, one of the constants is determined by the distribution of the external flow. For a wall jet, however, there is no such obvious quantity to consider. In the connection a valuable relation has been deduced by Glauert[37]. Integrating the momentum equation with respect to y between the limits y and ∞, multiplying the resulting equation by u, integrating again with respect to y between limits 0 and ∞, and making use of the continuity equation (5.4) and the boundary conditions (5.5) and (.56), the following relation is obtained.

$$R = \int_0^\infty u \left[\int_y^\infty u^2 dy \quad dy = \text{constant} \right] \tag{5.7}$$

5.3 VELOCITY DISTRIBUTION

Glauert has shown that a similarity solution of the momentum equation (5.1) in which the form of the velocity profile does not vary with x is available. This may be written

$$u = U(x) f'(\eta) \qquad \text{where} \qquad \eta = \frac{y}{\delta(x)} \tag{5.8}$$

Here the prime indicates differentiation of a function with respect to its argument. Equation (5.4) is satisfied by the introduction of the stream function ψ such that

$$u = \frac{\partial \psi}{\partial y} , \qquad v = - \frac{\partial \psi}{\partial x} \tag{5.9}$$

With the aid of Eq. (5.8), this may be integrated to give

$$\psi = U \delta f(\eta) \tag{5.10}$$

and Eq. (5.7) shows that

$$U^3 \delta^2 = \text{constant.} \tag{5.11}$$

Making use of Eqs. (5.10) and (5.11), Eq. (5.1) then reduces to

$$f''' - \frac{1}{2\nu} U' \delta^2 f'' - \frac{U' \delta^2}{\nu} f'^2 = 0 \tag{5.12}$$

The condition for the existance of similarity solution then is

$$U' \delta^2 = \text{constant} \tag{5.13}$$

If the constant in Eq. (5.13) is chosen to have the value of -2ν, Eq. (5.12) becomes

$$f''' + ff'' + 2f'^2 = 0 \tag{5.14}$$

The solutions to the simultaneous equations (5.11) and (5.13) are

$$U(x) = 2A\,[\nu(x+\ell)]^{-1/4} \quad , \qquad \delta(x) = \left(\frac{2}{A}\right)^{1/4}\,[\nu(x+\ell)]^{3/4} \tag{5.15}$$

where A and ℓ are arbitrary constants. The boundary conditions (5.5) and (5.6) require

$$f(0) = f'(0) = 0 \quad , \qquad f'(\infty) = 0 \tag{5.16}$$

Multiplying by f and using Eq. (5.16), Eq. (5.14) may be integrated to yield

$$f'' - \tfrac{1}{2} f'^2 + f^2 f' = 0 \tag{5.17}$$

Multiply by f and integrate again. Thus

$$f f^{-1/4} f' + \frac{2}{3} f^{3/2} = \text{constant} \tag{5.18}$$

Without loss of generality, it may be required that $f(\infty) = 1$ and the constant in Eq. (5.18) may be taken to have the value of 2/3.

It is convenient to make the transformation $f = g^2$. Then $f' = 2gg'$ and Eq. (5.18) becomes

$$g' = \frac{1}{3}\,(1-g^3)$$

Upon integration, it is found

$$\eta = \ln \frac{\sqrt{1+g+g^2}}{1-g} + \sqrt{3}\,\tan^{-1}\frac{\sqrt{3}\,g}{2+g} \tag{5.19}$$

The arbitrary constant A is to be determined by Eq. (5.7). It can be verified that

$$R = A^2 \int_0^\infty f' \left[\int_\eta^\infty f'^2 d\eta\right] d\eta = \frac{8}{5} A^2 \tag{5.20}$$

or

$$A = \tfrac{1}{2}(5R/2)^{1/4}$$

Hence we may write

$$\psi = \left[40R\nu(x+\ell)\right]^{1/4} f(\eta)$$

$$u = \left[\frac{5R}{2\nu(x+\ell)}\right]^{1/4} f'(\eta) \qquad (5.21)$$

$$\eta = \left[\frac{5R}{32\nu^3(x+\ell)^3}\right]^{1/4} y$$

The quantity R and the constant ℓ may be estimated roughly as follows. If the wall jet is the result of a free jet impinging on a flat plate, the magnitude of R may be obtained from the conditions in the free jet as

$$R = \tfrac{1}{2}(\text{typical velocity})(\text{volume flow/unit length})^2 \qquad (5.22)$$

The constant length ℓ can be determined by equating the maximum velocity at x = 0 as given by Eq. (5.21 to the maximum velocity in the impinging jet.

5.4 SIMILARITY SOLUTION OF THE ENERGY EQUATION

Having solved the momentum equation, the energy equation may now be considered. Making use of the results of the previous section, the following relations are obtained:

$$u = \left[\frac{5R}{2\nu(x+\ell)}\right]^{1/4} f'(\eta) \quad , \qquad \left(\frac{\partial u}{\partial y}\right)^2 = \left[\frac{5R}{2\nu(x+\ell)}\right]\left[\frac{5R}{32\nu^3(x+\ell)^3}\right]^{1/4} f''^2(\eta) \, ,$$

$$v = -\tfrac{1}{4}(40R\nu)^{1/4}(x+\ell)^{-3/4} f(\eta) + \tfrac{3}{4}(40R\nu)^{1/4}(x+\ell)^{-3/4} f'(\eta) \, ,$$

$$\frac{\partial T}{\partial x} = \frac{\partial T}{\partial x} + \frac{\partial T}{\partial \eta}\frac{\partial \eta}{\partial x} = \frac{\partial T}{\partial x} - \frac{3}{4}(x+\ell)^{-1}\eta\frac{\partial T}{\partial \eta} \, ,$$

$$\frac{\partial T}{\partial y} = \left[\frac{5R}{32\nu^3(x+\ell)^3}\right]^{1/4}\frac{\partial T}{\partial \eta}$$

and

$$\frac{\partial^2 T}{\partial \eta^2} = \left[\frac{5R}{32\nu^3(x+\ell)^3}\right]^{1/4} \frac{\partial^2 T}{\partial \eta^2}$$

Thus, with (x,η) as independent variables, the energy equation (5.2) may be written as

$$\frac{\partial^2 T}{\partial \eta^2} - 4Pr(x+\ell)f' \frac{\partial T}{\partial x} + Prf\frac{\partial T}{\partial \eta} = -\frac{Pr}{c_p}\left[\frac{5R}{2\nu(x+\ell)}\right]f''^2 \qquad (5.23)$$

with the boundary conditions

$$T = T_f \text{ at } y = 0 \quad , \qquad T = T_\infty \text{ at } y = \infty \qquad (5.24)$$

The general solution of Eq. (5.23) consists of a particular solution and suitable complementary solutions. The particular solution may be found in the form

$$T = T_o + K_o(x+\ell)^{-1}\theta_o(\eta) \qquad (5.25)$$

where T_o and K_o are constants. If K_o is chosen as $K_o = -5R/2c_p$, then $\theta_o(\eta)$ satisfies

$$\theta_o'' + Pr(f\theta_o' + 4f\,\theta_o) = Prf''^2 \qquad (5.26)$$

Eq. (5.23) also has an infinity of complementary functions of the form

$$T = K_1 + K_2(x+\ell)^{-\alpha}\,\theta_n(\eta) \qquad (5.27)$$

with $\theta_n(\eta)$ satisfying

$$\theta_n'' + Pr(f\theta_n' + 4\alpha f'\theta_n) = 0 \qquad (5.28)$$

Here α is a constant to be determined by appropriate boundary conditions. A complete picture of the temperature distribution in a particular problem can thus be obtained by adding to the particular solution (5.25) appropriate supplementary solutions of the type (5.27).

To examine the effects on temperature distribution of viscous heating in the wall jet, it is required to seek a solution of Eq. (5.23) in the form of Eq. (5.25) where $\theta_o(\eta)$ satisfies Eq. (5.23) with

$$\theta_o(\infty) = 0 \qquad (5.29)$$

and $\theta_o(0) = 0$ for constant wall temperature T_∞

since $T = T_\infty$ at $\eta = \infty$, $T_0 = T_\infty$. When the Prandtl number Pr is unity, Eq. (5.26) subject to (5.29) has the solution

$$\theta_0(\eta) = \tfrac{1}{2} f'^2(\eta) \tag{5.30}$$

For arbitrary Pr, no solution in the closed form has been found. The equation has been integrated numerically by Riley[39] for Pr = 0.72, the value appropriate for air. He gave $\theta_0'(0) = 0.0036$. Thus, the rate of heat transfer across the wall, per unit area, is

$$\begin{aligned} q &= -k\left(\frac{\partial T}{\partial y}\right)_{y=0} = -K_0 k(x+\ell)^{-1}\frac{d\eta}{dy}\,\theta_0'(0) \\ &= 0.0036(5/4)(k/c_p\nu)[5R^5/2\nu^3(x+\ell)^7]^{1/4} \end{aligned} \tag{5.31}$$

To study the effect on the temperature distribution of maintaining the wall at a constant temperature T_f, a complementary solution (5.27) with $\alpha = 0$ is required. To satisfy the boundary condition (5.24), Eq. (5.27) may be put

$$T = T_f + (T_\infty - T_f)\theta_1(\eta) \tag{5.32}$$

where $\theta_1(\eta)$ satisfies

$$\theta_1'' + \mathrm{Pr} f \theta_1' = 0 \tag{5.33}$$

and

$$\begin{aligned} \theta_1(0) &= 0 \\ \theta_1(\infty) &= 1 \end{aligned} \tag{5.34}$$

The solution of Eq. (5.33) subject to (5.34) may be immediately obtained. Direct integration of Eq. (5.33) gives

$$\theta_1'(\eta) = \theta_1'(0)\exp\left[-\mathrm{Pr}\int_0^\eta f\,d\eta\right]$$

Integrating once more, it is found

$$\theta_1(\eta) = \theta_1(\infty) - \theta_1'(0)\int_\eta^\infty \exp\left[-\mathrm{Pr}\int_0^\eta f\,d\eta\right]d\eta$$

Using Eq. (5.34) to obtain

$$\theta_1'(0) = 1\Big/\int_0^\infty \exp\left[-\mathrm{Pr}\int_0^\eta f\,d\eta\right]d\eta \tag{5.35}$$

the final solution of Eq. (5.33) becomes

$$\theta_1(\eta) = 1 - \int_\eta^\infty \exp\left[-Pr\int_0^\eta f d\eta\right] d\eta \Big/ \int_0^\infty \exp\left[-Pr\int_0^\eta f d\eta\right] d\eta$$

In Section 5.3 we have $f = g^2$ where $g' = (1-g^3)/3$, hence

$$-\int_0^\eta f d\eta = -\int_0^g \frac{3g^2 dg}{(1-g^3)} = \ln(1-g^3)$$

Thus in terms of g, Eq. (5.36) may be written

$$\theta_1 = 1 - \int_g^1 (1-g^3)^{Pr-1} dg \Big/ \int_0^1 (1-g^3)^{Pr-1} dg \qquad (5.37)$$

When Pr = 1, Eq. (5.37) may be readily integrated to give

$$\theta_1 = g \qquad (5.38)$$

When $Pr \neq 1$, writing $s = (1-g^3)$, Eq. (5.37) then becomes

$$\theta_1 = -\int_0^s s^{Pr-1}(1-s)^{-2/3} ds \Big/ \int_0^1 s^{Pr-1}(1-s)^{-2/3} ds$$

where the denominator is the beta function $B(Pr,1/3)$ and the numerator is the incomplete beta function $B_s(Pr,1/3)$. Therefore,

$$\theta_1 = 1 - B_s(Pr,1/3)/B(Pr,1/3) \qquad (5.39)$$

The rate of heat transfer per unit area across the wall is given by

$$q = -k\left(\frac{\partial T}{\partial y}\right)_{y=0} = -k(T_\infty - T_f)\left[5R/32\nu^3(x+\ell)^3\right]^{1/4} \theta_1'(0) \qquad (5.40)$$

From Eq. (5.35),

$$\theta_1'(0) = 1/B(Pr,1/3) = \Gamma(Pr+1/3)/\Gamma(Pr)\Gamma(1/3)$$

where the relation between the beta and gamma functions has been used. For Pr = 0.71, $\theta_1'(0) = 0.273$. The local heat transfer coefficient defined as

$$h(x) = -q(x)/(T_\infty - T_f)$$

is readily found from Eq. (5.40) to be

$$h(x) = k\theta_1'(0)(5R/32\nu^3)^{1/4}(x+\ell)^{-3/4} \tag{5.41}$$

Defining the local Nusselt number as

$$Nu(x) = hx/k$$

it follows from Eq. (5.41) that

$$Nu(x) = \theta_1(0)(5R/32\nu^3)^{1/4}x(x+\ell)^{-3/4} \tag{5.42}$$

5.5 SOLUTION OF THE DIFFUSION EQUATION

Upon comparison of Eq. (5.3) and (5.2), it is evident that complete analogy exists between the two equations when the viscous dissipation term in the energy equation is absent. By "complete analogy" it is meant that the two equations are similar in form. Perfect analogy between the transport processes through the boundary layers requires also that the boundary conditions be identical. Fortunately, this is the case for the problem under consideration, as can be seen from the boundary conditions (5.5) and (5.6). Therefore the solution of Eq. (5.3) can be obtained directly from the results of Section 5.4 by replacing the Prandtl number Pr by the Schmidt number Sc.

In terms of the independent variables x and η, the diffusion equation (5.3) assumes the form

$$\frac{\partial^2 w_1}{\partial \eta^2} - 4Sc(x+\ell)f' \frac{\partial w_1}{\partial x} + Scf \frac{\partial w_1}{\partial \eta} = 0 \tag{5.43}$$

and the boundary conditions become

$$w_1 = w_{1f} \text{ at } \eta = 0 \quad , \qquad w_1 = w_1 \text{ at } \eta = \infty \tag{5.44}$$

Introduction of the dimensionless variable

$$\varphi(\eta) = \frac{w_1 - w_{1f}}{w_{1_\infty} - w_{1f}}$$

in Eqs. (5.43) and (5.44) leads to

$$\varphi'' + Sc f \varphi' = 0$$

with

$$\begin{aligned} \varphi(0) &= 0 \\ \varphi(\infty) &= 1 \end{aligned} \tag{5.45}$$

The solution is, from Eq. (5.39),

$$\varphi = 1 - B_s(Sc,1/3)/B(Sc,1/3) \tag{5.46}$$

The rate of mass transfer per unit area across the wall is given by

$$m = -\rho D\left(\frac{\partial w_1}{\partial y}\right)_{y=0} = -\rho D(w_{1\infty}-w_{1f})\left[5R/32\nu^3(x+\ell)^3\right]^{1/4}\varphi'(0) \tag{5.47}$$

where

$$\varphi'(0) = 1/B(Sc,1/3)$$

For air in the temperature range between 0°F and 100°F, Sc = 0.53 and $\varphi'(0) = 0.258$. In analogous to the case of heat transfer, the local mass transfer coefficient is defined as

$$h_m(x) = -m(x)/\rho(w_{1\infty}-w_{1f})$$

and the local Sherwood number is defined by

$$Sh(x) = h_m x/D$$

It follows from Eq. (5.47) that

$$h_m(x) = D\varphi'(0)(5R/32\nu^3)^{1/4}(x+\ell)^{-3/4} \tag{5.48}$$

and

$$Sh(x) = \varphi'(0)(5R/32\nu^3)^{1/4}x(x+\ell)^{-3/4} \tag{5.49}$$

5.6 TWO-DIMENSIONAL WALL JET WITH $v_f \neq 0$

In the foregoing sections, it has been demonstrated that closed form solutions are available for the momentum, energy and diffusion equations when the transverse velocity v vanishes at the frost surface, i.e. when $v_f = 0$. The situation is quite different when the condition $v_f \neq 0$ is taken into consideration. In order to clarify the difficulties that arise, the governing equations (5.1) through (5.4) will be re-examined subject to the new boundary conditions that

$$\text{at } y = 0: \quad u = v, \quad v = v_f, \quad T = T_f, \quad w_1 = w_{1f} \tag{5.50}$$

$$\text{at } y = \infty: \quad u = 0, \quad T = T, \quad w_1 = w_{1\infty} \tag{5.51}$$

The relation (5.8) will be retained, but the stream function ψ defined by Eq. (5.9) will now be assumed to take a different form, namely,

$$\psi = U(x)\delta(x)f(\eta) + \psi_0(x) \tag{5.52}$$

The last term of Eq. (5.52) has been introduced to take care of the condition $v = v_f$ at $y = 0$. It follows from Eq. (5.52) that

$$\psi = -\frac{\partial \psi}{\partial x} = -(U\delta)'f + U\delta' f' - \psi_0' \tag{5.53}$$

and

$$v_f = \psi_0'(x) \tag{5.54}$$

With the help of Eqs. (5.8), (5.53) and (5.54), Eq. (5.1) leads to

$$f''' + \alpha_1 ff'' - \alpha_2 f'^2 + \alpha_3 f'' = 0 \tag{5.55}$$

where

$$\alpha_1 = \frac{(U\delta)'}{\nu}\ , \qquad \alpha_2 = \frac{U'\delta^2}{\nu} \text{ and } \alpha_3 = \frac{v_f\delta}{\nu} \tag{5.56}$$

are constants. Because of the relation between v_f and the material profile as indicated by Eq. (4.11) the momentum and diffusion equations are now coupled. Undoubtedly this makes the exact solution much more difficult to be obtained.

What makes the situation worse is the fact that the relation (5.7) is not valid any more. Instead the same procedure yields

$$\frac{\partial}{\partial x}\int_0^\infty u\left[\int_y^\infty u^2 dy\right]dy = v_f = v_f\int_0^\infty u^2 dy \tag{5.57}$$

which does not provide the additional relation required for the determination of the dependence on x and U and δ. That this is so can readily be seen by making the substitutions $U \alpha x^m$ and $\delta \alpha x^n$ in Eqs. (5.56) and (5.57). It appears that further investigation is necessary in order to determine whether similar solution still exists in this case. No efforts will be made along this direction in the present study.

An approximate estimate of the effects of v_f on the heat and mass transfer processes can be made using the integral method. Two cases, v_f differing considerably from zero, will be discussed separately in Sections 5.7 and 5.8.

5.7 TWO-DIMENSIONAL WALL JET WITH v_f SMALL BUT NOT ZERO

To examine the influence of small v_f on the heat and mass transfer processes in a two-dimensional laminar wall jet, a method used by Whitehurst[40] and by Barron[24] in consideration of frost formation under free convection conditions will be employed. The integral equations may be obtained in the same manner as in Chapter IV from Eqs. (5.1) through (5.4). They are:

$$\frac{\partial}{\partial x}\int_0^{\delta} u^2 dy = -\nu\left(\frac{\partial u}{\partial y}\right)_{y=0} \tag{5.58}$$

$$\frac{\partial}{\partial x}\int_0^{\delta_T}(1-\theta)u\,dy = \frac{\nu}{Pr}\left(\frac{\partial \theta}{\partial y}\right)_{y=0} \tag{5.59}$$

$$\frac{\partial}{\partial x}\int_0^{\delta_m}(1-\varphi)u\,dy = \frac{\nu}{Sc}\left(\frac{\partial \varphi}{\partial y}\right)_{y=0} + v_f \tag{5.60}$$

The boundary conditions which are to be satisfied by the velocity, temperature and material profiles are

$$\text{at } y = 0\ , \qquad u = \theta = \varphi = 0 \tag{5.61a}$$

$$\text{at } y = \delta\ , \qquad u = \frac{\partial u}{\partial y} = 0 \tag{5.61b}$$

$$\text{at } y = \delta_T\ , \qquad \theta = 1\ , \quad \frac{\partial \theta}{\partial y} = 0 \tag{5.61c}$$

$$\text{at } y = \delta_m\ , \qquad \varphi = 1\ , \quad \frac{\partial \varphi}{\partial y} = 0 \tag{5.62d}$$

It should be noted that the method ignores the boundary conditions that

$$\text{at } y = 0 : \qquad v_f \frac{\partial u}{\partial y} = \nu\frac{\partial^2 u}{\partial y^2}\ , \qquad v_f \frac{\partial \theta}{\partial y} = \frac{\nu}{Pr}\frac{\partial^2 \theta}{\partial y^2}\ , \qquad v_f \frac{\partial \varphi}{\partial y} = \frac{\nu}{Sc}\frac{\partial^2 \varphi}{\partial y^2} \tag{5.62}$$

The velocity, temperature and material profiles which satisfy the conditions (5.61) are

$$\frac{u}{u(x)} = \frac{Y}{\delta}\left(1 - \frac{Y}{\delta}\right)^2 \tag{5.63}$$

$$\theta = 2\frac{y}{\delta_T} - \left(\frac{y}{\delta_T}\right)^2 \tag{5.64}$$

$$\varphi = 2\frac{y}{\delta_m} - \left(\frac{y}{\delta_m}\right)^2 \tag{5.65}$$

Substituting Eqs. (5.63) through (5.65) in Eqs. (5.58) through (5.60), carrying out the indicated integrations and making use of Eq. (4.11), there results

$$\frac{1}{105}\frac{d}{dx}(U^2\delta) = -\frac{\nu U}{\delta} \tag{5.66}$$

$$\frac{d}{dx}(U\delta_T^{**}) = \frac{\nu}{Pr}\frac{2}{\delta_T} - \frac{\nu}{Sc}\frac{2B}{\delta_m} \tag{5.67}$$

$$\frac{d}{dx}(U\delta_m^{**}) = \frac{\nu}{Sc}\frac{2}{\delta_m} - \frac{\nu}{Sc}\frac{2B}{\delta_m} = +\frac{2\nu}{Sc\ \delta_m}(1-B) \tag{5.68}$$

where

$$\frac{\delta_T^{**}}{\delta} = \frac{1}{\delta}\int_0^{\delta_T}(1-\theta)\frac{u}{U}\,dy = \Delta_T^2\left(\frac{1}{12} - \frac{1}{15}\Delta_T + \frac{1}{60}\Delta_T^2\right) \tag{5.69}$$

and

$$\frac{\delta_m^{**}}{\delta} = \frac{1}{\delta}\int_0^{\delta_m}(1-\varphi)\frac{u}{U}\,dy = \Delta_m^2\left(\frac{1}{12} - \frac{1}{15}\Delta_m + \frac{1}{60}\Delta_m^2\right) \tag{5.70}$$

As noted earlier the relation (5.7) no longer holds true if v_f differs from zero. However when v_f is very small, it may be assumed that Eq. (5.7) still applies. Using the velocity profile (5.63) in Eq. (5.7) there results

$$U^3\delta^2 = 2500R \tag{5.71}$$

Equations (5.66) and (5.71) may be solved by means of the substitutions

$$U(x) = D_1(x+\ell)^m \qquad \text{and} \qquad \delta(x) = D_2(x+\ell)^n$$

Eqs. (5.66) and (5.71) then become

$$\frac{1}{105}(2m+n)D_1^2D_2(x+\ell)^{2m+n-1} = -\frac{D_1}{D_2}(x+\ell)^{m-n}$$

$$D_1^3D_2^2(x+\ell)^{3m+2n} = 2500R$$

Since these two equations must be valid for any value of x, each term must be in the same power of x. Therefore

$$2m + n - 1 = m - n$$

$$3m + 2n = 0$$

This gives

$$m = -\frac{1}{2} \quad \text{and} \quad n = \frac{3}{4}$$

Thus there results from Eqs. (5.66) and (5.71)

$$D_1D_2^2 = 420$$

and

$$D_1^3D_2^2 = 2500R$$

These two equations may be solved for D_1 and D_2

$$D_1 = \left(\frac{125R}{21\nu}\right)^{1/4}$$

$$D_2 = \left[\frac{5R}{16(21\nu)^3}\right]^{-1/4}$$

And hence

$$U(x) = \left[\frac{125R}{21\nu(x+\ell)}\right]^{1/4} \qquad (5.72)$$

$$\delta(x) = \left[\frac{5R}{16(21\nu)^3(x+\ell)^3}\right]^{-1/4} \qquad (5.73)$$

The linked equations (5.67) and (5.68) may now be solved for Δ_T and Δ_m, which will be assumed to be independent of x. With the aid of Eqs. (5.72) and (5.73), Eqs. (5.67) and (5.68) may be rewritten

$$\frac{D_1D_2^2}{4}\Delta_T^2\left(\frac{1}{12}-\frac{1}{15}\Delta_T+\frac{1}{60}\Delta_T^2\right)=\frac{\nu}{Pr}\frac{2}{\Delta_T}-\frac{\nu}{Sc}\frac{2B}{\Delta_m} \tag{5.74}$$

$$\frac{D_1D_2^2}{4}\Delta_m^2\left(\frac{1}{12}-\frac{1}{15}\Delta_m+\frac{1}{60}\Delta_m^2\right)=\frac{2}{Sc}\frac{1}{\Delta_m}(1-B) \tag{5.75}$$

When $\Delta_m \approx 1$, a very accurate approximate solution for Δ_m may be obtained from Eq. (5.75) by letting $\Delta_m = 1$ in the parenthesis, namely,

$$\Delta_m^3=\frac{240}{ScD_1D_2^2}(1-B)$$

or

$$\Delta_m=\frac{4}{7}\frac{(1-B)^{1/3}}{Sc} \tag{5.76}$$

Similarly, Eq. (5.74) leads to

$$\Delta_T^3+\frac{4}{7}\frac{B}{Sc\Delta_m}\Delta_T-\frac{4}{7}\frac{1}{Pr}=0$$

The only real root of this equation is

$$\Delta_T=\left\{\frac{2}{7Pr}+\left[\left(\frac{4}{21}\frac{B}{Sc\Delta_m}\right)^3+\left(\frac{2}{7Pr}\right)^2\right]^{1/2}\right\}^{1/3} + \left\{\frac{2}{7Pr}-\left[\left(\frac{4}{21}\frac{B}{Sc\Delta_m}\right)^3+\left(\frac{2}{7Pr}\right)^2\right]^{1/2}\right\}^{1/3} \tag{5.77}$$

The heat flux at the frost surface is

$$q=-k\left(\frac{\partial T}{\partial y}\right)_{y=0}=-2k\frac{T_\infty-T_f}{\delta_T}=-2k(T_\infty-T_f)/\Delta_T\delta$$

$$=-2k(T_\infty-T_f)\left[\frac{2R}{16(21\nu)^3(x+\ell)^3}\right]^{1/4}/\Delta_T \tag{5.78}$$

When B = 0 (that is $v_f = 0$), Eq. (5.78) reduces to

$$q = -2k(T_\infty - T_f)\left[\frac{5R}{16(21\nu)^3(x+\ell)^3}\right]^{1/4}\left[\frac{4}{7}\frac{1}{Pr}\right]^{1/3} \qquad (5.79)$$

For Pr = 0.71

$$q = -0.259k(T_\infty - T_f)\left[\frac{5R}{32\nu^3(x+\ell)^3}\right]^{1/4}$$

which is within 6% of the exact solution (5.39) with $\theta_1'(0) = 0.273$.

The mass flux at the frost surface is

$$m = -\rho D\left(\frac{\partial w_1}{\partial y}\right)_{y=0} = -2\rho D(w_{1\infty} - w_{1f})/\delta_m$$

$$= -2\rho D(w_{1\infty} - w_{1f})\left[\frac{5R}{16(21\nu)^3(x+\ell)^3}\right]^{1/4}\left[\frac{7Sc}{4(1-B)}\right]^{1/3} \qquad (5.80)$$

When B = 0,

$$m = -2\rho D(w_{1\infty} - w_{1f})\left[\frac{5R}{16(21\nu)^3(x+\ell)^3}\right]^{1/4}\left(\frac{7Sc}{4}\right)^{1/3}$$

For Sc = 0.53,

$$m = -0.244D(w_{1\infty} - w_{1f})\rho\left[\frac{5R}{32\nu^3(x+\ell)^3}\right]^{1/4}$$

which is a good approximation as compared with the exact solution obtained in Section 5.5 with $\varphi'(0) = 0.258$.

Substitution of Eqs. (5.78) and (5.80) in the definitions of the local heat and mass transfer coefficients and the local Nusselt and Sherwood numbers leads to, for B ≠ 0,

$$h(x) = 2k\left[\frac{5R}{16(21\nu)^3(x+\ell)^3}\right]^{1/4}/\Delta_T \qquad (5.81)$$

$$h_m(x) = 2D\left[\frac{5R}{16(21\nu)^3(x+\ell)^3}\right]^{1/4}\left[\frac{7Sc}{4(1-B)}\right]^{1/3} \qquad (5.82)$$

$$Nu(x) = 2\left[\frac{5R}{16(21\nu)^3}\right]^{1/4} x(x+\ell)^{-3/4}/\Delta_T \qquad (5.83)$$

and

$$Sh(x) = 2\left[\frac{5R}{16(21\nu)^3}\right]^{1/4} x(x+\ell)^{-3/4}\left[\frac{7Sc}{4(1-B)}\right]^{1/3} \tag{5.84}$$

5.8 SOLUTIONS FOR LARGER VALUES OF v_f

In Section 5.7, it has been assumed that v_f is so small that the relation (5.7) applies and that the forms of the velocity, temperature and material profiles are not affected by v_f. These two assumptions do not apply for the case where v_f deviates considerably from zero. To account for the effects of large v_f, a method similar to that used in Section 4.4 will be employed.

The governing equations are Eqs. (5.58) through (5.60) and the appropriate boundary conditions are Eqs. (5.61) and (5.62). As in Section 4.3, the velocity, temperature and material profiles will be assumed to be of cubic form, namely,

$$\frac{u}{U} = a_1\frac{y}{\delta} + a_2\left(\frac{y}{\delta}\right)^2 + a_3\left(\frac{y}{\delta}\right)^3 \tag{5.85}$$

$$\theta = b_1\frac{y}{\delta_T} + b_2\left(\frac{y}{\delta_T}\right)^2 + b_3\left(\frac{y}{\delta_T}\right)^3 \tag{5.86}$$

and

$$\varphi = c_1\frac{y}{\delta_m} + c_2\left(\frac{y}{\delta_m}\right)^2 + c_3\left(\frac{y}{\delta_m}\right)^3 \tag{5.87}$$

By consideration of the boundary conditions (5.61) and (5.62), and inserting the value of v_f from Eq. (4.11), there is obtained the following relations determining the coefficients.

$$a_1 = \frac{4}{B''} \quad , \quad a_2 = -2a_1 \quad , \quad a_3 = a_1 \tag{5.88}$$

$$b_1 = \frac{2}{B'}\left(1 - \sqrt{1 - \frac{3}{2}B'}\right)$$

$$b_2 = 3 - 2b_1 \quad , \quad b_3 = b_1 - 2 \tag{5.89}$$

$$c_1 = \frac{2}{B}\left(1 - \sqrt{1 - \frac{3}{2}B}\right)$$

$$c_2 = 3 - 2c_1 \quad , \quad c_3 = c_1 - 2 \tag{5.90}$$

where

$$B' = \frac{Pr B \delta_T c_1}{Sc \delta_m b_1} \qquad \text{and} \qquad B'' = \frac{B \delta c_1}{Sc \delta_m a_1} \tag{5.91}$$

Equations (5.88) through (5.90) indicate that the method is valid when $B \leq \frac{2}{3}$, $B' \leq \frac{1}{2}$ and $B'' \neq 0$.

Substituting Eqs. (5.88) through (5.90) in Eqs. (5.58), (5.59) and (5.90), there results the following ordinary differential equations

$$-\frac{105}{a_1} = \frac{\delta}{U\nu} \frac{d}{dx} (U^2 \delta) \tag{5.92}$$

$$(1-B')b_1 = \frac{Pr \Delta_T \delta}{\nu} \frac{\delta_T^{**}}{\delta} \frac{d}{dx} (U\delta) \tag{5.93}$$

$$(1-B)c_1 = \frac{Sc \Delta_m \delta}{\nu} \frac{\delta_m^{**}}{\delta} \frac{d}{dx} (U\delta) \tag{5.94}$$

where

$$\frac{\delta_T^{**}}{\delta} = \frac{1}{\delta} \int_0^{\delta_T} (1-\theta) \frac{u}{U} dy = a_1 \Delta_T^2 \left[\left(\frac{3}{20} - \frac{b_1}{30} \right) + \left(-\frac{2}{15} + \frac{b_1}{30} \right) \Delta_T + \left(\frac{1}{28} - \frac{b_1}{105} \right) \Delta_T^2 \right] \tag{5.95}$$

and

$$\frac{\delta_m^{**}}{\delta} = \frac{1}{\delta} \int_0^{\delta_m} (1-\theta) \frac{u}{U} dy = a_1 \Delta_m^2 \left[\left(\frac{3}{20} - \frac{c_1}{30} \right) + \left(-\frac{2}{15} + \frac{c_1}{30} \right) \Delta_m + \left(\frac{1}{28} - \frac{c_1}{105} \right) \Delta_m^2 \right] \tag{5.96}$$

The relation between B' and B" will be determined first. Dividing Eq. (5.93) by Eq. (5.94) and using the approximations $\Delta_T \approx 1$ and $\Delta \approx 1$ as in Section 4.3, there results

$$\left(\frac{\Delta_T}{\Delta_m} \right)^3 = \frac{(1-B')b_1}{(1-B)c_1} \cdot Le$$

Noting $\Delta_T/\Delta_m = \delta_T/\delta_m$, it follows from the first relation of Eq. (5.91) that

$$\frac{(1-B')b_1}{(B'b_1)^3 Le^3} = \frac{(1-B)c_1}{(Bc_1)^3}$$

This relation is the same as Eq. (4.59) and Fig. 7 can be used.

Turning next to the determination of the relation between B" and B, rewrite Eq. (5.92) as

$$-\frac{105}{a_1} - \frac{\delta^2}{\nu}\frac{dU}{dx} = \frac{\delta}{\nu}\frac{d}{dx}(U\delta)$$

and note that Eq. (5.96) reduces, when $\Delta_m \approx 1$, to

$$\frac{\delta_m^{**}}{\delta} = \Delta_m^2 a_1\left(\frac{11}{210} - \frac{c_1}{105}\right)$$

Dividing Eq. (5.92) by Eq. (5.94) and using the above two relations, there yields

$$\Delta_m^3 = \frac{(1-B)c_1}{Sca_1\left(\frac{11}{210} - \frac{c_1}{105}\right) - \left(\frac{105}{a_1} - \frac{\delta^2}{\nu}\frac{dU}{dx}\right)} \tag{5.98}$$

Substitution of this expression in the second relation of Eq. (5.91) leads to

$$\frac{(Bc_1)^3}{(1-B)c_1} = \frac{Sc^2(B''a_1)^3}{-a_1\left(\frac{11}{210} - \frac{c_1}{105}\right)\left(\frac{105}{a_1} + \frac{\delta^2}{\nu}\frac{dU}{dx}\right)}$$

To solve Eq. (5.99) the functions U and δ must be known. In principle two equations are required to determine these two functions and Eqs. (5.57) and (5.92) may be used for this purpose. As noted in Section 5.6, substitution of the relations $U \alpha x^m$ and $\delta \alpha x^n$ in these two equations fails to determine uniquely the exponential constants m and n. Therefore, a different approach must be adopted. In view of the similarity solution obtained in Section 5.3, U and δ may be expressed in the following form

$$U(x) = d_1 R(x)^{1/4}(x+\ell)^{-1/4} \tag{5.100}$$

and

$$\delta(x) = d_2 R(x)^{-1/4}(x+\ell)^{3/4} \tag{5.101}$$

where R is now assumed to be a function of x rather than a constant and d_1 and d_2 are constants

Defining, as in Section 5.2,

$$R(x) = \int_0^\infty u\left[\int_y^\infty u^2 dy\right]dy \tag{5.102}$$

and using Eqs. (5.85), (5.110) and (5.101), Eq. (5.57) becomes

$$\frac{dR}{dx} = -\frac{\nu B a_1^2 c_1 d_1^2}{105 Sc \Delta_m} \frac{R}{(x+\ell)} \tag{5.103}$$

Integration of this equation gives

$$R = R_o (x+\ell)^{-\nu B a_1^2 c_1 d_1^2 / 105 Sc \Delta_m} \tag{5.104}$$

Here the constant R_o can be interpreted as the value of R for B = 0. Because of its physical meaning, R_o may be roughly estimated by means of the relation (5.22). From Eqs. (5.100), (5.101) and (5.103), the quantity $\delta^2/\nu \, dU/dx$ is found to be

$$\frac{\delta^2}{\nu} \frac{dU}{dx} = -\frac{1}{2} \frac{d_1 d_2^2}{\nu} \left(1 + \frac{\nu B a_1^2 c_1 d_1^2}{105 Sc \Delta_m} \right) \tag{5.105}$$

It remains to determine the constant d_1 and d_2. Two algebraic equations relating these two constants may be obtained by inserting Eqs. (5.100) and (5.101) in Eqs. (5.92) and (5.102), and making use of Eq. (5.103), namely

$$\frac{\nu B a_1^2 c_1}{35 Sc \Delta_m} d_1^3 d_2^2 + d_1 d_2^2 = \frac{420 \nu}{a_1} \tag{5.106}$$

$$d_1^3 d_2^2 = \frac{83160}{31 a_1^3} \tag{5.107}$$

Substituting Eq. (5.107) in Eq. (5.106), it is obtained

$$d_1 d_2^2 = \frac{420 \nu}{a_1} - \frac{83160}{31 a_1^3} (\nu B a_1^2 c_1 / 35 Sc \Delta_m) \tag{5.108}$$

Equations (5.107) and (5.108) can be solved to give

$$d_1 = \left\{ \frac{83160}{\nu \left[13020 a_1^2 - 249480 \left(\frac{B a_1^2 c_1}{35 Sc \Delta_m} \right) \right]} \right\}^{1/3} \tag{5.109}$$

and

$$d_2 = \left\{ \frac{(31 a_1^3)^2 (83160)}{\nu^3 \left[13020 a_1^2 - 249480 \left(\frac{B a_1^2 c_1}{35 Sc \Delta_m} \right) \right]^3} \right\}^{-1/4} \tag{5.110}$$

The heat and mass transfer rates across the frost surface per unit area are, respectively,

$$q = -k\left(\frac{\partial T}{\partial y}\right)_{y=0} = -kPrBc_1(T_\infty - T_f)/B'Sc\Delta_m = -kPrB''a_1(T_\infty - T_f)/B' \tag{5.111}$$

and

$$m = -\rho D\left(\frac{\partial w_1}{\partial y}\right)_{y=0} = -Dc_1(w_{1\infty} - w_{1f})/\Delta_m\delta = -\rho DScB''a_1(w_{1\infty} - w_{1f})/B \tag{5.112}$$

The local heat and mass transfer coefficients are, respectively,

$$h = kPrBc_1/B'Sc\Delta_m\delta = kPrB''a_1/B'\delta \tag{5.113}$$

and

$$h_m = Dc_1/\Delta_m\delta = DScB''a_1/B\delta \tag{5.114}$$

The solutions obtained above are undersirable when B is very small, for it is evident from Eqs. (5.88) and (5.91) that

$$B''a_1 = 4 \qquad \text{and} \qquad \Delta_m = Bc_1/4Sc$$

When $B = 0$, $\Delta_m = 0$. This means that the material boundary layer does not exist when $B = 0$, in contrast with the results of the foregoing sections. To remedy this disadvantage the first condition of Eq. (5.62) may be released and the second relation of Eq. (5.91) defining B" must not be discarded. Since the coefficient a_1 may be absorbed in the constant d_1, there is no loss of generality by putting $a_1 = 1$. As a result, Eqs. (5.98), (5.109) and (5.110) become

$$\Delta_m^3 = \frac{(1-B)c_1}{-Sc\left(\frac{11}{210} - \frac{c_1}{105}\right)\left(105 + \frac{\delta^2}{\nu}\frac{dU}{dx}\right)} \tag{5.115}$$

$$d_1 = \left\{\frac{83160}{\nu\left[13020 - 249480\left(\frac{Ba_1^2c_1}{35Sc\Delta_m}\right)\right]}\right\}^{\frac{1}{2}} \tag{5.116}$$

$$d_2 = \left\{\frac{(31)^2(83160)}{\nu^3\ 13020 - 249480\left(\frac{Ba_1^2c_1}{35Sc\Delta_m}\right)}\right\}^{\frac{1}{4}} \tag{5.117}$$

For given value of B, B' may be found by means of Eqs. (5.97) and (5.89), while Eq. (5.115), with the help of Eqs. (5.105), (5.116) and (5.117) may be solved for Δ_m. With Δ_m so found, it follows that d_1, d_2, R, ℓ, q, m, h as well as h_m may all be determined.

CHAPTER VI

EXPERIMENTAL PROGRAM

6.1 EXPERIMENTAL APPARATUS

The initial objective of the experimental investigation was two-fold. In the first place, it was intended to determine the possible effects of electric fields upon frosting. The second objective was to provide an answer to the question: how effective the electric field effects, if there were any, would be as compared to other mass transfer processes such as forced or free convection? Because of the exploratory nature of the current study, it is logical to use as simple a test setup as possible. With this principle in mind, it was decided to use free convection conditions as reference state to which the experimental results would be compared.

A schematic of the test setup is shown in Fig. 11 and photographs of the apparatus are given in Fig. 12. The setup consisted of three parts:

a. Test plate
b. Refrigerating system
c. Electrical equipment

6.1.1 Test Plate

The test plate used in this investigation has been used, prior to the frosting work, by Velkoff and Miller[2] to study the condensation of vapor in an electrostatic field. The plate was made of $\frac{1}{2}$-inch-thick sheet copper and had a frosting surface measuring 6 by 9 inches. To the back of the plate was soldered $\frac{1}{4}$ inch copper tubing. Refrigeration of the plate was accomplished by pumping refrigerant through this tubing.

The test plate was installed in a hole cut in a vertical plexiglas wall which formed one side of a wooden box enclosing the tubing and the back of the plate. The wooden box was filled with insulating material to insulate the plate so that only the exterior surface of the plate, when exposed to the ambient air, was available for frosting and heat transfer.

Nine iron-constantan thermocouples were constructed and inserted through the back of the plate to within 1/32 inch of its fromt to measure the temperature of the frosting surface. To eliminate the effects of strong electric fields during the tests, a small amount of insulation was provided to insulate the thermocouples electrically from the plate. These thermocouples were located along the sides and at the center of 4 3/4 by 5 inch rectangle centered at the center of the plate as shown in Fig. 13.

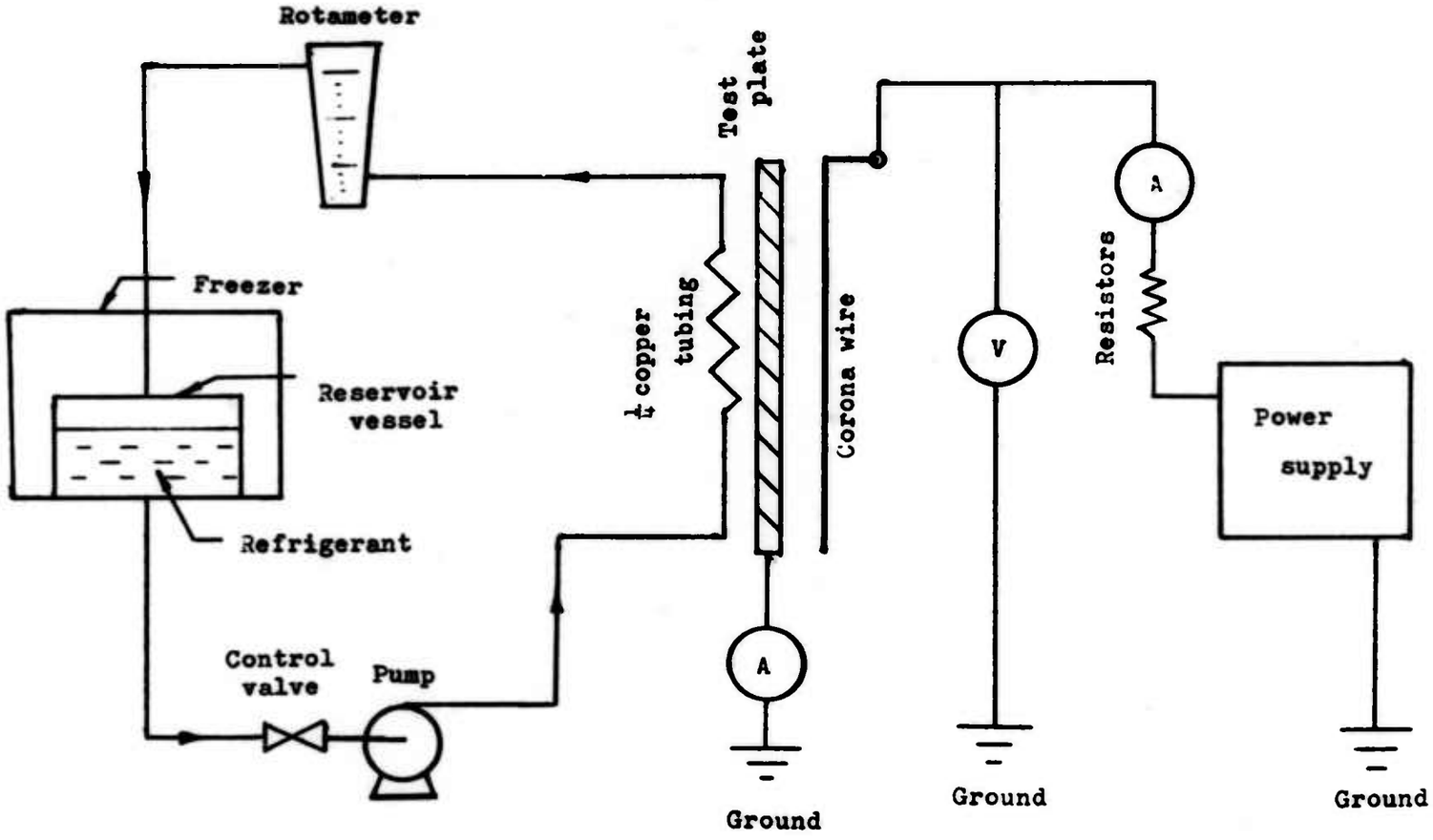

Fig. 11 Schematic of test setup

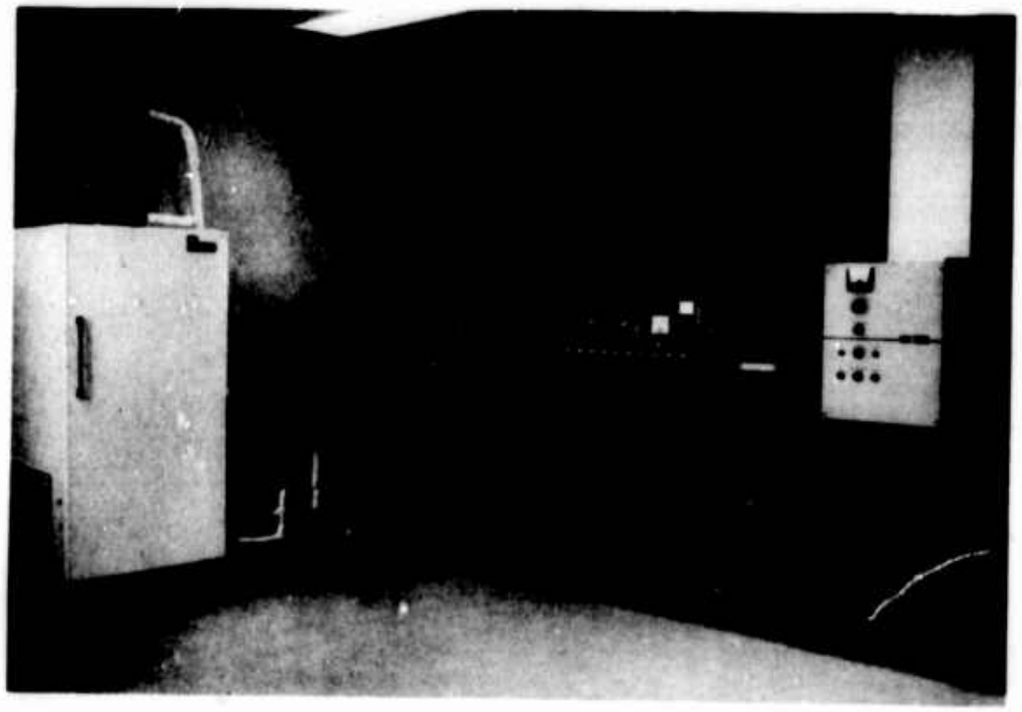

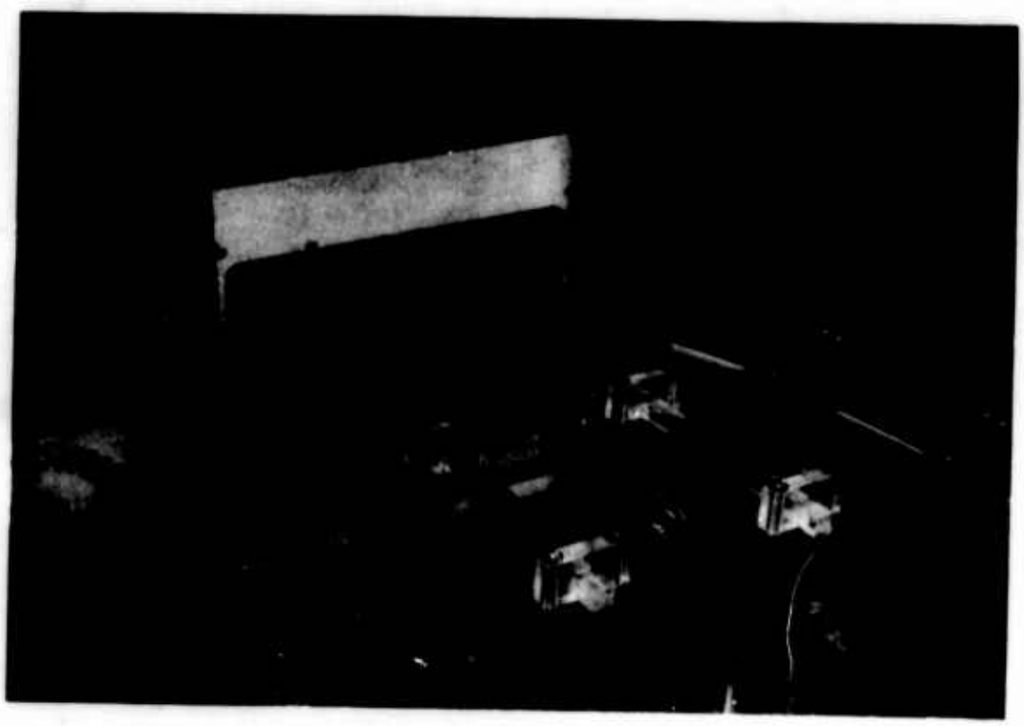

Fig. 12 - Photographs of Apparatus

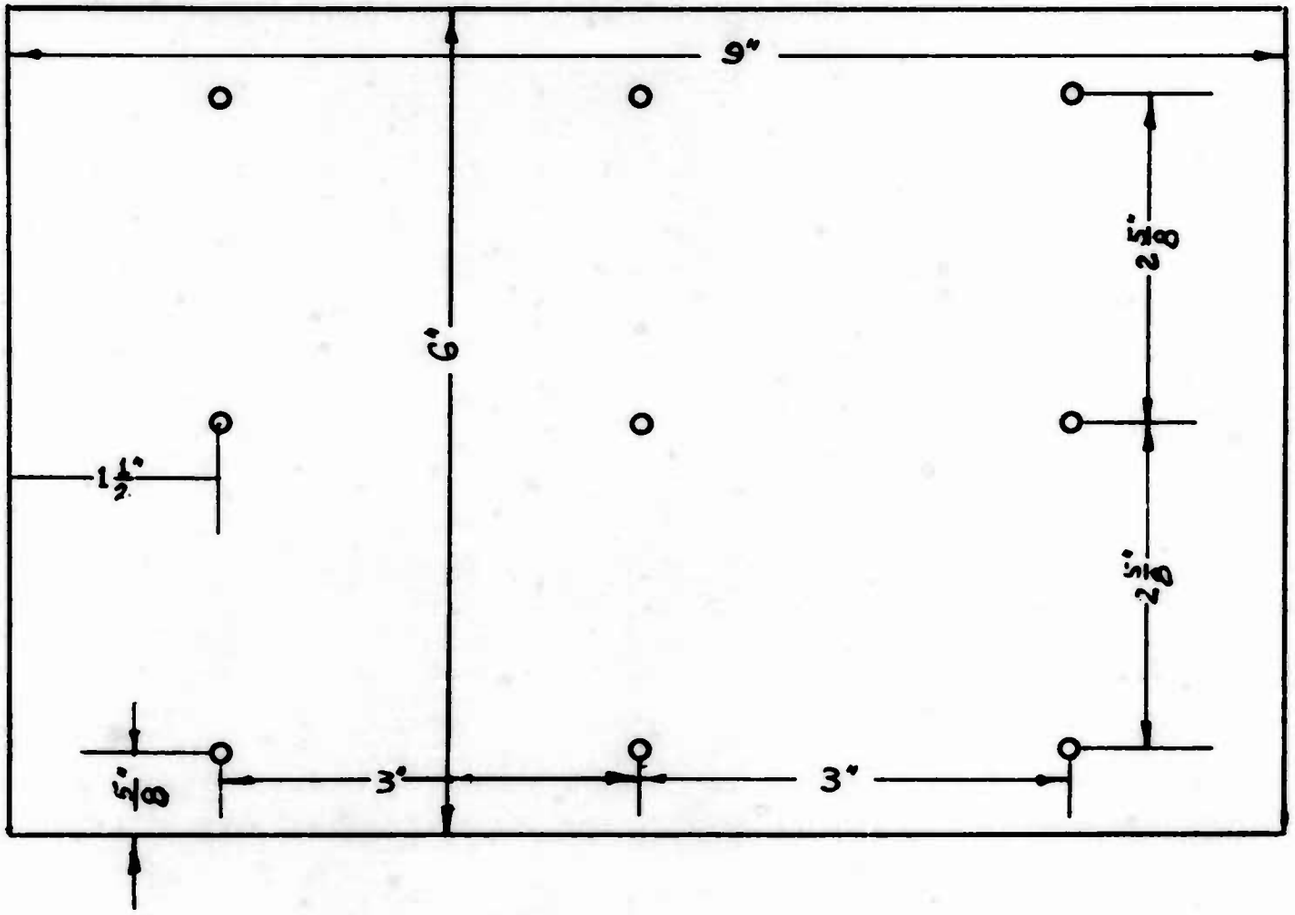

Fig. 13 Positions of thermocouples

6.1.2 Refrigerating System

The refrigerating system used to refrigerate the test plate consisted of a freezer, a refrigerant reservoir, a pump and a rotameter. Refrigeration of the frosting surface was accomplished by passing the precooled liquid through the copper tubing on the back of the test plate. A mixture of anit-freeze (ethylene glycol) and water was used as refrigerant. It was felt that such a mixture was adequate to furnish the desired test plate temperatures. In addition, it is not hazardous and can provide lubrication for the pump.

A $\frac{1}{4}$-ton commercial freezer was used to refrigerate the refrigerant. The latter was contained in a 10 gallon tank installed in the freezer to serve as refrigerant reservoir. Liquid was drawn from the tank, passed through the copper tubing and the rotameter, and then pumped back to the tank. Circulation of the liquid was achieved by means of a rotary pump. Liquid flow rate was measured with the rotameter.

Tygon plastic hose was used to connect the copper tubing on the back of the test plate to the rest of the flow circuits, thus insulating the plate electrically from the refrigerating system. Two four-junction copper-constantan thermocouples were constructed and inserted in the plastic hoses at the inlet and outlet to the copper tubing to measure the temperature difference between the inlet and the outlet refrigerant. Leads of the thermocouples were led through holes drilled in the plastic tubing walls.

6.1.3 Electrical Equipment

The electrical fields used during the tests were provided by a Sorensen high voltage power source with a capacity of 0-30 kv and up to a 4 milliamperes. The output from the high voltage supply was first connected to a series of resistors of the order of 5 meg ohms total and then to the positive electrode. The test plate which served as cathode was always grounded except for one occasion when the screen electrode inserted between the plate and anode was used as the cathode. In that case, the test plate was kept neutral electrically. The voltage across the field was measured by a Singer electrostatic voltmeter. Two milliammeters were used to measure the current. The one on the hot side was incorporated as part of the power supply. The other was connected from the test plate to the ground.

The electric field for negative corona was supplied by the same power source by reversing the polarity of the output. To provide an a.c. field for the a.c. corona, another high voltage power supply was used. A 0.006 inch diameter stainless steel wire was employed as the discharging electrode. The wire was stretched across a plexiglas frame which in turn was mounted on a movable plexiglas support. Distances of the wire from the test plate were adjusted by moving the support or the

frame. The support was designed so that the vertical position of the wire could be adjusted by lifting or lowering the frame relative to the support. Several parallel wires may be stretched on the plexiglas frame when electrode with more than one wire is desired.

6.2 EXPERIMENTAL PROCEDURE AND MEASUREMENT

6.2.1 Mass Transfer to the Test Plate

Because of the non-uniformity of the frost layer thickness and of the frost density along the entire plate, measurement of frost thickness distribution is not necessarily meaningful in the determination of mass transfer. In a situation like this, it is always necessary to measure local mass transfer rate. Such measurements, however, require either a measurement of the local concentration profile or a segmented test plate which facilitates the determination of the local frost deposition. The former requires an instrument which can measure accurately the local dry and wet bulb temperatures in the thin boundary layer in a strong electric field. The latter needs a special design of the test plate so that each segment of the plate can be maintained at the same temperature and can also be removed easily. Unfortunately, technical difficulties prevent such measurements to be accomplished in the limited time available. In the absence of a convenient method to determine the mass transfer rate locally, it was decided to measure the total amount of frost deposited on the test plate in a given period of time.

To facilitate the comparison of the total mass transfer for different electrical conditions, it is of necessity that the tests be conducted under identical test conditions, i.e. same test plate temperature and same specific humidity and temperature of the surrounding air. Furthermore, to determine the variation in time of the mass transfer under the influence of electric fields, it is also necessary to maintain the same test conditions over a long period of time. Limitations set by the present test facilities render this impossible. In spite of the difficulty, a qualitative trend of the electric field effects on frost formation can be obtained by shortening the test period so that it may be regarded that approximately the same test conditions prevail in each test.

The test period selected in accord with the capability of the test setup was five minutes. Two sets of tests were run in this relation. In the first set of tests, the distance between the plate and the wire was kept constant, while the current was varied. The second set of tests was aimed to measure the variation of frost deposition with distances of the wire from the plate for a given current.

The test plate temperature was measured with the nine thermocouples inserted to within 1/32 inch from frosting surface and was recorded by a self-blancing potentiometer on a continuous recorder. The nine

thermocouples were connected in parallel and then connected to the recorder. A reference junction in the open air was used. Temperature of the air was read from the dry bulb thermometer of sling type psychrometer. Specific humidity of the ambient air was determined from the dry and wet bulb temperatures read from the psychrometer. Barometer and psychrometer readings were taken immediately prior to the beginning and at the conclusion of the test run. Average value was used in the reduction of the data. The variation of the readings before and after a test run was usually small, less than $1^{o}F$.

In general, it took about eight minutes to cool the test plate down to a steady constant temperature. As soon as the test plate temperature became steady, as could be judged from the temperature-time curve on the recorder, the frost already formed on the plate during the cool-down period was scraped off and the electric field turned on and the current adjusted to a predetermined value. After five minutes the electric field was turned off and the frost scraped off for measurement. Another run of a given test was then started by turning on the field again and adjusting the current to a new value.

The frost scraped off for measurement was contained in a light rectangular tray made of aluminum foil. The tray, being weighed prior to containing frost, together with the frost was then weighed on a balance and measured to within 0.1 gram. The net weight of the frost was obtained from the gross weight by subtracting the weight of the tray.

6.2.2 Heat Transfer to the Test Plate

Measurement of heat transfer rate under various electrical conditions presented more serious difficulty than mass transfer. In contrast with mass transfer measurement where the total mass transfer can be measured for a given period of time, the heat transfer rate can only be measured instantaneously by reason of the unsteadiness of the frosting process. For the comparison of heat transfer rate for a variety of electrical conditions to make sense, it is desired to obtain a heat transfer rate versus time curve for each electric filed while other test conditions being maintained constant. In other words, a longer period of test is desired. That this requirement can not be met with the test facilities used in the present investigation has already been noted. Under such circumstances, it was decided to sacrifice the constancy of the test conditions. Each test lasted 30 minutes. Since it usually took 4 to 5 hours to cool down the refrigerant in the freezer, the test conditions might have changed during this long interval. It was hoped, however, that in this manner a qualitative observation might be obtained as to the effects of electric fields on heat transfer associated with frost formation, when changes in test conditions were not too drastic.

To start a test run, refrigerant was circulated through the back of the test plate to cool down the test plate. When the test plate temperature reached steady state, the field was applied. Readings of refrigerant flow rate and the temperature difference between the inlet and outlet refrigerant to the test plate were taken at two minute intervals. The rotameter had been calibrated prior to use. The calibration was plotted as a milliliter versus cm of rotameter scale so that the flow rate could be read directly from the curve for each reading on the rotameter scale. The two four-junction thermocouples installed in the inlet and outlet tygon plastic hoses to the back of the test plate were put in series and connected to a portable precision millivolt potentiometer. The accuracy of measurement was 0.03°F.

The total heat transfer rate was calculated using the equation

$$Q = Wc\Delta T$$

where W and c are the mass flow rate and specific heat, respectively, of the refrigerant and ΔT is the inlet and outlet temperature difference. For the purpose of comparing heat transfer data for various electrical conditions provided other conditions are identical, it suffices to compare only the product of volume flow rate and the inlet and outlet temperature difference for each case. On account of this, heat transfer through the edges of the test plate and radiation are disregarded.

In the course of a test, it was discovered that the current sometimes fluctuated considerably. Therefore, it was necessary to adjust the current constantly in order to maintain constant current throughout the test. In fact, the current tended to increase as the frost grew. It appeared interesting to observe the variation in time of the current. This was done by taking readings from the milliameter at two-minute intervals while the frost was allowed to form continuously. Typical curves thus obtained are to be shown in Section 6.3.4.

6.2.3 Velocity Profile Measurement

Measurement of velocity profile is of primary importance in the experimental investigation of a flow field. To help gain an insight into the actual flow field under the impingement of an electric wind, efforts were made to measure velocity profiles in certain regions of the flow field. Because of the limited space between the wire and the plate and because of the strong electric field present in the immediate vicinity of the stagnation point, measurement of velocity in the electric wind and the stagnation flow regime would have been difficult and was not attempted. Instead, two sets of measurements were made in regions away from the stagnation point. The first region under investigation was the wall jet flow. Only the data at a point two inches from the stagnation point along the vertical centerline of the plate were taken. More information in this region would have been available, were

the test plate sufficiently large to permit measurements at points further downstream.

The second set of measurements was directed to furnish information on the velocity distribution of an electric wind formed by a positive wire-plane corona in the absence of the obstruction by the plane electrode. Such measurement was made possible through the use of a screen as the cathode. It was directly behind the screen that the actual measurement was carried out.

The velocity distribution was measured by means of a 0.06-inch diameter total pressure probe, constructed of glass, connected to a micromanometer using atmospheric pressure for reference. The micromanometer consisted of a meniscus in an inclined tube. The displacement of the meniscus along the tube was read to 0.0001 inch with a Gaertner travelling microscope. By setting the inclined tube at an angle of approximately 10° relative to the horizontal, pressure could be read to within 0.00002 inch butyl alcohol.

For the measurement of velocity in the wall jet, a probe transverse was made perpendicular to the plate. Each of the traverses consisted, on the average, of 19 readings at about 0.01 inch intervals near the wall and intervals of about 0.05 inch in outer regions of the flow. In the measurement of electric wind velocity, a probe traverse was made perpendicular to the axis of the wind. An average of 15 readings at intervals of 0.1 inch was made for each traverse. The accuracy of setting the probe was 0.001 inch.

Flows with mixing layers are inherently unsteady. In this investigation, this unsteadiness was manifested as a timewise fluctuation of the pressure signal from the total pressure probe, particularly in the outer mixing zone and at higher currents. In view of this, two sets of data were recorded for each profile by traversing the total pressure probe twice. Average value of the two was used in the velocity calculations.

Apart from errors in pressure measurement, there is a source of error at the outer edge of the flows where the longitudinal velocity tends to zero, while the transverse inflow velocity tends to finite value. As a result, there is a yawed flow relative to the total pressure probe. The points within a few total pressure probe diameter from the wall are also subject to error.

6.2.4 Current Density Distribution Along the Plate

As has been pointed out in Chapter III, the velocity distribution of the electric wind depends on the current density distribution. Being unable to calculate the field intensity and charge density distributions analytically for given boundary conditions, it is

desirable to seek, experimentally, possible correlation between the electric wind velocity and the current density. It was for this purpose that the current density measurement was carried out.

A segmented plate with each segment insulated from its neighboring segments is required in order to measure the local current density along the plate. To achieve this with the existing setup, the test plate was modified by covering it an insulating covering painted with horizontal strips of conductive silver paint, each strip being separated from the adjacent ones by a thin unpainted area of 1/8 inch wide. The painted strips were so distributed that the entire configuration was symmetrical with respect to the corona wire.

To facilitate the measurement of the current, each strip was connected to a switch. Each switch has two positions, ground and meter. The current to any particular strip was read from the milliammeter by putting the appropriate switch in meter position, while the other switches remained in ground position. The switches allowed rapid reading of the current to each strip which when divided by the area of that strip gives the local current density at the location of that strip.

6.3 EXPERIMENTAL RESULTS

The preliminary experimental observations which formed the basis of this investigation have already been stated in Section 1.2 and will not be repeated. Only the data related to the measurements described in the preceding section are here presented. To facilitate interpretation, the data will be examined in the reverse order relative to the list of measurements in Section 6.2.

6.3.1 Current Density Distribution

The first series of test data to be investigated is the current density distribution at the plane electrode of a wire-plane corona. The results are plotted in Figs. 14 to 16. In each case the abscissa are the distances from the horizontal centerline along the plane electrode. Positive and negative values of x correspond to lower and upper half of the plane, respectively. The curves in each figure were obtained by varying the applied voltage while keeping constant the distance between the wire and the plane, d.

All of the current density distribution curves exhibit the same trend. The maximum current density occurs at the centerline as would be expected from the special electrode configuration used. As x increases in both directions the current density drops rapidly, forming a bell-shaped distribution. Essentially the current in each case is confined to a region within about one inch from the centerline. The

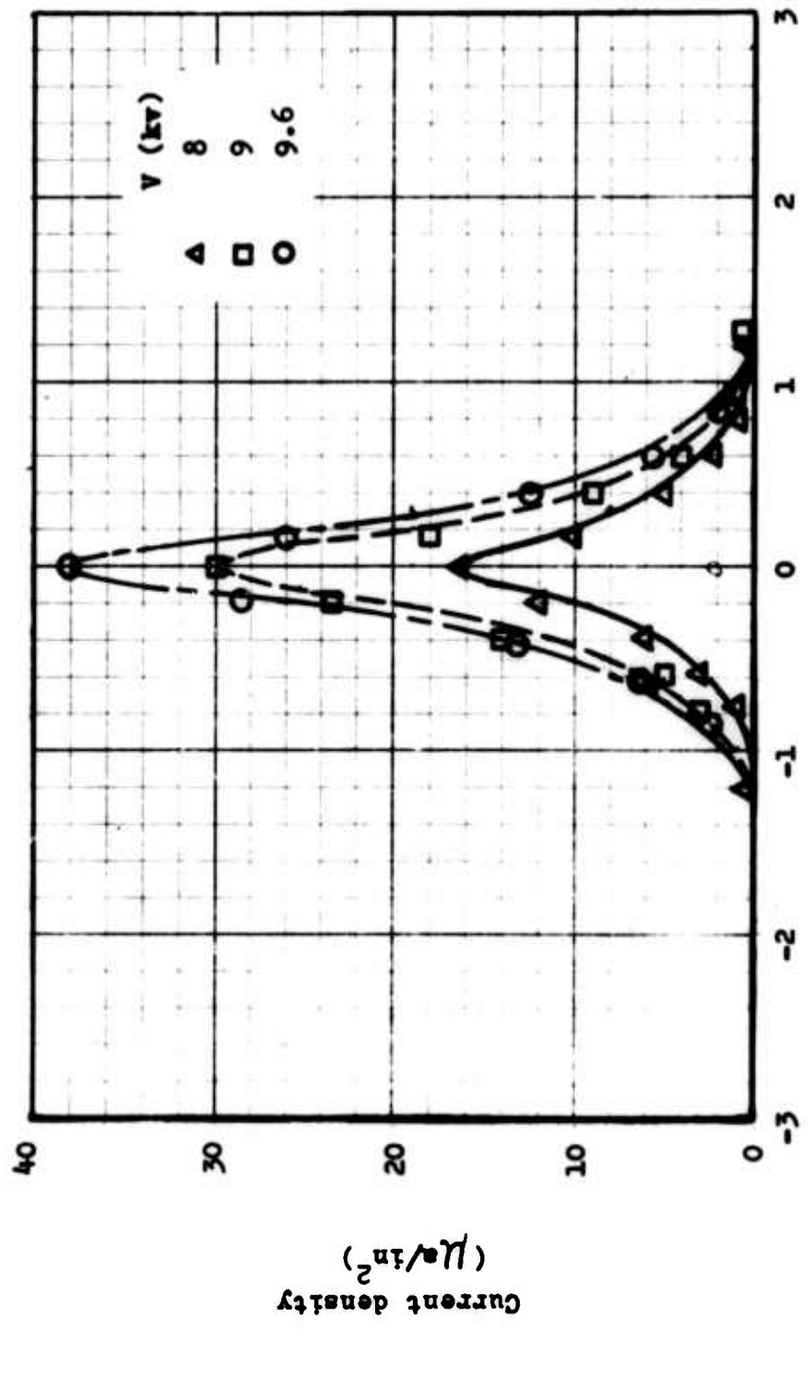

Fig. 14 Current density distribution along the plate, d = 0.5 inch

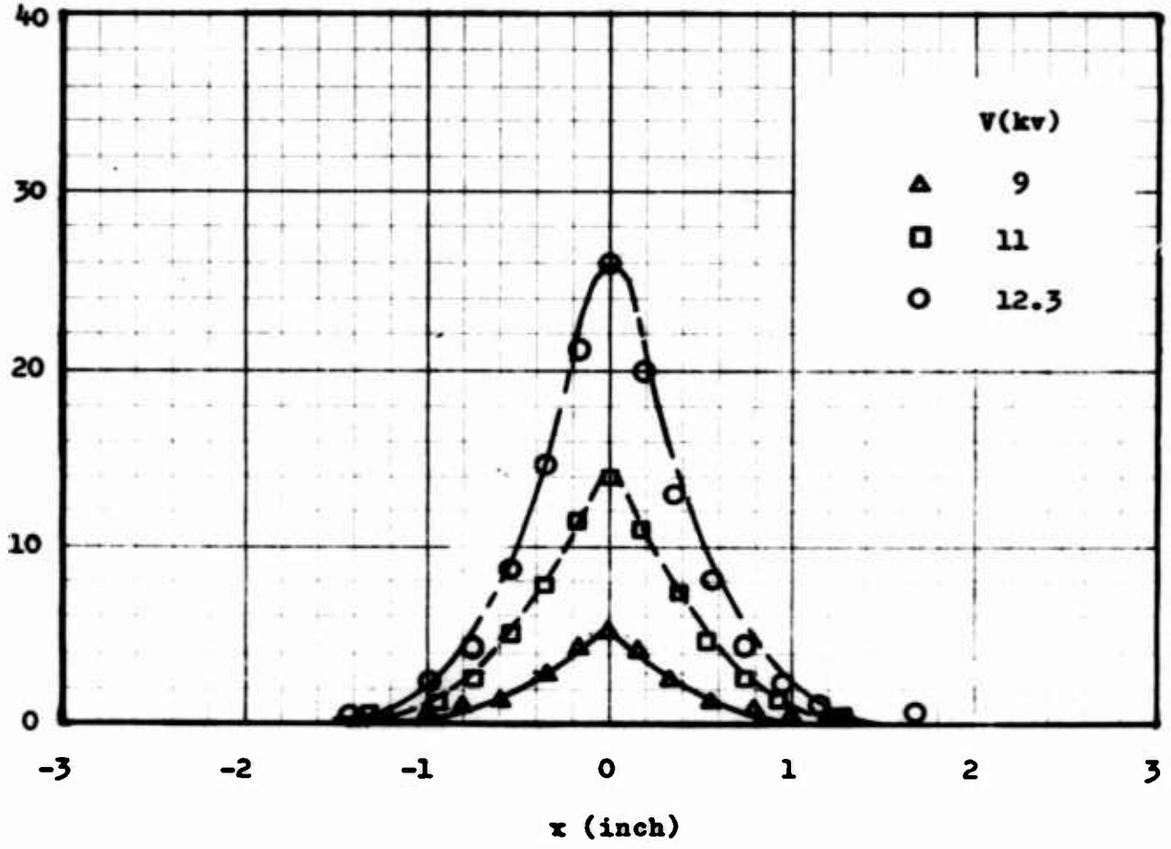

Fig. 15 Current density distribution along the plate, d = 0.75 inch

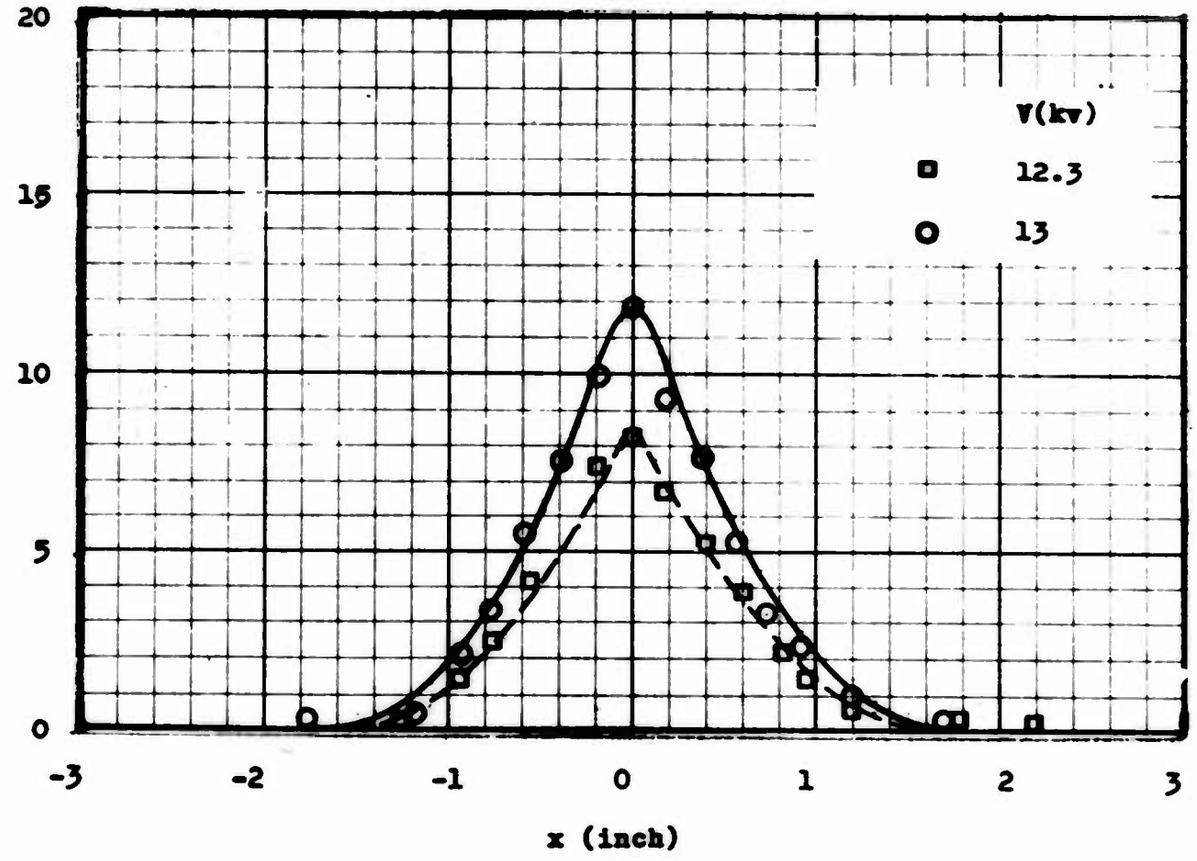

Fig. 16 Current density distribution along the plate, d = 1 inch

symmetry of the current density distribution with respect to the center-line seems to suggest that the corona discharge may be regarded to occur in a direction normal to the plane electrode without causing appreciable error.

The following points may also be noted in connection with the current density distribution curves:

1. The area over which the current is received (to be referred to as the current-area hereafter) seems not to be affected by increasing voltage V when d is kept constant. But increase in d tends to widen this area.

2. For constant V, the current-area increases and the maximum current density falls as d increases.

3. The values of x for which the current density is half the maximum current density are approximately constant for different voltages but constant d, and increases with d.

Figure 17 shows the variation of the maximum current density with voltage for three values of d as plotted from the data shown in Figs. 14 to 16. The points corresponding to zero current density are adapted from the characteristic current-voltage curves measured using the test plate as plane electrode. The latter curves are shown in Fig. 18 for reference. Upon comparison of Figs. 17 and 18, it is clear that, for a given d, the total current increases more rapidly than the maximum current density as voltage increases.

The data as presented above provide only qualitative information as to the influences upon the current density distribution of the applied voltage and the distance between the wire and plane electrodes. If it can be shown that a similarity exists among the curves presented in Figs. 14 to 16, the current density distribution for any V and d can be readily deduced from the foregoing data, provided there is corona and the characteristic values of J and x are known for the values of V and d of interest. By similarity it is meant here that the current density distributions for two sets of value of V and d differ only by a scale factor in J and x.

In an attempt to seek the possible similarity between the curves shown in Figs. 14 and 16, the current density will be normalized by J_{max}, the maximum current density. Furthermore, the abscissa variable x will be made dimensionless by $x_{1/2}$, which corresponds to the x-value where $J = \frac{1}{2}J_{max}$. The dimensionless current density distributions so constructed, Figs. 19 to 21, show that the curves in each of Figs. 14 to 16 can be fairly well represented by a single curve. From an inspection of the figures, it is seen that a small deviation from the tentative similarity profile occurs in the outer region of the curves in some occasions. The actual reason for this deviation is not clear.

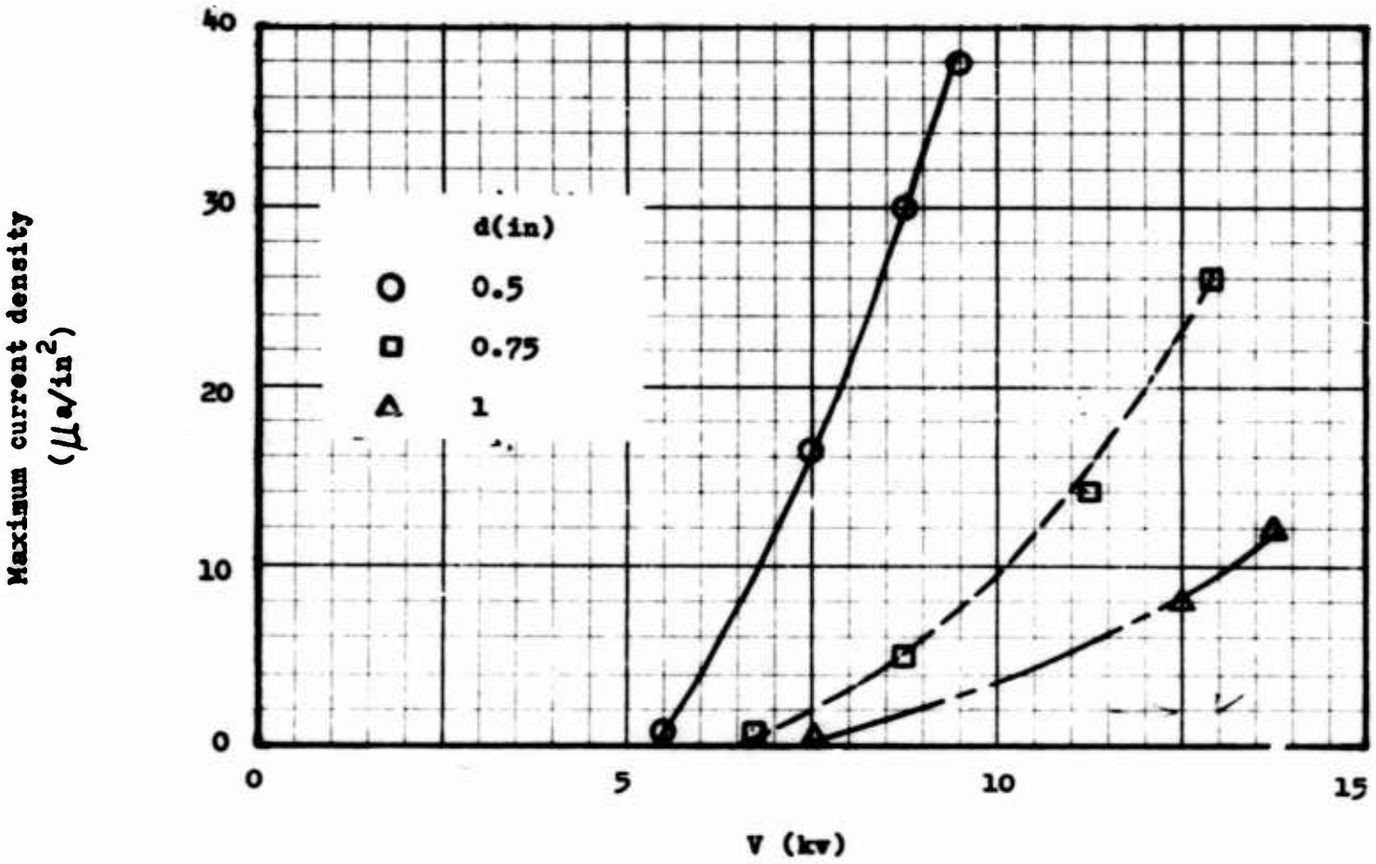

Fig. 17 Maximum current density on the plate vs voltage

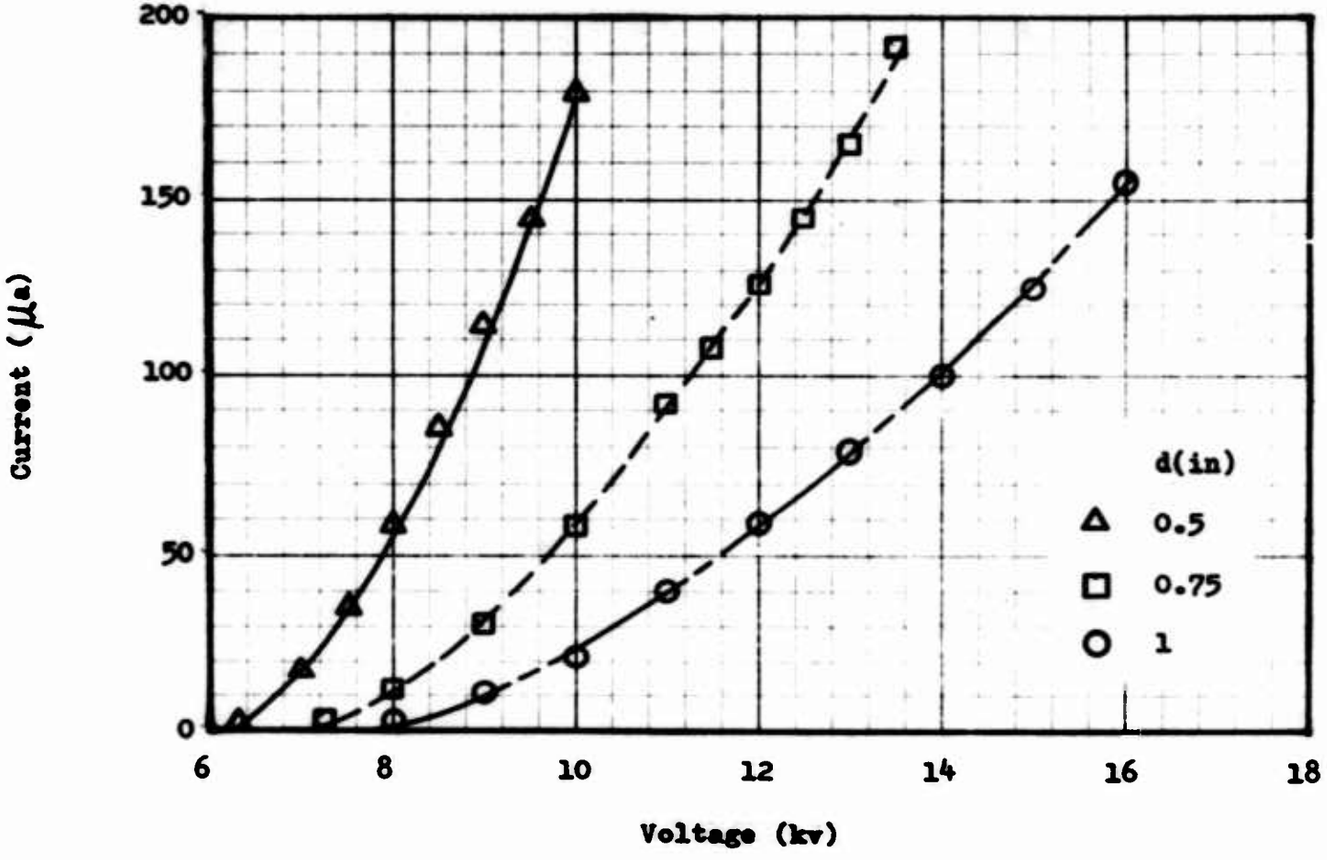

Fig. 18 Current-voltage curves for a corona discharge with 0.006 wire at centerline along 9-inch dimension of a 6x9-inch flat plate

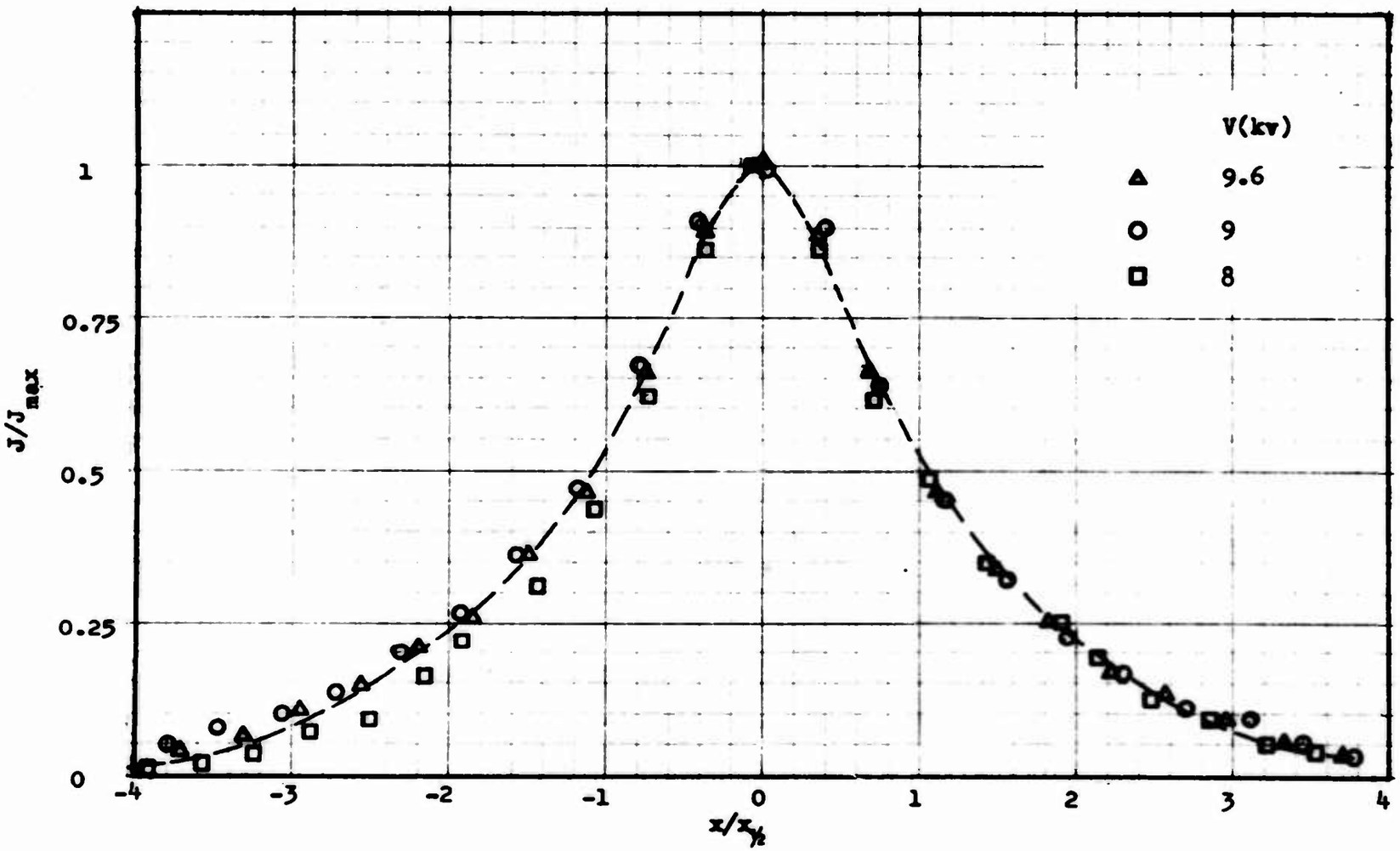

Fig. 19 Dimensionless current density distribution, d = 0.5 inch

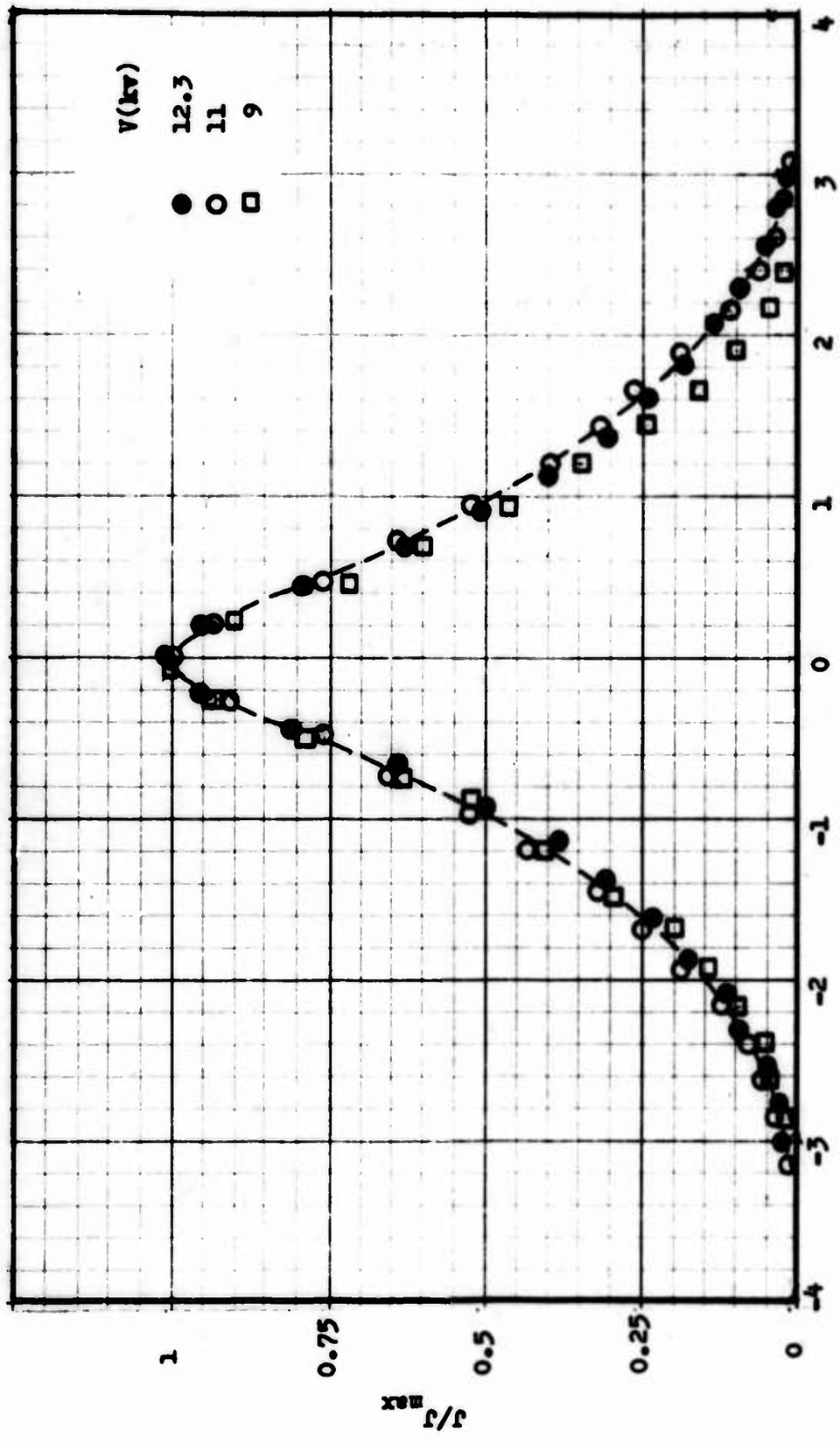

Fig. 20 Dimensionless current density distribution, d = 0.75 inch

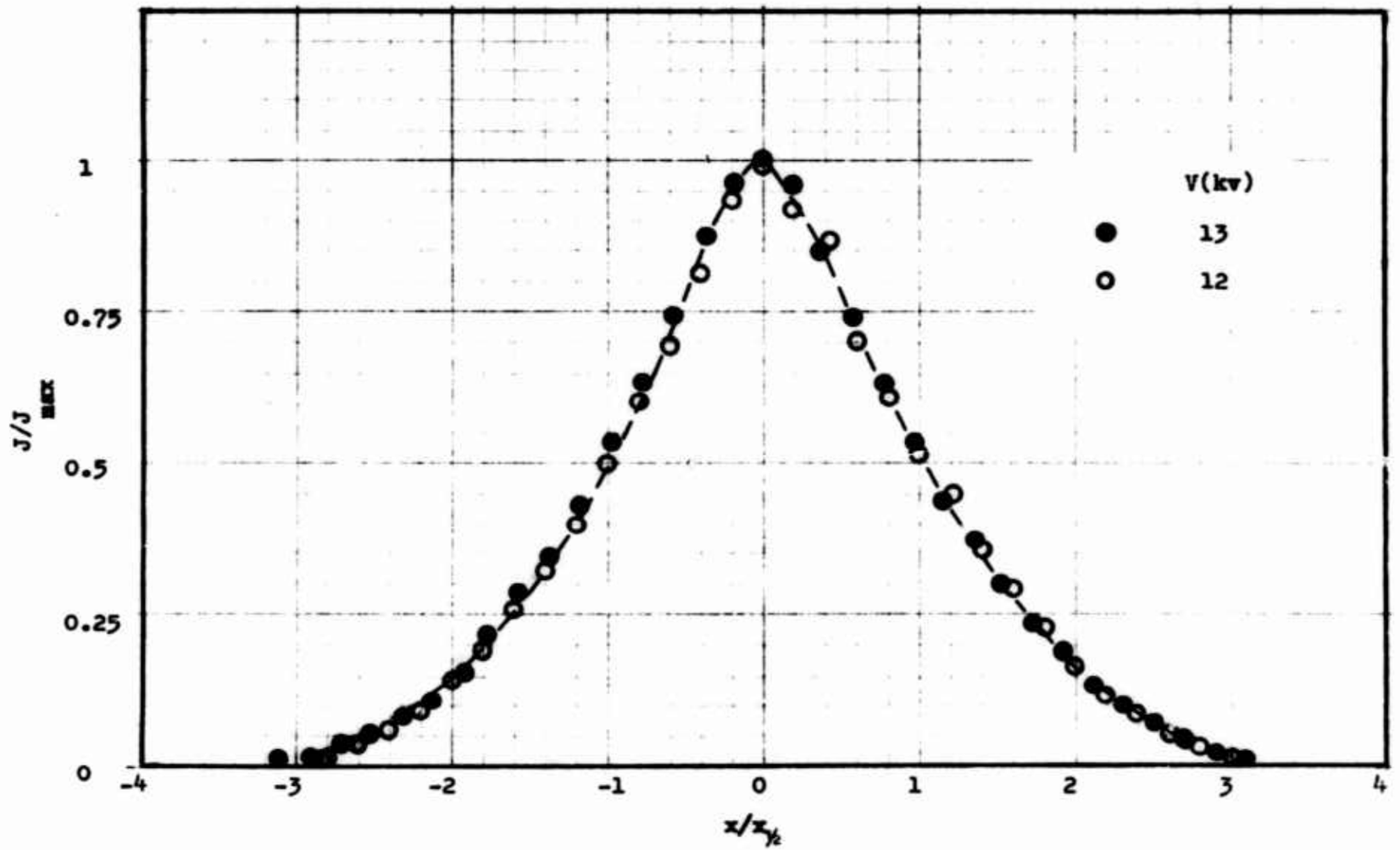

Fig. 21 Dimensionless current density distribution, d = 1 inch

When Figs. 19 to 21 are plotted together, there is obtained Fig. 22. Figures 20 and 21 are seen in this plot to coincide with each other fairly well. However, Fig. 19 does not seem to share the same trend. Considerable deviation is noted again in the outer regions. Despite this disagreement, a general conclusion is that the majority of the data is in favor of the existence of a similarity in the current density distribution.

6.3.2 Velocity Profiles in a Jet of Electric Wind

Figures 23 to 25 show the velocity profiles of an electric wind generated by a wire-screen corona for three distances of the wire from the screen: d = 0.5, 0.75 and 1 inch. Instead of voltage as in current density distribution, the total current has been used as a parameter in obtaining the curves in each figure. The abscissa in each case designate as in the previous section the distances from the centerline of the screen against which the corona wire was placed.

Because of the fact that the traversing mechanism on which the total pressure probe was mounted can only traverse a distance of 1-3/4 inches, measurement of the wind velocity was limited to a region within 3/4 inch from the centerline. Beyond this range the data curves were extrapolated (in accord with the measured data in the central portion of the wind). In this way the data curves as shown in Figs. 23 to 25 may be subject to inaccuracy in the outer regions.

The presence of the screen wires undoubtedly affects the passage of the air stream. As a matter of fact in the course of measurements it was found that the data point measured behind a screen wire did not fall on the same track as its neighboring points. Such points were omitted in plotting the velocity profiles.

In some cases the data points are scattered, especially near the outer edges of the flow. In the latter range, the scattering of data may be due to errors incurred by a yawed flow relative to the probe or to the decreasing accuracy of the measurements at the very low velocities encountered.

Despite these possible errors, Figs. 23 to 25 do provide some useful information in relation to the velocity distribution of the electric wind. A comparison of the velocity profiles, Figs. 23 to 25, and the current density distributions, Figs. 14 to 16, exhibits that these two series of data are closely related to each other. The similarity between the velocity field and the current density field may be summarized as follows:

1. The velocity profiles exhibit the same bell-shaped distribution as the current density.

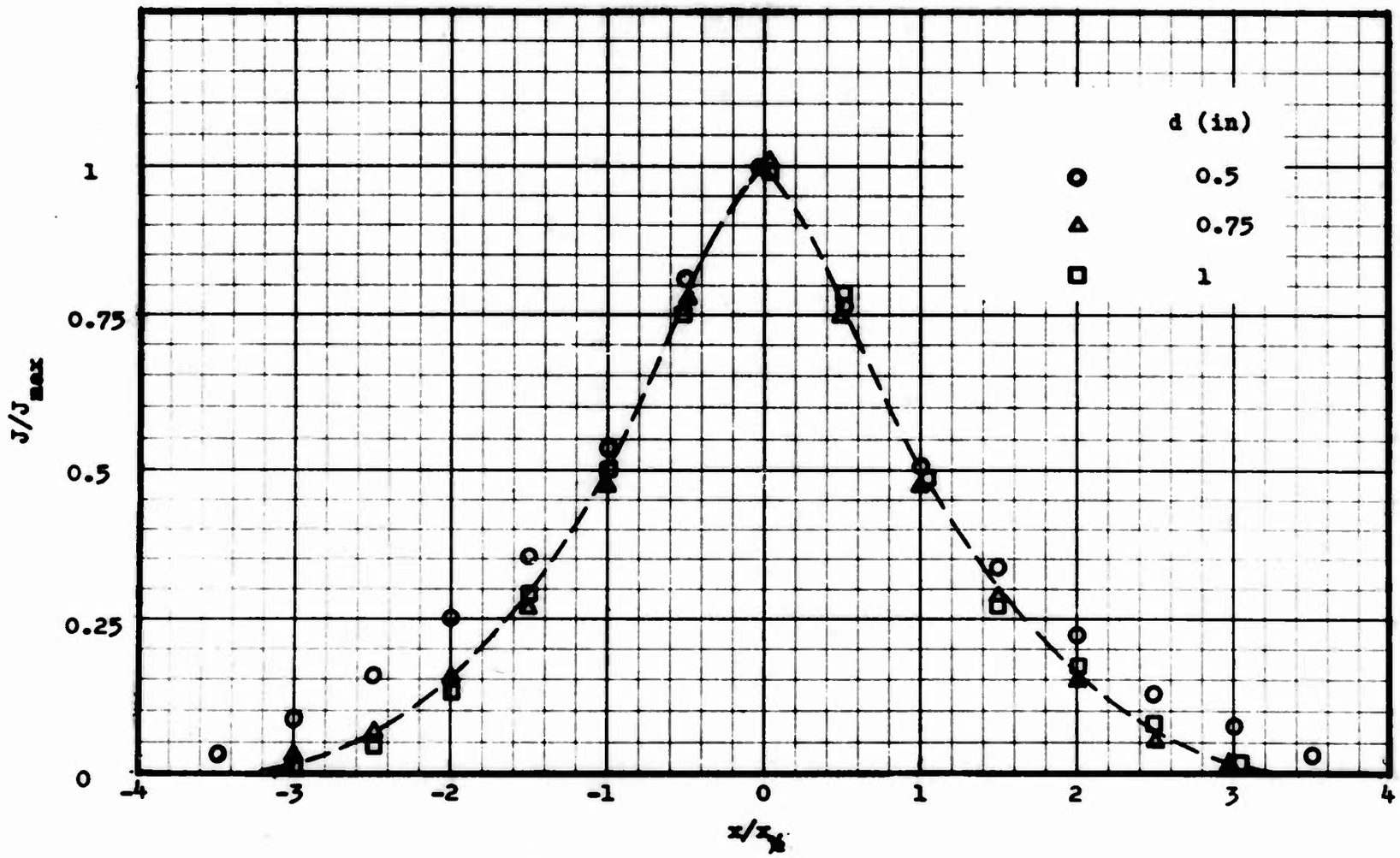

Fig. 22 Dimensionless current density distribution

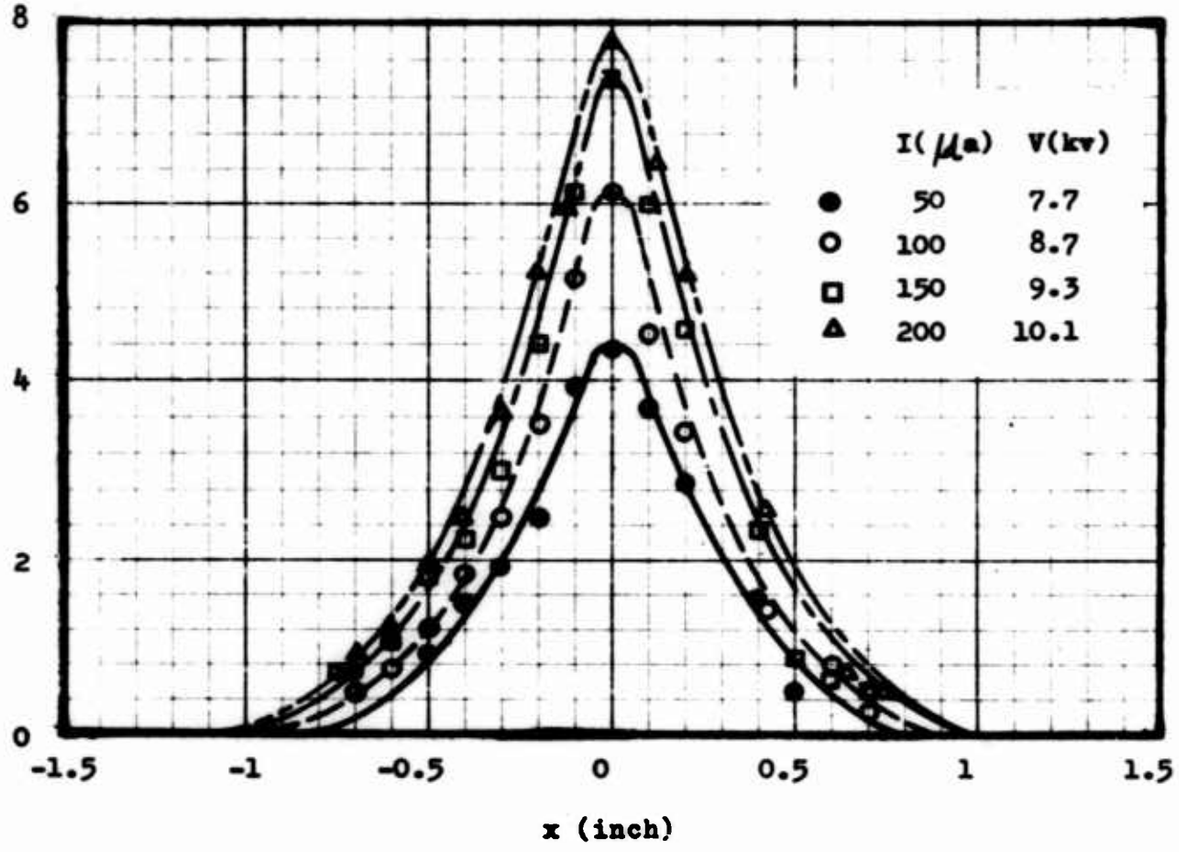

Fig. 23 Velocity distribution of electric wind, d = 0.5"

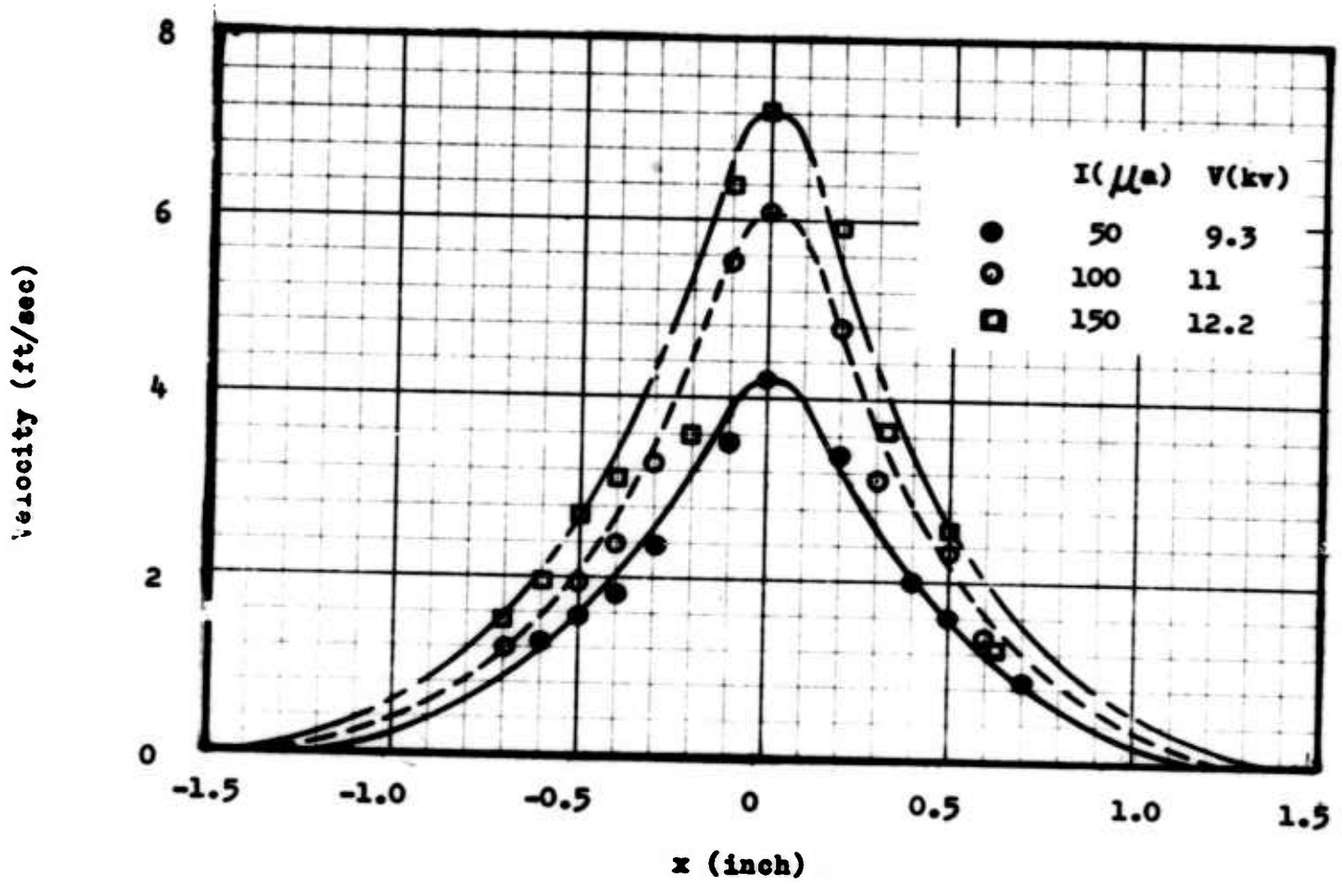

Fig. 24 Velocity distribution of electric wind, d = 0.75"

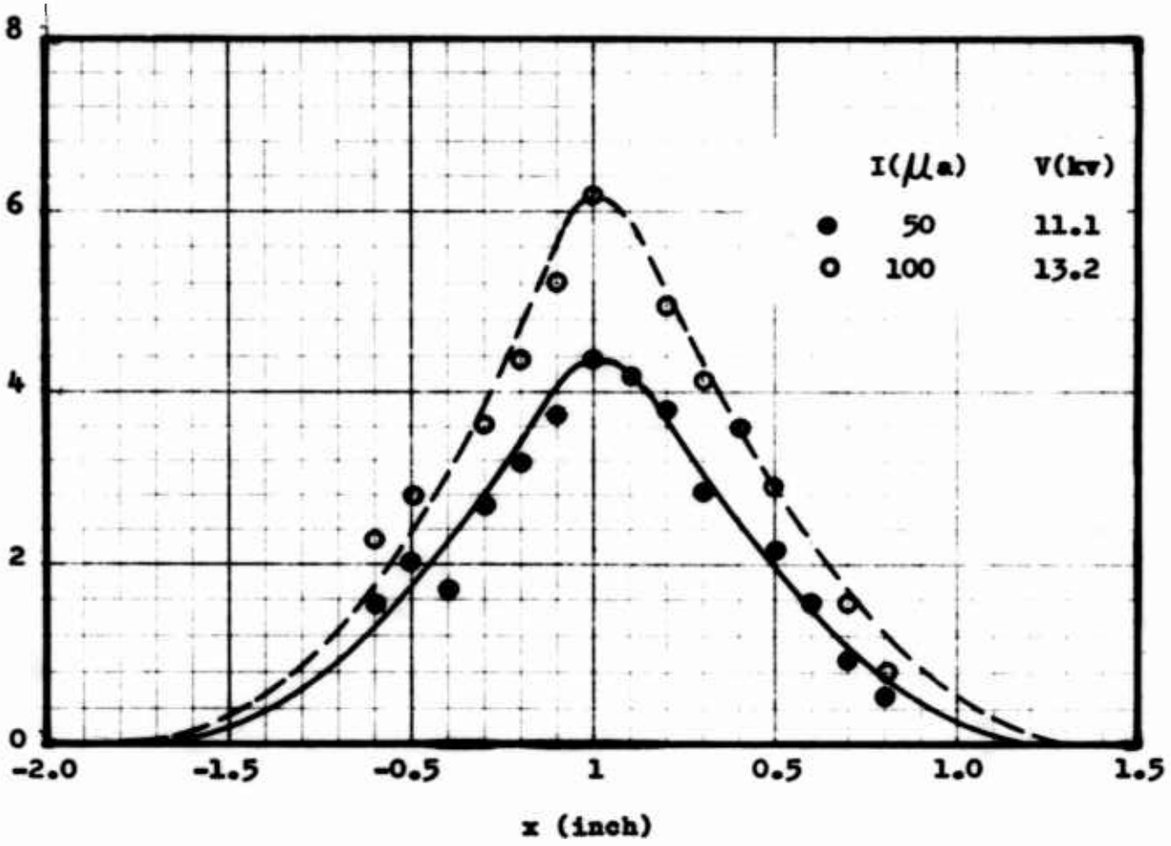

Fig. 25 Velocity distribution of electric wind, d = 1 inch

2. The velocity field is confined to a region about 1 inch from the centerline, just like the current density distribution.

3. Increase in d, the distance between the wire and the screen tends to widen velocity field. Similar observation has been made in connection with the current density distribution. One thing inconclusive is whether increase in total current will affect the area velocity field when d is kept constant. While the current density distribution data tend to suggest that the current-area remains unaffected for constant d when voltage and hence total current is increased, extrapolation in the velocity profiles do not seem to encourage a similar conclusion.

4. In parallel with the case of current density distribution, an inspection of the velocity profile shows that $x_{\frac{1}{2}}$, the value of x for which the velocity is half the maximum velocity v_{max}, is almost constant for constant d but increases with d.

To further the comparison between the velocity and current density fields, the velocity profiles are replotted in dimensionless form. In analogy with dimensionless current density distribution, velocities are normalized by v_{max}, and the coordinate x is made dimensionless by $x_{\frac{1}{2}}$. Figures 26 to 28 show the dimensionless velocity profiles as transformed from Figs. 23 to 25, respectively. Evidently each of Figs. 23 to 25 can be plotted into a single curve. The existence of the similarity of velocity profiles of electric wind is further evidenced by Fig. 29, which plots together the three curves shown in Figs. 26 to 28.

It is of interest to compare Figs. 22, current distribution, and 29 showing velocity distribution. When these figures are plotted toge together, Fig. 30 results. Clearly, a similarity between the current density distribution and the velocity profiles is convincingly indicated in this plot.

Figure 31 is a plot of the variation of the maximum velocity with the total current. It is noted from this plot that the maximum velocity in the electric wind is mainly a function of the total current and is almost independent of d. When the maximum velocity is replotted using the square root of the current as abscissa (Fig. 32), the data may be approximated by a straight line which can be expressed as

$$v_{max} = 0.557\sqrt{I} \qquad (6.1)$$

where v_{max} is in ft/sec and I is in μa. A similar relation has been derived theoretically in Chapter III for the one-dimensional model of electric wind. For the two-dimensional case, an analogous equation

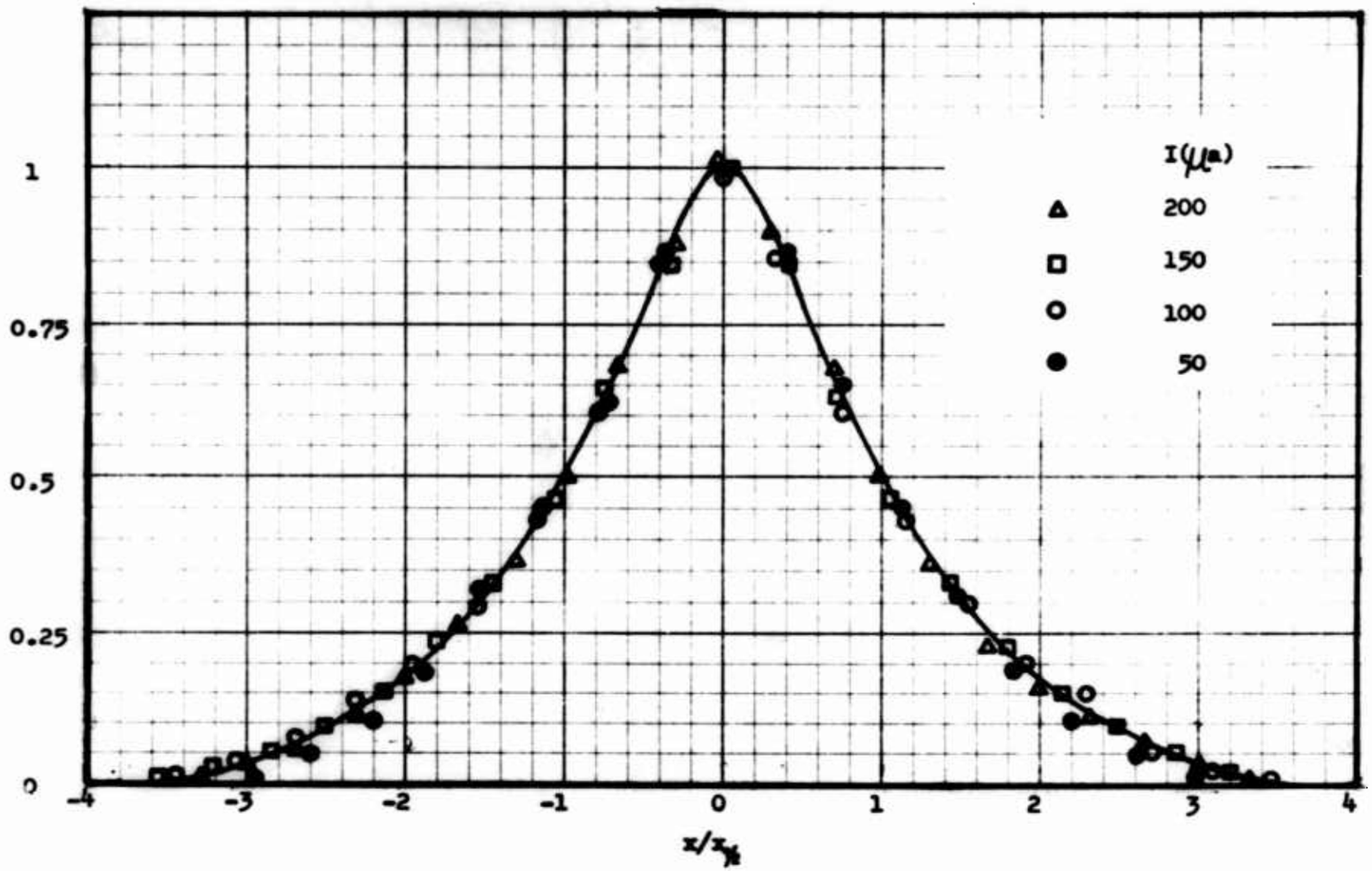

Fig. 26 Dimensionless velocity distribution of electric wind, d = 0.5"

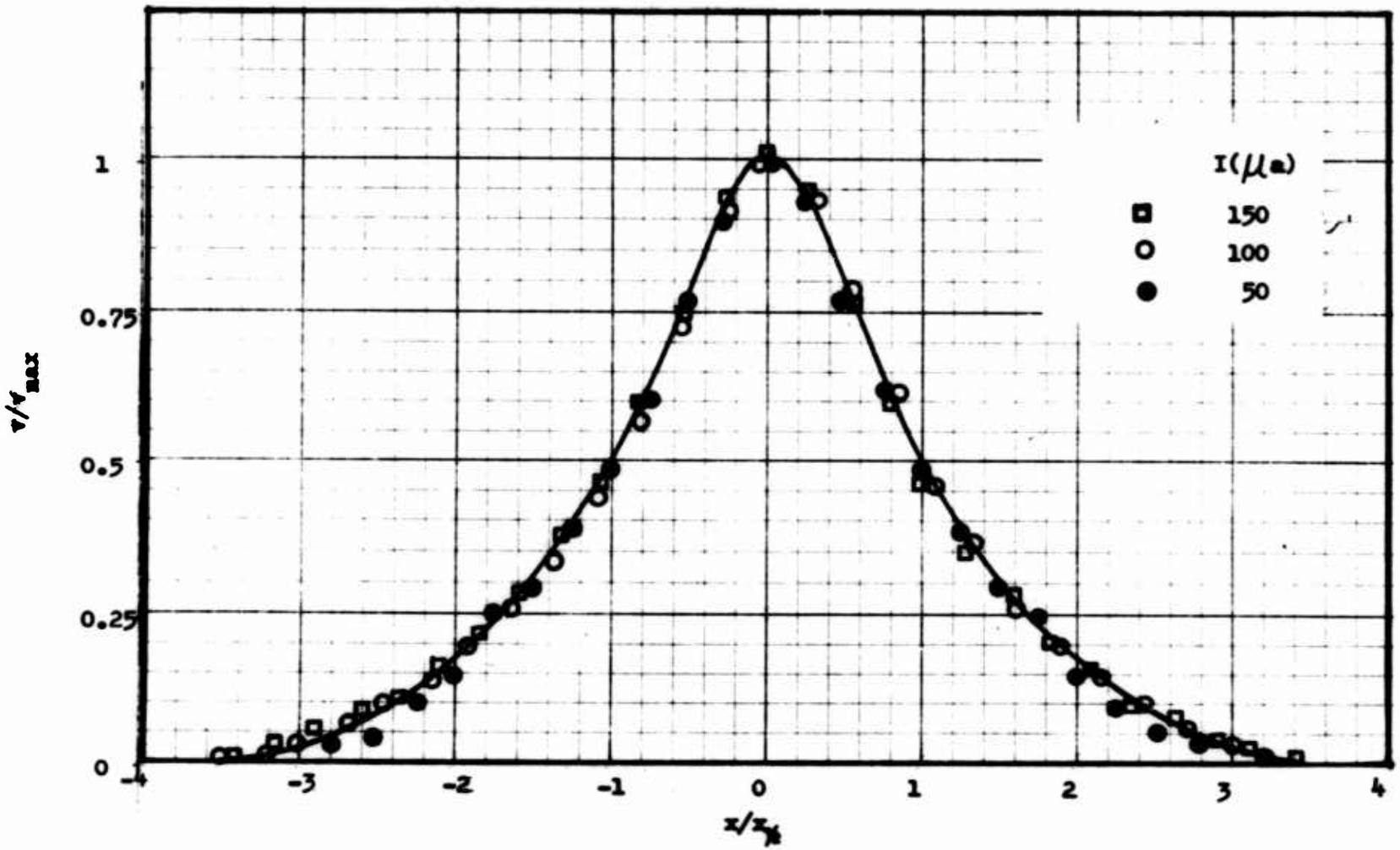

Fig. 27 Dimensionless velocity distribution of electric wind, d = 0.75"

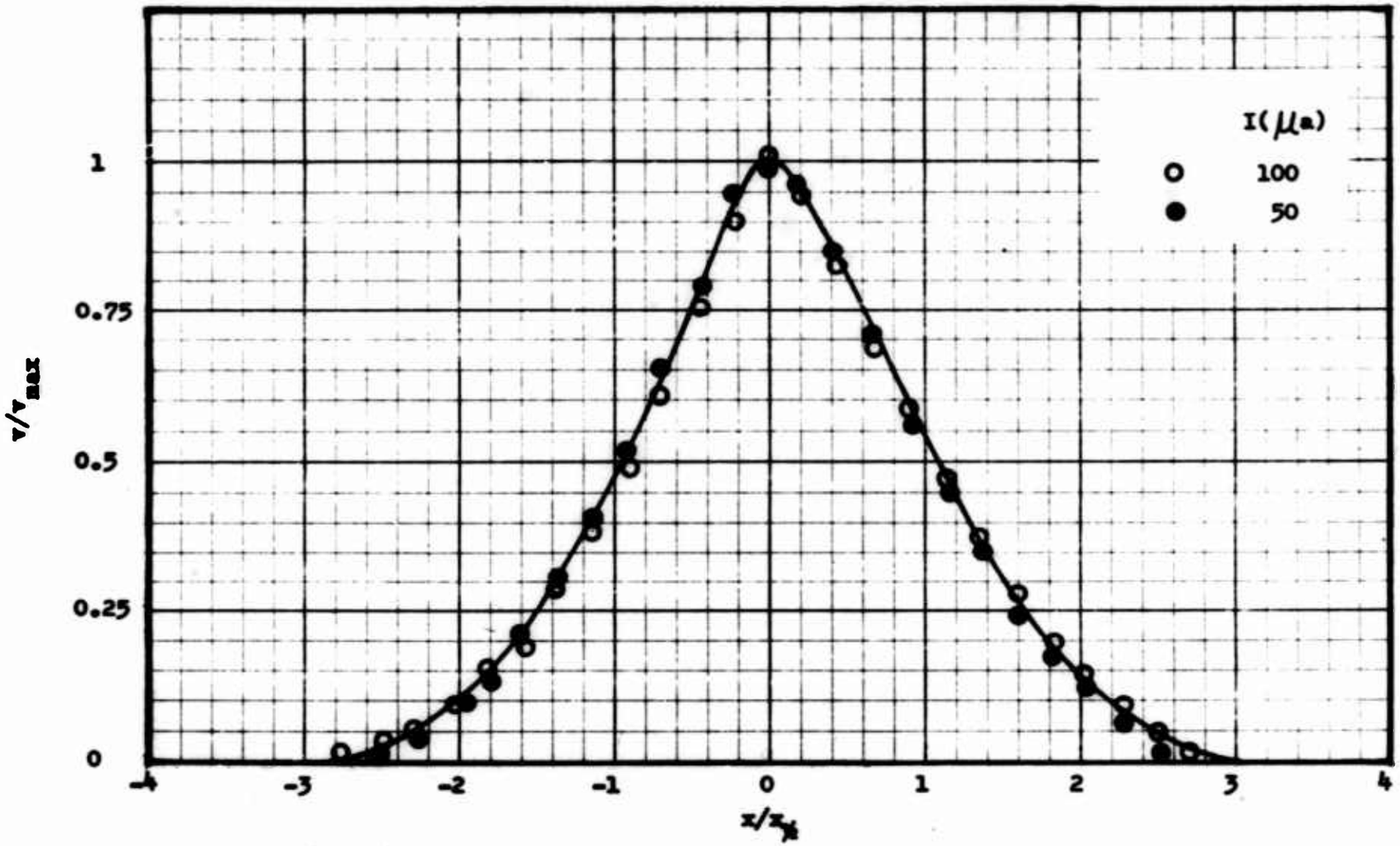

Fig. 28 Dimensionless velocity distribution of electric wind d = 1 inch

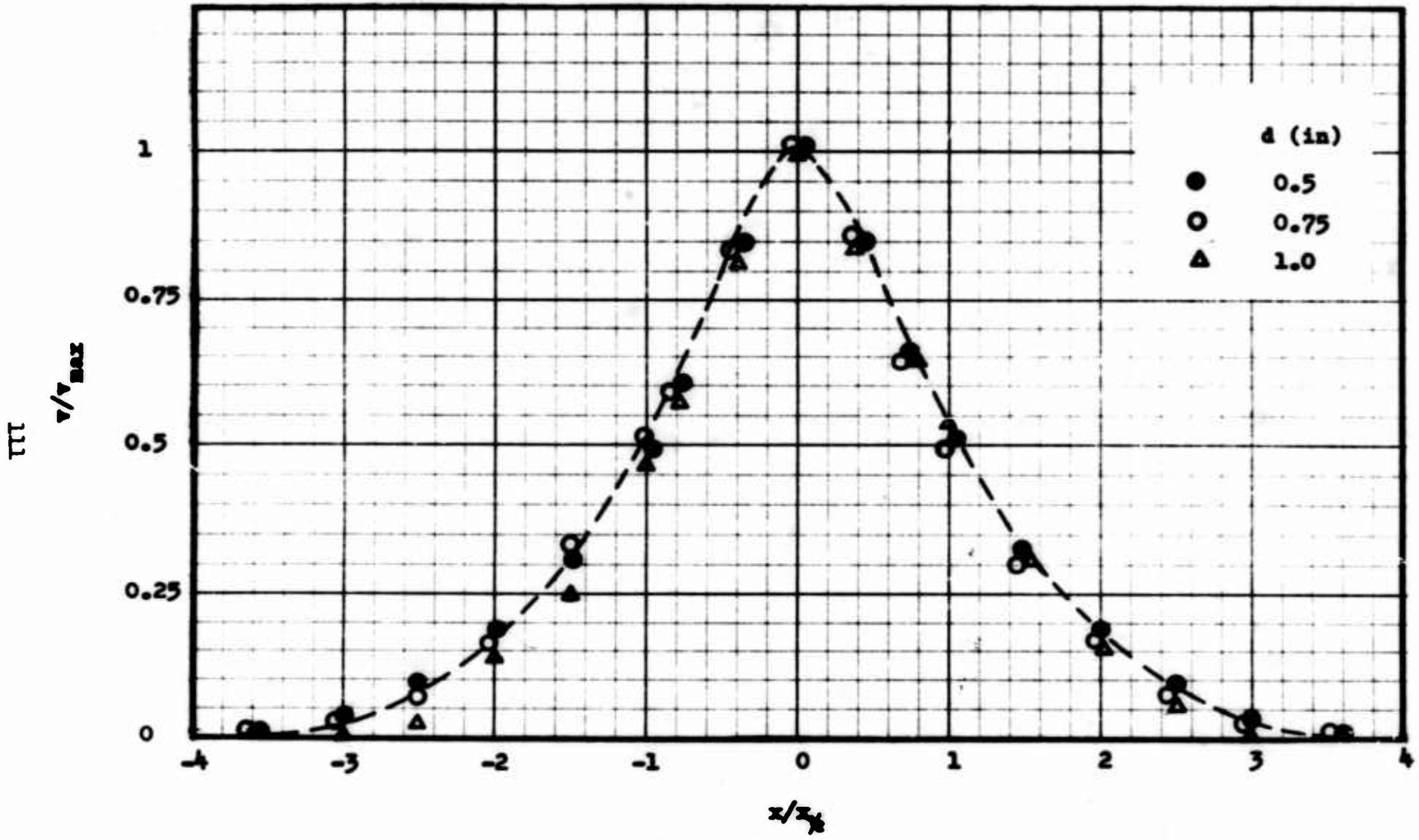

Fig. 29 Dimensionless velocity distribution of electric wind

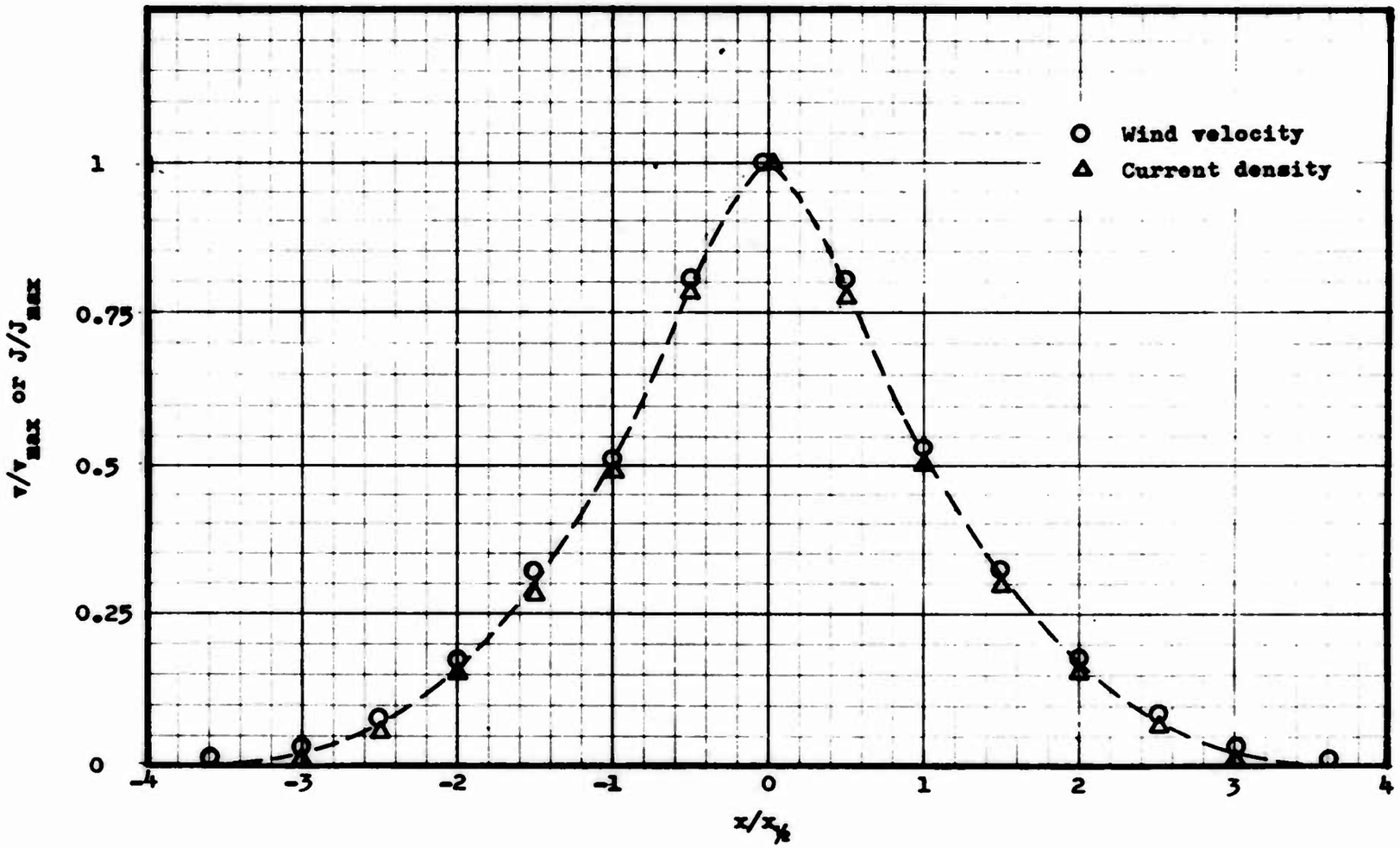

Fig. 30 Comparison between dimensionless current density & electric wind velocity distribution

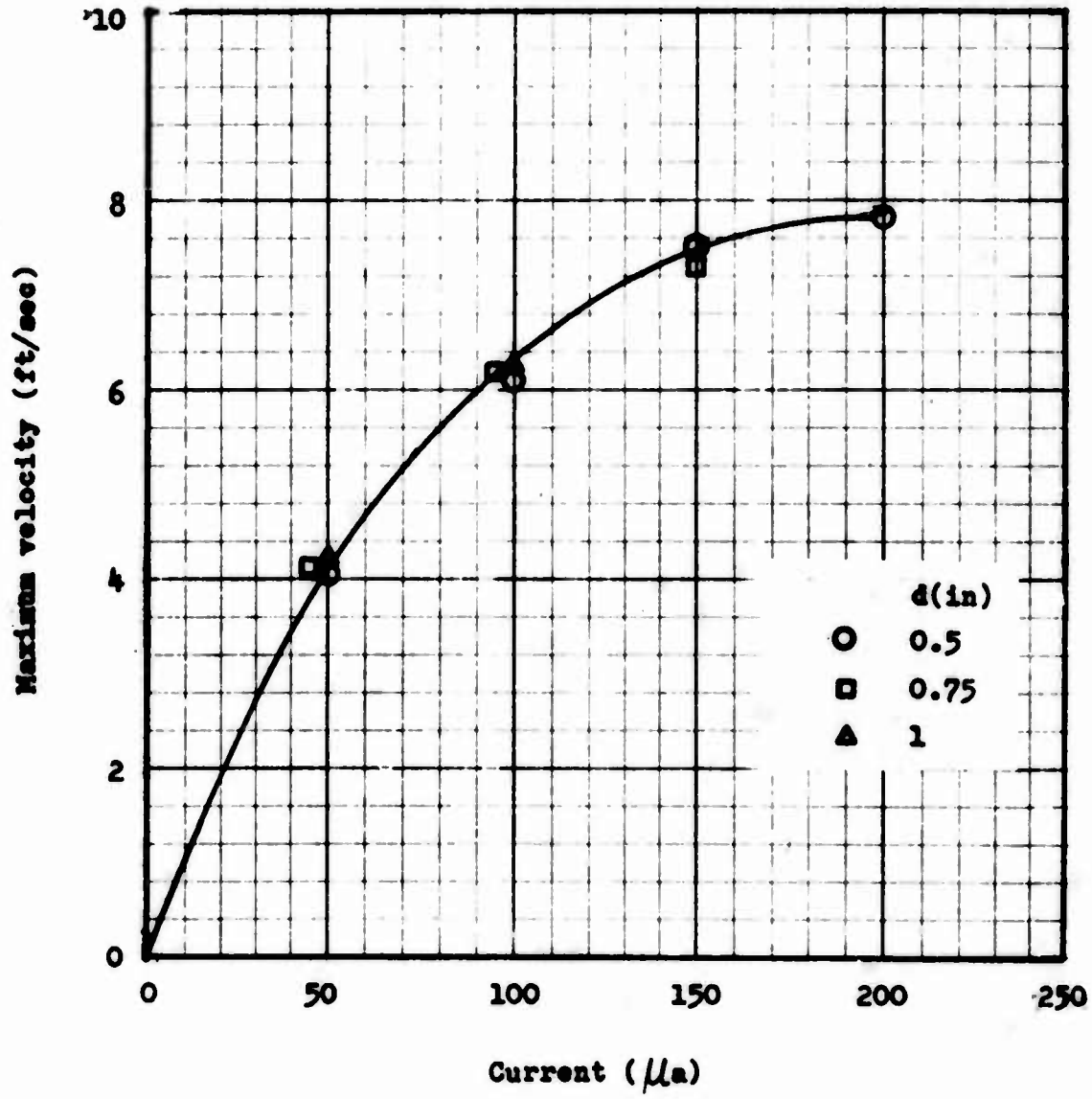

Fig. 31 Maximum velocity of electric wind vs total current

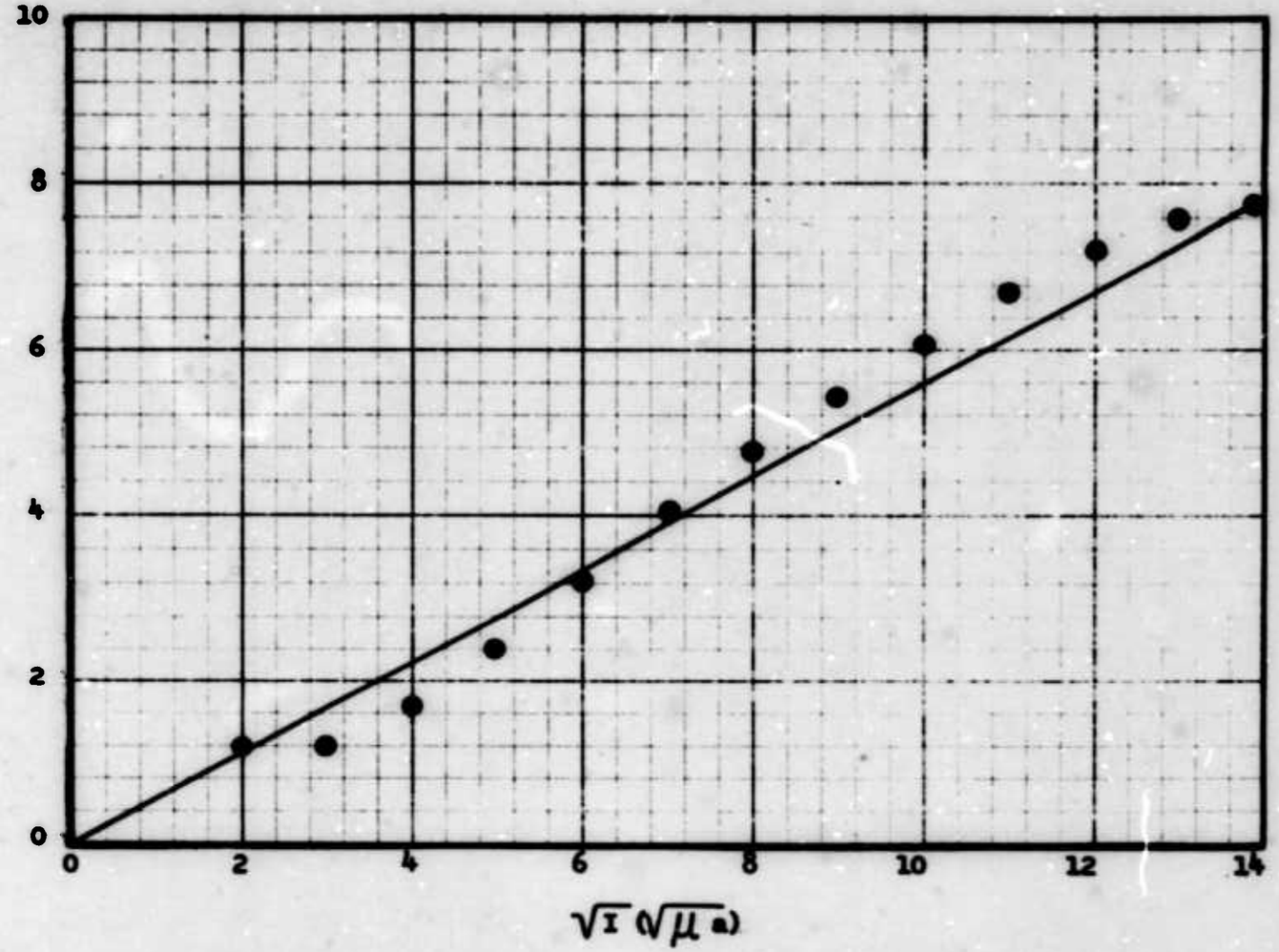

Fig. 32 Maximum velocity vs sqare root of total current

can also be obtained if the relation that the current density is proportional to the total current is used (Eq. (3.28).

6.3.3 Velocity Profiles in the Wall Jet

Figures 33 and 34 show the velocity profiles for two values of d, 0.5 and 0.75 inch respectively, and for three or four different total currents in each case. Measurements were made on the test plate without frost. The profiles represent the velocity distributions along the normal to the plate at a location 2 inches below the horizontal centerline along the vertical centerline of the plate. The corona wire was horizontal and at the horizontal centerline of the plate. The test data were evaluated under the assumption that static pressure is independent of the distance from the plate and is equal to the ambient atmospheric pressure. A justification of this assumption is evidenced if it is recalled that the current of and the velocity field produced by a wire-plane corona were confined primarily to an area approximately one inch form the centerline at which the corona wire was positioned. Outside this area the electric field and stagnation point effects on the static pressure distribution are practically negligible and the ambient pressure may be considered to impress on the flow.

An inspection of the velocity profiles, Figs. 33 and 34, indicates that the velocity increases rapidly with y from zero at the wall, reaches its maximum value at approximately y = 0.08 to 0.1 inch, and then falls gradually to null at y = 0.5 to 0.55 inch. Apparently the profiles are of wall jet type. However, it is not obvious whether they are laminar or turbulent. A Pitot tube can only meausre the mean velocity and is incapable of detecting the turbulent fluctuations. A preliminary determination of the actual flow pattern (turbulent or laminar) has to be judged from the shape of the velocity profiles. A closer examination of the foregoing profiles suggests that at higher currents (for example I = 150 μa and 200 μa for d = 0.75 inch and I = 200 μa for d = 0.5 inch) the flow is very likely turbulent. The main reasons for this prediction are that the maximum velocity appears at lower value of y as I increases and that the slope of the velocity profiles near the wall is steeper for higher current than for lower current. At low current the velocity profile may represent either laminar or more likely transition flow. When the flow is turbulent or laminar, similarity exists and the velocity profiles should have the same shape when plotted non-dimensionally. On the other hand, if the data were measured in transition region between stagnation and fully developed wall jet flows, no such similarity is expected.

Figures 35 and 36 are the dimensionless profiles plotted from Figs. 33 and 34 respectively. The velocity was normalized by $y_{½}$, the y-value at which $u = \frac{1}{2}u_{max}$. From an inspection of these two figures it is seen that in the major portion of the outer layer there is similarity of the various profiles, with the exception at the outer edge of the flow. However, in the inner layer, the profiles are non-similar, which

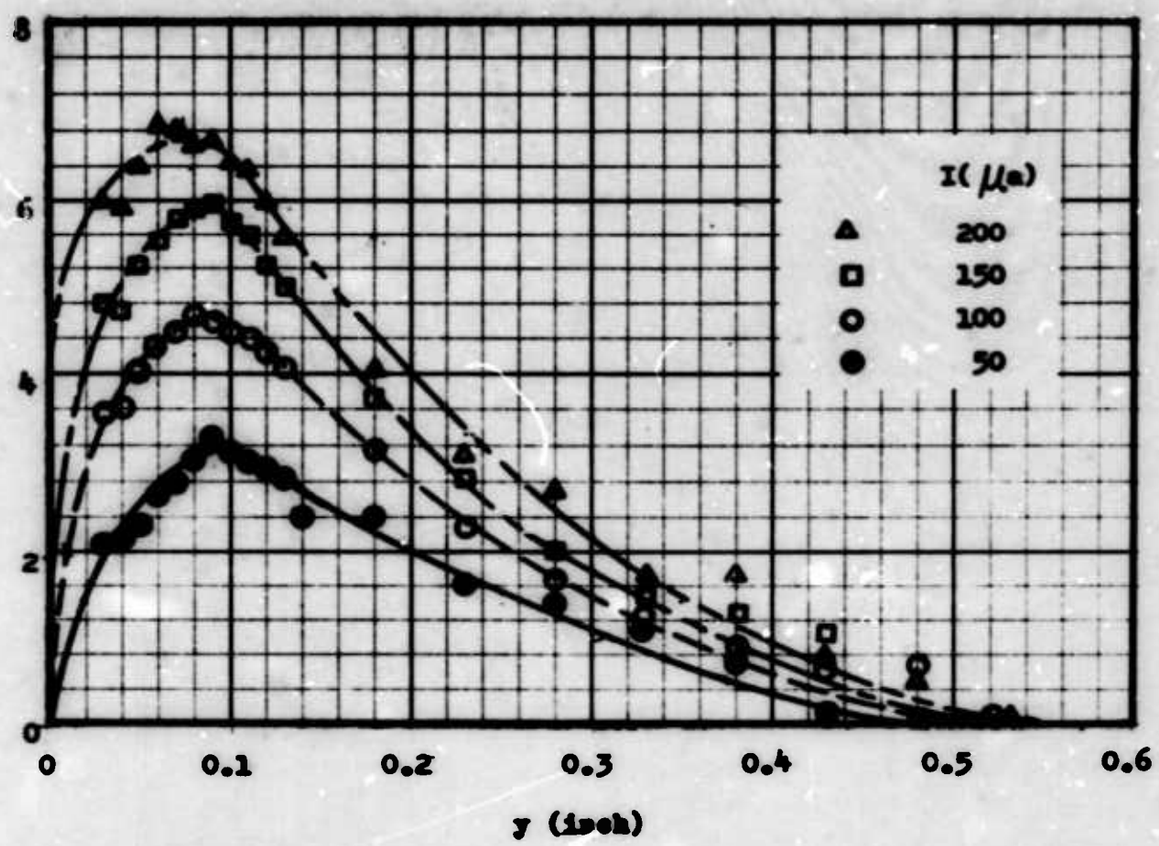

Fig. 33 Velocity profile of wall jet, d = 0.5 inch

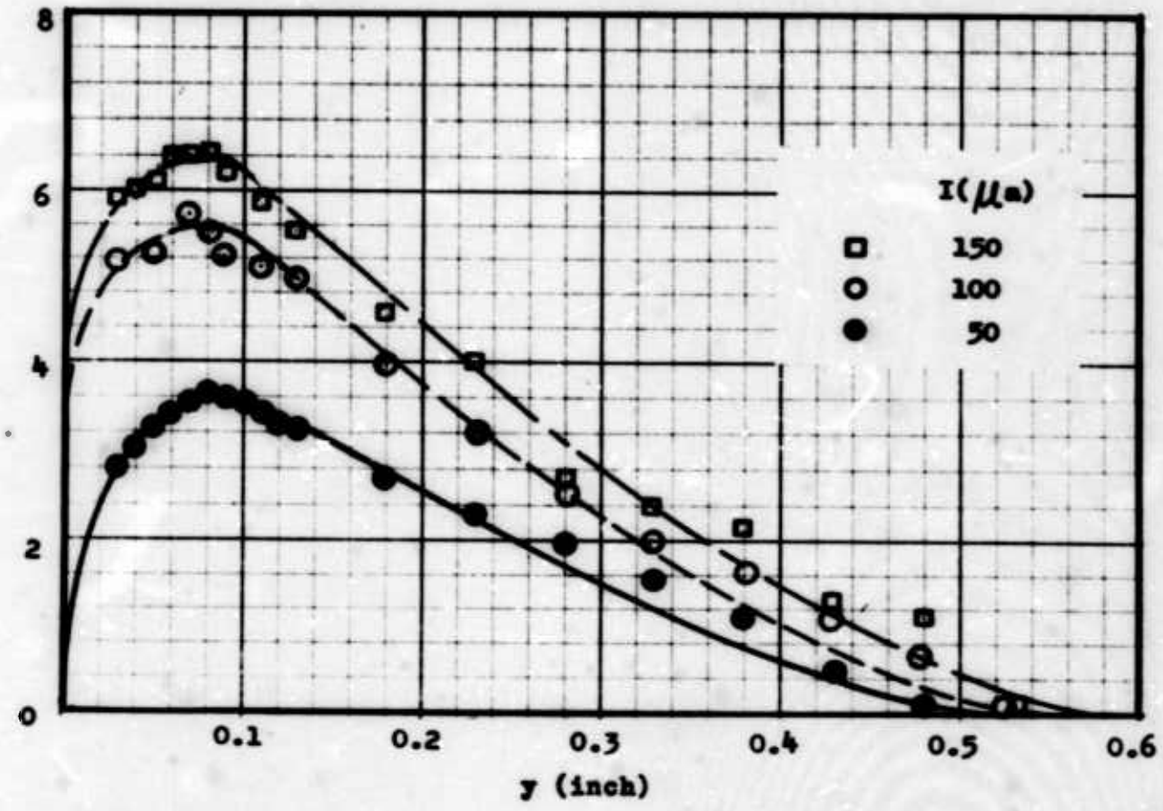

Fig. 34 Velocity profile of wall jet, d = 0.75 inch

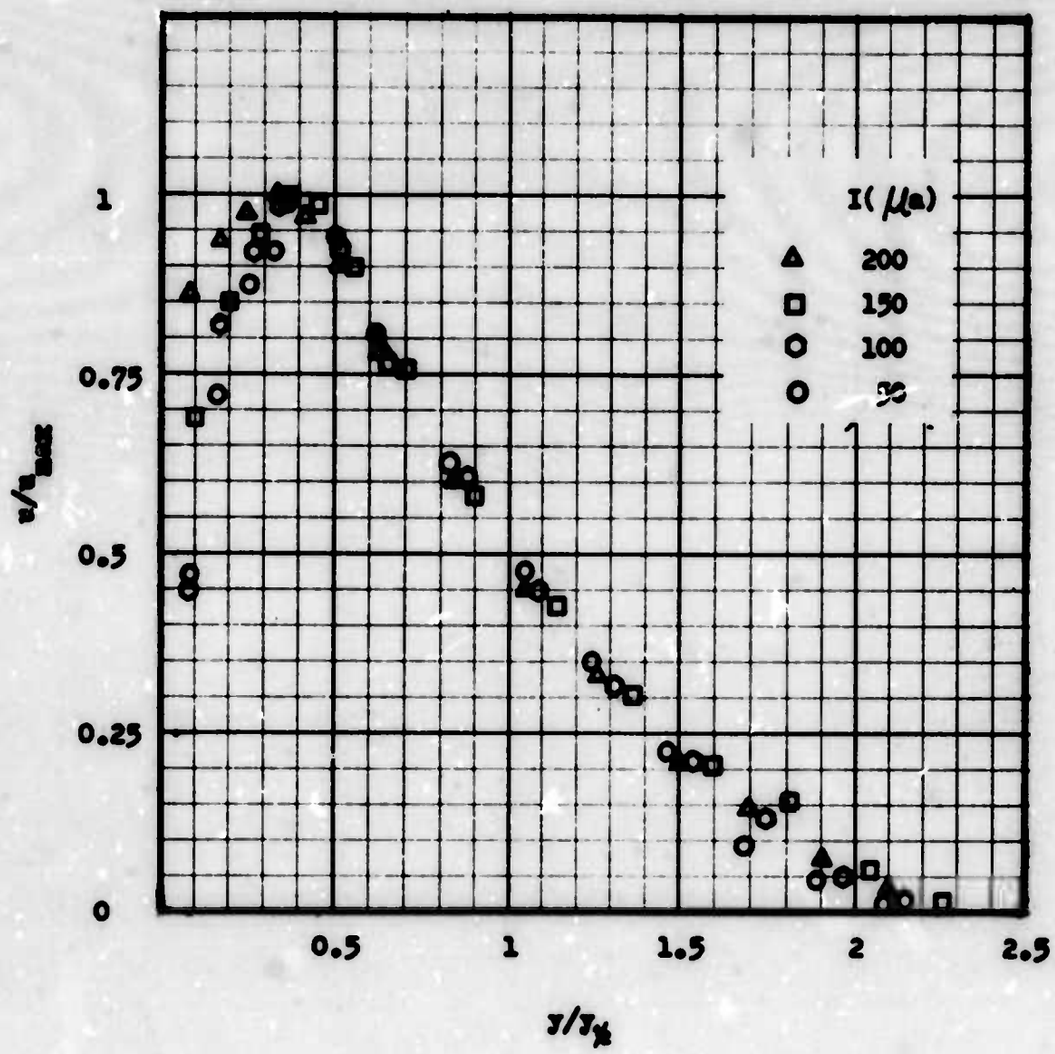

Fig. 35 Dimensionless velocity profile of wall jet, d = 0.5"

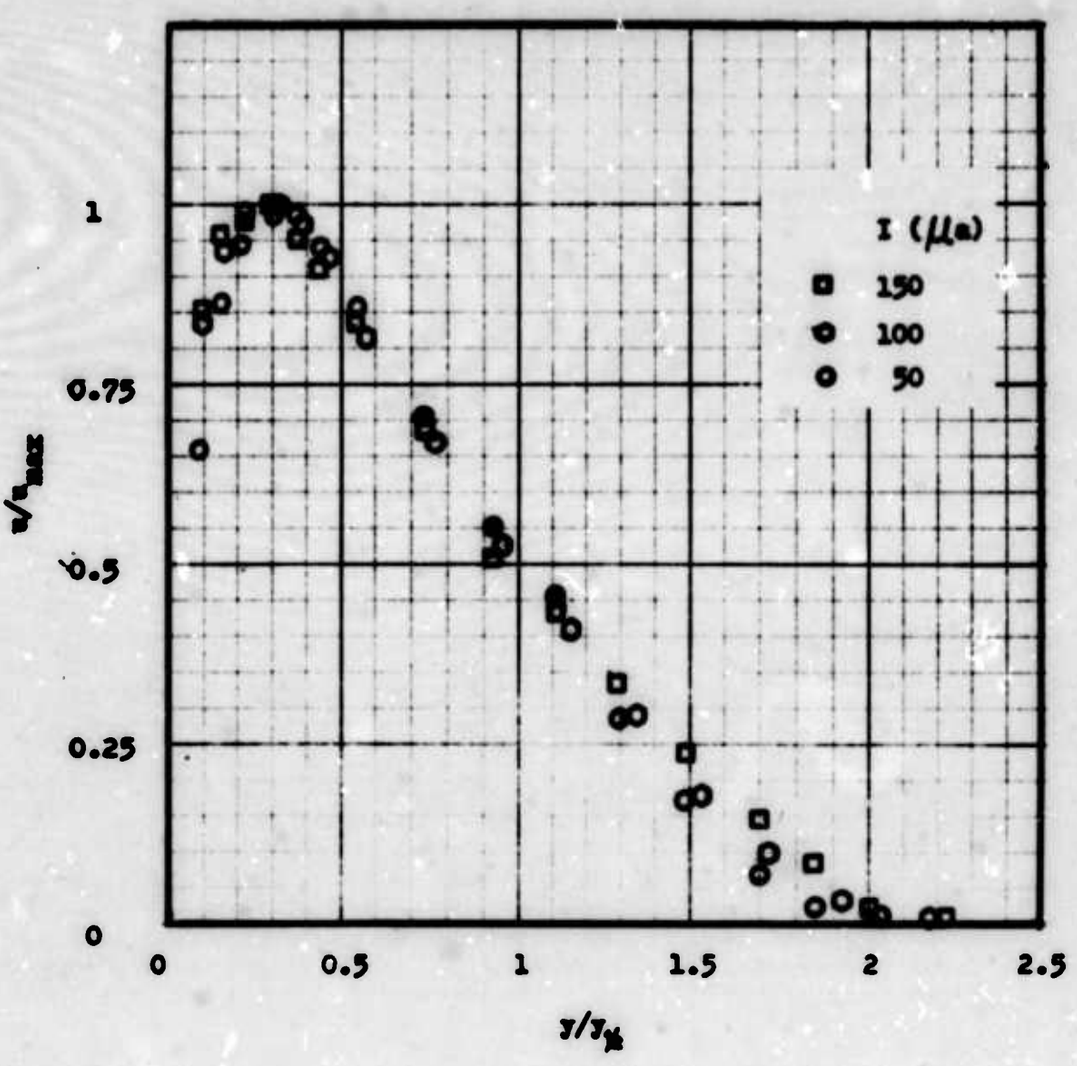

Fig. 36 Dimensionless velocity profile of wall jet, d = 0.75"

may be a manifestation of different flow patterns or caused by the decreasing accuracy of the measurements near the wall (a discussion on the measurements near the wall can be found in Dean[41]). Figure 37 is a plot of the following three profiles: I = 150 μa, d = 0.75 inch; I = 100 μa, d = 0.75 inch; I = 200 μa, d = 0.5 inch. For comparison the theoretical velocity profiles for laminar (Eq. (5.19)) and turbulent[27] wall jets are also shown in Fig. 37. As is evident from this figure, the three measured profiles agree satisfactorily with the theoretical turbulent profile. Further comparison between the low current profiles and the theoretical profiles indicates that the measured data are more in agreement with the theoretical turbulent profile. It thus appears that for higher current the flow at two inches from the centerline is of the turbulent wall jet form, whereas at lower current the same location may fall between the regions of transition flow and of turbulent wall jet and the flow in nearly turbulent.

6.3.4 Heat Transfer Data

A general trend is exhibited by the total heat transfer rate versus time data given in Figs. 38 to 40, which were obtained using as emitter a horizontal single wire at the plate centerline. The total heat transfer rate is seen to decrease with time, but has the tendency of approaching a constant value as to increases further. Similar observations have been reported by others in relation to frost formation under different circumstances. Sugawara et al[38], in examining the frosting process over a flat plate under forced convection conditions, demonstrated that the total heat transfer rate decreased with time and reached quasi-steady state in 60 to 80 minutes. In a study of frost formation on a cylinder surface in a humid air cross flow, Chung and Algren[18] also observed that the heat transfer became quasi-steady in 60 to 100 minutes. Similar trend was also noted by Whitehurst[40] when frost grew on a vertical plate under free convection conditions, but no indication was given as to the time when the heat transfer essentially became quasi-steady. Because each test run lasted only 30 minutes in the present investigation, it is difficult to estimate how long it actually takes for the heat transfer process to reach quasi-steady state. In view of the above mentioned evidences, it may generally be concluded that the impingement of an electric wind does not change the characteristics of the total heat transfer rate versus time relation in connection with frost formation.

It may be noted that a similar trend is also indicated by the analysis developed in Chapter II. If Eq. (2.44) is evaluated at y = 0, the relation between q and t (considering absolute value of q) can be written

$$q = a_0 - a_1 t + a_2 t^2 - \cdots$$

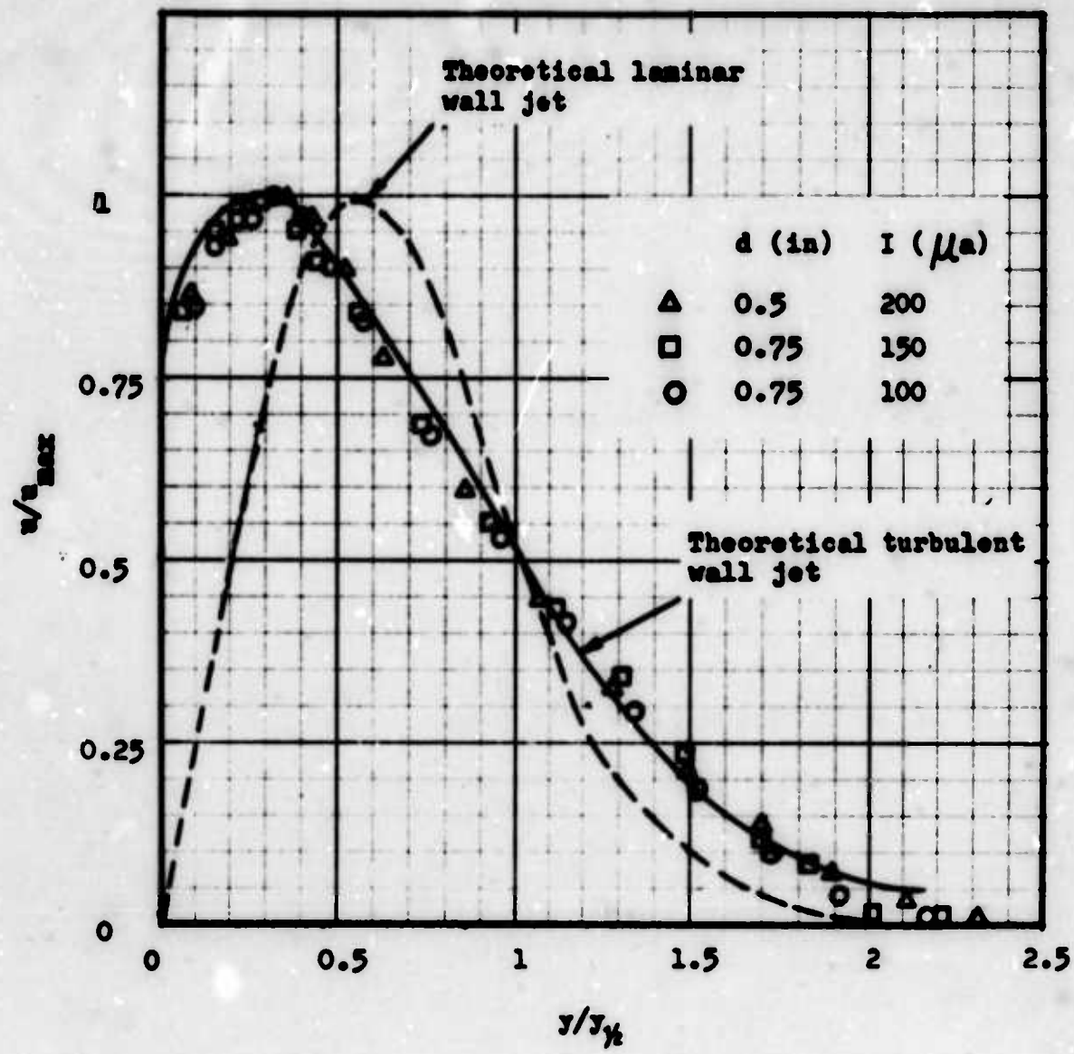

Fig. 37 Dimensionless velocity profile of wall jet

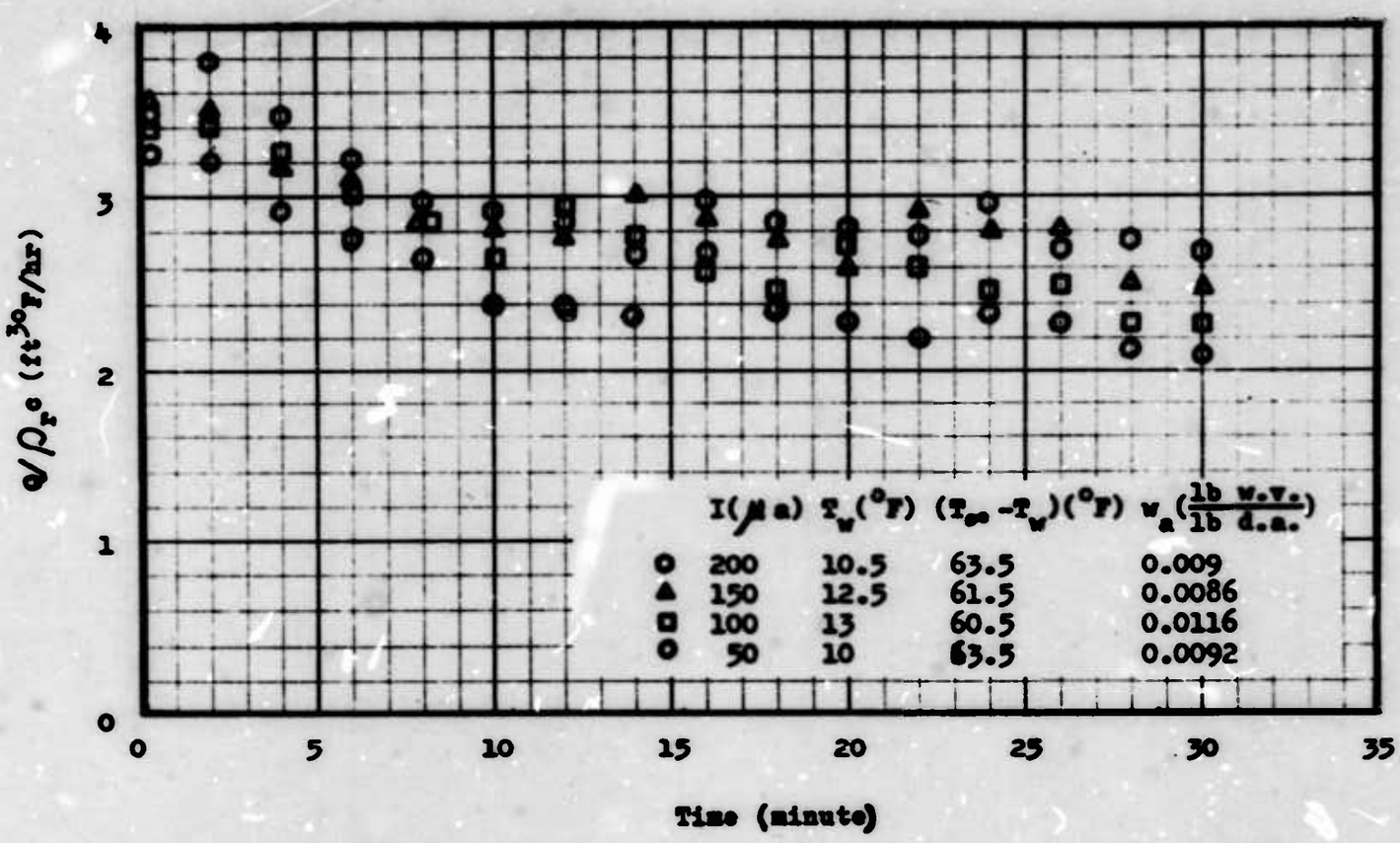

Fig. 38 Total heat transfer rate versus time, d = 0.5"

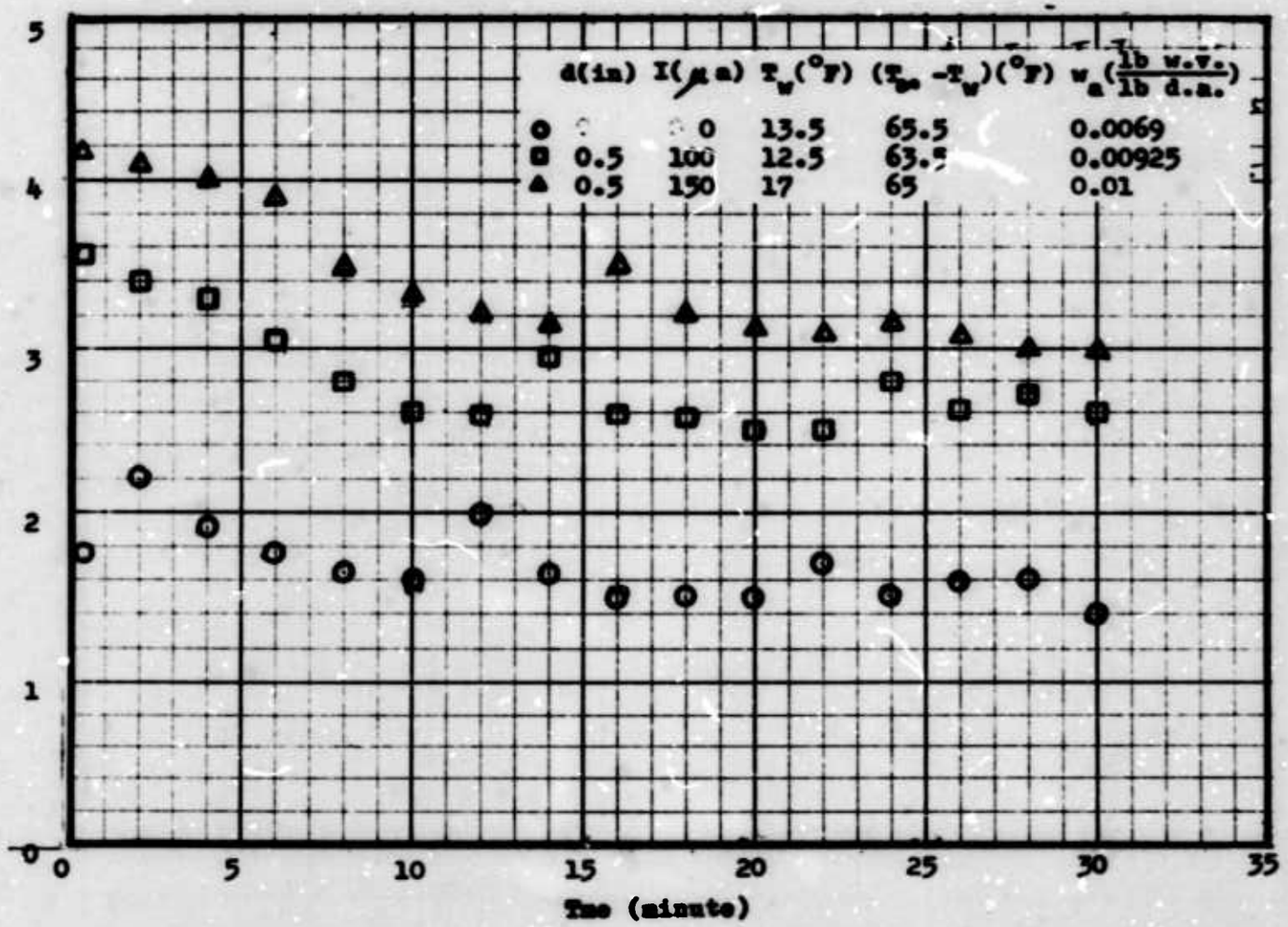

Fig. 39 Total heat transfer rate versus time

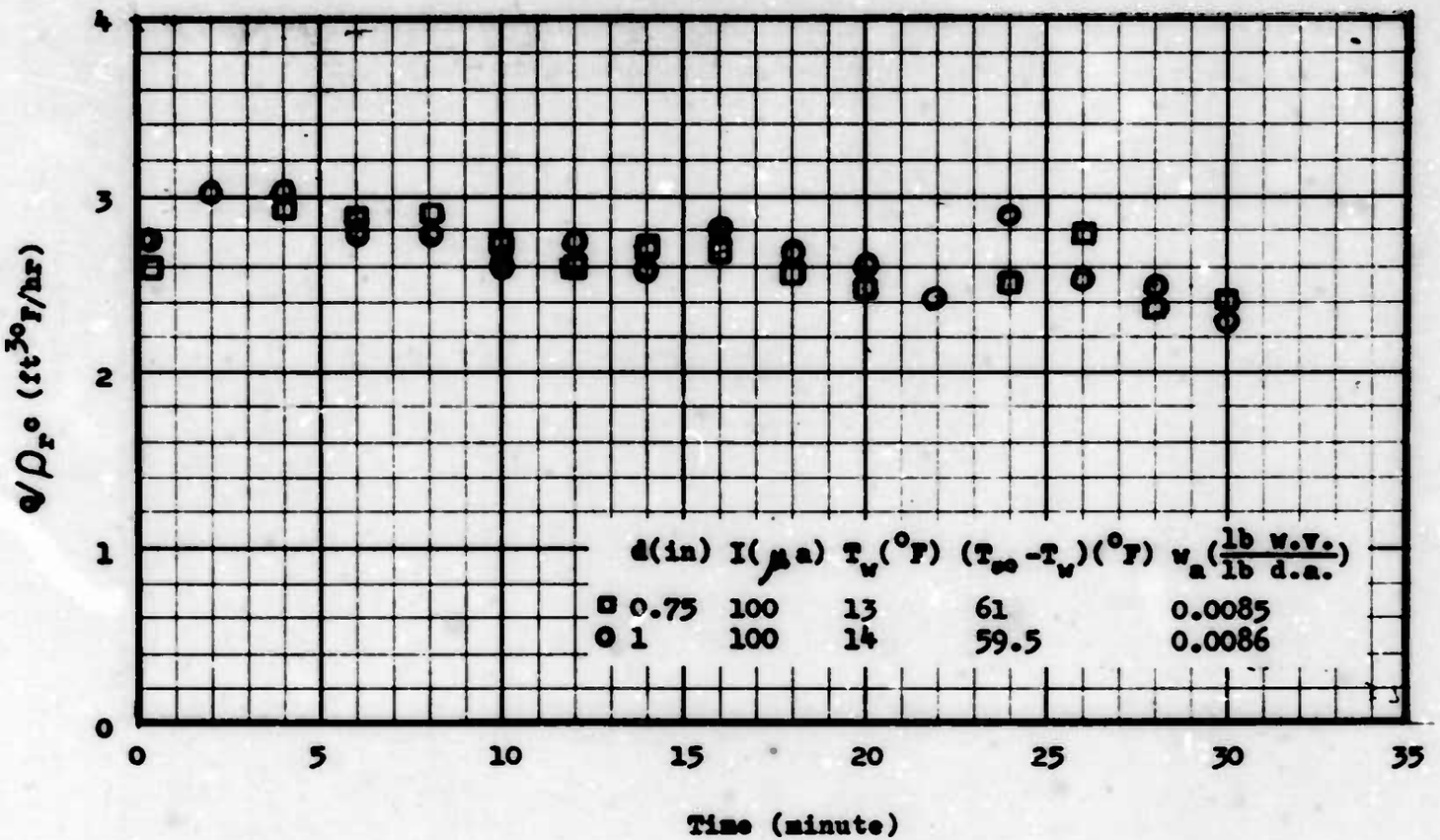

Fig. 40 Total heat transfer rate versus time

where a_0, and a_1 and a_2 are positive coefficients. Because of the nature of the solution, the series on the right-hand side is uniformly convergent. When t is small q decreases almost linearly with t, as t increases the rate of change of q decreases. As t tends to infinity, q approaches a constant value. This qualitative description is in agreement with the experimental results.

Figure 38, shows the data obtained for four different currents but constant d. Although an inspection of the data indicates that increase in current results in higher heat transfer, the effects is not significant. Another set of data given in Fig. 39 shows a considerable enhancement of heat transfer by the field. With free convection conditions (no filed) as reference state, an increase of 100% in total heat transfer rate is obtained at I = 150 μa. The increase in heat transfer at I = 150 μa over the case where I = 100 μa is about 20%, a much more significant increase than indicated by Fig. 38. While it is uncertain what actually caused the difference between the two sets of data, the facts that the test conditions differ from one test run to another and that the theoretical considerations indicate (Chapter VII) the heat transfer process is less sensitive to the variations in total current as compared to the mass transfer process may have contributed to this difference.

Figure 40 is a plot which illustrates the data for two different values of d but the same current. As is obviously seen, no difference can be noted. It appears that the entrainment as d increases is so small that it can not produce noticeable influence on heat transfer. More data are necessary before further comments can be made in this respect.

In each test run, readings were taken as soon as the field was turned on. The response of the inlet and outlet refrigerant temperature difference to the sudden increase of convection heat transfer did not take place instaneously. It usually took a couple of minutes for the refrigerant passing through the copper tubing at the back of the plate to reach a steady temperature. This adjustment on the part of the refrigerant is apparent in the figures. The first data point in each run is seen to fall below the tentative position as extrapolated from the rest of data. In the course of each test run, the refrigerant flow rate was increased a couple of times through the adjustment of the controlling valve in order to maintain as constant a plate temperature as possible. Each time the adjustment was made, it took a few minutes for the refrigerant to achieve a new equilibrium condition. Since the variation in time of the heat transfer rate is not drastic, nearly the same amount of heat was transfered to the refrigerant per unit time in the period of adjustment. Hence at lower flow rate the temperature increment in the refrigerant should be greater than at higher flow rate. If readings of the temperature increment were taken before new equilibrium state has been achieved, the data so obtained would overestimate the heat transfer. This is exactly what happens in the figures.

As noted in Section 6.2.2, the current was observed to increase as frost grew on the test plate. Figure 41 shows some typical variations of the current time. In the course of each test run, the voltage was found to remain approximately constant. Therefore, it is possible that the frost may act somewhat like a conductor. As the frost thickness increases, the distance between the wire and the effective plane electrode is shortened, resulting in higher current.

6.3.5 Mass Transfer Data

The results of mass transfer measurement are shown in Fig. 42 through 48, in which the total frost accumulated in a period of five minutes is plotted against the current. In all the figures the point corresponding to zero current represents mass transfer under free convection conditions. With the exception of Fig. 48, the data were obtained using a single wire electrode. The wire was horizontal and at the centerline of the plate, the centerline being parallel to the 9-inch edges of the plate. The test conditions for each curve are specified by the test plate temperature T_w, the specific humidity w_a and temperature T_∞ of the ambient air, and the distance d of the wire from the plate. A needle point was used as discharge electrode in obtaining Fig. 48.

Owing to the limited capacity of the test setup, only three or four data points were obtained for each curve. As a result the accuracy of the curves plotted on the basis of the scare data points available is difficult to estimate. Despite this disadvantage, the figures do provide a general qualitative information on the influence of electric wind upon frost formation. The figures unanimously indicate that the frost deposition can be considerably enhanced through the use of the corona discharge. An increase of over 200% can be achieved with a corona current of the order of 100 μa. A further inspection of the curves shows that the rate of increase of the frost deposition decreases with current, indicative of the fact that the mass transfer will asymptotically approach a miximum value as the current tends to infinity. A physically more reasonable statement of this is that beyond certain value of the current no further appreciable increase in mass transfer may be expected. The similarity in shape of the curves for wire-plane and point-plane coronas suggests that the same conclusions also hold true for point-plane corona, an evidence of the existence of similarity between the axially symmetric and two-dimensional flow fields created by point-plane and wire-plane coronas repectively.

In Figs. 49 and 50 respectively are plotted together Figs. 42 to 44 and 45 to 47 by shifting the ordinate, when necessary, such that the points at zero current coincide. It is seen in these figures that the data for different values of d can be fitted approximately by a single curve.

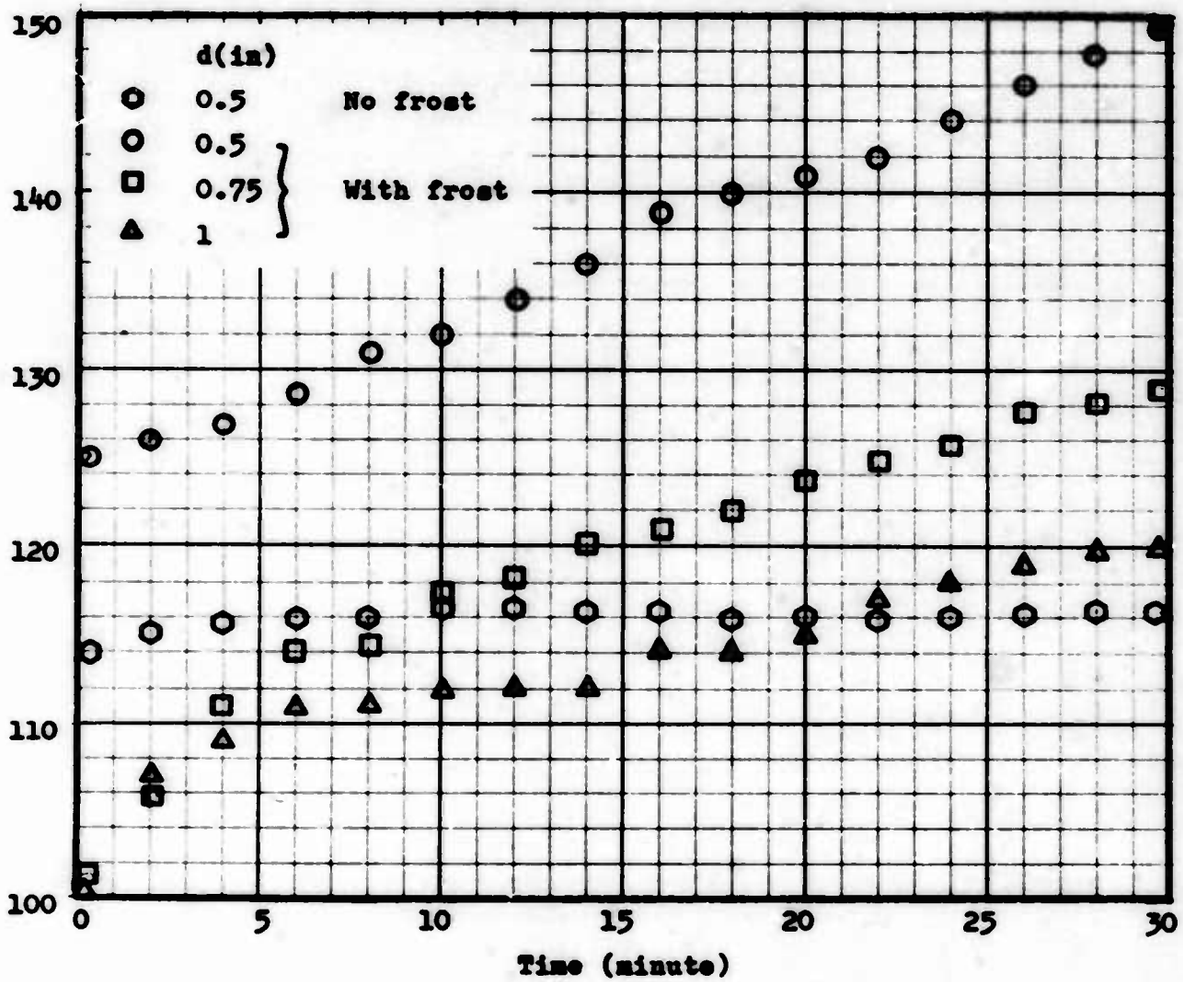

Fig. 41 Variation in time of total current as frost grows

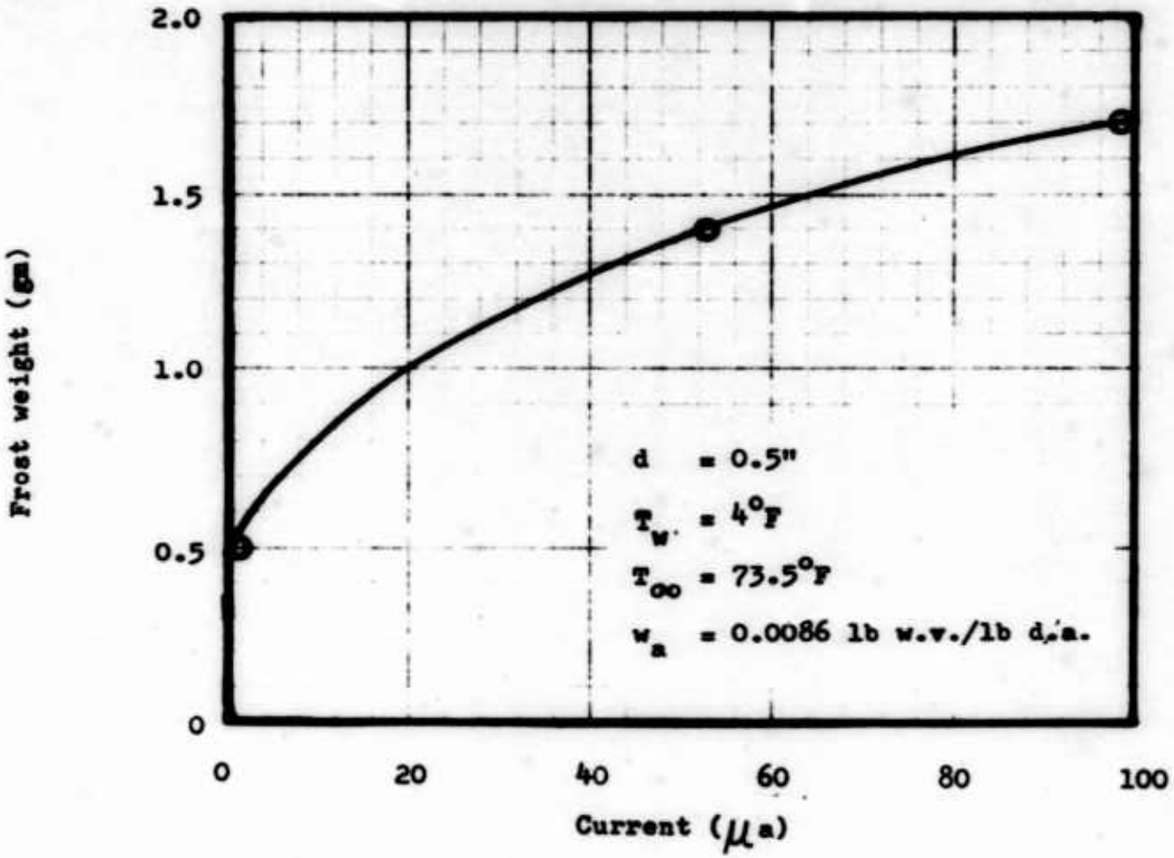

Fig. 42 Total frost weight vs current for a period of 5 minutes---wire corona

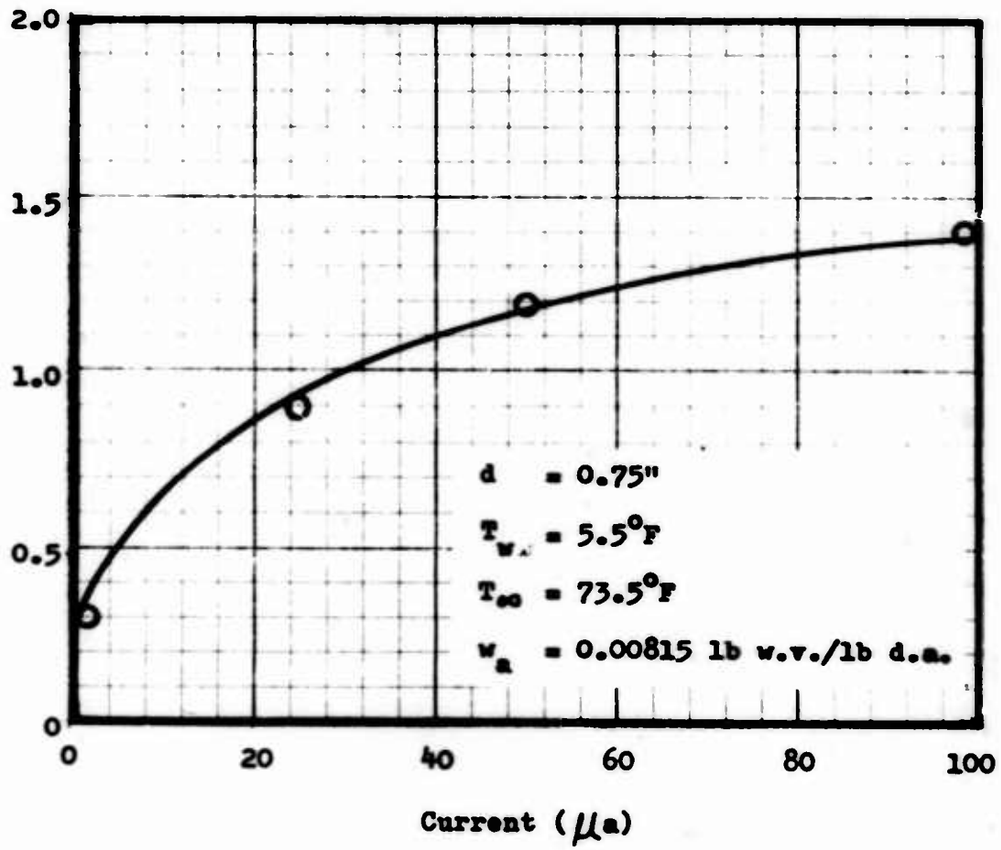

Fig. 43 Total frost weight vs current for a period of 5 minutes---wire corona

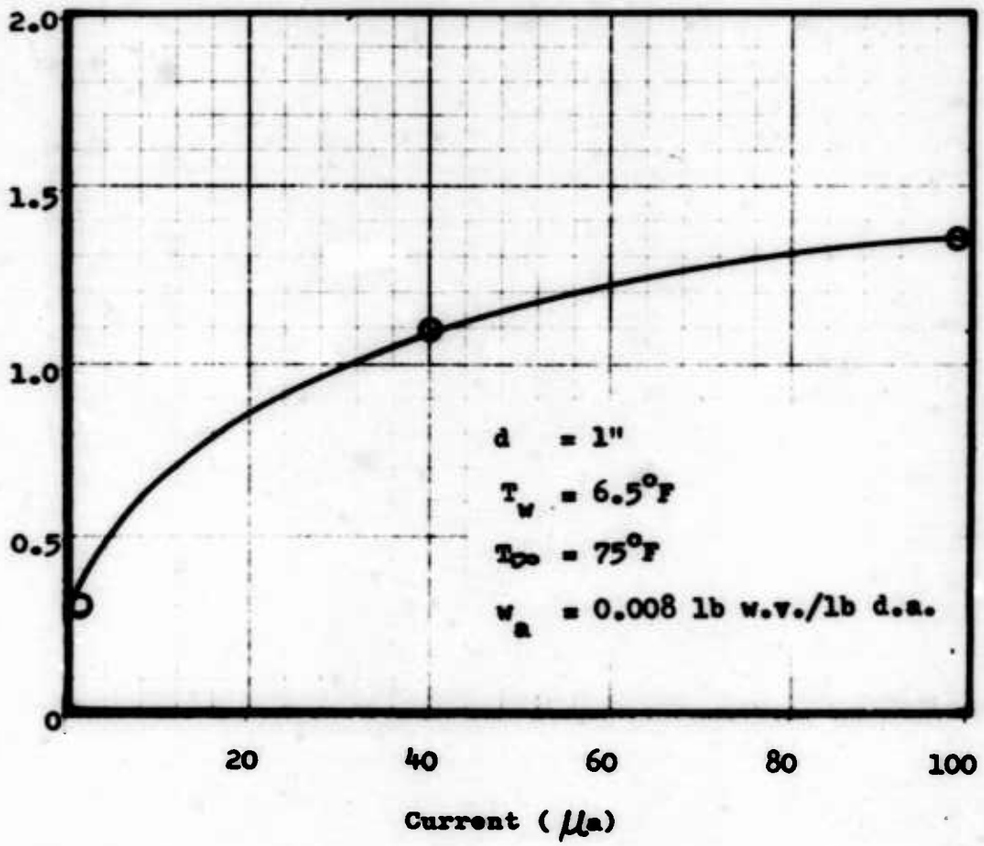

Fig. 44 Total frost weight vs current for a period of 5 minutes---wire corona

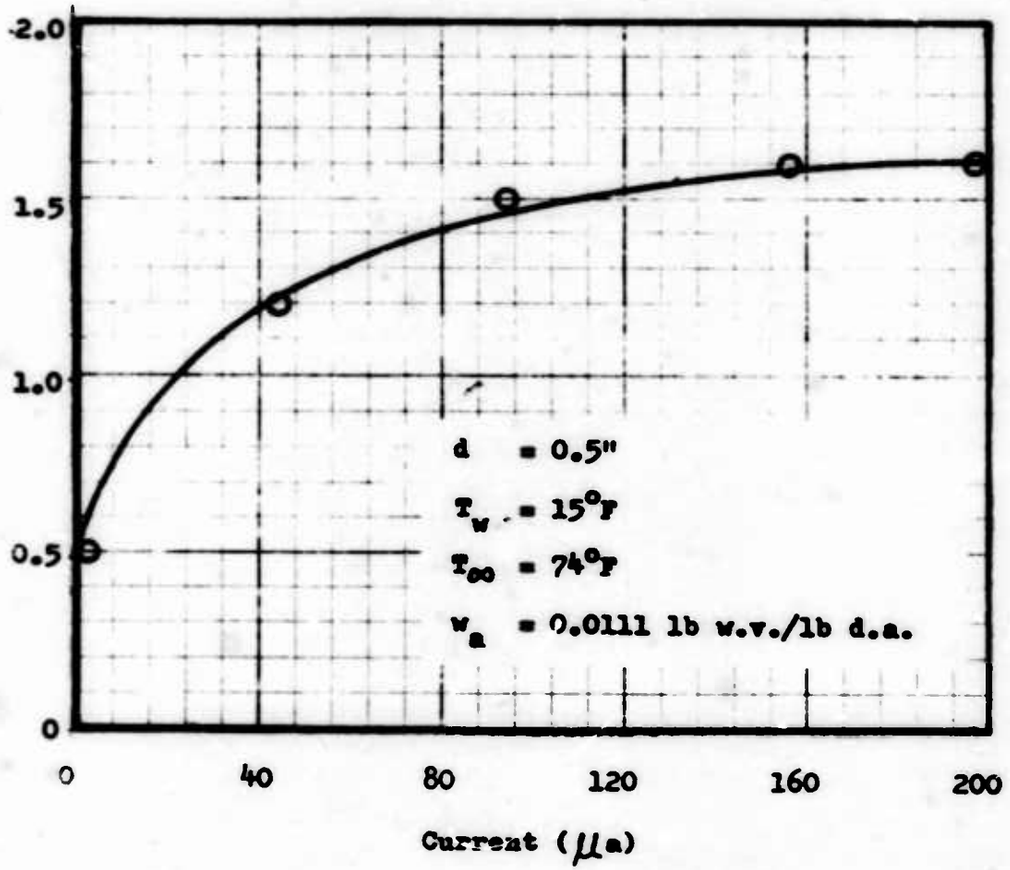

Fig. 45 Total frost weight vs current for a period of 5 minutes---wire corona

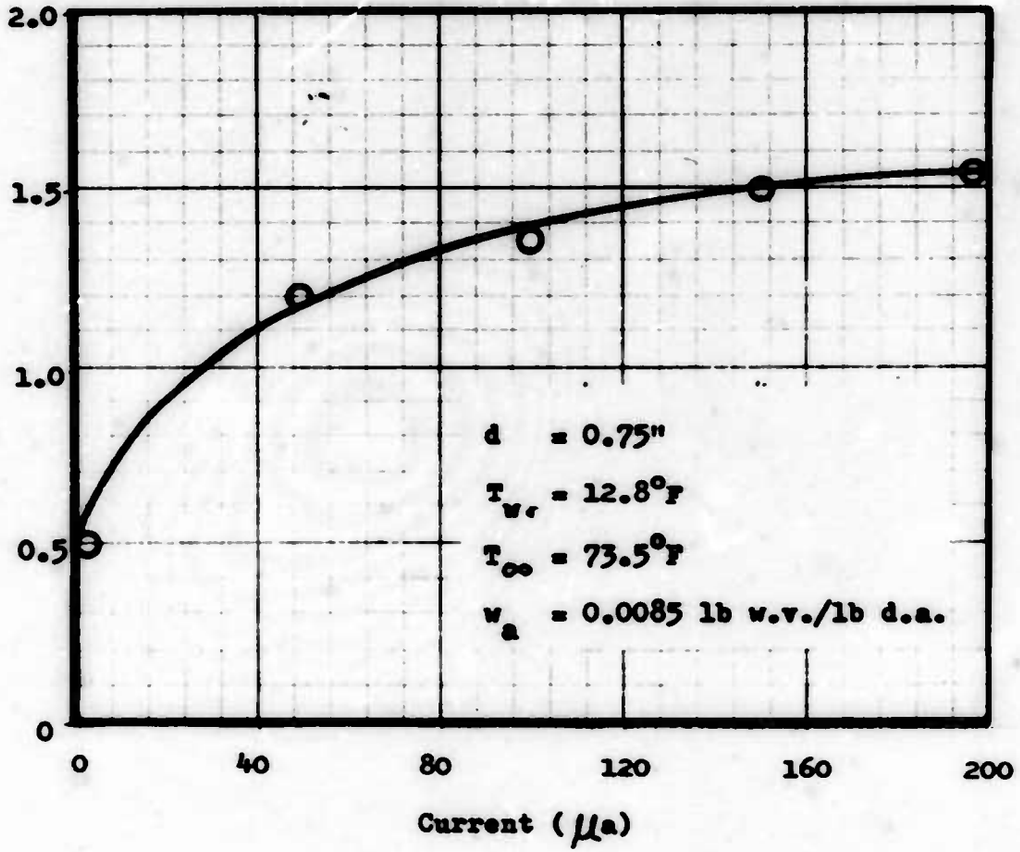

Fig. 46 Total frost weight vs current for a period of 5 minutes---wire corona

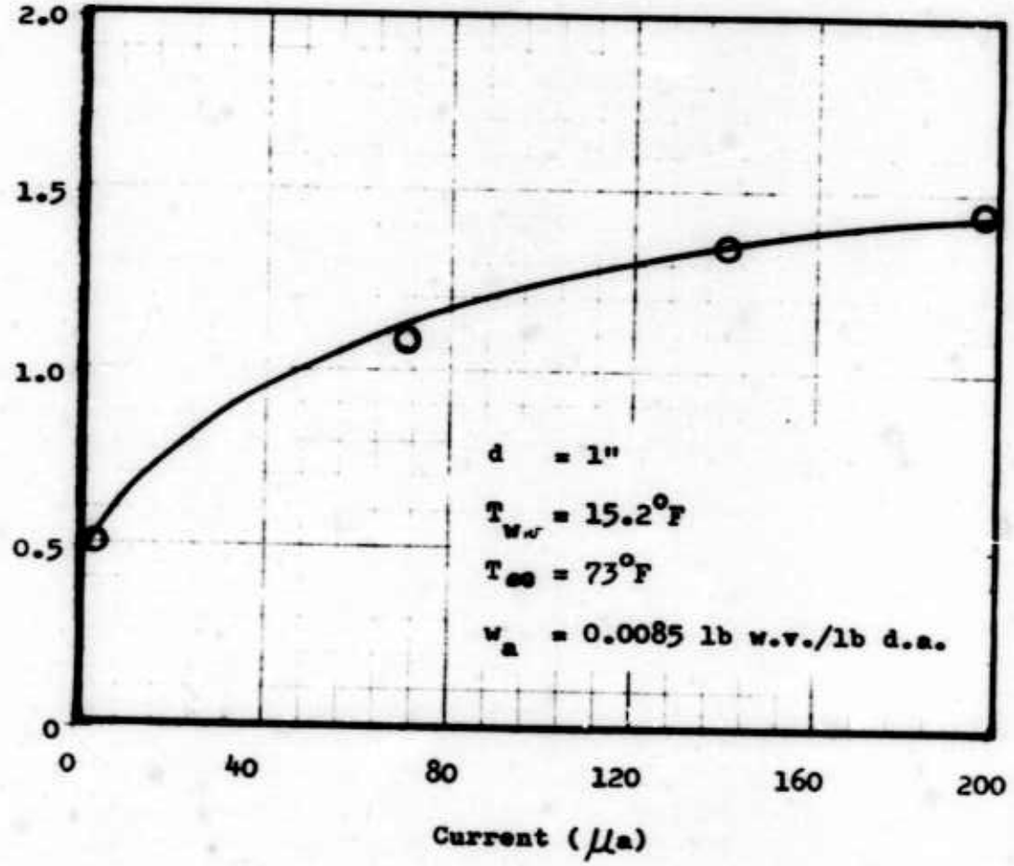

Fig. 47 Total frost weight vs current for a period of 5 minutes---wire corona

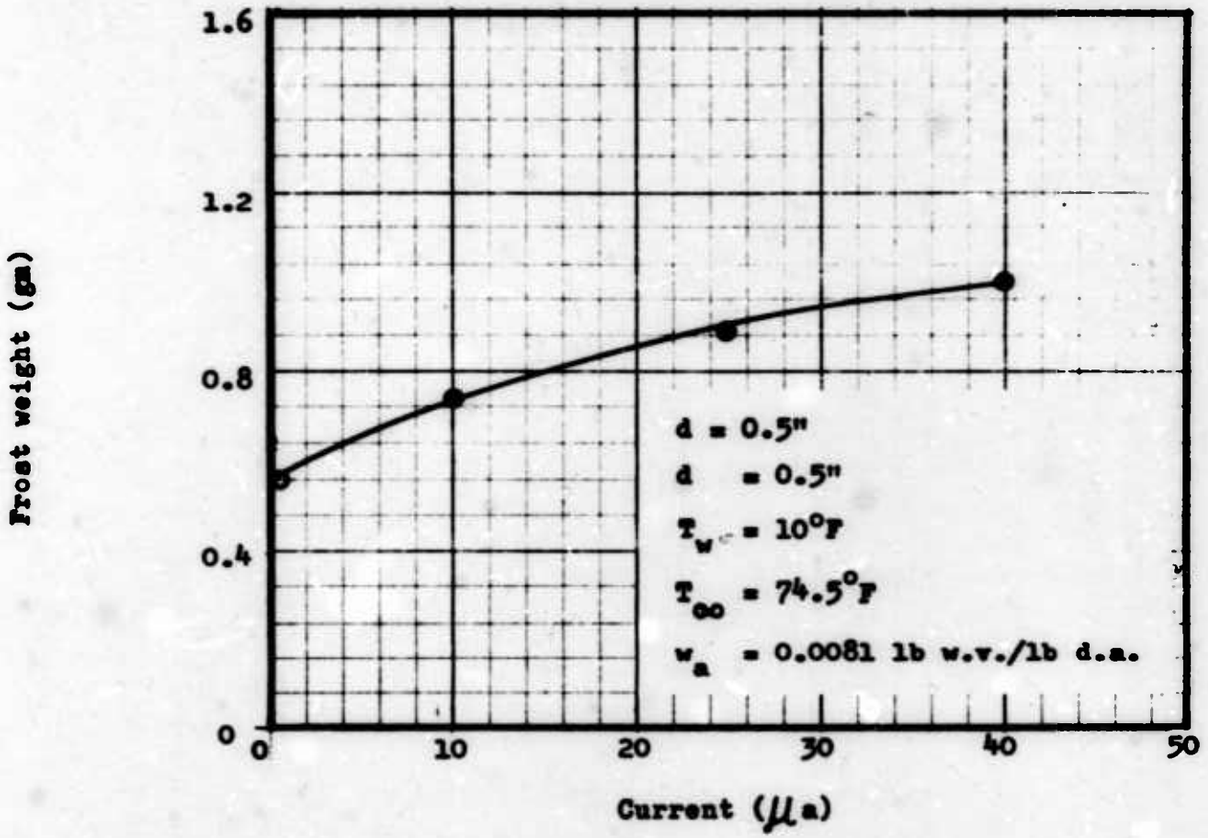

Fig. 48 Total frost weight vs current for a period of 5 minutes---point corona

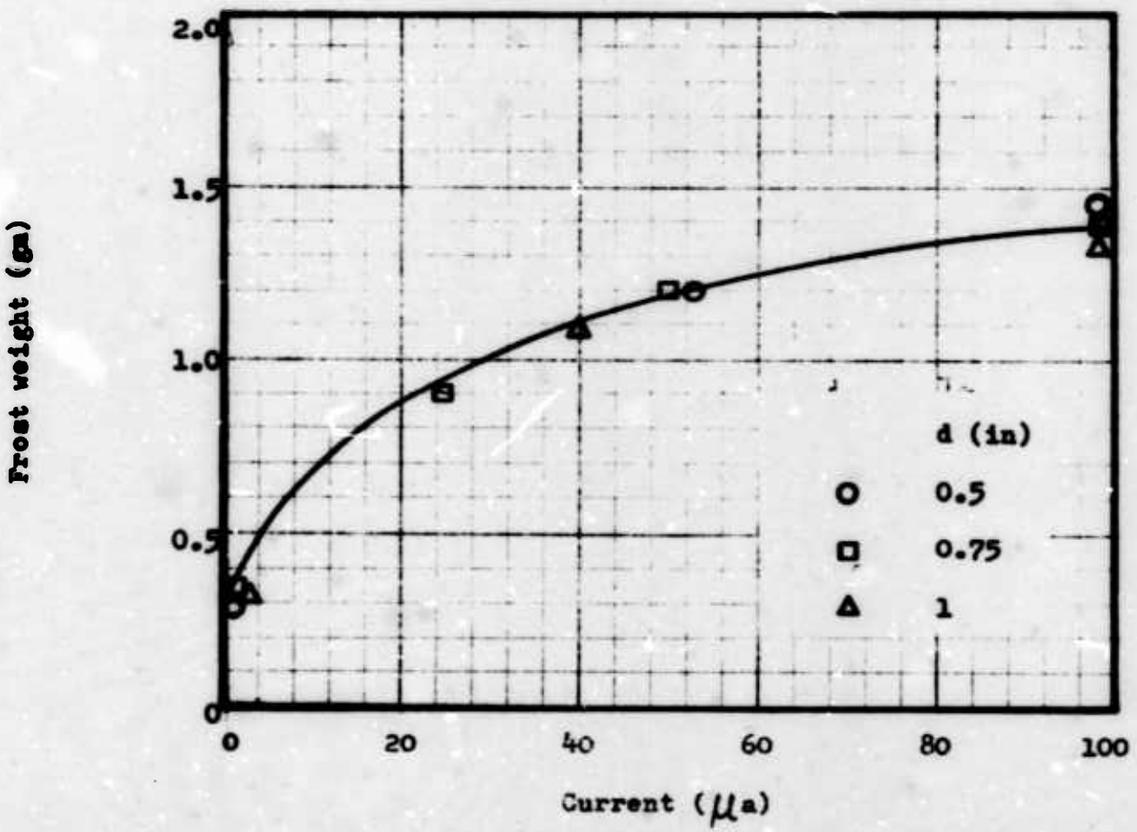

Fig. 49 Total frost weight vs current

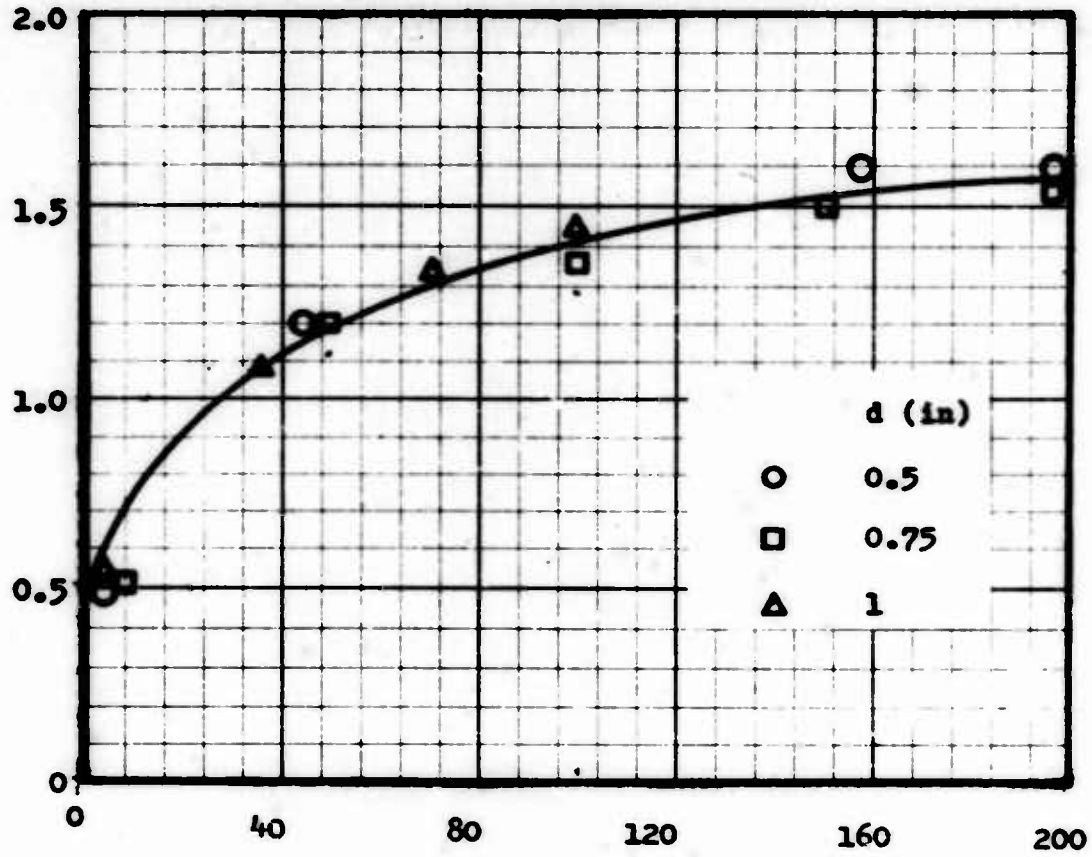

Fig. 50 Total frost weight-current

In Section 1.2 the increase of frost formation under the action of corona discharges has been attributed to the impingement of the electric wind and the total mass transfer. For convenience, let the velocity v_{max} at the location of the stagnation point, in the absence of a solid plane be taken as the characteristic velocity of the electric wind. A comparison between Figs. 31 and 50 sho s that the total current I has quite similar effects on v and the total mass transfer, thus substantiating the existence of a possible relation between the latter two quantities. The complexity of the flow field of an impinging electric wind seems to suggest that such a relation is not a simple one. That this is the case is further indicated in Fig. 51, which plots the total mass transfer versus v_{max} on the basis of Figs. 31 and 50.

An explanation of the behavioral characteristics of the total mass transfer data curves in terms of I goes as follows. At zero current, there is no electric wind and the mass transfer process is of free convection form in nature. When I differ from zero, an induced electric wind changes the transport mechanism from free to forced convection, resulting in escalation of the frost accumulation. Since the total mass transfer increases with v_{max} (Fig. 51) and v_{max} increases with I (Fig. 31), it follows that the total mass transfer increases with I. It has been shown previously that Fig. 31 can be approximated by Eq. (6.1). A differentiation shows that the rate of change of v_{max} with respect to I, dv_{max}/dI, is inversely proportional to $\sqrt{I}$. As I increase, dv_{max}/dI becomes smaller and smaller. Correspondingly, the rate of change of the total mass transfer with respect to I decreases with I. This accounts for the fact that all of the curves shown in Figs. 42 through 48 tend to level off as I increases.

It remains to explain how variation in v_{max} affects the total mass transfer. To this end, it is helpful to recourse to the theoretical considerations of Chapter IV and V. Eqs. (4.25) and (4.62) indicate that the mass transfer rate per unit surface area is proportional to $\sqrt{u_1}$ in the stagnation flow regime. The parameter u_1 is related to the velocity and the width of the impinging stream. For a uniform jet of velocity v_j and half width b_j, u_1 has been shown to take the value $u_1 = v_j\pi/4b_j$. To apply this expression to the case of two-dimensional electric wind, an acceptable selection for v_j and b_j is v_{max} and $x_{½}$ respectively. Thus, near the stagnation point, the mass transfer rate is proportional to $\sqrt{v_{max}}$. In the wall jet region, Eqs. (5.47) and (5.80) show that the mass transfer rate is determined by two parameters R and ℓ. According to the definition of R, it can be deduced that R is proportional to v_{max}^3. If ℓ is determined in the manner suggested in Section 5.3, it is readily seen that ℓ and v_{max} are related linearly. Using these above relations between R and v_{max}, and ℓ and v_{max} in Eq. (5.47) or (5.80), it is inconclusive as to how the mass transfer rate in a wall jet varies with v_{max}. On the basis of physical reasoning, it is anticipated that increase in v_{max} will result in higher mass transfer rate in a wall jet. Bearing this in mind, it is found that the special case when ℓ is negligible as compared to x, affords an

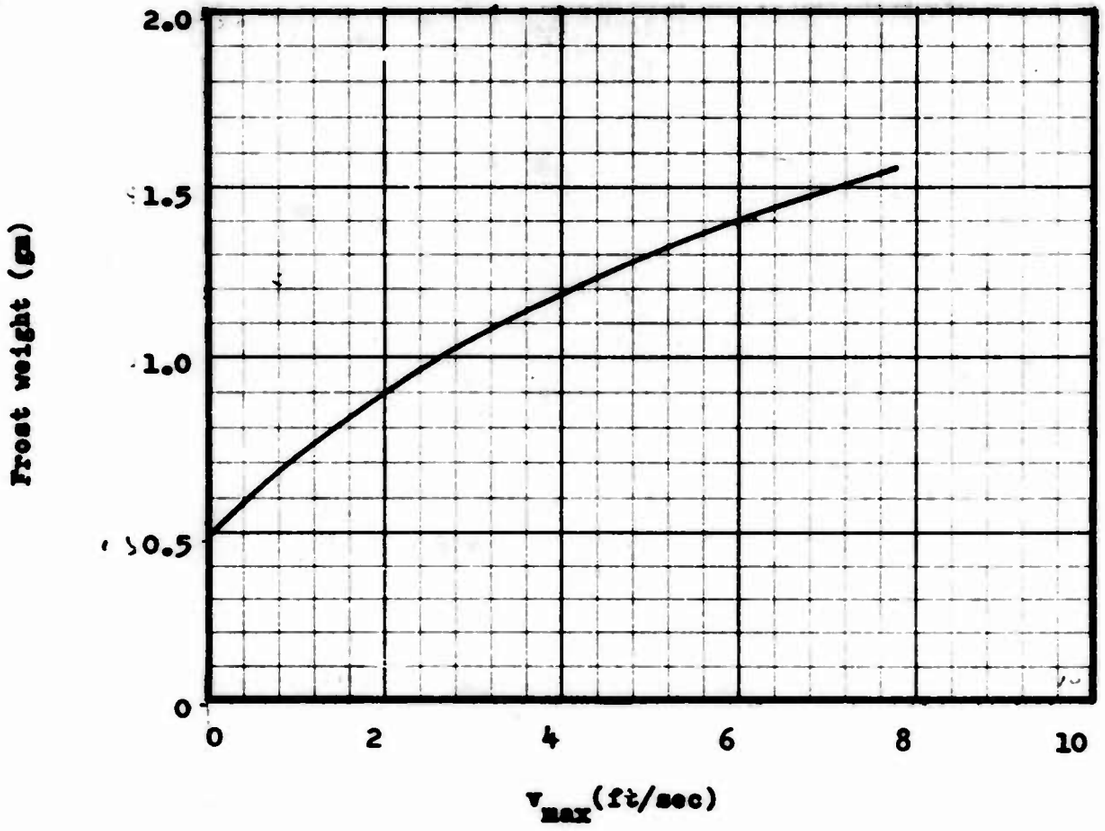

Fig. 51 Total frost weight vs maximum electric wind velocity

acceptable relation between the mass transfer coefficient and v_{max}. With $R \propto v_{max}^3$, h_m is thus proportional to $v_{max}^{3/4}$. Further discussion in this connection will be taken up in the next chapter.

While Figs. 49 and 50 tend to indicate that the total mass transfer is dominantly controlled by the total current and is not significantly affected by d, another test series aimed to investigate the possible variation of frost accumulation with d at fixed current showed that such variation did occur. Typical data of such tests are shown in Fig. 52. A general trend is that the frost accumulation tends to increase with d, I being maintained constant. It is known in two-dimensional laminar free jet problem that the volume rate of discharging per unit height of slit is proportional to $z^{1/3}$, where z is the distance from the slit along the axis of the jet. This relation is also plotted in Fig. 52 for comparison. As can be seen from this figure, frost accumulation increases with d in a similar manner as does the volume rate of flow of a free jet with z. It is thus deduced that an electric wind might behave like a free jet, as the air stream blows along fluid particles from the surroundings are carried away with the wind owing to friction on its boundary. Consequently, increase in d results in more air being discharged against the plane electrode and hence more frost accumulation. How this last step actually takes place requires further explanation. In 6.3.2, v_{max} has been found to remain approximately constant and $x_{\frac{1}{2}}$ has been noted to increase as d increases, an indication that the volume rate of flow increases with d. This means the u_1 will decrease as d increases and less frost will deposit per unit area in the stagnation region. On the other hand, it has been demonstrated that increase in d inclines to widen the range of the wind and hence the area of the stagnation flow. The net results of these two contradictory effects of d on mass transfer is expected to be in favor of increasing frost deposit. In the wall jet region, increase in flow rate definitely will increase mass transfer as is obvious from the definition of R. It may be noted in passing that in retrospect the data on electric wind and wall jet indicate that the flow rate does increase with d. Therefore, the speculation of the entrainment phenomenon in an electric wind is further substantiated.

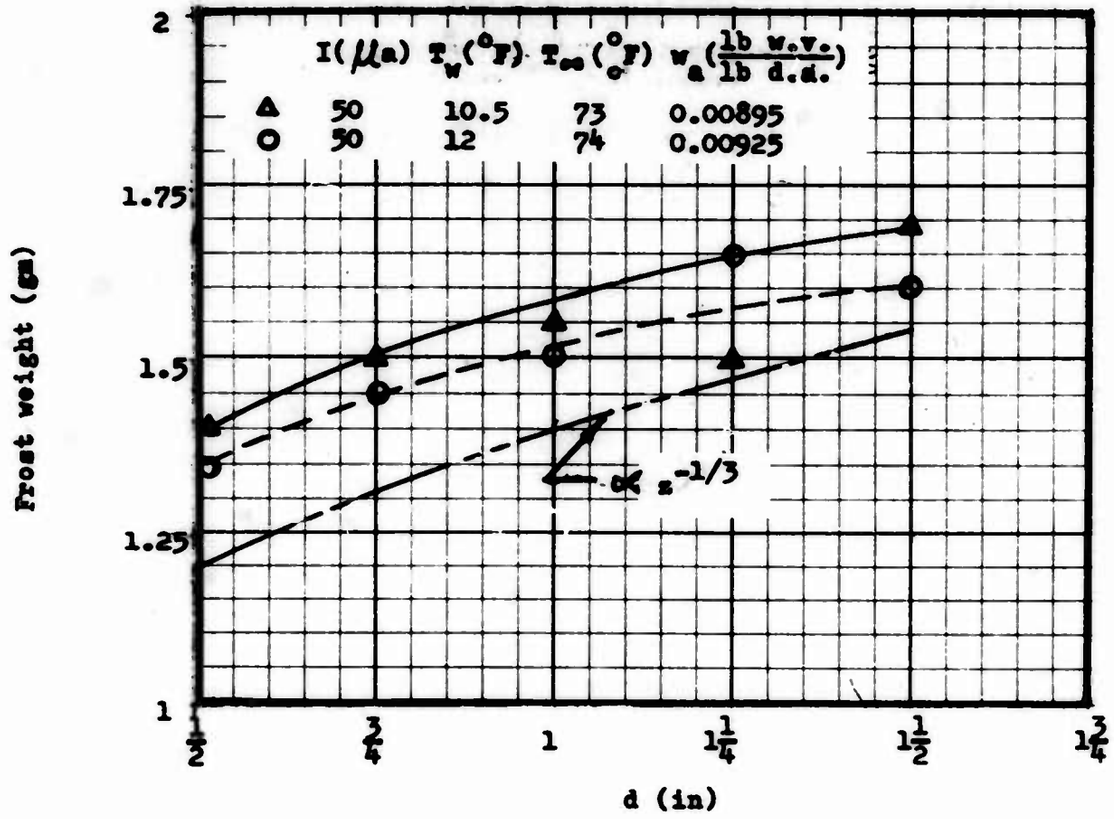

Fig. 52 Variation of frost deposit with d

CHAPTER VII

COMPARISON OF THEORY AND EXPERIMENT

7.1 METHODS OF CALCULATION

Efforts will be made in this chapter to attempt a comparison of theoretical and experimental results. Such a comparison in the present study presents considerable difficulty owing to a number of reasons. First, no satisfactory theory exists in the literature as regards the phenomenon of the electric wind. Second, the electric wind itself is highly non-uniform and the stagnation flow associated with its normal impingement on a plane surface has, as yet, not been solved. The theoretical consideration of Chapter IV have been based on one-dimensional model of electric wind and the results are strictly applicable only for a region in the neighborhood of the stagnation point small in comparison with the width of the oncoming stream. Third, the aerodynamic processes of transition from stagnation flow to fully developed wall jet have not yet been explored. Our knowledge concerning transport mechanisms in this region is practically void. Fourth, experimental evidences indicate turbulent flow prevails in the wall jet. Lack of adequate theory on transport processes in turbulent wall jet has forced one to consider laminar wall jet instead, which certainly can not provide a true picture. Fifth, the frost formation is a transient process, but the theoretical considerations have been based upon quasi-steady conditions. Finally, in view of the complicated flow field involved, it is most desirable to investigate local transport coefficients. Unfortunately, in the present investigation this was not accomplished. Owing to these above disadvantages that face the problem of interest, it is felt that the significance of the present chapter lies primarily on correct theoretical predictions of the qualitative trend of the variation of transport processes with current.

In order to compare the effectiveness of an electric wind in improving the transport processes relative to free convection, the heat and mass transfer coefficients in free convection, two-dimensional stagnation flow and two-dimensional laminar wall jet will be evaluated using the following values:

Plate surface temperature, $T_w = 10°F$,

Free stream temperature, $T_\infty = 70°F$,

Plate surface mass fraction of water vapor, $w_{1w} = 0.0013$,

Free stream mass fraction of water vapor, $w_{1\infty} = 0.01$.

The calculations will be based upon the theoretical expressions for zero normal velocity at the frost surface.

$$\bar{h} = \frac{0.677\sqrt{Pr}\left(Gr + \frac{Pr}{Sc}\,Gr'\right)^{\frac{1}{4}}}{(0.952 + Pr)^{\frac{1}{4}}\,L} \cdot k \qquad (7.1)$$

and

$$\bar{h_m} = \frac{0.677\sqrt{Sc}\left(Gr + \frac{Pr}{Sc}\,Gr'\right)^{\frac{1}{4}}}{(0.952 + Pr)^{\frac{1}{4}}\,L} \cdot D \qquad (7.2)$$

where

$Gr = \frac{g\beta_t(T_\infty - T_W)L^3}{\nu^2}$ is the average Grashof number,

$Gr' = \frac{g\beta_m(w_{1\infty} - w_{1W})L^3}{\nu^2}$ is the average Grashof number for mass transfer,

$\beta_t = \frac{1}{T}$ is the coefficient of thermal expansion,

$\beta_m = \frac{(M_2 - M_1)/M_1}{w_1\left(\frac{M_2 - M_1}{M_1}\right) + 1}$ is the concentration coefficient of expansion

and

M_1, M_2 = molecular weight of water vapor and dry air, respectively. All properties of the air will be evaluated at the mean film temperature, $T_m = 40°F$. At this temperature, the values of k, D, ν, Pr, Sc, $g\beta_t/\nu^2$ and $g\beta_m/\nu^2$ are:

$$\nu = 1.47 \times 10^{-4} ft^2/sec,$$

$$k = 0.0142 \text{ Btu/hr-ft-}°F,$$

$$D = 2.79 \times 10^{-4} ft^2/sec,$$

$$Pr = 0.714,$$

$$Sc = 0.528,$$

$$\frac{g\beta_t}{\nu^2} = 2.98 \times 10^{6} ft^{-3}\ °F^{-1},$$

and

$$\frac{g\beta m}{\nu^2} = 9.03 \times 10^{-8} ft^{-3} \quad .$$

For L = 6 inches, Gr and Gr' are:

$$Gr = 2.24 \times 10^{7} \quad ,$$

$$Gr' = 9.83 \times 10^{5} \quad ,$$

Since Gr' is small as compared to Gr, it will be neglected in the succeeding calculations. Substitution of the foregoing values into Eq. (7.1) and (7.2) gives the following values of average heat and mass transfer coefficients for free convection:

$$\bar{h} = 64k$$

$$\overline{h_m} = 50D$$

Proceeding next to the calculations of the heat and mass transfer coefficients at the stagnation point of an impinging two-dimensional electric wind, Eqs. (4.24) and (4.26) will be evaluated, namely,

$$h = \frac{3}{2} k \left(\frac{u_1}{7.052\nu} \right)^{\frac{1}{2}} (Pr)^{1/3} \tag{7.3}$$

and

$$h_m = \frac{3}{2} D \left(\frac{u_1}{7.052\nu} \right)^{\frac{1}{2}} (Sc)^{1/3} \tag{7.4}$$

The chief concern here is the determination of the parameter u_1. As noted earlier (Section 6.3.5), u_1 is related to the velocity v_j and the half width b_j of a uniform jet by $u_1 = \pi v_j / 4 b_j$. In order to utilize this relation to estimate the value of u_1 for a two-dimensional non-uniform electric wind, certain modification has to be exercised. It has been suggested in the preceding chapter to replace v_j and b_j by v_{max} and $x_{\frac{1}{2}}$, respectively, of the actual impinging wind. This same procedure will again be adopted here in carrying out the computations. To be specific, the case where $v_{max} = 7.8$ ft/sec and $x_{\frac{1}{2}} = 0.28$ inch, corresponding to I = 200 μa and d = 0.5 inch, will be used in a sample calculation. For this particular case u_1 is found to be $u_1 = 262$ sec^{-1} Substituting this value of u_1 and the required properties of the air at a mean temperature of 40°F into Eqs. (7.3) and (7.4), h and h_m are found to be $h = 675k$ and $h_m = 612D$.

Evaluation of the heat and mass transfer coefficients for laminar wall jet will be based upon Eqs. (5.41) and (5.48) with $\theta_1'(0) = 0.273$ and $\varphi'(0) = 0.258$, namely,

$$h(x) = 0.273k(5R/32\nu^3)^{\frac{1}{4}}(x+\ell)^{-3/4} \qquad (7.5)$$

and

$$h_m(x) = 0.258D(5R/32\nu^3)^{\frac{1}{4}}(x+\ell)^{-3/4} \qquad (7.6)$$

The main task now is the determination of the two constants R and ℓ. Arguing that the volume flow rate as well as the maximum velocity of the impinging jet remains practically unchanged after being deflected by the plane surface, Glauert[37,38] has suggested to estimate R and ℓ from the conditions of the impinging stream. From the definition of R (that is Eq. (5.7)), he has deduced Rq. (5.22) for R, namely,

$$R = \tfrac{1}{2}\ (\text{typical velocity})(\text{volume flow/unit length})^2 \qquad (7.7)$$

The constant length ℓ may be obtained by equating the maximum wall jet velocity at x=0 as given by Eq. (5.21) to the maximum initial velocity, namely,

$$\ell = (5R/2\nu)(0.315/v_{max})^2 \qquad (7.8)$$

where 0.315 is the maximum value of f'. Eqs. (7.7) and (7.8) have not been subject to experimental verification previously, and their validity should not be taken for granted. In the present program two other methods of determining R and ℓ are also considered. The transport coefficients calculated using the three methods of estimating R and ℓ will be compared with the case of free convection as well as experimental results. Conclusion will be made as to which method yields the most satisfactory values of h and h_m.

The determination of R by means of Eq. (7.7) depends on a suitably selected typical velocity of the impinging jet of air stream. Since the volume flow rate per unit length of the jet is constant, a typical velocity of the jet which will give an average value of R across the jet is the average of the jet. The flow rate per unit length and the average velocity of the jet of electric wind are determined from experimentally measured velocity profiles shown in the foregoing chapter. For the case pf I = 200 μa and d = 0.5 inch, the flow rate per unit length is 0.225 ft^2/sec and the average velocity is 2.7 ft/sec. Using these values in Eq. (7.7), it is found R = 0.0684 ft^5/sec^3. The value of ℓ determined by Eq. (7.8) is 1.89 ft. The heat and mass transfer coefficients at x=2 inches for this case are h = 41.7k and h_m = 39.7D.

The second method of determining R and ℓ is similar to the one described above, except that the wall jet data are used in lieu of the electric wind data. For I = 200 μa and d = 0.5 inch, the flow rate per unit length as measured from Fig. 33 is 0.133 ft^2/sec and the average velocity is 2.96 ft/sec. The values of R and ℓ thus found are 0.0262 ft^5/sec^3 and 0.818 ft, respectively. The corresponding transport coefficients are h = 52.5k and h_m = 49.5D.

The third methos is based on the assumption that ℓ is small as compared to x = 2 inches and can be neglected. And R is obtained by substituting the measured maximum wall jet velocity in the second of Eq. (5.21), putting x = 0.167 ft (that is x = 2 inches) and f' = 0.315, and solving for R, namely,

$$R = (0.334\nu/5)(u_{max}/0.315)^2 \qquad (7.9)$$

For the example considered above, R = 0.00445 ft^5/sec^3, h = 128k and h_m = 121D.

With the transport coefficients for stagnation and wall jet flows determined as above, the total heat and mass transfer rates will now be estimated. Since no information is available concerning the transport processes in the transition region, this region will be neglected. It will be assumed that the stagnation flow covers an area of $4x_{\frac{1}{2}}$ and the average transport coefficients in this region is one half the sum of the values at the stagnation point and at x = 2 inches for all jet, the latter are considered as the average transport coefficients outside the stagnation region.

7.2 DISCUSSION OF THEORETICAL PREDICTIONS

The heat and mass transfer coefficients at the two-dimensional stagnation point are listed in Table 1. As expected h and h_m increases with I for constant d and decreases with increasing d for constant I. A discussion of this has been given in Section 6.3.5 and no further comments will be made.

Table 1 - Transport coefficients at two-dimensional stagnation point

I (μa)	d (in)	v_{max} (ft/sec)	$x_{\frac{1}{2}}$ (in)	u_1 (sec^{-1})	h/k (ft^{-1})	h_m/D (ft^{-1})
200	0.5	7.8	0.28	262	675	612
150	0.5	7.4	0.28	249	655	595
100	0.5	6.1	0.28	205	595	540
50	0.5	4.4	0.28	148	506	459
150	0.75	7.2	0.38	179	555	504
100	0.75	6.1	0.38	154	516	468
50	0.75	4.2	0.38	104	425	386
100	1.0	6.2	0.44	133	479	435
50	1.0	4.3	0.44	92	402	364

For the two-dimensional laminar wall jet, the local heat and mass transfer coefficients evaluated using the three methods show a certain peculiar behavior. Tables 2 and 3 give the values of h and h_m determined by using the electric wind and the wall jet data, respectively. An inspection of these tables indicated that no unique relation exists between the transport coefficients and the total current. An increase in I does not always result in higher values of h and h_m, in constrast to expectation. It is all the more surprising to also note that the transport coefficients for wall jets are at most of the same magnitude as those for free convection. According to the theory on free convection[28], the maximum velocity at a position x from the upper edge of the vertical plate is given by

$$u_{max} = 3\nu \left[\frac{g\beta t(T_\infty - T_f)}{4\nu^2} \right]^{1/4} x^{1/4}$$

At x = 6 inches, u_{max} = 0.272 ft/sec, which is the maximum attainable velocity along the test plate under free convection conditions and is much smaller than the measured maximum velocity in the wall jet. It is rather mysterious that higher velocity does not have the effect of enhancing transport processes. Furthermore this theoretical result contradicts the experimental finding that frost was found to form more rapidly even in regions far away from the stagnation region (i.e. in the wall jet region) under the action of electric wind than in the absence of field. Apparently, Eqs. (7.7) and (7.8) do not seem to provide correct information for the wall jet.

Table 2 - Transport coefficients for two-dimensional laminar wall jet --- based on electric wind data

I (μa)	d (in)	v_{max} (ft/sec)	V.F.R.[a] (ft^2/sec)	A.V.[b] (ft/sec)	R (ft^3/sec^3)	ℓ (ft)	h/k (ft^{-1})	h_m/D (ft^{-1})
200	0.5	7.8	0.225	2.7	0.0684	1.89	41	39.7
150	0.5	7.4	0.196	2.35	0.0451	1.39	47	44.4
100	0.5	6.1	0.162	1.95	0.0255	1.23	46.6	44.1
50	0.5	4.4	0.121	1.45	0.0132	1.28	39.3	37.2
150	0.75	7.2	0.275	2.36	0.0891	2.9	31.6	29.9
100	0.75	6.1	0.233	2.15	0.0584	2.65	30.6	28.9
50	0.75	4.2	0.154	1.54	0.0183	1.75	31.2	29.5

(a) V.F.R. = volume flow rate

(b) A.V. = average velocity

Table 3 - Transport coefficients of two-dimensional laminar wall jet --- based on wall jet data

(μa)	(in)	(ft/sec)	(ft^2/sec)	(ft/sec)	(ft^5/sec^5)	(ft)	(ft^{-1})	(ft^{-1})
200	0.5	6.7	0.133	2.96	0.0262	0.818	52.5	49.5
150	0.5	5.9	0.112	2.49	0.0156	0.59	56.1	53.0
100	0.5	4.7	0.09	2.0	0.008	0.465	54.3	51.3
50	0.5	3.2	0.057	1.26	0.002	0.167	62.3	58.8
150	0.75	6.4	0.15	3.34	0.038	1.38	40.8	38.6
100	0.75	5.6	0.12	2.67	0.019	0.863	47.0	44.4
50	0.75	3.6	0.078	1.74	0.053	0.528	45.7	43.2

Tabulated in Table 4 are the transport coefficients for laminar wall jets as predicted by the third method. It is noted that h and h_m increase with I and are approximately twice the magnitude of the corresponding average free convection transport coefficients. Thus, it is concluded that the values of h and h_m determined by this method are more reasonable.

Table 4 - Transport coefficients of two-dimensional laminar wall jet -- based on Eq. (7.9)

I (μa)	d (in)	u_{max} (ft/sec)	R (ft^5/sec^3)	h/k (ft^{-1})	h_m/ν (ft^{-1})
200	0.5	6.7	0.00455	128	121
150	0.5	5.9	0.00344	119.5	113
100	0.5	4.7	0.00214	106	100
50	0.5	3.2	0.00101	89.8	84.9
150	0.75	6.4	0.00405	125	118
100	0.75	5.6	0.00311	116.5	110
50	0.75	3.6	0.00128	93.5	88.3

The total heat and mass transfer rates given in Table 5 are predicted on the basis of Tables 1 and 4. The ratio of the predicted total mass transfer rate with field and the corresponding value for free convection (no field) is plotted in Fig. 53 as function of current. Since the effect of free convection is not considered in the analysis, the predicted mass transfer rate vanishes at zero current. For comparison, Fig. 50 is also shown in Fig. 53, using the value of total mass transfer at zero current as a reference. The theoretical prediction is observed to agree quite well with experiment. However, it should be cautioned that the present investigation is aimed only to provide means of comparing qualitatively the simplified theoretical considerations

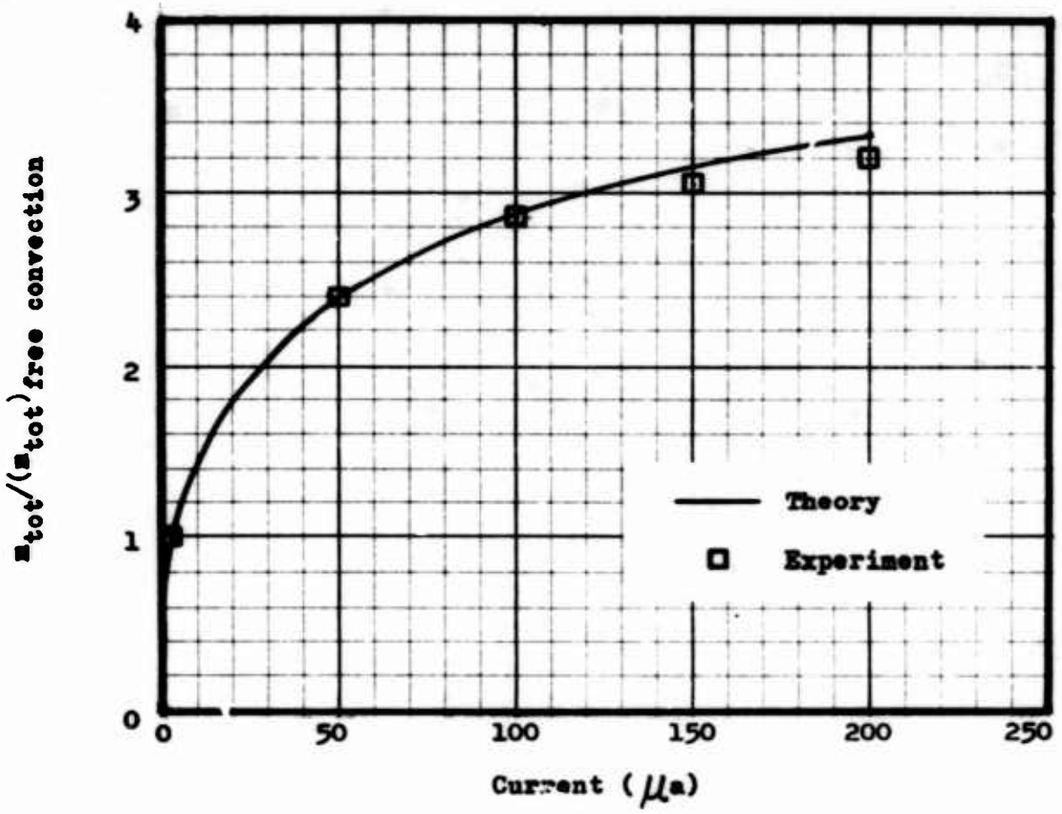

Fig. 53 Comparison between theory and experiment for mass transfer

and the experiment, and no quantitative accuracy is claimed. It is worth-while to emphasize that while the laminar wall jet theory tends to underestimate the mass (as well as heat) transfer in the wall jet region (which is actually turbulent), the assumption that the situation is quasi-steady at the test plate conditions inclines to overestimate the total mass (and heat) transfer. Another point worth noting is the selection of the stagnation flow area and the average transport coefficient in the wall jet region is rather arbitrary, for no information on the position of transition is available.

Table 5 - Total heat and mass transfer rates

(μa)	(in)	$\frac{q_{tot}}{k(T_\infty - T_w)}$ (ft)	$\frac{m_{tot}}{\rho D(w_{1_\infty} - w_{1_w})}$ (ft)
200	0.5	67.1	62.7
150	0.5	63.4	59.3
100	0.5	56.8	52.9
50	0.5	48.3	44.9
150	0.75	67.3	62.7
100	0.75	62.7	58.2
50	0.75	50.9	47.3
Free convection		24	18.75

A similar comparison between theory and experiment for total heat transfer is given in Fig. 54, the experimental data being taken from Fig. 40. The correlation between theory and experiment is poor in this case. The discrepancy may be attributed to the fact that the measured total heat transfer rate represents the total heat gain to the refrigerant through convection, radiation and conduction. While the theoretical curve considers convective heat transfer only, the uncorrected data actually represent the ratio $Q/(Q)_{\text{free conv}}$, where Q and $(Q)_{\text{free conv}}$ are the total heat transfer rates with and without field respectively. If the radiative and conductive heat transfer is independent of the electric field, then

$$\frac{q_{tot}}{(q_{tot})_{\text{free conv}}} > \frac{Q}{(Q)_{\text{free conv}}}$$

The conductive heat transfer, which includes heat gain from the environment through the edged of the test plate and the insulating material, is estimated to be small as compared with the radiative heat transfer. After making correction for radiative heat transfer, the measured data are seen to be in closer agreement with the theory.

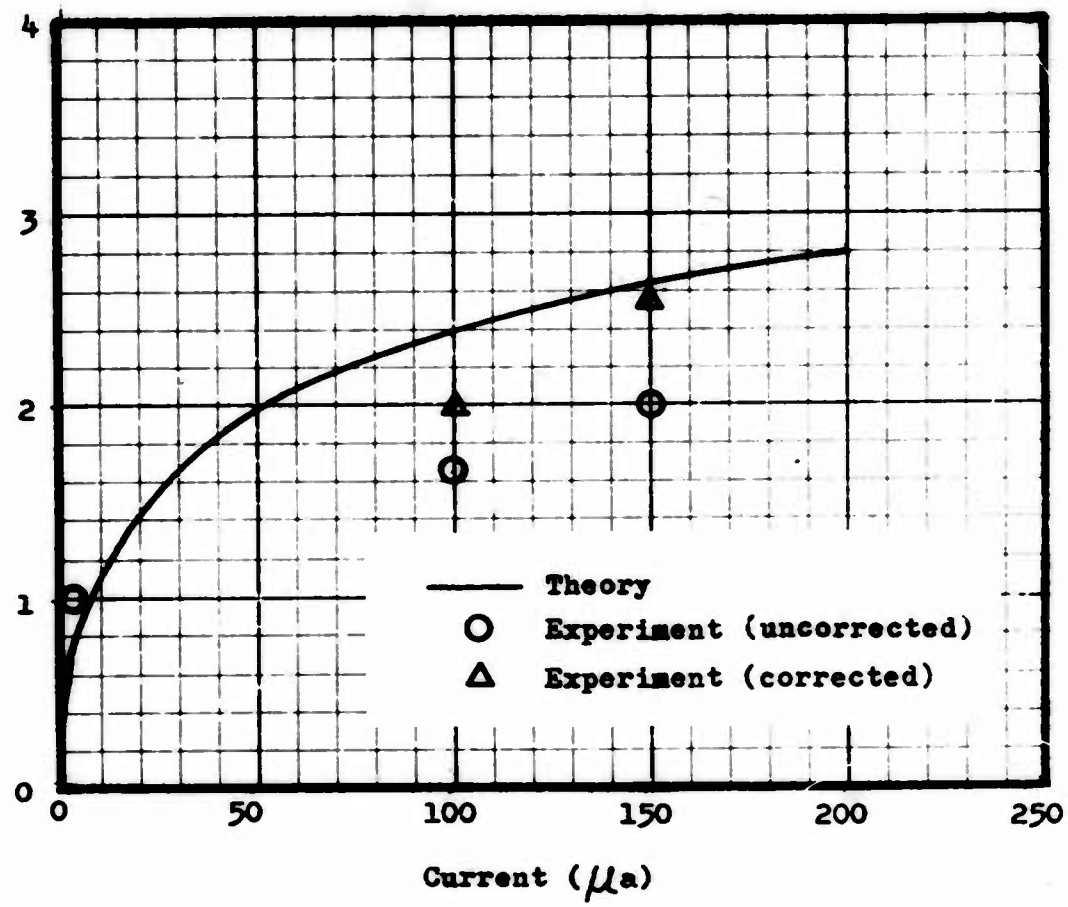

Fig. 54 Fig. 54 Comparison between theory and experiment for heat transfer

To further the comparison between theory and experiment, a numerical value of the magnitude of the total mass transfer will be given and compared with the measured frost deposit. For the case I = 200 μa and d = 0.5 inch, the total mass transfer for a period of five minutes is

$$m_{tot} = 62.7\rho D(w_{1_\infty}-w_{1_W}) \frac{5}{60}$$

At a mean temperature of 40°F, the density of the air is 0.0795 lbm/ft^3. Using this value of ρ and the value of $(w_{1_\infty}-w_{1_W})$ given in the previous section, the total mass transfer to the test plate is calculated to be 1.65 gm. In the case of heat transfer, the magnitude of the measured convective heat transfer rate is found to be approximately 2.5 times greater than the value estimated by the theory. The reason for this discrepancy is rather obscure and further research is required in order to made a more conclusive comparison between theory and experiment.

On the ground of the close agreement between theory and experiment as indicated in Fig. 53 for the total mass transfer, a number of conclusions may be drawn. First, within the velocity range of the experiments, the assumption of laminar flow in the wall jet region provides a reasonable prediction on mass transfer. Second, the deviation of the actually transient frosting process from the quasi-steady assumption within an interval of 5 minutes is not significant under the test conditions. Finally, the method of calculation adopted in estimating the total mass transfer is very satisfactory. An example of the distribution of the mass transfer coefficient over the entire test plate used in the present calculation is displayed in Fig. 55 by the dashed line. Judging from the velocity distribution of the impinging electric wind, it is expected that the transfort coefficients may also assume a bell-shaped distribution. The predicted distribution based on the simplified model is shown in the same figure by the curve made up of alternate long and short dashes. For comparison, the mass transfer coefficients as predicted by laminar wall jet alone is also indicated by Fig. 55 by solid lines.

Figure 56 shows the relative effectiveness of an electric wind in enhancing the heat and mass transfer as predicted by the theory for the test plate under consideration. A general conclusion is an electric wind is more effective in increasing mass transfer than heat transfer. For example, at I = 200 μa the increase in mass transfer relative to free convection conditions is 233%; whereas the increase in heat transfer is only 180%. Of course the above percentage increase are valid only for the particular test plate considered in the present investigation.

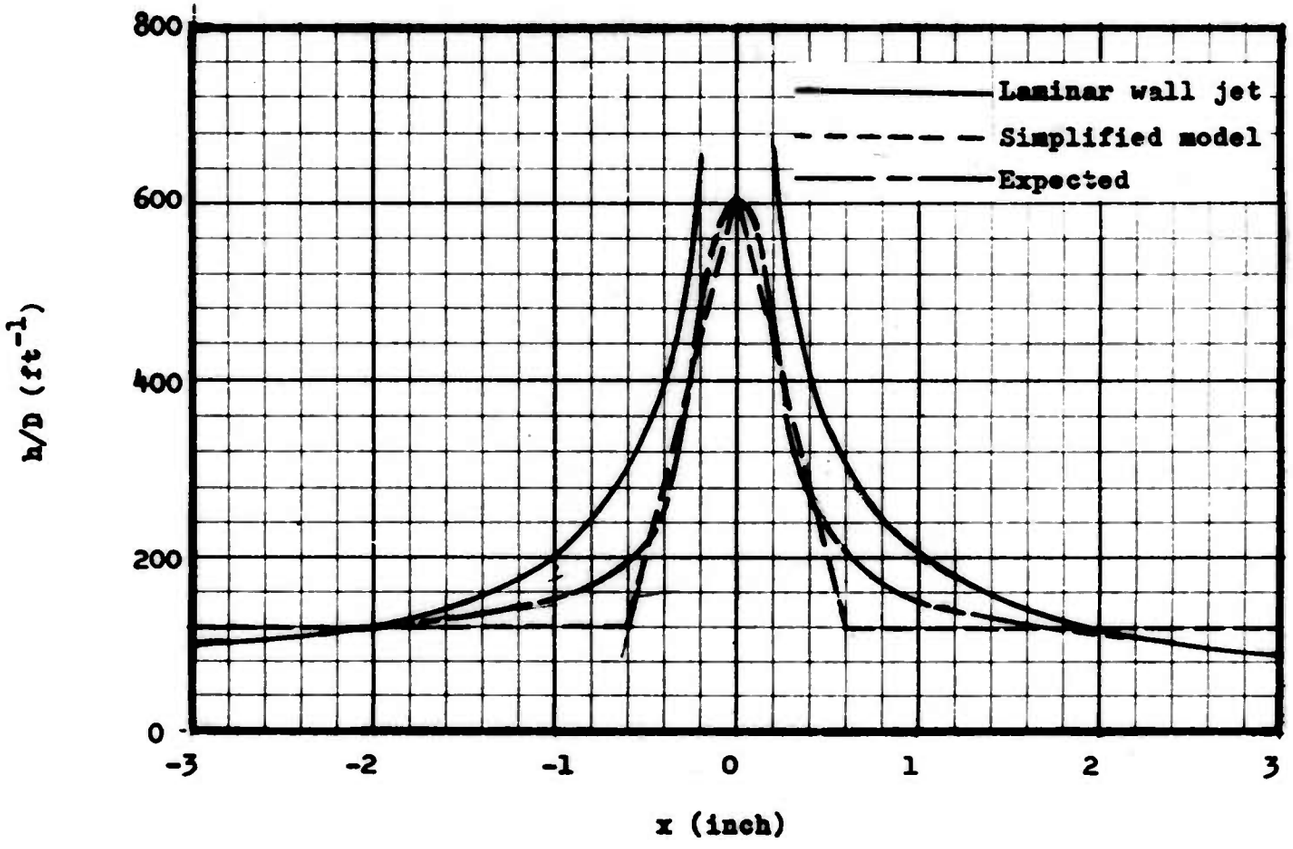

Fig. 55 Distribution of mass transfer coefficient for I = 200 a and d = 0.5"

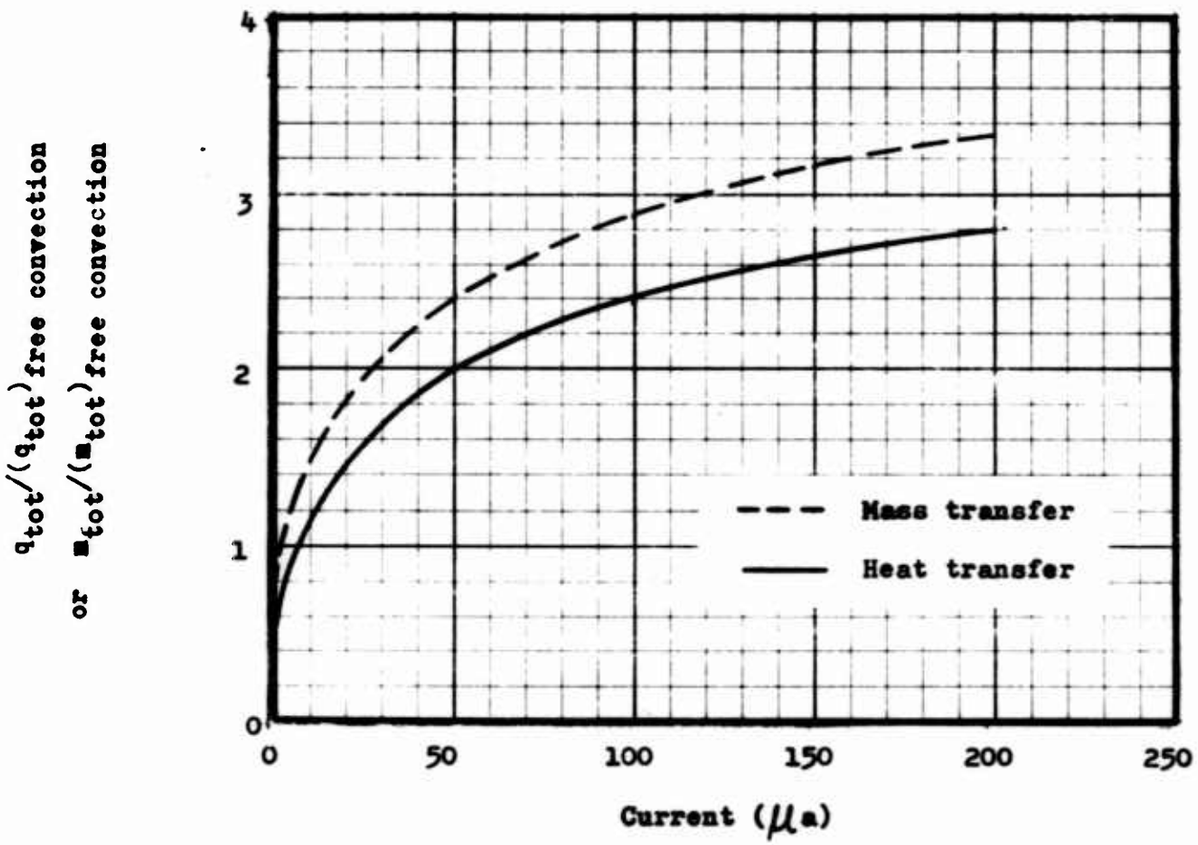

Fig. 56 Comparison of electric wind effects on heat and mass transfer as predicted by theory

CHAPTER VIII

CONCLUSIONS AND RECOMMENDATIONS

8.1 SUMMARY AND CONCLUSIONS

An experimental program was undertaken to investigate the behavior of frost formation in an electric field. To facilitate comparison of the effectiveness relative to free convection conditions of an electric field in improving the heat and mass transfer processes associated with frost formation, the test plate was installed vertically and the experiments were carried out under ambient air conditions.

The experimental study included two phases. The preliminary exploratory tests were aimed to explore the possible effects of electric fields upon the frosting phenomenon. The following conclusions may be drawn from the results of this test sequence:

1. A uniform electric field does not appear to have any observable effects on frost formation at the initial stages of the process.

2. A non-uniform field characterized by a corona discharge can enhance considerably the frost formation.

3. The effects of corona discharges on frosting can be attributed to the impingement of electric wind induced by the corona, changing the flow field from free convection to forced convection.

On the basis of the preliminary experimental findings, a second experimental sequence, using single wire electrode configuration, was designed to study the flow field generated by the impinging electric wind and to provide further information on the electric wind effects upon heat and mass transfer in connection with frost formation. The mass transfer data indicated that at a total current of between 100 μa and 200 μa, the total frost deposit for five minutes could be increased up to 200% for the particular test plate used in this investigation, as compared to the case of no field. The rate of increase in total frost accumulation was found to decrease with increading current and to approach zero asymptotically as the current tended to infinity. The heat transfer data also showed significant increase in total heat transfer rate in the presence of electric wind and an increase of up to 100% at 150 μa was measured for the 6 x 9 inches test plate. However, the data were insufficient to indicate a similar trend as exhibited by the mass transfer data.

From velocity measurements behind a wire-screen collector, the electric wind was found to be confined to within approximately one inch

from the stagnation point and the velocity assume a bell-shaped distribution. Outside this region, the velocity was essentially zero. When plotted non-dimensionally, the data favored the existence of a similarity not only among the velocity profiles but also between the current density distribution and the velocity profile for various electric conditions. At a distance two inches from the stagnation point along the test plate, the velocity profile normal to the plate was found to be of a turbulent wall jet type at high current. At lower current the profile was observed to deviate slightly from the turbulent one.

The above velocity measurements substantiate the postulate that, in analogy with the impingement of a free jet, the flow field produced by an impinging electric wind may be divided into four regions. Prior to impingement, the flow is controlled by the electric field and may be called the electric wind proper. After impingement, the wind is spread out over the plate. In the vicinity of the stagnation point, a stagnation flow is expected and its properties will be determined by the static pressure distribution on the plate. At distances from stagnation point sufficiently large to approximate a zero static pressure gradient at the plate, the flow will assume the form of a wall jet. The regions of stagnation flow and wall jet are separated by a transition zone.

An analytical program was conducted to study the heat and mass transfer processes in the stagnation and wall jet flow regimes of an impinging electric wind. Evaluation of the heat and mass transfer rates at the stagnation point was carried out by approximating the electric wind by a uniform jet of velocity v_{max}, the maximum velocity of the actual wind, and half width $x_{\frac{1}{2}}$, the value of x at which the velocity of the wind is $\frac{1}{2}v_{max}$. Analysis for the wall jet region was based upon laminar flow. Comparison between theory and experiment was accomplished through the introduction of a simplified model for calculating the total heat and mass transfer to the test plate. According to this model, the stagnation flow region extends to $2x_{\frac{1}{2}}$ from the stagnation point and the transport coefficients between the stagnation point and the wall jet follow a linear relation. In the wall jet region, the average transport coefficients are assumed to take the values at a point two inches from the stagnation point.

Theoretically the transport coefficients for wall jets depend on two parameters R and ℓ. Three different methods were proposed to determine these two constants. On the ground of physical arguments, the transport coefficients in a wall jet are expected to increase with the maximum wall jet velocity. The only method which gives results in agreement with this expectation is the one which assumes ℓ negligible and R determinable from the maximum wall jet velocity.

The total mass transfer versus current relation predicted by the theory was found to agree satisfactorily with the experimental results. Validity of the theory was further verified by the agreement between the absolute magnitude of the predicted frost deposit and the measured data. It is therefore beleived that the present theoretical model

should also be adequate to predict the heat transfer. However, the comparison between experimental and theoretical heat transfer results was found to be less satisfactory. The causes of this discrepancy demand further investigation.

The theoretical predictions on heat and mass transfer were based on the assumption of negligible normal velocity at the frost surface. The assumption appears to be a good one under the test conditions. With a view of furthering the study to include the electric wind effects upon other mass transfer processes such as drying or other evaporation processes where the assumption is no longer valid, an analysis was made of the heat and mass transfer in the presence of non-negligible normal velocity at the surface for plane stagnation flows as well as plane laminar wall jet, using an integral method. No explicit expressions for heat and mass transfer coefficients are possible for this case and, therefore, numerical or graphical solutions must be employed. No examples are given in this connection.

A simplified model of heat conduction in a frost layer was also analyzed using a power series solution introduced by Portnov. As expected, the controlling factor responsible for the unsteadiness of the transport mechanisms in the frost layer was found to be the mass flux from the surroundings to the wall. The heat flux, on the other hand, was found to have the effect of counteracting the unsteadiness caused by the mass flux.

8.2 RECOMMEDATIONS FOR FURTHER RESEARCH

The impinging flow associated with an electric wind is of particular interest because of its close analogy to a free jet impinging on a surface. In recent years the so-called impingement flow has been increasingly utilized to enhance the intensity of heat and mass transfer processes in various industries. At the present time no satisfactory theory on the impingement flow has yet been developed. A study of the flow and the heat and mass transfer processes in connection with the impingement of an electric wind may provide useful information on the impingement flow.

The present investigation was preliminary and incomplete. More extensive and systematic research remains to be done to furnish a clearer picture and to explore potential applications of the phenomena. The following are some suggestions for further research:

a. Experimental

Since the heat and mass transfer coefficients depend on the flow field, the investigation of the flow pattern in various regions of the flow field is of primary importance. The first region to be studied is the electric wind itself. It appears that the flow development of an

electric wind along its own axis has never been investigated before and it would be a valuable contribution to the understanding of the aerodynamic processes of an electric wind if such measurements can be accomplished. Two cases have to be considered. The first is to investigate the variation of the velocity profile with distance from the emitting electrode in the absence of the obstruction by plane electrode. The other case is to examine the influence of the solid collecting electrode on the development of the wind. It is also desirable to determine whether the flow is turbulent or laminar in the electric wind.

Systematic measurement of the velocity profile at various distances from the stagnation point along the plane surface is indispensable in understanding the transition from stagnation flow to wall jet. It helps locate the position of transition and is also essential in determining the effects on the stagnation flow of the ambient still fluid and of the non-uniformity of the impinging stream. Measurement of pressure distribution along the plane electrode is helpful in providing further insight in the stagnation flow generated by a non-uniform impinging stream. Such measurement has been made by Velkoff for positive wire-plane corona and by Chattock for point-plane corona, both positive and negative.

In view of the complex nature of the flow field under consideration, measurement of local heat and mass transfer coefficients is highly desirable and should form the core of further research programs. Other measurements which are significant and should be attempted in future research include temperature and concentration profiles and frost density distribution along the plate.

b. Theoretical

Although experimental evidence suggested the existence of a similarity between the current density distribution and the velocity profile of an electric wind, it should be emphasized that this tentative similarity needs further analytical verification. Further analytical research should, therefore, be directed toward establishment of the observed similarity. It is also necessary to determine the role played by viscosity and entrainment in an electric wind. Attention should be called to a possible analogy between an electric wind an thermal plume generated by a line or point heat source.

Further analytical work is needed in determining the viscous flow and the associated heat and mass transfer processes in the stagnation region of an impinging non-uniform stream. According to the stagnation flow theory of a uniform stream, the boundary layer thickness and hence the heat and mass transfer coefficients are constant in this region. Experimental evidences, however, indicated that the local heat transfer coefficients also showed a bell-shaped distribution in the vicinity of stagnation point[4]. Evidently, this discrepancy is due to the non-uniformity of the impinging stream.

Two other problems deserving theoretical considerations are the instability of a laminar wall jet and the transition from stagnation flow to wall jet. To the author's knowledge, the first problem has not even been mentioned in the literature. A prompt question that one intends to ask is: Is the instability theory of a free jet applicable to a wall jet? As to the second problem, preliminary prediction of the position has been made by Brady and Ludwig[10]. However, the problem is still far from being completely solved.

APPENDIX A

PHOTOGRAPHS OF THE GROWTH OF FROST AND FROST THICKNESS DISTRIBUTION

Shown in Figs. 57 and 58 are the photographs of the growth of the frost strip under the action of an electric wind. Although several corona wires were mounted on the electrode support, only one of them (the third one from the top) was active. The active corona wire was located along and at a distance of $\frac{1}{2}$ inch from the horizontal centerline of the test plate. The pictures were taken successively at 4 minute intervals with the first one taken one minute after the application of the field. In the figures the letter t designates the time when the picture was taken (the field being applied at t = 0). The total current for this test run was about 150 μa and the test plate temperature was about 10°F. The specific humidity of the ambient air was not recorded. The vertical ridges mentioned in Section 1.2 can also been seen in the pictures.

Measurement of the frost thickness distribution along the test plate was made with a depth gauge micrometer mounted on a sliding member, the latter including the micrometer. Measurements were made along the vertical centerline of the test plate at $\frac{1}{2}$ inch intervals by positioning the sliding member along the channel. Two readings were taken at each location, one at the frost surface and the other at the test plate surface. The difference of the two readings is the frost thickness at that location. To facilitate locating the position of the frost surface, a pointed cap was attached to the end of the measuring rod of the micrometer. When the tip of the modified measuring rod approached the frost surface, a flash light was turned on to illuminate the frost surface near the rod tip. The rod was advanced until it reached the test plate surface and then a second reading was taken. In order to make the measurements the field was turned off after the frost had been allowed to grow for a predetermined period of time, the discharging electrode removed, and then the measuring device put in position.

This method of measuring the frost thickness is not precise, for it is very difficult to determine the exact position of the frost surface. Furthermore, it usually took about ten minutes to complete the entire readings for each test run. To prevent the frost from melting it was necessary to keep circulating the refrigerant through the tubing of the test plate. Hence in the course of measurement, the frost thickness in the portion yet to be measured might have changed during this period of time. In addition, the variation in time of the frost thickness distribution can not be measured with the present device. Because of these disadvantages no extensive measurements were attempted, nor was it intended to provide quantitative information. Rather it was only intended to give some idea of the pattern of frost thickness distribution at an arbitrarily selected instant under arbitrary test conditions.

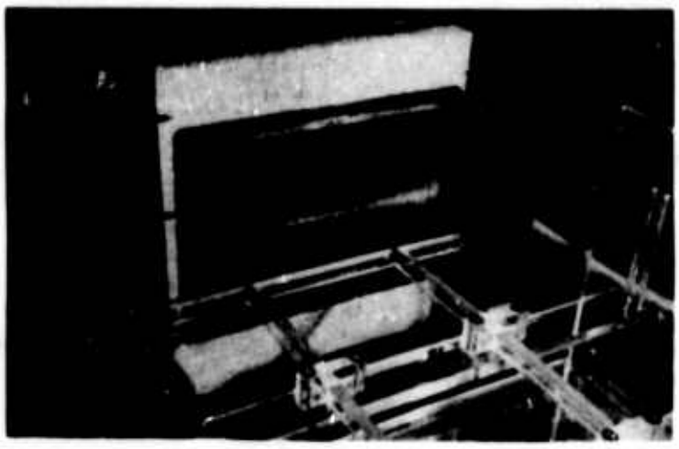

a. t = 1 min.

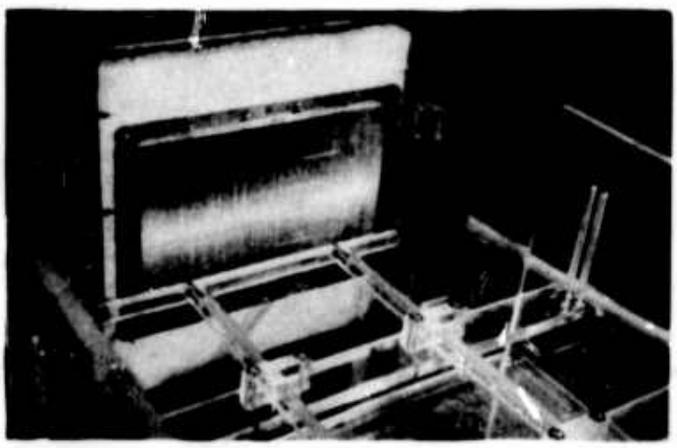

b. t = 5 min.

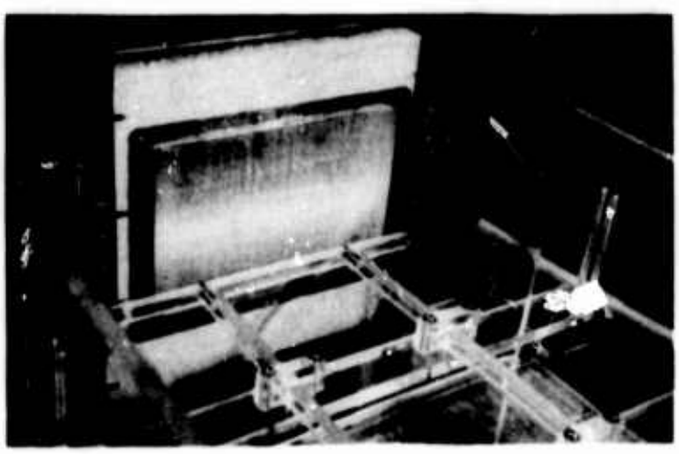

c. t = 9 min.

Fig. 57 Photographs of the growth of frost

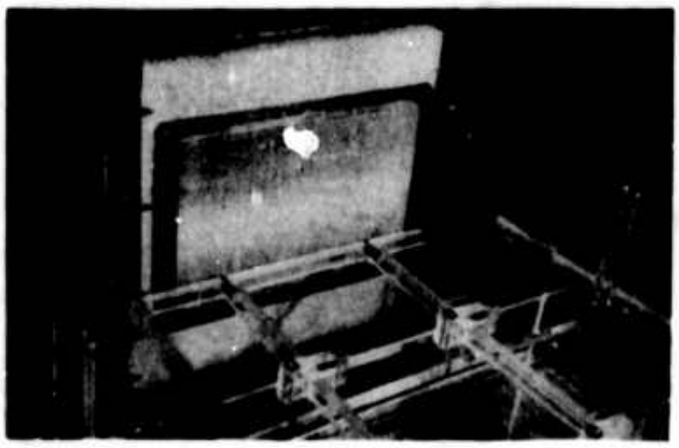

a. t = 13 min.

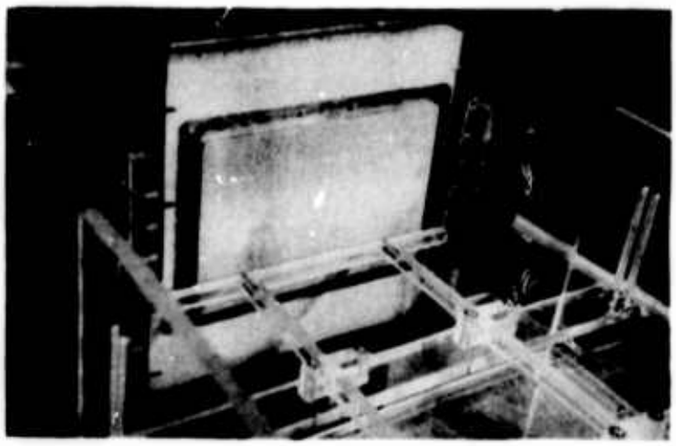

b. t = 17 min.

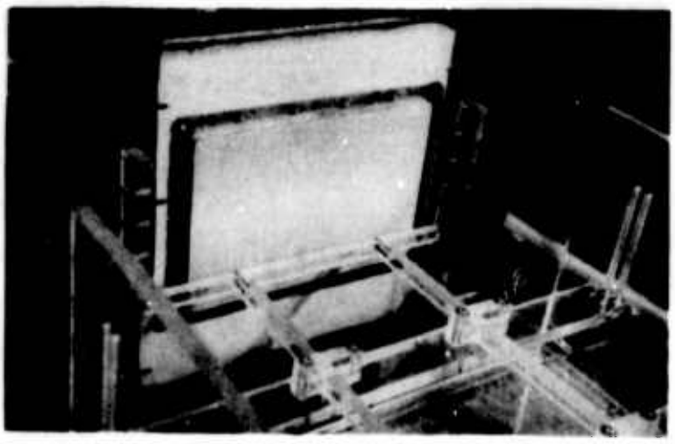

c. t = 21 min.

Fig. 58 Photographs of the growth of frost

Given in Fig. 59 are frost thickness distributions for three test runs, each being measured approximately ten minutes after the field was applied. The total current in each case was about 120 μa and the test plate temperature was about 10°F. No specific humidity of ambient air was recorded. Positive x in the figure corresponds to the lower half and negative x the upper half of the test plate. Again a single horizontal wire located at the centerline of the test plate was used as discharging electrode.

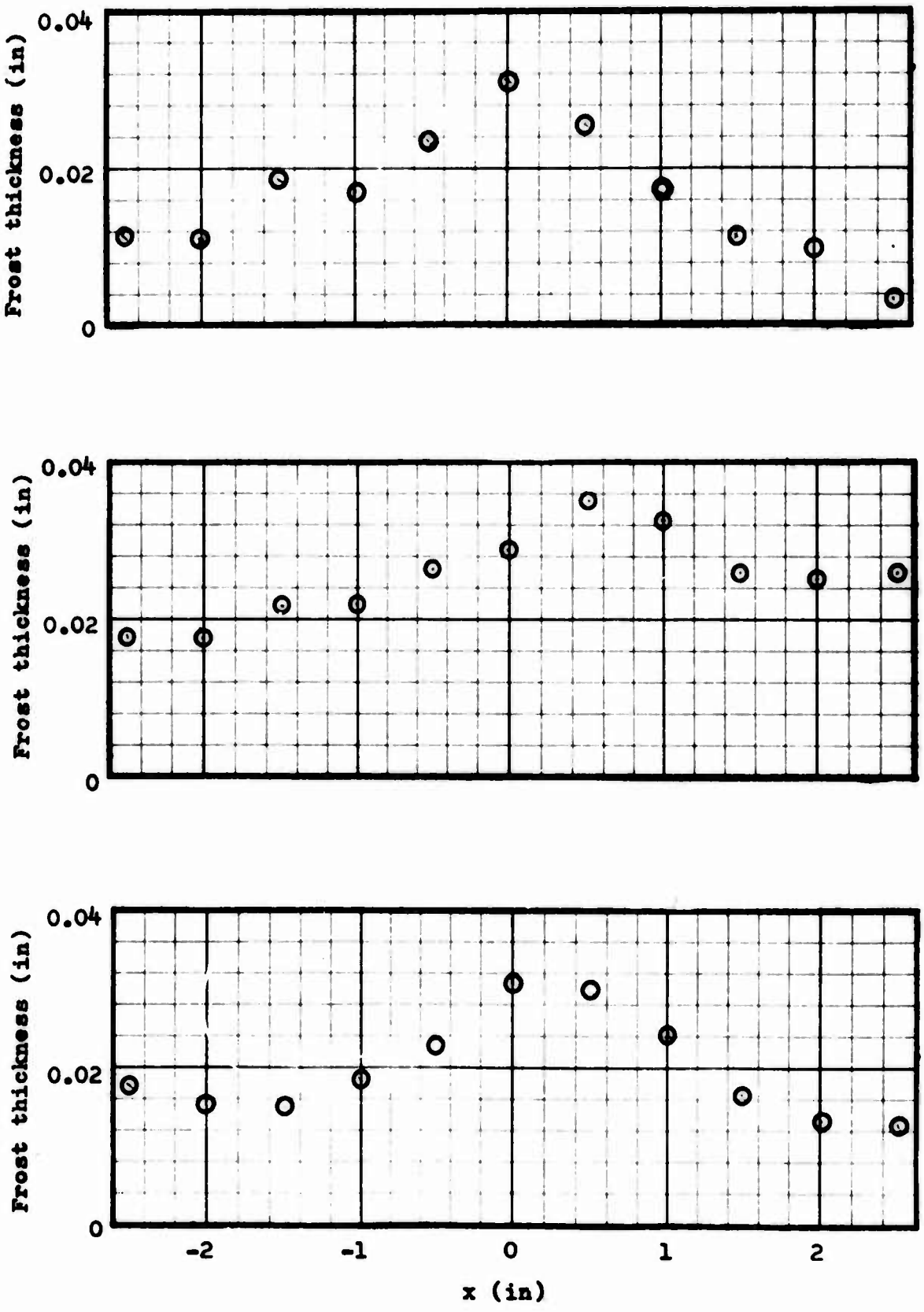

Fig. 59 Frost thickness distribution

APPENDIX B

CALCULATION OF WATER VAPOR CLUSTER SIZE

The calculation will be carried out for the case where the current is 150 μa and the total frost deposit on the test plate is 1.5 gm for five minutes.

Consider each ion being singly charged and each water vapor cluster containing only one ion. The total number of ions reaching the test plate in 5 minutes for a current of 150 μa is

$$N_i = \frac{150 \times 10^{-6} \times 300}{1.6 \times 10^{-19}} = 2.81 \times 10^{17}$$

where 1.6×10^{-19} coulomb is the electronic charge. The total number of water molecules condensed as frost on the test plate corresponding to a total frost deposit of 1.5 gm is

$$N_V = \frac{1.5}{18} \times 6.023 \times 10^{23} = 5.02 \times 10^{22}$$

where 6.023×10^{23} is Avogadro's number. If each water vapor cluster has only one ion, then each cluster must consist of the following number of water molecules.

$$\frac{N_V}{N_i} = 1.78 \times 10^5$$

APPENDIX C

THE SIX COEFFICIENTS OF Y, φ_1 AND φ_2

$$\varphi_{10} = \varphi_{20} = T_w \quad , \qquad Y_1 = 0$$

$$\varphi_{11} - \varphi_{21} = 0 \quad , \qquad \varphi_{11} + \varphi_{21} = \frac{2}{k}(C_3 - C_4 T_w)$$

$$Y_2 = \frac{1}{4a}\left[C_1 - \frac{C_2}{2}(\varphi_{10}+\varphi_{20})\right]$$

$$\varphi_{12} = \varphi_{22} = 0 \quad , \qquad Y_3 = 0$$

$$\varphi_{13} = \varphi_{23} = 0$$

$$\varphi_{13} + \varphi_{23} = -\frac{2}{k} C_4 Y_2(\varphi_{11}+\varphi_{21})$$

$$Y_4 = -\frac{C_2}{16a} Y_2(\varphi_{11}+\varphi_{21})$$

$$\varphi_{14} = \varphi_{24} = 0 \quad , \qquad Y_5 = 0$$

$$\varphi_{25} - \varphi_{25} = 0$$

$$\varphi_{15} + \varphi_{25} = -\left\{\frac{C_4}{45k}\left[18Y_2(\varphi_{13}+\varphi_{23}) + 12Y_4(\varphi_{11}+\varphi_{21})\right] + \frac{4}{5}(Y_2)^2(\varphi_{13}+\varphi_{23})\right\}$$

$$Y_6 = -\frac{C_2}{288a}\left[18Y_2(\varphi_{13}+\varphi_{23}) + 12Y_4(\varphi_{11}+\varphi_{21})\right]$$

In terms of the given quantities T_w, T_∞, $w_{1\infty}$, w_{1f}, L_f, h, h_m, a, k, ρ, ρ_f and b, the following expressions are obtained.

$$Y_2 = \frac{1}{4}\frac{\rho h_m}{\rho_f a}(w_{1\infty} - w_{1w})$$

$$Y_4 = -\frac{bk}{32}\left(\frac{\rho}{\rho_f}\frac{h_m}{ak}\right)^2\left[\rho L_f h_m(w_{1\infty}-w_{1w}) + h(T_\infty - T_w)\right](w_{1\infty}-w_{1w})$$

$$Y_6 = \frac{bk}{288}\left(\frac{\rho h_m}{\rho_f a k}\right)^3\left\{\frac{9}{2}(w_{1\infty}-w_{1w})(\rho b L_f \rho h_m + h)\cdot\left[\rho L_f h_m(w_{1\infty}-w_{1w}) + h(T_\infty - T_w)\right] + \frac{3}{4}b\left[\rho L_f h_m(w_{1\infty}-w_{1w}) + h(T_\infty - T_w)\right]^2\right\}(w_{1\infty}-w_{1w})$$

$$\varphi_{10} = \varphi_{20} = T_w$$

$$\varphi_{11} = \varphi_{21} = \frac{1}{k}\left[\rho L_f h_m (w_{1\infty} - w_{1w}) + h(T_\infty - T_w)\right]$$

$$\varphi_{13} = \varphi_{23} = -\frac{1}{2}\frac{\rho}{\rho_f}\frac{h_m}{ak^2}(\rho b L_f h_m + h)(w_{1\infty} - w_{1w})$$

$$\cdot\left[\rho L_f h_m (w_{1\infty} - w_{1w}) + h(T_\infty - T_w)\right]$$

$$\varphi_{15} = \varphi_{25} = \frac{(\rho b L_f h_m + h)}{90k}\left\{\left(\frac{\rho h_m}{\rho_f ak}\right)^2 (w_{1\infty} - w_{1w})(\rho b L_f h_m + h)\right.$$

$$\cdot\left[\rho L_f h_m (w_{1\infty} - w_{1w}) + h(T_\infty - T_w)\right]\left[\frac{9}{2} + \frac{1}{20}\left(\frac{\rho h_m}{\rho_f ak}\right)\right.$$

$$\left.\cdot (w_{1\infty} - w_{1w})\right] + \frac{3b}{4}\left(\frac{\rho h_m}{\rho_f ak}\right)^2\left[\rho L_f h_m (w_{1\infty} - w_{1w})\right.$$

$$\left.\left. + h(T_\infty - T_w)\right]^2 (w_{1\infty} - w_{1w})\right\}$$

REFERENCES

1. Choi, H. Y., "Electrohydrodynamic Boiling Heat Transfer," Tufts University Mechanical Engineering Report, T. U. M. E. R. 62-3, Tufts University, Boston, Mass., 1962.

2. Velkoff, H. R. and Miller, J. H., "Condensation of Vapor on a Vertical Plate with a Transverse Electrostatic Field," Journal of Heat Transfer, Vol. 87, pp. 197, 1965.

3. Choi, H. Y., "Electrohydrodynamic Condensing Heat Transfer," J. of Heat Transfer, Vol. 90, pp. 98, 1968.

4. Velkoff, H. R., "Electrofluidmechanics: Investigation of the Effects of Electrostatic Fields on Heat Transfer and Boundary Layers," ASD-TDR-62-650, Aeronautical System Division, Air Force System Command, WPAFB, Ohio, 1962.

5. Godfrey, R. D. and Velkoff, H. R., "An Interferometer Study of the Effects of Corona Discharge on the Temperature Profiles on a Flat, Uniform Temperature Plate in Forced Convection," Technical Report No. 3, Project 1864, Research Foundation, The Ohio State University, Columbus, Ohio, 1967.

6. Bartlett et al, J. T., "The Growth of Ice Crystals in an Electric Field," ZAMP, Vol. 14, pp. 599, 1963.

7. Arabadzhi, V. I., Bull. Izvestiya Acad. Sci. USSR, Geophys. Ser. 4, 1961; see also Prupacher, H. R., "The Effects of Electric Fields on Cloud Physical Processes," ZAMP, Vol. 14, pp. 590, 1963.

8. Poreh, M. and Cermak, J. E., "Flow Characteristics of a Circular Submerged Jet Impinging Normally on a Smooth Boundary," 6th midwest Conference on Fluid Mechanics, pp. 198, 1959.

9. Schrader, H., "Trocknung Ferchter Oberflachen Mittels Warmluftstrahlen; Stromungsvorgange und Stoffubertragung," VDI-Forschungsheft 484, 1961.

10. Brady, W. G. and Ludwig, G., "Theoretical and Experimental Studies of Impinging Uniform Jets," IAS Paper No. 13-29, 1963.

11. Malkus, W. V. R. and Vernis, G., "Surface Electroconvection," Physics of Fluid, Vol. 4, pp. 13, 1961.

12. Melcher, J. R., "Field Coupled Surface Waves," M. I. T. Press, Cambridge, Mass., 1963.

13. Taylor, G. I. and McEwan, A. D., "Stability of a Horizontal Fluid Interface in a Vertical Electric Field," J. of Fluid Mechanics, Vol. 22, pp. 1, 1965.

14. Lee, C. O. and Choi, H. Y., "Electrohydrodynamic Ridge Instability of a Thin Film Flowing Down an Inclined Plate," J. of Heat Transfer, Vol. 90, pp. 135, 1968.

15. Stach, V., "Influence of Electric Field on the Cooling Gas Flow in a Nuclear Reactor," International J. of Heat and Mass Transfer, Vol. 5, pp. 445, 1962.

16. Chuang, T. and Velkoff, H., "Analytical Studies of the Effects of Ionization on Fluid Flows," Technical Report No. 6, Project 1864, Research Foundation, The Ohio State University, Columbus, Ohio, 1967.

17. Velkoff, H. R. and Pejack, E. R., "The Deflection of Electrically-Induced Secondary Flows in a Pipe by Means of Electrostatic Probes," Technical Report No. 7, Project 1864, Research Foundation, The Ohio State University, Columbus, Ohio, 1967.

18. Chung, R. M. and Algren, A. B., "Frost Formation and Heat Transfer on a Cylinder Surface in Humid Air Cross Flow," ASHRAE Transactions, Vol. 65, pp. 213, 1958.

19. Portnov, I. G., "Exact Solution of Freezing Problem with Arbitrary Temperature Variation of Fixed Boundary," Soviet Physics - Doklady, Vol. 7, pp. 186, 1962.

20. Van der Pol, B. and Bremmer, H., "Operational Calculus Based on Two-sided Laplace Integral," Cambridge University Press, Cambridge, England, 1955.

21. Jackson, F., "The Solution of Problems Involving Melting and Freezing of Finite Slabs by a Method due to Portnov," Proc. Edinburgh Math. Soc., Vol. 14, pp. 109, 1964.

22. Westphal, K. O., "Series Solution of Freezing Problem with the Fixed Surface Radiating into a Medium of Arbitrary Varying Vol. 10, pp. 195, 1967.

23. Beatty, K. O., Finch, E. B. and Schoenborn, E. M., "Heat Transfer From Humid Air to Metal Under Frosting Conditions," Refrigerating Engineering, Vol. 59, pp. 1203, 1951.

24. Barron, R. F., "Heat and Mass Transfer to a Cryosurface in Free Convection," Ph.D. Dissertation, Department of Mechanical Engineering, The Ohio State University, Columbus, Ohio, 1964.

25. Yonko, J. D. and Sepsy, C. F., "An Investigation of the Thermal Conductivity of Frost While Forming on a Flat Plate Horizontal Plate," Transactions ASHRAE Vol. 73, Part II, No. 2043, 1967.

26. Chattock, A. P., "On the Velocity and Mass of Ions in the Electric Wind in Air," Philosophical Magazine, Vol. 48, pp. 401, 1899.

27. Robinson, M., "Movement of Air in the Electric Wind of the Corona Discharge," Transactions AIEE, Vol. 80, Part I, pp. 143, 1961.

28. Schlichting, H., Boundary Layer Theory, McGraw-Hill Book Co., Inc., New York, 1960.

29. Landau, L. D. and Lifshitz, E. M., Fluid Mechanics, Pergamon Press, Oxford, 1959.

30. Stuetzer, O. M., "Ion Drag Pressure Generation," J. of Applied Physics, Vol. 30, pp. 984, 1959.

31. Kapzow, N. A., Electronic Processes in Gases and in Vacuum, veb deutscher Verlag der Wissenschaften, Berlin, 1955.

32. Eckert, E. R. G. and Drake, R. M., Heat and Mass Transfer, McGraw-Hill Book Co. Inc., New York, 1959.

33. Sparrow, E. M., "Unsteady Stagnation Point Heat Transfer," NASA TN D-77, 1959.

34. Eckert, E. R. G. and Lieblein, V., "Berechnung des Stoffuberganges an einer ebenen, langs angestromten Oberflache bei grossen Teildruckgefalle," Forschung auf dem Gebiete des Ingenieurwesens, Vol. 16, pp. 33, 1949.

35. Spalding, D. B., "Mass Transfer in Laminar Flow," Proc. Roy. Soc. Lond., Ser. A, Vol. 221, pp. 78, 1954.

36. Sugawara, S., et al., "Research on Heat Transfer during the Period of Frost Formation," Transactions Japan Society of Mechanical Engineers, 1957.

37. Glauert, M. B., "The Wall Jets," J. of Fluid Mechanics, Vol. 1, pp. 625, 1956.

38. Glauert, M. B., "On Laminar Wall Jets," in Boundary Layer Research, edited by H. Goertler, Springer-Verlag, Berlin, pp. 72, 1958.

39. Riley, N., "Effects of Compressibility on a Laminar Wall Jet," J. of Fluid Mechanics, Vol. 4, pp. 615, 1958.

40. Whitehurst, C. A., "An Investigation of Heat and Mass Transfer by Free Convection From Humid Air to a Metal Plate Under Frosting Conditions," Ph.D. Dissertation, Texas A and M, 1962.

41. Dean, R. C., Aerodynamic Measurements, pp. 73, M. I. T. Press, 1953.

Unclassified
Security Classification

DOCUMENT CONTROL DATA - R & D

(Security classification of title, body of abstract and indexing annotation must be entered when the overall report is classified)

1. ORIGINATING ACTIVITY (Corporate author)
The Ohio State University Research Foundation
Columbus, Ohio

2a. REPORT SECURITY CLASSIFICATION
Unclassified

2b. GROUP
N/A

3. REPORT TITLE
HEAT AND MASS TRANSFER TO A SUBFREEZING SURFACE IN A NON-UNIFORM ELECTRIC FIELD

4. DESCRIPTIVE NOTES (Type of report and inclusive dates)
Technical

5. AUTHOR(S) (First name, middle initial, last name)
Chuang, Teng Hsueh and Velkoff, Henry, R.

6. REPORT DATE
September 1968

7a. TOTAL NO. OF PAGES
188

7b. NO. OF REFS
41

8a. CONTRACT OR GRANT NO.
DA-31-124-ARO-D-246

b. PROJECT NO.
2001050B700, 1D12, 40A142

c.

d.

9a. ORIGINATOR'S REPORT NUMBER(S)
Technical Report # 9

9b. OTHER REPORT NO(S) (Any other numbers that may be assigned this report)

10. DISTRIBUTION STATEMENT
Distribution of this document is unlimited.

11. SUPPLEMENTARY NOTES

12. SPONSORING MILITARY ACTIVITY
US Army Research Office - Durham
Durham, North Carolina

13. ABSTRACT

An experimental and analytical program was undertaken to investigate the behavior of frost formation under an impinging electric wind induced by a positive wire-plane corona in a nonuniform electric field. A vertical test plate precooled to subfreezing temperatures was exposed to the ambient air and the effects of electric fields were studied through the application of a high voltage between the grounded test plate and a corona wire. Considerable increases in heat and mass transfer were found. The changes were attributed to the alteration of flow field from free convection to forced convection.

A simple theoretical model was developed for predicting the effects of electric fields upon the heat and mass transfer processes associated with frost formation. Two regions of the flow field created by the impinging electric wind are of primary importance in heat and mass transfer, namely, the stagnation flow and the wall jet regimes. In the stagnation flow, a linear relation for the local heat and mass transfer coefficients was assumed between the stagnation point and the wall jet region. In the wall jet, the analysis was based on laminar flow. The mass transfer predicted by this model agrees quite satisfactorily with experimental results, but discrepancy between theory and experiment was observed in heat transfer.

An analysis was also made of a simplified model of transient heat conduction in a frost layer. Using a method due to Portnov the position and the temperature of the progressing frost-air interface was obtained in a series expansion in powers of $\sqrt{t}$. The coefficients up to the power $n = 6$ were given.

DD FORM 1 NOV 65 1473

Unclassified
Security Classification

14 KEY WORDS	LINK A		LINK B		LINK C	
	ROLE	WT	ROLE	WT	ROLE	WT
Electric fields Heat transfer Transient heat conduction Impinging electric wind						